MOLECULAR, SUPRAMOLECULAR AND BIOHYBRID AQUEOUS PHTHALOCYANINE SYSTEMS AS PHOTOACTIVE MATERIALS FOR ENERGY CONVERSION AND NANOMEDICINE

DOCTORAL THESIS

EDUARDO ANAYA PLAZA

Madrid, 2016

FACULTAD DE CIENCIAS

DEPARTAMENTO DE QUÍMICA ORGÁNICA

MOLECULAR, SUPRAMOLECULAR AND BIOHYBRID AQUEOUS PHTHALOCYANINE SYSTEMS AS PHOTOACTIVE MATERIALS FOR ENERGY CONVERSION AND NANOMEDICINE

EDUARDO ANAYA PLAZA

Doctoral Thesis

Supervised by Dr. Andrés de la Escosura Navazo and

Prof. Tomás Torres Cebada

Madrid, May 6, 2016

Moving forward, shoulder to shoulder, trying to become Giants

The present work has been developed at the Organic Chemistry Department of Universidad Autónoma de Madrid, under the supervision of Dr. Andrés de la Escosura Navazo and Prof. Tomás Torres Cebada.

During the development of the present work, the following predoctoral research internships have been conducted in the following research centers:

Fiedrich-Alexander-Universität Erlangen-Nüremberg, Erlangen, Germany, under the supervision of Prof. Dirk M. Guldi from September 1st to 30th, 2014.

Biohybrid Materials research group, School of Chemical Technology, Aalto University, Espoo, Finland, under the supervision of Prof. Mauri A. Kostiainen, from April 1st to June 30th, 2015.

To date, the results reported in the present work have led to the following publications:

(i) "Small molecule solar cells based on a series of water-soluble zinc phthalocyanine donors", J.W. Ryan, E. Anaya-Plaza, A. de la Escosura, T. Torres and E. Palomares, *Chem. Commun.*, **2012**, *48*, 6094-6096.

(ii) "Self-assembly triggered by self-assembly: Optically active, paramagnetic micelles encapsulated in protein cage nanoparticles", J.G. Millan, M. Brasch, E. Anaya-Plaza, A. de la Escosura, A.H. Velders, D.N. Reinhoudt, T. Torres, M.S.T. Koay and J.J.L.M. Cornelissen, *J. Inorg. Biochem.*, **2014**, *136*, 140-146.

(iii) "Quaternized Pyridyloxy Phthalocyanines Render Aqueous Electron-Donor Carbon Nanotubes as Unprecedented Supramolecular Materials for energy Conversion", E. Anaya-Plaza, M.M. Oliva, A. Kunzmann, C. Romero-Nieto, R.D. Costa, A. de la Escosura, D.M. Guldi and T. Torres, *Adv. Funct. Mater.*, **2015**, *25*, 7418-7427.

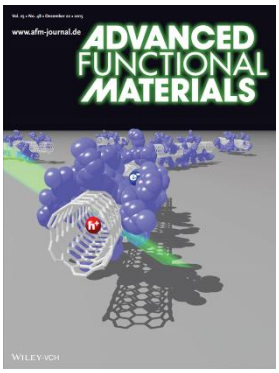

(iv) "Hierarchical Organization of Organic Dyes and Protein Cages into Photoactive Crystals", J. Mikkila, E. Anaya-Plaza, V. Liljeström, J.R. Caston, T. Torres, A. de la Escosura and M.A. Kostiainen, *ACS Nano*, **2016**, *10*, 1565-1571.

(v) "Photoactive Cellulose Nanocrystals by Supramolecular Surface Immobilization of Phthalocyanine Photosensitizers", E. Anaya-Plaza, E. van de Winckel, J. Mikkilä, J.-M. Malho, O. Ikkala, T. Torres, M.A. Kostiainen and A. de la Escosura, *Submitted*.

(vi) "Aqueous Phthalocyanine-Fullerene Supramolecular Hybrids as a Novel Type of Donor-Acceptor Photosynthetic Reaction Centre", E. Anaya-Plaza, M. Sekita, S. Bauroth, A. de la Escosura, D.M. Guldi and T. Torres, *Manuscript in preparation*.

(vii) "Unprecedented Aggregation Mode of Phthalocyanines in Aqueous Media Triggered by the Incorporation of Pyrene-Containing Cationic Substituents", E. Anaya-Plaza, M. Sekita, S. Bauroth, A. de la Escosura, D.M. Guldi and T. Torres, *Manuscript in preparation*.

Abbreviations and Acronyms

ABs:	Antibodies
AFt:	Apoferritin
CA:	Contrast Agent
CCMV:	Cowpea Chlorotic Mottle Virus
CP:	Coat Protein
CT:	Computed Tomography
EPR:	Enhanced Permeability and Retention
FONs:	Functional Organic Nanoparticles
FPLC:	Fast Protein Liquid Chromatography
FTO:	Fluorine-doped Tin Oxide
ISC:	Intersystem Crossing
MOFs:	Metal-Organic Frameworks
MSNs:	Mesoporous Silica Nanoparticles
NIR:	Near-Infrared
NPs:	Nanoparticles
OCT:	Optical Coherence Tomography
OFET:	Organic Field-Effect Transistor
PAI:	Photoacustic Imaging
PDT:	Photodynamic Therapy
PET:	Positron Emission Tomography
PS:	Photosensitizer
PTT:	Photothermal Therapy
QDs:	Quantum Dots
ROS:	Reactive Oxigen Species

SERS:	Suface Enhanced Raman Scattering
SMOSC:	Small-Molecule Organic Solar Cell
SPECT:	Single-Photon Emission Computed Tomography
SPR:	Surface Plasmonic Resonance
STM:	Scanning Tunneling Microscopy
SWCNT:	Single-Walled Carbon Nanotube
TGA:	Thermogravimetric Analysis
US:	Ultrasound
VLPs:	Virus-like Particles
VPF:	Vascular Permeability Factor

Agradecimientos

Llegar a escribir una tesis doctoral, representa un gran paso a nivel académico y personal, en el que recuerdas a mucha gente que te ha inspirado o ayudado a conseguirlo. En estas líneas me gustaría rendirles un pequeño homenaje y hacerles partícipes de este logro ya que, si hay algún momento para ponerse sentimental, es este.

En primer lugar me gustaría agradecer el apoyo recibido de mis supervisores. A **Tomás** que, desde aquel momento en el que subimos a su despacho a preguntar por una beca de colaboración, supo ver más allá de unas calificaciones y decidió apostar por mí. Espero haber estado a la altura de las expectativas y, si en algún momento de mi vida está en mis manos tomar decisiones similares, espero ser capaz de seguir tu ejemplo y ser capaz de ver a la persona. De ti me llevo, a parte de los conocimientos científicos que has sido capaz de trasmitirme, la importancia del networking y el no dejar de ser persona, independientemente del cargo que ocupes. Ah, y lo de la FPI ya está olvidado, no te preocupes. Por otro lado querría expresar mi más sincera gratitud a **Andrés**. Desde el primer momento, incluso siendo aún estudiante de licenciatura, siempre mantuviste una actitud abierta y dialogante hacia mis ideas y propuestas. Así, sintiéndote valorado incluso en casos en los que estaba equivocado, es muy fácil crecer como persona y como profesional. Me llevo conocimientos y habilidades en áreas muy distintas y, sorprendentemente, un gusto especial por la rigurosidad a la hora de preparar textos y figuras. Si hoy esta tesis es una realidad es, sin duda alguna, por un esfuerzo por tu parte comparable al mío.

En segundo lugar no puedo si no agradecerles a **mis padres** su incondicional apoyo desde siempre pero, especialmente, cuando tomé la decisión de doctorar. Gracias por vuestros consejos y vuestra presencia constante. Espero que este trabajo, que culmina un esfuerzo de casi seis años, os haga estar al menos tan orgullosos como yo lo estoy. **Bea**, querría Me gustaría añadir aquí a quien sin duda sabrá apreciar este logro de manera un poco más especial: **Manolo**, mira lo que he conseguido.

Volviendo a la rama académica, me gustaría recordar a maestros que han influido en mi trayectoria académica/profesional. Desde aquellos que hicieron que me picara el gusanillo por la química en el instituto, como **José Luis Serna** y **Jose Ignacio del Barrio**, a aquellos que una vez en la carrera, se quedaron grabados como excelentes maestros. Entre ellos querría destacar a **Juan Carlos Carretero**, **Jose Manuel Yáñez**, **Ramón Gómez** y **Christian Claessens**. De este último querría destacar no solo su labor como maestro en la

carrera como en el master, así como posteriormente compañero en el laboratorio. Dejaste un gran hueco entre nosotros.

De la carrera quizá no me llevo a mucha gente, pero sin duda, de gran calidad. Siempre os lo he dicho, si fuimos una buena generación no fue únicamente por que hubiera estudiantes brillantes (que los había), si no por que supimos/supisteis trabajar en equipo, de manera desintersada. Para vosotros va mi frase introductoria, en la que he querido resumir todos estos años (2006-2016): al ir hombro con hombro nos estamos convertiendo en pequeños gigantes. Desde el principio esto no hubiera sido posible sin gente como **Pablito**, **Jorge**, **Vio**, **Carlos** o **Dani**. Un hueco especial os reservo a vosotros, **Javi** y **Germán**, que me arrastrasteis a este laboratorio y, aunque las malas lenguas dicen que al principio íbamos juntos hasta a rotar, yo juraría que no era para tanto. Me siento muy orgulloso de haber compartido este tiempo con vosotros y ver lo que estais consiguiendo.

Quisiera seguir con la gente del labo: si algo ha caracterizado a la tercera planta es el buen ambiente de trabajo, y mira que somos gente de mil sitios. Desde los seniors como **Gema**, **Mariví**, **Gianni**, **Gunther**, **David** y **Puri**, pasando por los "mandos intermedios" como **Miguelito**, **Ismael** y **Max** y terminando por el resto de compañeros que están o han pasado por el labo: **Laura**, **Lara**, **Giulia**, **Mine**, **Irene**, **François**, **Uwe**, **Mari-Eleni**, **Olga**, **Francesca**, **Anita**, **Vanessa**, **Carol**, **Ettore**, **Angel**, **Nico**, **Julia**, **Juan**, **Maria Medel**, **David Guzmán** y **Joana**. Seguro que me dejo a gente, espero que lo entendáis y sepáis disculparme. De nuevo, un hueco especial para **Eveline**, **Alja** y **Sara**, el Tea Time Team. Pues no nos lo hemos pasado bien… A los nuevos: bienvenidos y ánimo, que todo se cura, hasta un doctorado.

I would like to thank as well the oportunity given by **Prof. Mauri A. Kostiainen** and his research group, which kindly host me in Espoo for three months and where I met a bunch of wonderful people. Special mention has to be given to **Joona**, who took care of me and guided me throught the Finnish bureaucracy as well as through the Finnish way of life. Aditionally, I would like to thank **Prof. Dirk M. Guldi** and his research group as well, which kindly host me in Erlangen, not only in the lab but also afterworks. Especially to my closest co-workers there, **Michael** and **Stefan**, that kindly taught me those complex physical experiments. I would like to add **Lukasz** to this international list, even if we met for a short period of time in Madrid, I'm sure we will meet again.

Sin duda alguna hay mucha gente fuera del ámbito académico que, directa o indirectamente, se han visto involucrados en este trabajo: **Alex**, **Serj**, **Mike**, **Moe**, **Pons**, los

lunes del **CTA**… Disculpadme que no os nombre a todos, pero sabed que estais muy presentes.

Y como en las publis, el autor principal va al final. A mi alma gemela desde hace nueve años, con quien tengo la maravillosa oportunidad de casarme en octubre y con quien no solo he pasado la carrera y el doctorado, si no todo lo que me quede por vivir. **Astrid**, nunca podré expresar, mucho menos por escrito, lo que el tenerte a mi lado ha significado. Pero gracias.

Table of contents

INTRODUCTION
Nanotechnology: a big breakthrough in science

Introduction

1. Nanotechnology: a big breakthrough in science

Basic science has the role to of describe and understand natural processes that, once applied to society, improves the standard of living. Since the industrial revolution at the XVIII century, the search for new materials like metal derivatives as steel, ceramic materials as thermal and electrical insulators, and synthetic fibers as Nylon, continuously rises new and enhanced properties in comparison to the old ones. Development of new materials has gone hand-in-hand with an increasingly faster application by the industry and, subsequently, their implementation in the society. In 1959, Nobel Prize Richard Feynman in his famous "*There's Plenty of Room at the Bottom*" dissertation,[1] proposed an atom-to-atom manipulation as a novel strategy for the synthesis of new materials. These ideas became an entire new research field called nanoscience by two capital breakthroughs: (i) the development of the scanning tunnelling microscope (STM), and (ii) the discovery of two new allotropic forms of carbon (fullerene and carbon nanotubes). The STM, developed in 1981, allowed atomic resolution microscopy and thereafter, in 1989, allowed atom-by-atom manipulation. On the other hand, the discovery of C_{60} fullerene[2] and single-walled carbon nanotubes (SWCNTs),[3] with completely new properties, opened a field where not only the atomic composition but also organization rises unprecedented and outstanding properties.

In the last three decades, nanotechnology has been a hot research topic in fields such as medicine (nanobiotechnology or nanomedicine), energy conversion, environmental science, information technology, communications and heavy industry. Hence, this relatively young multidisciplinary field is making a huge impact by synthesizing and characterizing old and new materials in the nanoscale and exploiting the arising properties. To this end, two different strategies so-called *top-down* and *bottom-up* has been follow, depending on the approach employed to produce nanoscaled materials.[4] (i) The *top-down* approach is based on the clasical microfabrication, a collective term used for various kinds of material removal techniques like cutting, etching, grinding, and most employed, lithography (such as photo-, ion beam-, electron- or X-ray- lithography). Most common technique used today is the photolithography, i.e. the use of ultraviolet (UV) light as a pattern source. Light carves

---

1 Richard Feynman, "There's Plenty of Room at the Bottom" at the American Physical Society meeting at Caltech, December 29th, **1959**.

2 H. W. Kroto, J. R. Heath, S. C. O'Brien, R. F. Curl and R. E. Smalley, *Nature*, **1985**, *318*, 162-163.

3 a) S. Iijima, *Nature*, **1991**, *354*, 56-58.; b) A. Oberlin, M. Endo and T. Koyama, *J. Cryst. Growth*, **1976**, *32*, 335-349.

4 G.A. Ozin and A. Arsenault, in *Core Concepts in Supramolecular Chemistry and Nanochemistry*, ed. J.W. Steed, D.R. Turner and K.J. Wallace, John Wiley & Sons, Ltd, Chinchester, West Sussex, England, **2007**, pp. 229-271.

the pattern on a photoactive organic polymer (the photoresists) which is coated onto a silicon wafer. The pattern then defines which areas of the underlying wafer are exposed for material deposition or removal. This process is used to etch integrated circuits that are used in modern computer processors and memory chips.[5] On the other hand, the *bottom-up* approach consists of the building up of nanomaterials from smaller building blocks. This approach has given rise to nanochemistry, typically with the use of self-assembly methods for the formation of highly ordered two- and three-dimensional nanoscale structures, mimicking the natural world. On this behalf, molecules linked by supramolecular interactions are good potential building blocks for nanoscale architectures. Molecules are more convenient building blocks than atoms, as free atomos are highly reactive and difficult to generate and handle. More over, despite that employed molecules exhibit distinct shapes and might already have particular properties, the underliying aim of self-organization is rise new and enhanced properties when comparing to their monomeric form.[6]

In this thesis, we will focus on *bottom-up* approaches toward application in nanomedicine and solar energy conversion. The next subsections serves as an introduction to both fields.

1.1 Nanomedicine

Nanostructured materials present numerous advantages in different areas of medicine, yet making its biggest impact in oncology.[7] One of the fundamental difficulties in cancer treatment is the great genetic distribution even in individual patients.[8] Nanomedicine displays a new set of strategies, as shown in Figure 1, facilitating personalized therapies that can be adapted to the every individual patient. Various aspects related to those strategies are shorly discussed below.

---

5 J. Henzie, J.E. Barton, C.L. Stender and T.W. Odom, *Acc. Chem. Res.*, **2006**, *39*, 249-257.

6 S. Zhang, *Nat. Biotech.*, **2003**, *21*, 1171-1178.

7 a) K. K. Jain, *BMC Med.*¸**2010**, *8*, 83. b) T. L. Doane and C. Burda, *Chem. Soc. Rev.*, **2012**, *41*, 2885-2911. c) H. Maeda, *J. Control. Release*, **2012**, *164*, 138-144.

8 a) T. Sjöblom, S. Jones, L.D. Wood, D.W. Parsons, J. Lin, T.D. Barber, D. Mandelker, R.J.Leary, J. Ptak, N. Silliman, S. Szabo, P. Buckhaults, C. Farrell, P. Meeh, S.D. Markowitz, J. Willis, D. Dawson, J.K. Willson, A.F. Gazdar, J. Hartigan, L. Wu, C. Liu, G. Parmigiani, B.H. Park, K.E. Bachman, N. Papadopoulos, B. Vogelstein, K.W. Kinzler and V.E. Velculescu, *Science*, **2006**, *314*, 268–274. b) L.D. Wood, D.W. Parsons, S. Jones, J. Lin, T. Sjöblom, R.J. Leary, D. Shen, S.M. Boca, T. Barber, J. Ptak, N. Silliman, S. Szabo, Z. Dezso, V. Ustyanksky, T. Nikolskaya, Y. Nikolsky, R. Karchin, P.A. Wilson, J.S. Kaminker, Z. Zhang, R. Croshaw, J. Willis, D. Dawson, M. Shipitsin, J.K. Willson, S. Sukumar, K. Polyak, B.H. Park, C.L. Pethiyagoda, P.V. Pant, D.G. Ballinger, A.B. Sparks, J. Hartigan, D.R. Smith, E. Suh, N. Papadopoulos, P. Buckhaults, S.D. Markowitz, G. Parmigiani, K.W. Kinzler, V.E. Velculescu and B. Vogelstein, *Science*, **2007,** *318*, 1108–1113.

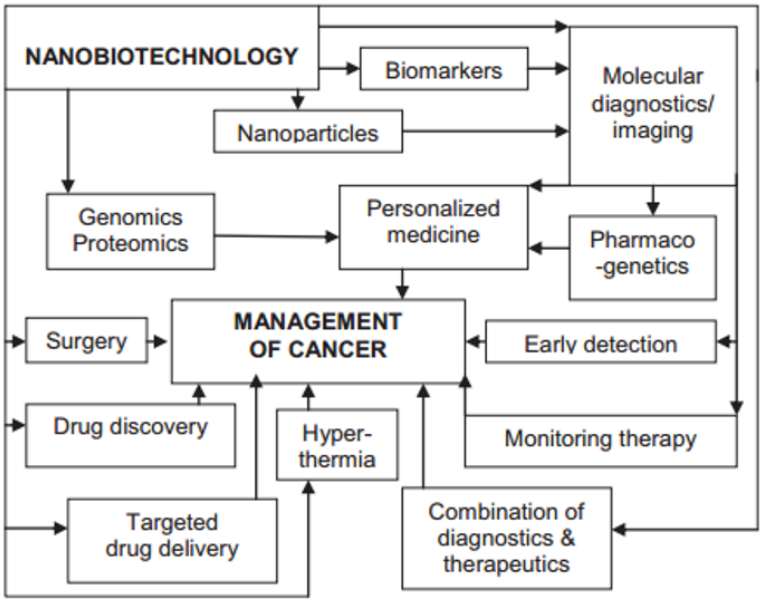

Figure 1. Schematic role of nanobiotechnology and its interaction with various other technologies and approaches used in the management of cancer, as shown in 7b.

1.1.1 Nanodrug building blocks

Nanotechnology provides a wide catalogue of materials to be employed as nanocarriers, targeting, labeling or therapeutic agents (Figure 2), which range from inorganic systems[7a] like mesoporous silica nanoparticles (MSNs),[9] metallic nanoparticles (NPs),[10] semiconducting nanoparticles or *quantum dots* (QDs),[11] and metal-organic frameworks (MOFs),[12] passing through organic molecular materials like dye photosensitizers (PS), dendrimers and polymers,[13] ending with biomimetic materials[14] that involve such as nucleic acids, peptides, liposomes, micelles and virus-like particles (VLP).[15]

---

9 a) F. Tang, L. Li and D. Chen, *Adv. Mater.*, **2012**, *24*, 1504-1534. b) Z. Li, J.C. Barnes, A. Bosoy, J.F. Stoddart and J.I. Zink, *Chem. Soc. Rev.*, **2012**, *41*, 2590-2605.

10 N. Khlebtsov and L. Dykman, *Chem. Soc. Rev.*, **2011**, *40*, 1647-1671.

11 a) H.M.E. Azzazy, M.M.H. Mansour and S.C. Kazmierczak, *Clin. Biochem.*, **2007**, *40*, 917-927. b) Y. Volkov, *Biochem. Bioph. Res. Co.*, **2015**, *468*, 419-427.

12 P. Horcajada, T. Chalati, C. Serre, B. Gillet, C. Sebrie, T. Baati, J.F. Eubank, D. Heurtaux, P. Clayette, C. Kreuz, J-S. Chang, Y.K. Hwang, V. Marsaud, P-Nhi. Bories, L. Cynober, S. Gil, G. Férey, P. Couvreur and R. Gref, *Nat. Mater.*, **2010**, *9*, 172-178.

13 M. Elsabahy and K.L. Wooley, *Chem. Soc. Rev.*, **2012**, *41*, 2545-2561.

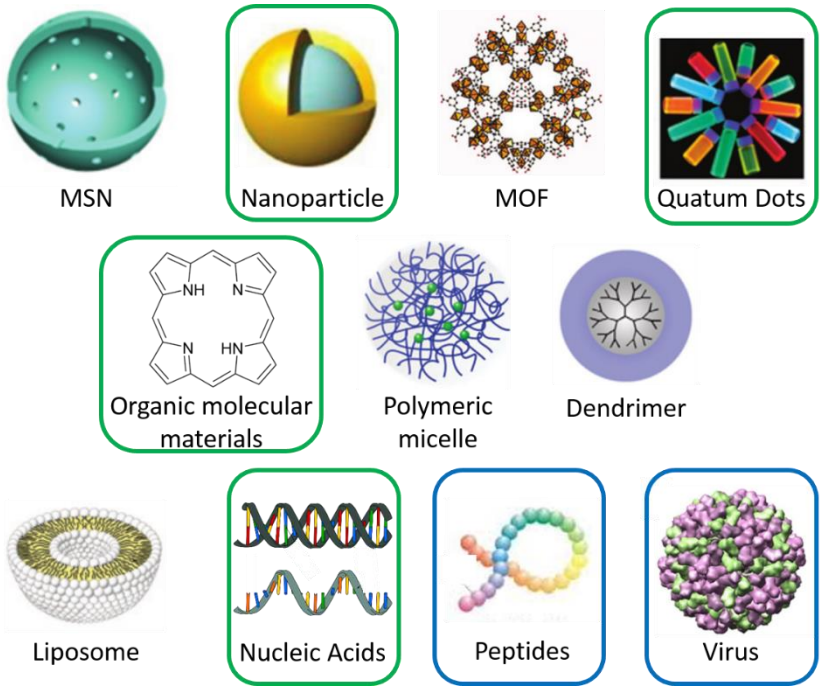

Figure 2. Main building blocks to be employed as nanocarriers, targeting, labelling or therapeutic agents. Highlighted, those used as therapeutical (green) and selective targeting (blue) aggents.

1.1.2. Targeting and drug delivery

Apart from controlled design and synthesis of new drugs, other important factor that boosts nanomedicine contribution to oncology is the natural trend of macromolecules and nanoscale materials to accumulate in solid tumours, known as the enhanced permeability and retention (EPR) effect or passive targeting. Due to an increased cellular growth in cancerous cells, a stimulated production of blood vessels or angiogenesis is required, mediated by vascular endothelial growth factor or vascular permeability factor (VPF) signal protein.[16] These newly formed vessels presents abnormal form and architecture with enhanced vascular permeability due to a poor align of endothelial cells. Lack of lymphatic drainage leads to an increased accumulation of macromolecules in solid

---

[14] W.R. Algar, D.E. Prasuhn, M.H. Stewart, T.L. Jennings, J.B. Blanco-Canosa, P.E.Dawson and I.L. Medintz, *Bioconjugate Chem.*, **2011**, *22*, 825-858.

[15] Y. Ma, R.J.M. Nolte and J.J.L.M. Cornelissen, *Adv. Drug Deliver. Rev.*, **2012**, *64*, 811-825.

[16] a) Y. Matsumura, H. Maeda, *Cancer Res.*, **1986**, *46*, 6387-6392. b) H. Maeda, H. Nakamura, J. Fang, *Adv. Drug Deliver. Rev.*, **2013**, *65*, 71-79.

tumors. However, there is a heterogeneity among the tumors types and, even in the same tumor type, there is a difference in pore size depending on the location (i.e. primary or methastases).[17]

Active targeting, on the other hand, implies that targeting ligands such as saccharides, antibodies, peptides, nucleic acid aptamers or other small biomolecules are conjugated to the surface of the nanodevice. Those biomolecules recognise and bind selectively receptors that are unique or are overexpressed in cancerous cells, enhancing tumor binding and shortening the time between drug administration and treatment.[18]

In this regard, foremost has been made in recent years toward efficient targeting/delivery.[19] Targeting the disease in a specific manner avoids undesired effects and extents the drug circulation time by inhibiting an early clearance from the organism. New nanocarrier platforms exhibiting great potentials in improving drug packaging, delivery and targeting are currently emerging. These systems could offer several advantages, e.g. (i) prevention of premature drug degradation or interaction with the host organism, (ii) enhancement of drug targeting to the desired tissues (e.g. tumors) and (iii) control over the drug tissue distribution profile. Some nanocarriers also present a specific design to trigger drug release by endogenous (i.e. enzymes or variations in pH and/or redox conditions) or exogenous (i.e. thermal, magnetic or electric fields, ultrasounds or light) stimuli.[20]

1.1.3. Multimodal Imaging

Multimodal imaging[7a,21] is based on the combination of two or more contrast agents (CAs) (Table 1) in order to overcome limitations of most commonly used multiple imaging techniques; which are briefly described below. (i) Optical Imaging: based on UV, visible or near-infrared (NIR) light absorption by a light-absorbing CA and subsequent emission at a determined wavelength (λ). This interaction can be due to fluorescence of organic dyes, enhanced scattered light from surface plasmonic resonance (SPR) in metallic NPs or

---

17 a) U. Prabhakar, H. Maeda, R. K. Jain, E. M. Sevick-Muraca, W. Zamboni, O. C. Farokhzad, S. T. Barry, A. Gabizon, P. Grodzinski and D. C. Blakey, *Cancer Res.* **2013**, *13*, 2412-2417. b) H. Maeda, *Cancer Science*, **2013**, *104*, 779-789.

18 a) M. Wang, M. Thanou, *Pharmacol. Res.*, **2010**, *62*, 90-92. b) V. Soundararajan and R. Sasisekharan in *Handbook of Nanophysics: Nanomedicine and Nanorobotics*, ed. K.D. Sattler, Taylor & Francis, Florida, **2001**, vol. 7, ch. 34.

19 A.Z. Wang, R. Langer and O.C. Farokhzad, *Annu. Rev. Med*., **2012**, *63*, 185-198.

20 a) D. Peer, J.M. Karp, S. Hong, O.C. Farokhzad, R. Margalit, R. Langer, *Nat. Nanotechnol.*, **2007**, *2*, 751–760. b) S. Mura, J. Nicolas and P. Couvreur, *Nat. Mater.*, **2013**, *12*, 991-1003.

21 a) D-E. Lee, H. Koo, I-C. Sun, J.H. Ryu, K. Kim and I.C. Kwon, *Chem. Soc. Rev.*, **2012**, *41*, 2656-2672. b) W. Cai and X. Chen, *Small*, **2007**, *11*, 1840-1854. c) J. Kim, Y. Piao and T. Hyeon, *Chem. Soc. Rev.*, **2009**, *38*, 372-390. d) A. Louie, *Chem. Rev.*, **2010**, *110*, 3146-3195.

photoluminescence in QDs; (ii) Magnetic Resonance Imaging (MRI): takes advantage of paramagnetic ions like Gd^{+3} and Mn^{+2} or superparamagnetic nanoparticles such as Fe_3O_4 as contrast agents; (iii) Optical Coherence Tomography (OCT): a technique based on the interaction of NIR light with tissues, enhanced by the NPs accumulation. (iv) Positron Emission Tomography (PET) and Single-Photon Emission Computed Tomography (SPECT): both techniques based on the emission of γ-rays of a radionuclide. (v) Computed Tomography (CT): uses a combination of different X-Ray images to set up a 3D model. Heavy metal NPs enhance the interaction with the radiation. (vi) Ultrasound (US) and Photoacoustic Imaging (PAI): based on non-radiative relaxation of NPs upon light-induced excitation, generating vibrations in the US range. (vii) Surface Enhanced Raman Spectroscopy (SERS): Raman spectroscopy provides a signal 14 orders of magnitude less scattered than fluorescence, resulting into a much sensitive detection of tumor-accumulated NPs.

Table 1. Imaging modalities using nanomaterials.

Modality	Components
Optical Imaging	Organic dyes, dye-doped silica, quantum dots, lanthanide atoms, carbon nanotubes.
MRI	Paramagnetic ions (Gd^{3+}, Mn^{2+}) and NPs (Gd_2O_3, MnO), and superparamagnetic NPs (Fe_3O_4, $MnFe_2O_4$, FeCo).
OCT	Gold nanostructures (spherical NPs, nanorods, nanoshells, nanocages).
PET, SPECT	Radioisotopes (^{18}F, ^{124}I, ^{64}Cu, ^{99}Tc, ^{11}In).
CT	Iodine, gadolinium, gold NPs and bismuth sulfide nanoplates.
US, PAI	Perfluorocarbon NPs and gold nanostructures.
SERS	Gold nanostructures.

MRI: magnetic resonance imaging. OCT: optical coherence tomography. PET: positron emission tomography. SPECT: single photon emission computed tomography. CT: computed tomography. US: ultrasound. PAI: Photoacoustic Imaging. SERS: Surface Raman Spectroscopy.

1.1.4. Theranostics

Theranostics[22] is a young but promising medical paradigm that arises from the comination of therapy and diagnosis within a single formulation. This strategy provides real-time feedback on pharmacokinetics, the target site localization and the off-target healthy organ accumulation. The possibility of tracking the therapeutic agent and monitoring its effect enables evaluating the therapeutic outcome in the patient and therefore allows a personalized treatment. Theranostic agents can be classified by the therapeutic agent that is used to modify selected nanocarrier/imaging agents (Table 2). (i) Nucleic acid therapy: in addition to traditional "gene therapy", in which a defective copy of a gene is replaced with a functional one, other forms of nucleic acids exist as potential therapeutics. These polynucleotides does not substitute the gene but alter gene expression at the transcriptional or post-transcriptional level, opening new possibilities but also presenting cellular uptake and stability problems. Big efforts have been put forth to design and develop delivery methods that allow delivering an intact polynucleotide to the final intracellular destination, like viral vectors or functionalized QDs or NPs as carriers/imaging agents. (ii) Chemotherapy: As example, calcium phosphate NPs can be tracked by NIR microscopy and be effective for the delivery of hydrophobic, insoluble drugs such as ceramide and camptothecine. A slightly acidic pH (pH = 6.5) triggers drug delivery in certain compartments of the cell, like endosomes and lysosomes, reducing the off-target toxicity. (iii) Photodynamic therapy (PDT): Based on a PS-containing drug that, once delivered to the tumour cell and upon light irradiation, generates reactive oxygen species (ROS) (e.g. singlet oxygen), which induces cell apoptosis. Porphyrins (Pors) and porphyrin-related chromophores are good candidates as PDT agents due to a minimized systemic or "dark" toxicity, drug diffusion in the diseased region, and high singlet oxygen quantum yield in order to minimize thermal damage due to photoirradiation. (iv) Hyperthermia: photothermal therapy (PTT) takes advantage of SPR of gold NPs with NIR light and subsequently non-radiative relaxation that produces heat. Iron oxide and gold core-shell NPs combine the PTT effect of gold shell with the MRI response of the iron oxide core, leading to a strategy known as magnetic field-directed hyperthermia.[23] (v) Radiation therapy: Including a radionuclei that emits X-rays, *γ*-rays or charged particles that, upon their decay, produce irreversible damage in the DNA, leading to cell death. In this technique, the use of a targeted nanocarrier minimizes off-target damage.

---

[22] a) S.S. Kelkar and T.M. Reineke, *Bioconjugate Chem.*, **2011**, *22*, 1879-1903. b) T. Lammers, S. Aime, W.E. Hennink, G. Storm and F. Kiessling, *Accounts Chem. Res.*, **2011**, *44*, 1029-1038. c) J. Xie, S. Lee and X. Chen, *Adv. Drug Deliver. Rev.*, **2010**, *62*, 1064-1079.

[23] J. Kim, S. Park, J.E. Lee, S.M. Jin, J.H. Lee, I.S. Lee, I. Yang, J-S. Kim, S.K. Kim, M-H. Cho and T. Hyeon, *Angew. Chem., Int. Ed.*, **2006**, *45*, 7754-7758.

Table 2. Therapy modalities using nanomaterials.

Modality	Component
Nucleic Acid Therapy	Plasmids, antisense oligonucleotides, ribozymes, DNAzymes, aptamers, and siRNA.
Chemotherapy	Anticancer drugs (e.g. doxorubicin, camptothecin, paclitaxel…).
PDT	Organic photosensitizers, and QDs.
PTT	Gold nanostructures, carbon nanotubes and graphite carbon shells.
Radiotherapy	Radionucleous.

PDT: photodynamic therapy. PTT: photothermal therapy.

In conclusion, despite the promising scope of those materials, many challenges still remain to be resolved prior to widespread use of nanobiotechnology in clinical oncology. There is some concern about the toxicity of NPs, and extensive investigations are in progress to resolve this issue. However, nanomedicine is becoming a very powerful tool, especially in treatment of complex disseasses (e.g. cancer, Alzheimer, VIH, etc.).[24] In the case of nanooncology, the broad catalog of boulding blocks availables and the possibility to combine them in a multifunctional drug, facilitates the personal development of personalized management of cancer, based on the molecular profiles of individual patients.

1.2. Energy conversion: Solar energy

In 2011, 82% of the world's energy consumption was supplied by fossil fuels as the primary energy source.[25] For the last decades, growing concern about the negative impact of energy conversion by-products in the environment encourages the development of new and optimized ways of energy conversion. In this topic, nanotechnology supplies a wide range of nanostructured materials that can improve energy conversion efficiencies, lowering, in the case of fossil fuels, the so-called "greenhouse effect" produced by gas emissions.

---

[24] E. Boisselier and D. Astruc, *Chem. Soc. Rev.*, **2009**, *38*, 1759-1782.

[25] Extracted from *"2014 Key World Energy Statistics"*, ed. International Energy Agency, **2014**, 6.

In this respect, the biggest efforts of nanoscience have been focused into renewable energy sources such as photovoltaics, wind energy, geothermal, hydro-/tidal power and biomass. Among them, solar energy conversion stands as the most viable option to cover worldwide energy needs[26] despite that the actual global production of solar energy is less than 1%.[25]

Solar energy can be transformed into electricity either thermodynamically or electronically. The solar thermal energy[27] is based on the concentration of solar heat by concave mirrors to heat a fluid that drives a turbine connected to an electrical generator. The second method is based on the direct conversion of solar energy into electricity in phtovoltaic devices. The so-called solar cells are nowadays commercially available and represent one of the fastest growing renewable energy technologies. However, new initiatives to harvest incident photons more efficiently are still required in order to boost solar energy production.

1.2.2. Classification of solar cells

Inorganic solar cells: In this particular topic, photovoltaic devices based in silicon have been heavily developed due to the intrinsic semiconductor properties as well as natural abundance of this material. Mono- or polycrystalline solar cells, known as f*irst generation* solar cells, present a maximum efficiency of 25.0 and 20.4 %, respectively.[28] This kind of cells dominates the photovoltaic market due to their efficiencies and long active life (ca. 20 years, despite suffering from high production cost in obtain highly pure silicon. In this regard, nanostructured materials provide the basis for new and cheaper systems, yet not as effective as the *first generation* ones. The *second generation*[29] devices take advantage of thin film deposition techniques of silicon and polycrystalline semiconductors, lowering production costs, making them competitive in efficiency, compared to those of first generation. Modules based primarily on chemical vapour deposited amorphous silicon (13.4%), as well as polycrystalline CdTe (21.5%), $CuInGaSe_2$ or CIGS (21.7%) have reached outstanding performances. Nevertheless, massive production of the previously mentioned cells provokes new problems such as scarcity and toxicity of the materials employed. To this end, *third-generation* solar cells are based on novel concepts like hot carrier solar cells, multiple exciton generation, tandem or multijunction solar cells.[30]

---

[26] Q. Schiermeier, J. Tollefson, T. Scully, A. Witze and O. Morton, *Nature*, **2008**, *454*, 816-823.

[27] B. Norton, *Harnessing Solar Heat*, Lecture in Energy 18, Springer, Dordrecth, **2014**.

[28] M.A. Green, K. Emery, Y. Hishikawa, W. Warta and E.D. Dunlop, *Prog. Photovolt: Res. Appl.*, **2015**, *23*, 1-9.

[29] L.M. Peter, *Phil. Trans. R. Soc. A*, **2011**, *369*, 1840-1856.

[30] M.A. Green in *Third Generation Photovoltaics*, Springer-Verlag, Berlin, **2003**.

Organic Solar cells: Complementary to the generally known as inorganic solar cells, a particular case of *third-generation* solar cells based in organic or mixed materials, present some advantages as reduced production costs, easy preparation by solvent-based fabrication techniques, non-toxic active materials, and flexibility and light-weight, allowing new applications. To achieve this end, many common organic dyes such as methylene blue, carotenes, chlorophylls, Pors or related synthetic analogues such as phthalocyanines (Pcs) have been found to present semiconducting properties. A key aspect of the organic solar cells evolution relates to the device configuration. In 1986 Tang prepared a two-component, donor:acceptor active layer which became the first example of the planar bilayer heterojunction (PHJ, Figure 3a) or p-n solar cell.[31] This particular architecture takes advantage of the facile formation of the charge carriers (electrons and holes) by electron transfer from the photoexcited donor to the acceptor component. Another advantage is the ensured connectivity between the active layer to the correct electrode, minimizing the chances of recombination of the charge carriers. An important drawback of the PHJ cells, however, is that excitons (i.e. electron-hole pairs formed by light excitation) are formed in the interface between the donor and acceptor layers, and then dissociate, limiting the donor-acceptor interface. In order to enhance the contact surface among the two active layers, Yu *et al.* proposed the bulk-heterjunction (BHJ, Figure 3b) configuration,[32] in wich a blend of a donor and an acceptor with a bicontinual phase separation is formed, enlarging the interface area.[33] Ultimately, another type of architectures called tandem solar cells (Figure 3c) have gained a lot of attention. Their advantage relies in the combination of different devices places one on top of the other, thus absorbing in different wavelength ranges. This strategy allows a wider sunlight spectrum coverage, with efficient absorption at all wavelengths, something difficult to achieve with a single heterjunction.

Another way to classify the organic solar cells is attending to the type of active material. Thus, two categories can be established: small-molecule and polymer-based photovoltaic cells. Small molecule photovoltaic devices[34] are based in discrete chromophores to form the active layers. On the other hand, polymer-based solar cells, also

---

31 a) C.W. Tang, *Appl. Phys. Lett.*, **1986**, *48*, 183-186.

32 G. Yu, J. Gao, J.C. Hummelen, F. Wudl and A.J. Heeger, *Science*, **1995**, *270*, 1789-1791.

33 a) M. Hiramoto, H. Fujiwara, M. Yokoyama, *Appl. Phys. Lett.*, **1991**, *58*, 1062-1064. b) J.J.M. Halls, C.A. Walsh, N.C. Greenham, E.A. Marseglia, R.H. Friend, S.C. Moratti and A.B. Holmes, *Nature*, **1995**, *376*, 498-500. c) G. Li, V. Shrotriya, J. Huang, Y. Yao, T. Moriarty, K. Emery and Y. Yang, *Nature Mat.*, **2005**, *4*, 864-868. d) S.H. Park, A. Roy, S. Beaupre, S. Cho, N. Coates, J.S. Moon, D. Moses, M. Leclerc, K. Lee and A.J. Heeger, *Nature Photon.*, **2009**, *3*, 297-303.

34 a) B. Walker, C. Kim and T.-Q. Nguyen, *Chem. Mater.*, **2011**, *23*, 470-482. b) A. Mishra and P. Bauerle, *Angew. Chem. Int. Ed.*, **2012**, *51*, 2020-2067. c) Y. Lin, Y. Li, X. Zhan, *Chem. Soc. Rev.*, **2012**, *41*, 4245-4272. d) Y. Sun, G.C. Welch, W.L. Leong, C.J. Takacs, G.C. Bazan, A. J. Heeger, *Nat. Mater.*, **2012**, *11*, 44-48. e) W. Ni, X. Wan, M. Li, Y. Wang and Y. Chen, *Chem. Commun.*, **2015**, *51*, 4936-4950.

known as plastic solar cells,[35] are constituted by conjugated polymers that improve the charge-carrier migration from the donor-acceptor interface to the corresponding electrodes.

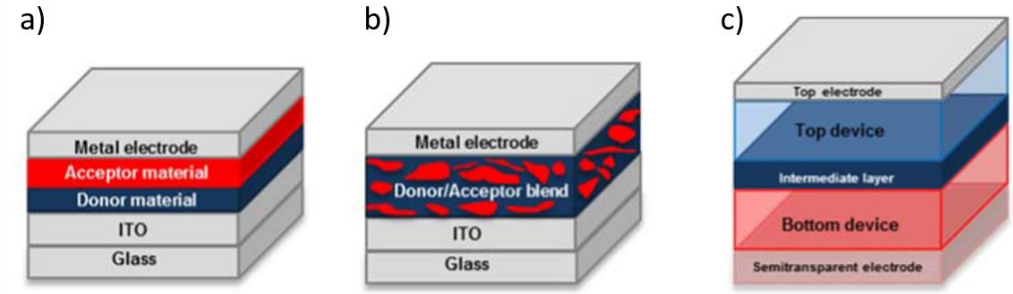

Figure 3. Schematic representation of a) planar heterojunction, b) bulk heterojunction and c) tandem solar cells arquitectures.

Hybrid solar cells: A third kind of solar cells emerge from the combination of organic and inorganic materials, having great relevance in recent years. The development of dye-sensitized solar cells (DSSCs) opened up new horizons and have been presented for the last two decades as one of the winning candidates in the cost-efficiency race.[36] DSSCs present the following architecture: an organic light-absorbing dye is anchored to a mesoporous inorganic n-type semiconductor film (usually TiO_2) that works as photoanode, and the cell is filled with a redox-active electrolyte. Research on light-absorbing dyes is very much developed, with different benchmark molecules, ranging from expensive and toxic ruthenium complexes to organic chromophores such as Pors and Pcs.[37] The main drawback of DSSCs is the liquid formulation of the cells, that limits the cell lifetime and increases the

---

[35] a) C.J. Brabec, S.N. Sariciftci, in *Electroactive Materials*, (J.O. Besenhard, W. Sitte, F. Stelzer and H. Gamsjager, Ed.) Springer-Verlag Wien, Vienna, **2001**, pp 1-11. b) J. Peet, M.L. Senatore, A.J. Heeger and G.C. Bazan, *Adv. Mater.*, **2009**, *21*, 1521-1527. c) M.T. Dang, L. Hirsch and G. Wantz, *Adv. Mat.*, **2011**, 23, 3597-3602. d) C.E. Small, S. Chen, J. Subbiah, C.M. Amb, S.-W. Tsang, T.-H. Lai, J.R. Reynolds and F. So, *Nat. Photonics*, **2012**, *6*, 115-120. e) H. Zhou, L. Yang and W. You, *Macromolecules*, **2012**, *45*, 607-632. f) Y. Lee, E.D. Gomez, *Macromolecules*, **2015**, *48*, 7385-7395.

[36] a) B. O'Regan and M. Gratzel, *Nature*, **1991**, *353*, 737-740. b) A. Hagfeldt, G. Boschloo, L. Sun, L. Kloo, h. Pettersson, *Chem. Rev.*, **2010**, *110*, 6595-6663. c) M.K. Nazeeruddin, E. Baranoff and M. Gratzel, *Solar Energy*, **2011**, *85*, 1172-1178.

[37] a) N. Robertson, *Angew. Chem., Int. Ed.*, **2006**, *45*, 2338-2345. b) N. Koumura, Z.-S. Wang, S. Mori, M. Miyashita, E. Suzuki and K. Hara, *J. Am. Chem. Soc.*, **2006**, *128*, 14256-14257. c) A. Mishra, M.K.R. Fischer and P. Bauerle, *Angew. Chem., Int. Ed.*, **2009**, *48*, 2474-2499. d) M.V. Martinez-Diaz, G. de la Torre and T. Torres, *Chem. Commun.*, **2010**, *46*, 7090-7108. e) Y. Wu and W. Zhu, *Chem. Soc. Rev.*, **2013**, *42*, 2039-2058.

costs in sealing. To avoid this inconvenient, developing all-solid DSSCs is the latest tendency toward a future commercialization.[38]

Finally, it is worthy to mention a really young but outstandingly promising new family of solar cells, the perovskite-based solar cells.[39] This family takes advantage of the perovskite crystalline structure due to its intense broad-band absorption, high charge carrier mobility, low-cost precursor materials and simple solution processing. Perovskites have the general formula of ABX_3 (Figure 4). In this structure, A is a monovalent cation, generally an organic ammonium salt; B is a metallic divalent cation, generally Pb^{+2}; and X is either O, C, N or, for solar cell applications, a halogen.

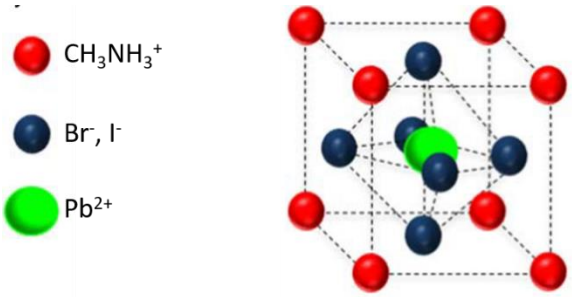

Figure 4. Structure for $CH_3NH_3PbBr_3$, a common perovskite currently employed in solar cell application.

Since the first peer-reviewed journal publication in 2009, where a 3.5% of efficiency was reported,[40] a meteoric rise in efficiencies has led to a highest efficiency of 20.1%,[41] as a consequence of morphology optimization (thickness and homogeneity),[42] broadening the absorption, and photostability. Only the toxicity of lead and the moisture-sensitivity of perovskites can limit somehow the imminent commercialization of perovskite-based devices.

---

38 a) P. Docampo, S. Guldin, T. Leijtens, N.K. Noel, U. Steiner and H.J. Snaith, *Adv. Mater.*, **2014**, *26*, 4013-4030. b) A. Fakharuddin, R. Jose, T.M. Brown, F. Fabregat-Santiago and J. Bisquert, *Energy Environ. Sci.*, **2014**, *7*, 3952-3981.

39 a) H. J. Snaith, *J. Phys. Chem. Lett.*, **2013**, *4*, 3623-3630. b) M. A. Loi and J. C. Hummelen, *Nat. Mater.*, **2013**, *12*, 1087-1089. c) S. Kazim, M. K. Nazeeruddin, M. Gratzel and S. Ahmad, *Angew. Chem. Int. Ed.*, **2014**, *53*, 2812-2824. d) M. A. Green, A. Ho- Baillie and H. J. Snaith, *Nature Photon.*, **2014**, *8*, 506-514. e) W. Chen, Y. Wu, Y. Yue, J. Liu, W. Zhang, X. Yang, H. Chen, E. Bi, I. Ashraful, M. Grätzel and L. Han, *Science*, **2015**, *350*, 944-948.

40 A. Kojima, K. Teshima, Y. Shirai and T. Miyasaka, *J. Am. Chem. Soc.*, **2009**, *131*, 6050-6051.

41 W.S. Yang, J.H. Noh, N.J. Jeon, Y.C. Kim, S. Ryu, J. Seo and S.I. Seok, *Science*, **2015**, *348*, 1234-1237.

42 J. Burschka, N. Pellet, S.-J. Moon, R. Humphry-Baker, P. Gao, M.K. Nazeeruddin and M. Gratzel, *Nature*, **2013**, *499*, 316-319.

2. Dyes in nanotechnology

2.1. Dye-based molecular and biohybrid materials

Among the wide set of materials that nanoscience offers, organic chromophores are among the most related ones to natural systems. Synthetic efforts have been made to tune their photophysical properties for different applications. In this regard, many chromophore derivatives have been synthesized, characterized and applied (Figure 5).

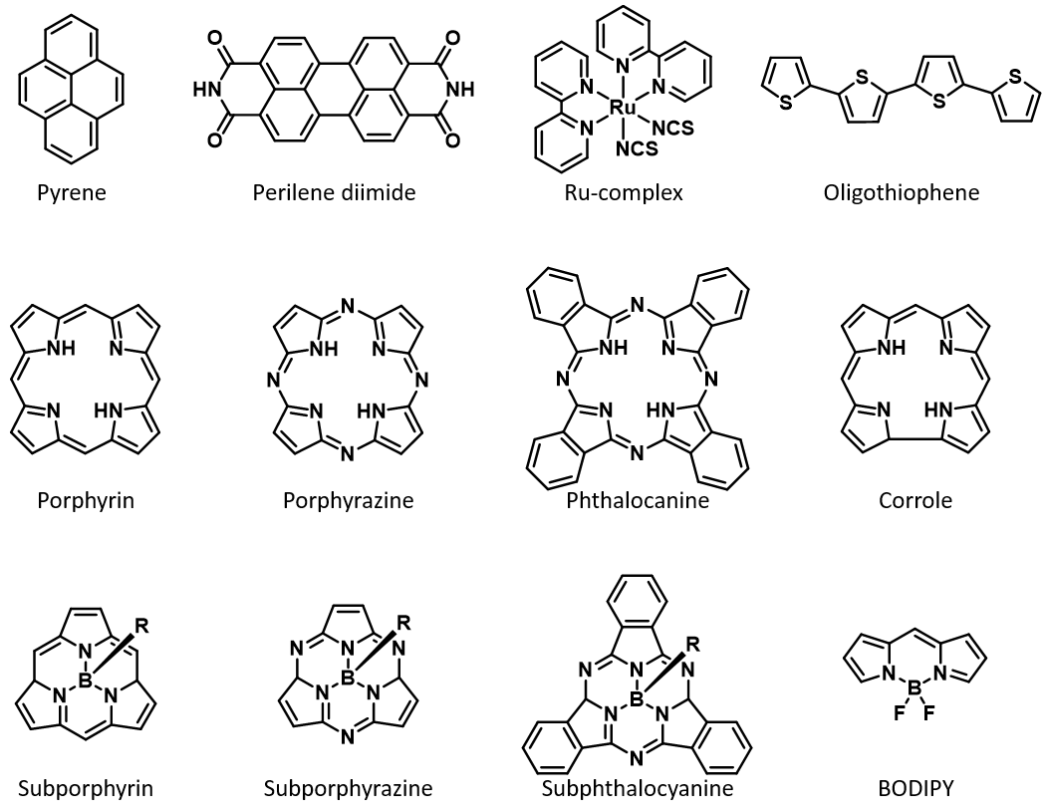

Figure 5. Chemical structure of most common dyes in nanotechnology.

Polycyclic aromatic hydrocarbons (PAH)[43] like pyrene, corannulene or higher derivatives like graphene nanoribons or graphene quantum dots,[44] presents a remarkable

[43] C. Achten and J.T. Andersson, *Polycycl. Aromat. Comp.*, **2015**, *35*, 177-186

fluorescence quatum yield but highly energetic absorption. In order to tune the absorption, synthetic derivatives as perylene diimide (PDI)[45] or extended tetrathiafulvalene (exTTF)[46] shift the absorption to the visible region, maintaining the fluorescence properties. Other dyes like organo-metallic complexes such as ruthenium bipyridine has been employed as antennas in dye-sensitized solar cells (DSSCs).[47] Conjugated oligomers or polymers as oligophenylenevinylene (OPV)[48] or oligothiophene[49] has been studied as conducting polymers. Along with previously described chromophores, a family of pyrrole-based nature-inspired derivatives have demonstrated a huge synthetic versatility, allowing a fine tunability of the photophysical properties.[50] This family is constituted by tetrapyrroles linked by a methylene or aza groups (Pors and porphyrazines, respectively). Extended derivatives as phthalocyanines (Pcs), naphthalocyanines (Ncs) or link-mixed derivatives as corroles, provide a wide range of photophysical and photochemical properties. Modifications in the number of member rings (i.e. subporphyrines, subporphyrazines, subphthalocyanines and BODIPYs), triggered by B coordination, expand the available possibilities even further.

Concerning nanomedicine and environmental science applications, extensive research has been made in the last decade to incorporate or formulate fluorophores and chromophores in biological media. One important drawback in this respect is the biocompatibility of hydrophobic dyes that present inexistent or low solubility in aqueous media and, in most of cases, when soluble they show aggregation effects that decrease excited state properties as fluorescence or singlet oxygen generation. The last aspect is of

---

44 a) K.A. Ritter, J.W. Lyding, *Nat. Mater.*, **2009**, *8*, 235-242. b) J. Cai, P. Ruffieux, R. Jaafar, M. Bieri, T. Braun, S. Blakenburg, M. Muoth, A.P. Seitsonen, M. Saleh, X. Feng, K. Müllen and R. Fasel, *Nature*, **2010**, *466*, 470-473. c) J. Shen, Y. Zhu, X. Yang and C. Li, *Chem. Commun.*, **2012**, *48*, 3686-3699. d) A. Cayuela, M.L. Soriano, C. Carrillo-Carrión and M. Valcárcel, *Chem. Commun.*, **2016**, *52*, 1311-1326.

45 a) S.T.J. Ryan, R.M. Young, J.J. Henkelis, N. Hafezi, N.A. Vermeulen, A. Henning, E.J. Dale, Y. Wu, M.D. Krzyaniak, A. Fox, W.M. Nau, M.R. Wasielewski, J.F. Stoddart and O.A. Scherman, *J. Am. Chem. Soc.*, **2015**, *137*, 15299-15307. b) A.J. Jimenez, R.M.K. Calderon, M.S. Rodriguez-Morgade, D.M. Guldi and T.Torres, *Chem. Sci.*, **2013**, *4*, 1064-1074. c) S. Stappert, C. Li, K. Muellen and T. Basche, *Chem. Mater.*, **2016**, *28*, 906-914. d) C. Li and H. Wonneberger, *Adv. Mater.*, **2012**, *24*, 613-636. e) S. Suzuki, M. Kozaki, K. Nozaki and K. Okada, *J. Photochem. Photobiol. C*, **2011**, *12*, 269-292.

46 a) F.G. Brunetti, J.L. Lopez, C. Atienza and N. Martin, *J. Mater. Chem.*, **2012**, *22*, 4188-4205. b) A. Molina-Ontoria, M. Gallego, L. Echegoyen, E.M. Perez and N. Martin, *RSC Advances*, **2015**, *5*, 31541-31546. c) Y. Takano, C. Schubert, N. mizorogi, L. Feng, A. Iwano, M. Katayama, M.A. herranz, D.M. Guldi, N. Martin, S. Nagase and T. Akasaka, *Chem. Sci.*, **2013**, *4*, 3166-3171.

47 a) B. Bozic-Weber, E.C. Constable and C.E. Housecroft, *Coord. Chem. Rev.*, **2013**, *257*, 3089-3106. b) G.C. Vougioukalakis, A.I. Philippopoulos, T. Stergiopoulos, P. Falaras, *Coord. Chem. Rev.*, **2011**, *255*, 2602-2621. c) Y. Chi, K.-L. Wu and T.-C. Wei, *Chem. Asian J.*, **2015**, *10*, 1098-1115.

48 J.D. Tovar, *Acc. Chem. Res.*, **2013**, *46*, 1527-1537.

49 L. Zhang, N.S. Colella, B.P. Cherniawski, S.C.B. Mannseld, A.L. Brisseno, *ACS Appl. Mat. Interf.*, **2014**, *6*, 5327-5343.

50 H. Schultz, H. Lehmann, M. Rein and M. Hanack in *Structure and Bonding*, ed. J.W. Buchler, Springer, Berlin, **1991**, vol. 74, pp. 41-146.

capital interest not only in nanomedicine, but also in environmental science and organic synthesis, where dye PS can be used for water treatments and in photooxidation reactions, respectively. Designing carrier scaffolds is thus a challenge in order to formulate PS systems in aqueous media. A growing strategy in this direction consists in mimicking nature and use biologically inspired hybrid materials to maintain or even enhance the optical properties of the chromophores in water. These biohybrid materials can be classified by the nature of the corresponding nanocarrier, which are summarized below.

(i) Protein-based materials

Genetically,[51] covalently[52] or supramolecularly modified protein derivatives such as cell penetrating or antimicrobial peptides,[53] antibodies[54] or protein cages[55] has been employed to target and deliver photosensitizers into selected cells or microorganisms.[56] Protein cages available in nature, such as virus capsids[15] and iron storage protein ferritin (Figure 6) have attracted growing interest in the past decade due to a broad selection of sizes in the nanometer scale, monodispersity and highly organized self-assembled structure. Moreover, the possible functionalization of protein cages inside their hollow structure, in the external wall or even in the intersticial space between the protein monomers, make them an optimal scaffold to design multifunctional agents.

---

51 a) Z. Varpness, P.A. Suci, D. Ensign, M.J. Young and T. Douglas, *Chem. Commun.,* **2009**, *25*, 3726-3728. b) H. Moon, J. Lee, J. Min and S. Kang, *Biomacromolecules*, **2014**, *15*, 3794-3801.

52 F. Giuntini, C.M.A. Alonso and R.W. Boyle, *Photochem. Photobiol. Sci.,* **2011**, *10*, 759-791.

53 a) I. Sehgal, M. Sibrian-Vazquez and M.G.H. Vicente, *J. Med. Chem.*, **2008**, *51*, 6014-6020. b) A.M. Fales, H. Yuan and T. Vo-Dinh, *Mol. Pharmaceutics*, **2013**, *10*, 2291-2298. c) F. Moret, M. Gobbo and E. Reddi, *Photochem. Photobiol. Sci.*, **2015**, *14*, 1238-1250.

54 a) G.A.M.S. van Dongen, G.W.M. Visser and M.B. Vrouenraets, *Adv. Drug. Deliver. Rev.*, **2004**, *56*, 31-62. b) P.M.R. Pereira, B. Korsak, B. Sarmento, R.J. Schneider, R. Fernandes and J.P.C. Tomé, *Org. Biomol. Chem.,* **2015**, *13*, 2518-2529.

55 a) L.A. Lee and Q. Wang, *Nanomed. Nanotechnol.*, **2006**, *2*, 137-149. b) P.A. Suci, Z. Varpness, E. Gillitzer, T. Douglas and M. Young, *Langmuir*, **2007**, *23*, 12280-12286. c) M. Uchida, M. T. Klem, M. Allen, P. Suci, M. Flenniken, E. Gillitzer, Z. Varpness, L.O. Liepold, M. Young and T. Douglas, *Adv. Mater.*, **2007**, *19*, 1025-1042. d) A. de la Escosura, R.J.M. Nolte and J.J.L.M. Cornelissen, *J. Mater. Chem.*, **2009**, *19*, 2274-2278.

56 a) A. MaHam, Z. Tang, H, Wu, J. Wang and Y. Lin, *Small*, **2009**, *5*, 1706-1721. b) J.P. Celli, B.Q. Spring, I. Rizvi, C.L. Evans, K.S. Samkoe, S. Verma, B.W. Pogue and T. Hasan, *Chem. Rev.*, **2010**, *110*, 2795-2838. c) A. Srivatsan, J.R. Missert, S.K. Upadhyay and R.K. Pandey, *J. Porphyrins Phthalocyanines*, **2015**, *19*, 109-134.

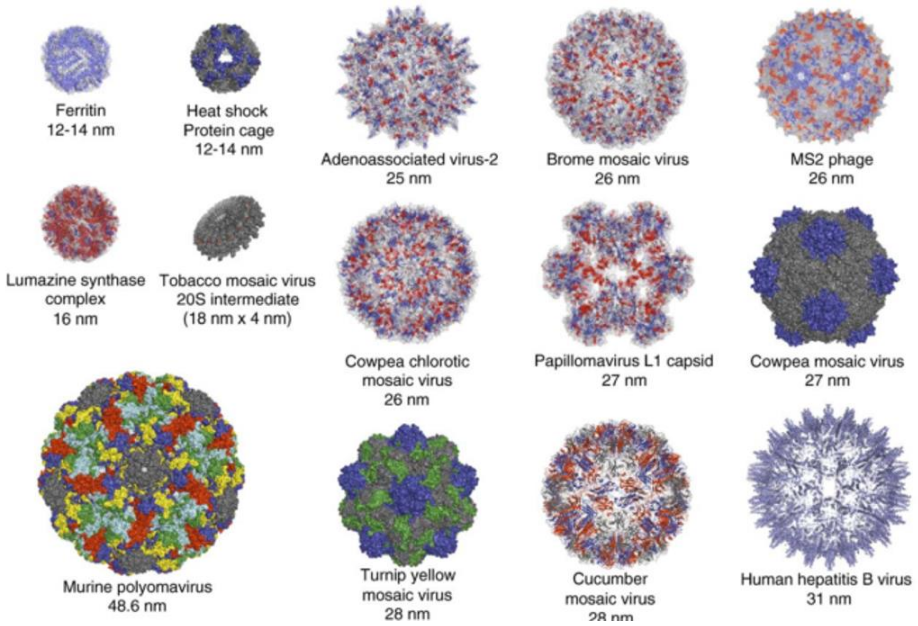

Figure 6. Structure of most commonly employed protein cages, as shown in 55a

(ii) DNA/RNA-based materials

Natural photosynthetic systems, where arrays of pigments are spatially distributed, presens high absorption and effective energy/electron transmission. These spatially distributed arrays have been a matter of study for decades, as inspiration for improved light-harvesting systems in photovoltaic devices, due to its predictable supramolecular structure.[57] Since the late 1970's decade, where Por intercalation in DNA was described,[58] nucleic acid derivatives have been employed as scaffold to build highly ordered chromophore arrays.[59]

---

[57] a) B. Albinsson, *Nature Chem.*, **2011**, *3*, 269-270. b) W. Su, V. Bonnard and G. A. Burley, *Chem. Eur. J.*, **2011**, *17*, 7982-7991. c) Y.N. Teo and E.T. Kool, *Chem. Rev.*, **2012**, *112*, 4221-4245. d) G. Sargsyan and M. Balaz, *Org. Biomol. Chem.*, **2012**, *10*, 5533-5540.

[58] a) R.J. Fiel, J.C. Howard, E.H. Mark and N.D. Gupta, *Nucleic Acid Res.*, **1979**, *6*, 3093-3118. b) M.A. Sari, J.P. Battioni, D. Dupre, D. Mansuy and J.B. Le Pecq, *Biochemistry*, **1990**, *29*, 4205-4215. c) S. Ghimire, P.E. Fanwick and D.R. McMillin, *Inorg. Chem.*, **2014**, *53*, 11108-11118.

[59] a) L.-A. Fendt, I. Bouamaied, S. Thöni, N. Amiot and E. Stulz, *J. Am. Chem. Soc.*, **2007**, *129*, 15319-15329. b) J.G. Woller, J.K. Hannestad and B. Albinsson, *J. Am. Chem. Soc.*, **2013**, *135*, 2759-2768.

(iii) Liposomes

Liposomes, with their high loading capacity and, most interestingly, a broad surface modification, are excellent nanocarriers with tuneable size, surface charge and targeting ligands.[21d,60] Most interestingly, the liposomal cargo can be released by different stimuli, ranging from temperature, pH, enzymes and most recently ultrasounds, light, a magnetic field or combined effects. Liposomes are therefore excellent nanocarriers of PS as well.[60d,61] Moreover, lipidic bylayer structures have been also employed to build up nanostructured electron donor-acceptor systems[62] and as nanoreactors.[63]

(iv) Carbohydrate-based materials

Different glycosylated moieties have been employed in the nanomedicine field. Conjugation of chromophores with sugars provides them adequate physicochemical properties for biomedical applications, such as amphiphilicity, and solubility in physiological media. Carbohydrates also appear conjugated to other biological components such as proteins, lipids and nucleic acids, being involved in many cellular processes (e.g. cell-substrate and cell-cell recognition, drug transport, etc.).[64] Moreover, due to the so-called "Warburg effect" (i.e. an increased sugar consumption of cancerous cells due to an accelerate metabolism),[65] sugar-PS derivatives have become a powerful tool in nanooncology. The type and number of carbohydrate moieties attached to the

---

60 a) A.S.L. Derycke, P.A.M. de Witte, *Adv. Drug Deliver. Rev.*, **2004**, *56*, 17-30. b) T.M. Allen and P.R. Cullis, *Adv. Drug Deliver. Rev.*, **2013**, *65*, 36-48. d) R. Weijer, M. Broekgaarden, M. Kos, R. van Vught, E.A.J. Rauws, E. Breukink, T.M. van Gulik, G. Storm and M. Heger, *J. Photochem. Photobiol. C*, **2015**, 103-131. e) J. Lee, J. Kim, M. Jeong, H. Lee, U. Goh, H. Kim, B. Kim and J.-H. Park, *Nano Lett.,* **2015**, *15*, 2938-2944.

61 a) M. Sadasivam, P. Avci, G.K. Gupta, S. Lakshmanan, R. Chandran, Y.-Y. Huang, R. Kumar and M.R. Hamblin, *Eur. J. Nanomed.*, **2013**, *5*, 115-129. b) A. Puri, *Pharmaceutics*, **2014**, *6*, 1-25.

62 a) A. Ikeda, M. Akiyama, T. Ogawa and T. Takeya, *ACS Med. Chem. Lett.*, **2010**, *1*, 115-119. b) J. Matsumoto, T. Beppu, T. Shiragami, M. Yasuda, *J. Photochem. Photobiol. A*, **2012**, *249*, 47-52. c) B. Limburg, G. Laisné, E. Bouwman and S. Bonnet, *Chem. Eur. J.*, **2014**, *20*, 8965-8972.

63 a) R. Genç, G. Clergeaud, M. Ortiz and C.K. O'Sullivan, *Langmuir*, **2011**, *27*, 10894-10900. b) G. Clergeraud, R. Genç, M. Ortiz and C.K. O'Sullivan, *Langmuir*, **2013**, *29*, 15405-15413. c) S. Gudlur, C. Sandén, P. Matouskova, C. Fasciani and D. Aili, *J. Colloid. Interf. Sci.*, **2015**, *456*, 206-209.

64 a) G. Fülling, D. Schröder and B. Franck, *Angew. Chem. Int. Ed.*, **1989**, *28*, 1519-1521. b) P. Maillard, S. Gaspard, J.L. Guerquin-Kern and M. Momenteau, *J. Am. Chem. Soc.*, **1989**, *111*, 9125-9127. c) X. Chen, L. Hui, D.A. Foster and C. Drain, *Biochemistry*, **2004**, *43*, 10918-10929. d) I. Laville, S. Pigaglio, J.-C. Blais, F. Doz, B. Loock, P. Maillard, D.S. Grierson and J. Blais, *J. Med. Chem.*, **2006**, *49*, 2558-2567.

65 O. Warburg, *Science*, **1956**, *123*, 309-314.

photosensitizer can be finely tuned, providing a wide range of solubility, formulation and recognition properties.[66]

In addition to mono- and oligosaccharides, biological relevant polysaccharides such as chitosan,[67] heparin,[68] cyclodextrin,[69] or cellulose derivatives[70] are being utilized.

2.2. Porphyrinoids: chromophores inspired by nature

Nature has developed plentiful strategies and systems that can be used to deal with some of the nowadays problems. For example, plants, algae and bacteria solved the synthesis of highly energetic molecules through CO_2 fixation by a very effective light harvesting system evolved millions of years ago. In photosynthesis, light-harvesting antennas generate a photoinduced charge-separation reaction from the excited states of certain chromophores, which are transferred to the reaction site. This electron transfer mechanism in the photosynthetic reaction centre has been throughly studied.[71] The building blocks of the antenna are chromophores selected by their size and shape, which determines the self-assembly in the system, as well as the absorption intensity and wavelength of the absorbed light. Nature's choice includes chlorophylls as light-harvesting molecules and linear tetrapyrroles and carotenoids as excited energy transfers.[72] Chlorophylls (Figure 7) are chlorine derivatives, a reduced form of Pors that are responsible for the typical green colour in higher plants and algae (λ^{max} = 650-670 nm). Bacteriochlorins

---

66 a) A. Lyubimtsev, Z. Iqbal, G. Crucius, S. Syrbu, T. Ziegler and M. Hanack, *J. Phorphyrins Phthalocyanines,* **2012**, *16*, 434-463. b) F. Figueira, P.M.R. Pereira, S. Silva, J.A.S. Cavaleiro and J.P.C. Tomé, *Current Org. Synthesis*, **2014**, *11*, 110-126. c) L.M.O. Lourenco, M.G.P.M.S. Neves, J.A.S. Cavaleiro and J.P.C. Tomé, *Tetrahedron*, **2014**, *70*, 2681-2698. d) M. Hanack, G. Crucius, M.J.F. Calvete and T. Ziegler, *Curr. Org. Synth.*, **2014**, *11*, 59-66.

67 a) W.R. Chen, R.L. Adams, R. Carubelli and R.E. Nordquist, *Cancer Lett.*, **1997**, *115*, 25-30. b) S.J. Lee, K. Park, Y.-K. Oh, S.-H. Kwon, S. Her, I.-S. Kim, K. Choi, S.-J. Lee, H. Kim, S.G. Lee, K. Kim and I.C. Kwon, *Biomaterials*, **2009**, *30*, 2929-2939. c) S.Y. Park, H.J. Baik, Y.T. Oh, K.T. Oh, Y.S. Youn and E.S. Lee, *Angew. Chem. Int. Ed.*, **2011**, *50*, 1644-1647.

68 a) L. Li, B.-C. Bae, T.H. Tran, K.H. Yoon, K. Na and K.M. Huh, *Carbohyd. Polym.*, **2011**, *86*, 708-715. b) L. Li, H. Cho, S. Kim, H.C. Kang and K.M. Huh, *Carbohyd. Polym.*, **2015**, *121*, 122-131.

69 a) S.D.P. Baugh, Z. Yang, K.K. Leung, D.M. Wilson and R. Breslow, *J. Am. Chem. Soc.*, **2001**, *123*, 12488-12494. b) S. Monti, S. Sortino, *Chem. Soc. Rev.*, **2002**, *31*, 287-300. c) J.M. Lee, K.T. Oh, Y.S. Youn and E.S. Lee, *Polym. Adv. Technol.*, **2015**, doi: 10.1002/pat.3612.

70 a) E. Feese, H. Sadeghifar, H.S. Gracz, D.S. Argyropoulos and R.A. Ghiladi, *Biomacromolecules*, **2011**, *12*, 3528-3539. b) C. Ringot, V. Sol, M. Barriere, N. Saad, P. Bressollier, R. Granet, P. Couleaud, C. Frochot and P. Krausz, *Biomacromolecules*, **2011**, *12*, 1716-1723. c) A.K. Siddhanta, N.D. Sanandiya, D.R. Chejara and S. Kondaveeti, *RSC Adv.*, **2015**, *5*, 59226-59239. d) B.L. Carpenter, F. Schole, H. Sadeghifar, A.J. Francis, J. Boltersdorf, W.W. Weare, D.S. Argyropoulos, P.A. Maggard and R.A. Ghiladi, *Biomacromolecules*, **2015**, *16*, 2482-2492.

71 T. Renger, *Photosynth. Res*., **2009**, *102*, 471-485.

72 G.D. Scholes, G.R. Fleming, A. Olaya-Castro and R. van Grondelle, *Nature Chem.*, **2011**, *3*, 763-774.

(18 π e^-), present in some bacteria, are a reduced form of chlorophylls and absorb at even higher wavelengths (λ^{max} = 730-800 nm), their colour varying from green to purple. As a final remark, these aromatic macrocycle are present in nature as free ligands or as Mg^{2+} chelates.

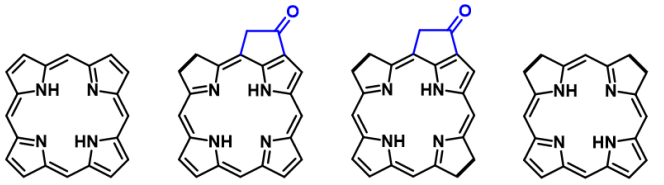

Figure 7. Reduced Pors derivatives, corresponding biological derivatives (blue) and number of aromatic electrons.

Apart from light-harvesting functions, Por derivatives accomplish other functions in biological media. The heme group, a Por macrocycle with a Fe^{2+} ion chelated in it, is for example responsible for different functions such as gas transport in animal's blood, electron transport in the mitochondrial electron chain and as part of the reactive site in some enzymes like peroxidases.

3. Phthalocyanines in nanotechnology

3.1. Structure

As previously mentioned, Nature is a powerful source of inspiration for the study and development of systems with new functionalities and enhanced performances. Among molecular materials, metallomacrocycles has been developed extensively. In this group, Pcs[37d,73] (Figure 8) hold a privileged position due to their outstanding optical, electronical and physicochemical characteristics, which allow their utilization in multiple applications (i.e. dyes, gas sensors, catalists and optoelectronic devices).

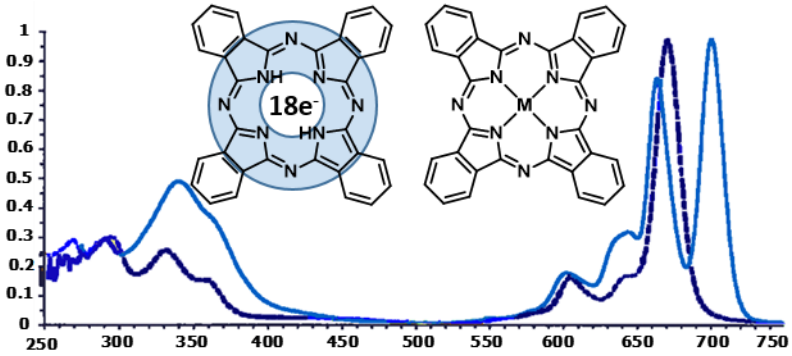

Figure 8. Structures of metal-free phthalocyanine (left), showing aromatic delocalization in the macrocycle's core and metallophthalocyanine (MPc, right) derivatives. Their typicall absorption spectra are shown in light and dark blue, respectively.

Pcs are planar 18 π-electron aromatic macroheterocycles consisting of four isoindole subunits linked together in positions 1,3 through aza bridges. These macroheterocycles are thermally and chemically stable, but their most remarkable feature is a high structural versatility that enables fine-tuning of the optical, electronical and aggregation properties. For example, synthetic functionalization at the periphery of the macrocycle is complemented by the possibility of including up to 70 metal atoms in the inner cavity, enabling in some cases also chemical modification at axial positions. These structural aspects have a strong effect on MPcs performance for different applications, ranging from energy conversion, non-linear optics (NLO) and nanomedicine.

---

[73] a) *Phthalocyanines. Properties and Applications*, ed. C.C. Leznoff, A.B.P. Lever, VCH Publishers (LSK) Ltd., Cambridge, **1996**, vols 1-4. b) *Phthalocyanine Materials. Synthesis, Structure and Function*, ed. N.B. McKeown, Cambridge University Press, Cambridge, **1998**. *c*) C.G. Claessens, U. Hahn and T. Torres, *Chem. Rec.* **2008**, *8*, 75-97. d) G. de la Torre, G. Bottari, U. Hahn and T. Torres, *Struct. Bonding*, **2010**, *135*, 1-44. e) F. Dumoulin, M. Durmus, V. Ahsen and T. Nyokong, *Coord. Chem. Rev.*, **2010**, *254*, 2792-2847. f) J. Mack and N. Kobayashi, *Chem. Rev.*, **2011**, *111*, 281-321. g) *Handbook of Porphyrin Science*, ed. K.M. Kadish, K.M. Smith and R. Guilard, World Scientific, Singapore, **2013**.

The delocalization of 18 π-electrons over the inner 16 atoms of the macrocycle generates absorption spectra with two major bands: the Q-band and the Soret or B-band, both corresponding to π-π* transitions (Figure 8). The Soret band is centered tipically around in the range of 350 nm, normally presents a broad and low intensity, and corresponds to a (HOMO-1) – LUMO transition. On the contrary, the Q-band, corresponding to a HOMO-LUMO transition, is centered in the visible region, in the range between 620-720 nm presents typically a high extinction molar coefficient (ε), up to values of 10^5 M^{-1} cm^{-1}. The position and shape of this band is responsible for the characteristic green-blue colour of these compounds. Free base phthalocyanine (H_2Pc) derivatives, with D_2h symmetry, present a split Q-band due to doubly degenerated LUMO. In the case of metallophthalocyanines (MPcs), the LUMO level is fully degenerated due to a higher symmetry (D_4h), showing a single Q-band corresponding to a single HOMO-LUMO transition.

Other photophysical properties like electronic absorption, fluorescence and phosphorescence spectra, as well as the triplet excited state generation,[74] are also strongly influenced by the presence and nature of the central atom. Transition metal ions give MPcs with short triplet lifetimes, whereas closed-shell and diamagnetic metals lead to dyes with high triplet state quatum yields. Apart from the electronic shell of the metal ion, the heavy atom effect promotes the intersystem crossing from singlet- to triplet-excited state as long as the atom mass increases.[75]

The large extended conjugation in Pcs lead to a high aggregation tendency, driven primarily by π-π interactions and solvophobic effects. The presence of peripheral or axial substituents tunes the type and extent of aggregation.[76] Excitonic coupling theory developed by Kasha and co-workers[77] describes the excitonic interaction of the transition dipole moments of stacking chromophores with respect to their geometrical arrangement (Figure 9). According to this theory, coplanar assemblys of Pcs, with parallel dipolar

---

[74] a) A. Morandeira, I. López-Duarte, M.V. Martínez-Díaz, B. O'Regan, C. Shuttle, N.A. Haji-Zainulabidin, T. Torres, E. Palomares and J.R. Durrant, *J. Am. Chem. Soc.*, **2007**, *129*, 9250-9251. b) Y. Rio, M.S. Rodríguez-Morgade and T. Torres, *Org. Biomol. Chem.*, **2008**, *6*, 1877-1894. c) A. Listori, I. López-Duarte, M.V. Martinez-Díaz, T. Torres, T. Dos Santos, P.R.F. Barnes and J.R. Durrant, *Energy Environ. Sci.*, **2010**, *3*, 1573-1579. d) X.F. Zhang, X. Shao, H. Tian, X. Sun and K. Han, *Dyes Pigm*. **2013**, *99*, 480-488.

[75] a) J.W. Perry, K. Mansour, S.R. Marder and K.J. Perry, *Opt. Lett.*, **1994**, *19*, 625-627. b) A.V. Vannikov, A.D. Grishina, Y.G. Gorbunova, V.I. Zolotarevskii, T.V. Krivencko, A.S. laryushkin, L.A. Lapkina, V.V. Savel'ev and A.Y. Tsivadze, *High Energ. Chem.*, **2015**, *49*, 36-43. c) M.E. Alberto, B.C. de Simone, G. Mazzone, E. Sicilia and N. Russo, *Phys. Chem. Chem. Phys*., **2015**, *17*, 23595-23601.

[76] a) M.J. Cook and A. Jafari-Fini, *Mat. Chem. Commun.*, **1997**, *7*, 2327-2329. b) S. Siddiqui and F. Spano, *Chem. Phys. Letters*, **1999**, *308*, 99-105. c) F. Würthner, T.E. Kaiser and C.R. Saha-Möller, *Angew. Chem. Int. Ed.*, **2011**, *50*, 3376-3410. d) T.T. Tasso, Y.T. Furuyama and N. Kobayashi, *Dalton Trans.*, **2014**, *43*, 5886-5892. e) K.K. Ng and G. Zheng, *Chem. Rev.*, **2015**, *115*, 11012-11042.

[77] E.G. McRae and M.Kasha, *J. Chem. Phys.*, **1958**, *28*, 721-722.

moments aligned in 90 degrees one to each other (*H*-aggregates), produces a higher energy transition that corresponds to a hypsochromic shift in the absorption spectra. On the other hand, in some particular cases the Pc substitution pattern leads to a shift in the columnar aggregation direction, forming staircase or brickwall aggregates. In this kind of aggregates (*J*-aggregates), the parallel dipolar moments are shifted 54.7 degrees or less, rising a lower energy transition that corresponds to a bathochromic shift in the absorption spectra. Self-aggregation interferes in other excited-state processes by exciton coupling, excimer/exciplex formation, resonance energy transfer, intermolecular heavy atom effect, and triplet-triplet annihilation.[76e]

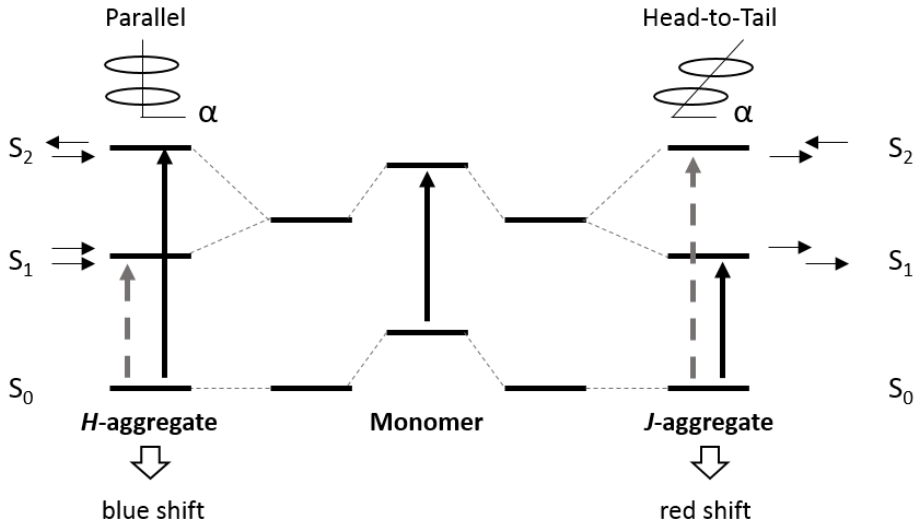

Figure 9. Schematic representation of the relationship between chromophore arrangement and spectral shift based on the molecular exciton theory, as shown in ref. 76b

3.2. Synthesis of phthalocyanines

The synthesis of Pcs takes place in most cases by cyclotetramerization of the appropriately substituted precursors, usually phthalonitriles or 1,3-diiminoisoindolines. Furthermore, chemical modification can be carried out at the Pc ring itself. Metallated Pcs can be synthesized by metalation of a base-free Pc or, more commonly, by cyclotetramerization in presence of a metallic salt that acts as template, as shown in Scheme 1.

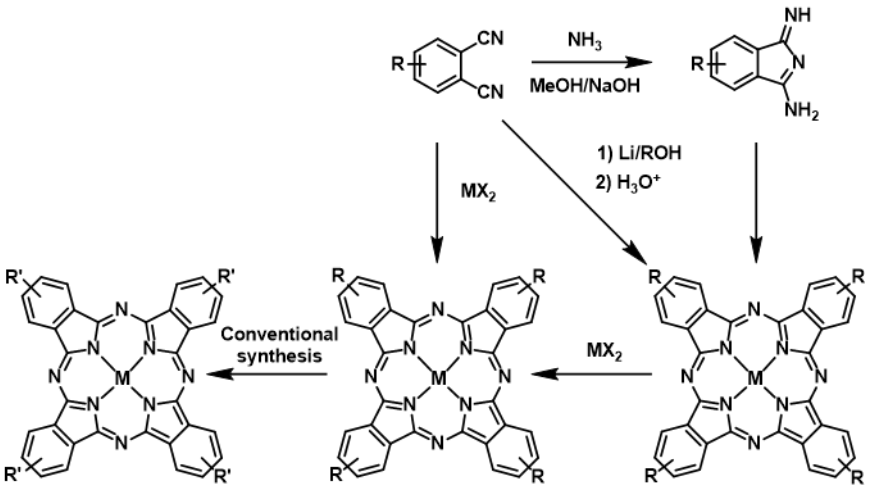

Scheme 1. Different synthetic pathways toward Pc.

The most usual method to prepare MPcs is the metal-templated reaction, in which a phthalonitrile derivatives (or more reactive species as 1,3-diiminoisoindolines) are heated in a solvent with high boiling point (e.g. DMAE, DMF, *o*-DCB) in presence of a metallic salt as template. In cases of low reactivity, basic catalysis with 1,8-diazabicyclo[5.4.0]undec-7-ene (DBU) is employed.[78] Lithium alkoxides or magnesium salts are also used with phthalonitriles, giving rise to the corresponding MPcs that can be easily converted into the free base by treatment with a mineral acid.[79] More recently, methods that allow preparing Pcs with higher efficiencies and milder conditions have been described. The treatment of phthalonitriles with metal salts and hexamethyldisilazane in DMF,[80] double-addition of oximes to phthalohthalonitriles[81] or microwave-assisted syntheses[82] are examples of simple and efficient novel synthetic strategies toward Pcs.

---

78 H. Tomoda, S. Saito, S. Ogawa and S. Shiraishi, *Chem. Lett*., **1980**, *9*, 1277-1280.

79 C.C. Leznoff, M. Hu and K.J.M. Nolan, *Chem. Commun.*, **1996**, *10,* 1245-1245.

80 H. Uchida, H. Tanaka, H. Yoshiyama, P. Y. Reddy, S. Nakamura and T. Toru, *Synlett.* **2002**, 1649-1652.

81 M.N. Kopylovich, V.Y. Kukushkin, M. Haukka, K.V. Luzyanin and A.J.L. Pombeiro, *J. Am. Chem. Soc.* **2004**, *126*, 15040-15041.

82 a) A. Loupy, D. Bogdal, A. Petit, *Tetrahedron*, **2005**, *61*, 179-188. b) I. Acar, H. Kantekin and Z. Biyikliouglu, *J. Organomet. Chem.*, **2009**, *695* (2), 151-155. c) C. Kantar, H. Akal, B. Kaya, F. Islamoglu, M. Turk and S. Sasmaz, *J. Organomet. Chem.*, **2015**, *783*, 28-39.

In relation to the formation of Pcs, various different mechanistic hypotheses have been proposed. However, there are some common features to all of these proposals.[83] In general, te macrocyclation in the presence of a nucleophile, like a sodium o lithium alkoxide starts with the formation of the corresponding salt of 1-imido-3-alcoxyindoline (Scheme 2A).[84] The next step in the reaction sequence consists in the nucleophilic attack of this intermediate to the cyano group of another phthalonitrile, resulting in a dimer formation (Scheme 2B). This dimer can react in the same way with other phthalonitriles (Scheme 2B) and finally binds the metallic ion or the metal-template triggers the subsequently addition of phthalonitriles.[83a,b] Other possibility consist in, from the dimer, using the metallic ion as template to self-condensation, forming the metallated Pc (Scheme 2D).

---

[83] a) V.W. Day, T.J. Marks and W.A.Wachter, *J. Am. Chem. Soc.*, **1975**, *97* (16), 4519-4527. b) D. Bush and N. Stephenson, *Coord. Chem. Rev.*, **1990**, *100*, 119-154. c) C.R. Rager, G. Schmid and M. Hanack, *Chem, Eur. J.*, **1999**, *5* (1), 280-288. b) C.C. Leznoff, A.M. Castaño and S.Z. Yidiz, *J. Porphyrins Phthalocyanines*, **2000**, *4*, 103-111.

[84] S.W. Oliver and T.D. Smith, *J. Chem. Soc. Perkin Trans. II*, **1987**, *11*, 1579-1582.

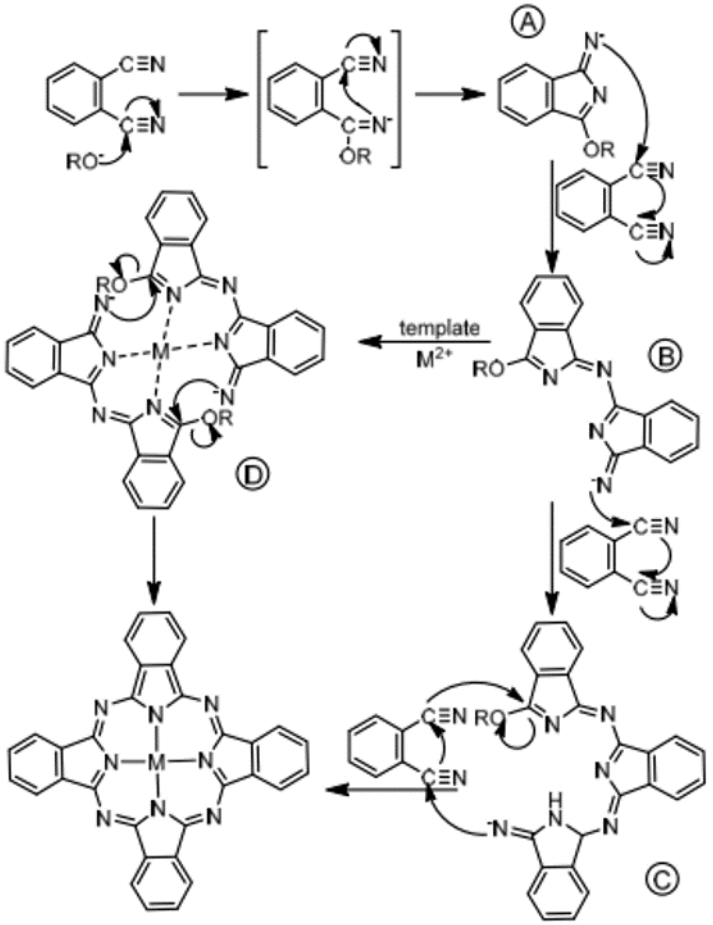

Scheme 2. Hypothetical mechanism for the synthesis of metallophthalocyanines by cyclotetramerization of phthalonitriles in the presence of a metal salt.

In case of using 3- or 4-substituted phthalonitriles, the resulting tetrasubstituted Pcs are obtained as mixtures of four structural isomers with C_{4h}, D_{2h}, C_{2v} and C_{2s} symmetries (Figure 10)[85] that sometimes can be separated by chromatographic methods[86] or separately obtained by a regioselective synthesis of Pcs.[87]

---

[85] a) M. Sommerauer, C. Rager and M. Hanack, *J. Am. Chem. Soc.* **1996**, *118*, 1085-1093; b) S. Rodríguez-Morgade and M. Hanack, *Chem. Eur. J.* **1997**, *3*, 1042-1051.

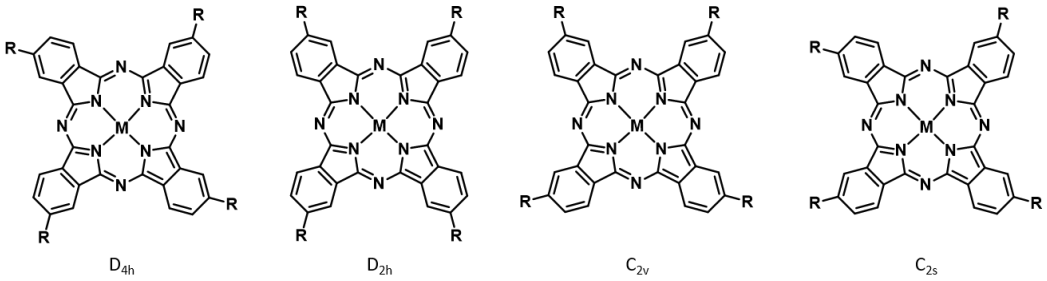

Figure 10. Structures of the four constitutional isomers of 2(3)-tetrasubstituted metallophthalocyanines.

The great versatility of Pcs can be expanded through the synthesis of unsymmetrically substituted Pc derivatives. Inclusion of two different substitution patterns in the isoindole units (A and B) leads to a relative distribution of possible macrocycle products (A_3B, A_2B_2 or ABAB) in the reaction mixture.[87e,88] Selective synthetic methodologies of targeted unsymmetrically substituted Pcs have been developed in the recent years: (i) solid-phase synthesis,[89] where phthalonitrile B is linked to an insoluble polymer and is reacted with an excess of phthalonitrile A. The synthesized A_3B Pc is then cleaved from the solid support. (ii) Ring expansion reaction,[90] where an A_3 subPc ring is opened by reaction with a differently substituted 1,3-diiminoisoindolines (B). (iii) Cross-condensation reaction,[91] that takes advantage of the limited reactivity of species like 1,1,3-

---

86 a) G. Schmid, M. Sommerauer and M. Hanack, *Angew. Chem. Int. Ed.*, **1993**, *32*, 1422-1424. b) S. Rodríguez-Morgade and M. Hanack, *Chem. Eur. J.*, **1997**, *3*, 1042-1051. c) W.D. Dabney, F.G. Anila and R. Brian, *J. Porphyrins Phthalocyanines*, **2004**, *8*, 1300-1310. d) S. Shimizu, H. Zhu and N. Kobayashi, *Chem. Eur. J.*, **2010**, *16*, 11151-11159.

87 a) N. Kobayashi, Y. Kobayashi and T. Osa, *J. Am. Chem. Soc*. **1993**, *115*, 10994-10995. b) D.M. Drew and C.C. Leznoff, *Synlett*, **1994**, *8*, 623-624. c) D.M. Drew and C.C. Leznoff, *Can. J. Chem.*, **1996**, *74* (3), 307-318. d) M. Kimura, Y. Sugihara, T. Muto, K. Hanabusa, H. Shirai and N. Kobayashi, *Chem. Eur. J.*, **1999**, *5* (12), 3495-3500. e) G. de la Torre, C. Claessens and T. Torres, *Eur. J. Org. Chem.*, **2000**, *16*, 2821-2830. f) N. Iida, K. Tanaka, E. Tokunaga, H. Takahashi and N. Shibata, *ChemistryOpen*, **2015**, *4* (2), 102-106.

88 a) T. Torres, *J. Porphyrins Phthalocyanines*, **2000**, *4*, 325-330. b) G. de la Torre and T. Torres, *J. Porphyrins Phthalocyanines*, **2002**, *6*, 274-284. c) J. Mack and N. Kobayashi, *Chem. Rev.*, **2011**, *111*, 281-321.

89 a) C.C. Leznoff and T.W. Hall, *Tetrahedron Lett.*, **1982**, *23* (30), 3023-3026. b) A. Hirth, A.K. Sobbi and D. Wohrle, *J. Porphyrins Phthalocyanines*, **1997**, *1*, 275-279. c) S.S. Erdem, I.V. Nesterova, S.A. Soper and R.P. Hammer, *J. Org. Chem.*, **2008**, *73* (13), 5003-5007. d) M. Mudyina, N.M. Ndinguri, A.S. Steven and P.R. Hammer, *J. Porphyrins Phthalocyanines*, **2010**, *14*, 892-903. e) K.N. Porchelvi, S. Meenakshi and K. Pandian, *Adv. Mat. Res.*, **2014**, *938*, 40-45.

90 a) A. Weitemeyer, H. Kliesch and D. Whorle, *J. Org. Chem.*, **1995**, *60*, 4900-4904. b) A. Sastre, T. Torres and M. Hanack, *Tetrahedron Lett.*, **1995**, *36* (46), 8501-8504. c) A. Sastre, B. del Rey and T. Torres, *J. Org. Chem.*, **1996**, *61* (24), 8591-8597. d) W.M. Sharman and J.E. van Lier, *J. Porphyrins Phthalocyanines,* **2005**, *9*, 651-659. e) L. Zhao, K. Wang, H. Shang and J. Jiang, *Dyes Pigments*, **2015**, *120*, 52-56.

91 a) J.G. Young and W. Onyebuagu, *J. Org. Chem.*, **1990**, *55* (7), 2155-2159. b) N. Kobayashi, T. Ashida and T. Osa, *Chem. Lett.*, **1992**, *10*, 2031-2034. c) M. Hanack and P. Stihler, *Eur. J. Org. Chem.*, **2000**, *2*, 303-311. d) J-.D. Wang, M-.J. Lin, S-.F. Wu and Y. Lin, *J. Organometallic Chem.* **2006**, *691* (23), 5074-5076.

trichloroisoindolenines. Such species that cannot self-condense, yielding ABAB Pcs when reacted with phthalonitriles or 1,3-diiminoisoindolines.

In addition to the previously described targeted synthetic methodologies, statistical cyclotetramerization[88] is based on the mixed condensation of two differently functionalized phthalonitriles (A and B) to produce a mixture of Pcs (Figure 11) that, in a second step, are separated by chromatography. Despite of being the less efficient method to synthesize unsymmetrically substituted Pc, this is the most widespread methodology to obtain A_3B compounds due to its simplicity. The separation of A_2B_2 and ABAB isomers is usually difficult to separate, other strategies being necessary like the inclusion of bulky groups in the 3,6- possitions to selectively form the desired regioisomer.[92]

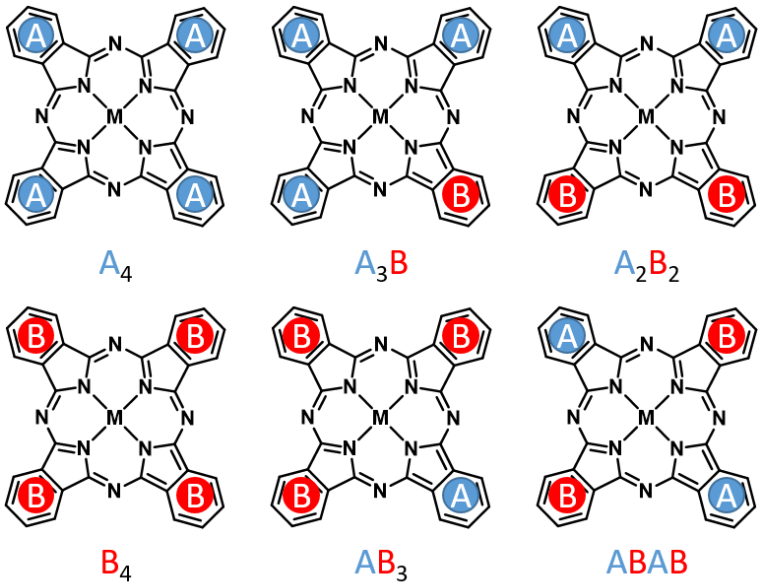

Figure 11. Set of phthalocyanines obtained via statistical cyclotetramerization of two differently functionalized phthalonitriles or 1,3-diiminoisoindolines, A and B.

Depending on the metal in the inner cavity of the macrocycle, a further functionalization site is possible to achieve in the axial position. More details will not been given because this reactivity lays out of the scope of the present thesis.

---

92 a) E. Fazio, J. Jaramillo-Garcia, G. de la Torre and T. Torres, *Org. Lett.*, **2014**, *16* (18), 4706-4709.

3.3. Properties and application of phthalocyanines in nanotechnology

Since their first serendipitous synthesis at the beginning of the last century, Pcs have been stablished as blue and green dyes for inks, plastics, metal surfaces, and clothing as jeans. More recently, the high optical stability, semiconductivity and excellent photophysical properties of Pcs, new fields of application and, therefore, of commercial utility have been opened.. Potential uses of Pcs include chemical sensors,[93] electrochromic display devices, NLO, information storage systems (optical computers read/write discs), catalysis, electron- and photocatalysis, liquid crystal colour display applications, etc.[94] In the following paragraphs we discuss some groups of properties that make Pcs ideal building blocks for those applications.

(i) Optical properties of Pcs:

The inherent strong absorption of Pcs in the NIR region of the visible light spectrum, where light penetration through tissues is higher, have attracted a lot of attention on Pcs as PDT agents. Besides, NLO organic materials have been studied in the last 30 years. For this application, non-centrosymmetric organic materials, comprising a highly polarizable π-system are required. Unsymmetrically substituted Pcs and analogues, with electron-donor and electron-acceptor groups present a polarized π-aromatic cloud suitable for this application.[95] Research in this field has been mainly focused on the study of second harmonic generation (SHG), where two incident waves of frequency ω are absorbed and combined in the material, emitting a wave of frequency 2ω. In a similar way, a third harmonic generation (THG) processes emit a 3ω frequency wave. Other non-linear effect known as optical limiting (OL), consisting on a decrease of the transmittance of the NLO material under high-intensity illumination, has found utility as a protection of the human eye from intense light sources.[96] Finally, Pcs and SubPcs are essential components in the manufacturing of CDs and DVDs, most of them being patented.[97]

---

93 a) E. Palomares, R. Vilar and J.R. Durrant, *Chem. Commun.*, **2004**, *4*, 362-363. b) F.I. Bohrer, C.N. Colesniuc, J. Park, I.K. Schuller, A.C. Kummel and W.C. Trogler, *J. Am. Chem. Soc.*, **2008**, *130* (12), 3712-3713.

94 *Porphyrin Handbook: Application of Phthalocyanines*, Ed. C.M. Kadish, K.M. Smith and R. Guilard, *19*, **2003.**

95 a) G. de la Torre, P. Vázquez, F. Agulló-López and T. Torres, *Chem. Rev.,* **2004**, *104* (9), 3723-3750. b) M. Quintiliani, J. Perez-Moreno, I. Asselberghs, P. Vazquez, K. Clays and T. Torres, *J. Phys. Chem. C,* **2010**, *114* (19), 6309-6315. c) G.N. Ngubeni, J. Britton, J. Mack, E. New, I. Hancox, M. Walker, T. Nyokong, T.S. Jones and S. Khene, *J. Mat. Chem. C*, **2015**, *3* (41), 10705-10714. d) A. Fashina, T. Nyokong, *J. Lumin.*, **2015**, *167*, 71-79.

96 a) S.M. O'Flaherty, S.V. Hold, M.J. Cook, T. Torres, Y. Chen, M. Hanack and W.J. Blau, *Adv. Mater.*, **2003**, *15* (1), 19-32. b) G.Y. Yang, M. Hanack, Y.W. Lee, D. Dini and J.F. Pan, *Adv. Mater.*, **2005**, *17* (7), 875-879.

97 a) A. Zafirov, S. Rakosvski, J. Bakardjieva-Eneva, L. Prahov, L. Assenova, F. Marrandino (Vivastar Mastering & Materials A.-G., Switzerland), PCT Int. Appl. WO 2002080158 A1, **2002**. b) Y. Usami, T. Kakuta and T. Ishida (Fuji Photo Film Co., Ltd., Japan), Eur. Pat. Applo., EP 1434207 A2, **2004**.

(ii) Electrical properties

Pcs, displaying in some cases conductivities in the range of 10^{-4} to 10^{-2} Ω^{-1} cm^{-1}, are considered within the low-dimensional semiconducting molecular materials.[98] Conductivity in MPc systems can be due either to the intrinsic properties given by the metallic atom, or to the organization of the molecules at the supramolecular level. Lutetium bisphthalocyaninato ($Lu(Pc)_2$) or lithium phthalocyanine (LiPc) are intrinsic molecular semiconductors and have been applied in some devices as OFETs.[94,99] The supramolecular arrangement of Pcs can also be responsible for their semiconducting properties, generating new conducting bands by overlapping of the π-orbitals. Generally, dopping these systems with an oxidizing or reducing agent increases their conductivity. Variations in semiconducting properties by redox reaction of the Pc with different gasses (ammonia, nitrogen monoxide and dioxide and carbon monoxide) have been exploited to design molecular sensors.

(iii) Magnetic properties of Pcs[100]

The magnetic properties of Pcs have been less studied because, in many cases, MPcs with one or more unpaired electrons behave as simple paramagnetic substances. However, some complexes can exhibit spontaneous magnetization depending on the metallic core. (i) d-metal Pcs (Mn^{+2}, Fe^{+2}, Cr^{+2}, Co^{+2}, Ni^{+2}, Cu^{+2}). (ii) π-radical derivatives (LiPc and π-radical bis(Pc)). (iii) 4f metal Pcs (Tb^{+3}, Dy^{+3}).

Apart from the previously described applications, Pcs have recently demonstrated their potential in two other capital areas of nanotechnology like nanomedicine and photovoltaics. These two hot topics will be exhaustively discussed in Chapters 2 and 3 of the present thesis, respectively.

---

98 a) H. Schultz, H. Lehmann, M. Rein and M. Hanack, *Struct. Bonding*, **1991** *74*, 41- 146. b) D. Schelettwein, D. Wohrle, F. Karmann and U. Melville, *Chem. Mater.*, **1994**, *6* (1), 3-5. c) J. Simon, T. Toupance in *Comprehensive Supramolecular Chemistry,* vol. 10. *Intrinsic molecular semiconductors: electronics and ionoelectronics finalities*¸Ed. D.N. Reinhoudt, Pergamon, Exeter, **1996**. d) M.F. Craciun, S. Rogge, M.-J.L. den Boer, S. Margadonna, K. Prassides, Y. Iwasa and A.F. Morpurgo, *Adv. Mater.*, **2006**, *18* (3), 320-324. e) A. Farooq, KH.S. Karimov, F. Wahab, T. Ali and S. Z. Abbas, *J. Optoelectron. Adv. M.*, **2015,** *17* (5), 822-826.

99 a) G. Guillaud, J. Simon and J.P. Germain, *Coord. Chem. Rev.*, **1998**, *178*, 1433-1484. b) T. Okuda, S. Shintoh and N. Terada, *J. Appl. Phys.*, **2004**, *96*, 3586-3588. c) J. Zhang, J. Wang, H. Wang and D. Yan, *Appl. Phys. Lett.*, **2004**, *84*, 142-144. d) L. Li, Q. Tang, H. Li, W. Hu, X. Yang, Z. Shuai, Y. Liu and D. Zhu, *Pure Appl. Chem.*, **2008**, *80* (11), 2231-2240. e) E. Kaki, A. Altindal, B. Salih and Ö. Bekaroglu, *Dalton Trans.*, **2015**, *44* (17), 8293-8299.

100 a) N. Ishikawa, M. Sugita, T. Ishikawa, S-.Y. Koshihara and Y. Kaizu, *J. Am. Chem. Soc.*, **2003**, *125* (29), 8694-8695. b) S. Cardona-Serra, J.M. Clemente-Juan, E. Coronado, A. Gaita-Ariño, A. Camon, M. Evangelisti, F. Luis, M.J. Martinez-Perez and J. Sese, *J. Am. Chem. Soc.*, **2012**, *134* (36), 14982-14990.

GENERAL OBJECTIVES

General Objectives

The main goal of the present Doctoral Thesis is the synthesis of novel ZnPc derivatives designed with specific peripheral substitution patterns for their application as PS in different fields. ZnPcs, in combination with suitable biologically related nanoestructures can render photoactive biohybrid materials with potential applications in nanomedicine or environmental science. On the other hand, ZnPcs in combination with carbon allotropes have been employed as photoactive materials in environmentally friendly processed energy conversion technologies. In detail, the thesis has been specifically structured in three chapters.

Chapter 1: Synthesis and characterization of water-soluble phthalocyanines

Pcs, which are well-known for their outstanding photochemical and photophysical properties, belong to the most promising candidates for biomedical, environmental and energy conversion technologies. In order to prepare ZnPc derivatives suitable for the aforementioned applications, a selection of ionic functional groups has been incorporated to their aromatic structure, aiming to render aqueous solubility (Figure 12). Is noteworthy to mention that the synthesis and characterization of water-soluble Pc derivatives presents additional challenges in comparison to the conventional synthesis developed for their hydrophobic analogues. The hydrophilic groups commonly employed as substitution pattern in the periphery of the ZnPc core present high polarity, even prior to quaternization, and low solubility in most of organic solvents, rendering macrocycles more prone to aggregate. These factors limit the purification possibilities by column chromatography, the most common technique to obtain asymmetrically substituted ZnPcs. The development of synthetic strategies and methods to overcome these issues will be a major task within this chapter.

To this end, two main groups of ZnPcs has been synthesized and described in separated sections:

- The first one is focused on a series of symmetric and asymmetrically functionalized anionic sulfonated ZnPc derivatives.
- The second one, devoted to the synthesis and characterization of cationic ZnPcs, is further subdivided in three subsections, attending to the nature of the quaternized

moiety (i.e. trimethylammonium, *tert*-butylphenylpyridinum and pyrene-containing pyridinium substituents).

For most of the water-soluble ZnPc derivatives synthesized, the hydrophobic aromatic macrocycles trends to aggregate in aqueous media, typically as columnar stacks (*H*-type aggregates), due to π-π interactions. This behaviour has been thoroughly studied in Chapter 1, especially in section 1.3.3., where a novel kind of aggregation will be described.[101] In order to disrupt this self-aggregation behaviour, with the objective of maintaining or enhancing the photophysical and photochemical properties of ZnPc PS in aqueous media, various strategies have been developed within this thesis, such as insertion in micelles (Chapter 1.3.1. and Chapter 2.2.1), supramolecular complexation with alternative building blocks (Chapter 2.2.3 and Chapter 3.4.1.2.) or by conjugation with nanocrystalline cellulose (Chapter 2.2.4).

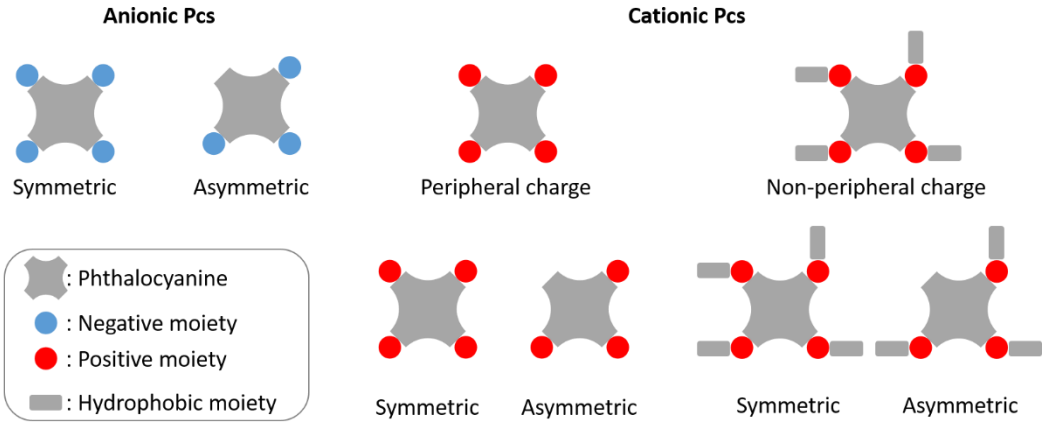

Figure 12. Schematic representation of the hydrophilic and amphiphilic ZnPcs synthesized during the present thesis.

Chapter 2: Synthesis and characterization of Pc-based biohybrid materials

The main goal of this chapter is to develop and study three different photoactive biohybrid materials based on water-soluble ZnPcs. The potential application of these systems lies in the inherent properties of ZnPcs such as fluorescence, for optical imaging, and singlet oxygen generation, for their use in a broad variety of technologies such as PDT

[101] E. Anaya-Plaza, M. Sekita, S. Bauroth, A. de la Escosura, D.M. Guldi and T. Torres, *manuscript in preparation*.

and PDI, pollutant oxidation in water or chemical oxidation in aqueous organic synthesis. Having control of the chromophore aggregation once conjugated is a key aspect, in order to assure an optimal performance of the resultant biohybrid material. In detail, Chapter 2 has been divided in three sections, each describing a different material:

In the first section, optically active and paramagnetic micelles of Gd^{3+}/DOTAC10 complex have been incorporated inside VLPs through a hierarchical process of self-assembly triggered by self-assembly (Figure 13).[102] The incorporation of ZnPc molecules in the paramagnetic micelles led to a higher capsid loading with Gd^{3+}, as the micelles were stabilized by the amphiphilic dye encapsulation. The resulting VLPs show an improved r_1 relaxivity, suggesting the possible use of these nanostructures as contrast agents for MRI. Since the encapsulated ZnPc also has a potential PDT and imaging value, this biohybrid material represents a first step towards the consecution of fully self-assembled protein NPs for multimodal imaging and therapy.

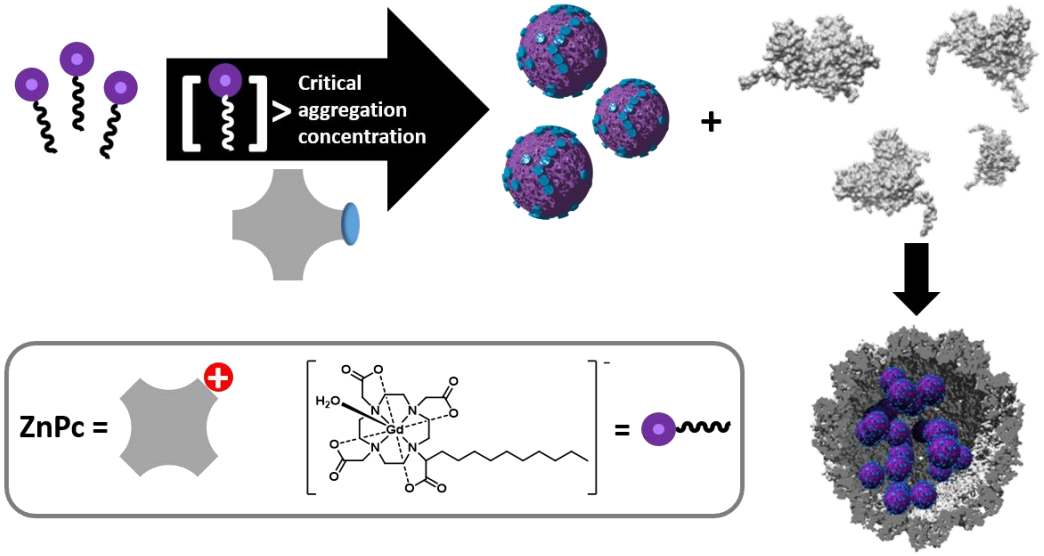

Figure 13. Schematic representation of the hierarchical self-assembly of multimodal imaging micelles coated a virus protein.

[102] J.G. Millan, M. Brasch, E. Anaya-Plaza, A. de la Escosura, A.H. Velders, D.N. Reinhoudt, T. Torres, M.S.T. Koay and J.J.L.M. Cornelissen, *J. Inorg. Biochem.*, **2014**, *136*, 140-146.

The second section describes the combination of a supramolecular photoactive complex and apoferritin protein cages into a photoactive biohybrid crystals (Figure 14).[103] Toward this end, a hierarchical organization process has been designed, starting with the formation of the complex between an octacationic ZnPc and a tetraanionic pyrene derivative in a 1:1 ratio, driven by electrostatic and π-π interactions. The resulting tetracationic supramolecular complex acts as a molecular glue that binds to the outer surface anionic patches of the apoferritin cage, triggering the co-crystallization process. The obtained ternary face-centered cubic (fcc) packed cocrystals, with diameters up to 100 µm, retain the optical properties of the pristine dye molecules, such as fluorescence and efficient $^1O_2$ photoproduction. Therefore, these results demonstrate a powerful methodology to create functional biohybrid materials with unprecedented long-range order and potential applications in PDT/PDI, water treatments, diagnostic arrays and as an oxidant in organic synthesis.

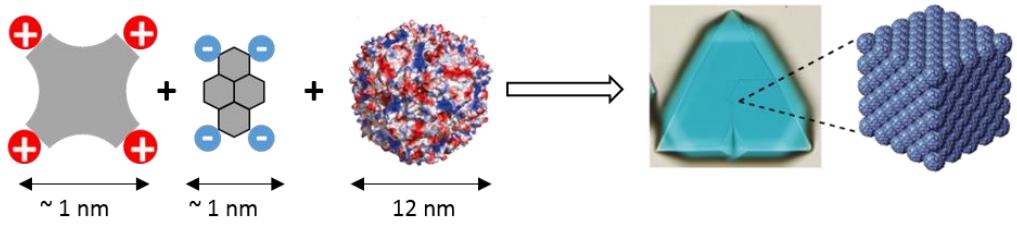

Figure 14. Schematic representation of the hierarchical crystallization process involving cationic ZnPc, anionic pyrene-derivative and apoferritin.

The third sections describes an easy, cheap and straightforward strategy to attach cationic ZnPcs onto sulphated CNCs surface, based on their electrostatic interaction with the sulfate moieties grafted on the cellulose surface (Figure 15).[104] Apart from disrupting the previously discussed ZnPc stacking, CNC aggregation is a critical aspect in the design of these materials,which determine the photosensitizing capacity of the obtained biohybrids. The resulting photoactive nano-whiskers show a potential interest for the aforementioned technologies, as suggested by their enhanced capacity for singlet oxygen generation.

---

[103] J. Mikkilä, E. Anaya-Plaza, V. Liljeström, J.R. Caston, T. Torres, A. de la Escosura and M.A. Kostiainen, *ACS Nano*, **2016**, *10*, 1565-1571.

[104] E. Anaya-Plaza, E. van de Winckel, J. Mikkilä, J.-M. Malho, O. Ikkala, T. Torres, M.A. Kostiainen and A. de la Escosura, *submitted*.

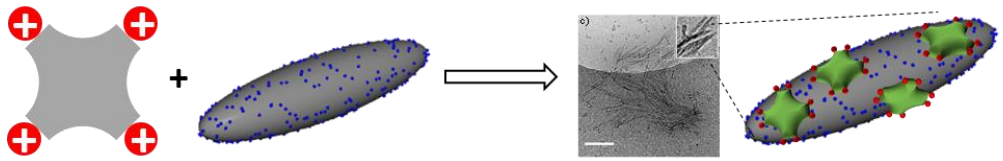

Figure 15. Schematic representation of sulfated CNCs coated with octacationic ZnPc, resulting in photoactive nanocrystalline cellulose.

Chapter 3: Water-soluble phthalocyanine systems for energy conversion.

Pcs are well-known materials for energy conversion technologies due to their remarkable optoelectronic properties. Their synthetic versatility allows the incorporation of these outstanding chromophores to photovoltaic devices with different architectures. The growing concern about the environmental impact of large-scale solution processing techniques of the devices, however, has developed an increasing interest on organic solar cells processed from aqueous solution. As consequence, the third chapter of the present thesis is devoted to the development of water-soluble photoactive materials to be applied into energy conversion schemes. In detail, this chapter has been divided in three sections:

The first one describes the preparation of small molecule organic solar cells (SMOSCs) by spin-coating of the water-soluble chromophores and subsequently vacuum deposition of pristine C_{60} fullerene.[105] This represents the first study on the influence of the frontier orbitals, tuned by peripheral substitution pattern, in the photocurrent of this kind of devices (Figure 16). This, along with a morphology study of the photoactive layer, results in an efficiency improvement compared to the previous work on water-solube Pc-based photovoltaic devices.

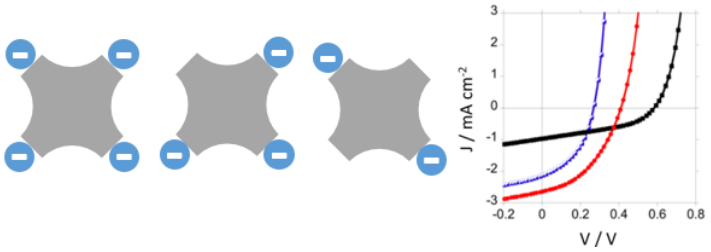

Figure 16. Photocurrent to voltage curves of SMOSCs processed from aqueous solutions of a tetra- (black line), tri- (blue line) or dianionic (red line) ZnPcs as photoactive material.

[105] J.W. Ryan, E. Anaya-Plaza, A. de la Escosura, T. Torres and E. Palomares, *Chem. Commun.*, **2012**, *48*, 6094-6096.

The second section develops a novel approach to produce aqueous electron-donor SWCNT based on the noncovalent immobilization of octacationic ZnPcs.[106] The electron-acceptor nature of the ZnPcs synthesized in Chapter 1.3.2 enables switching the electronic role of SWCNTs within the resulting supramolecular hybrids (Figure 17). Finally, a proof-of-concept demonstration of the SWCNT/ZnPc hybrids' capacity for energy conversion is presented, paving their way to their possible use as active layer material in solar cells processed entirely from aqueous solutions.

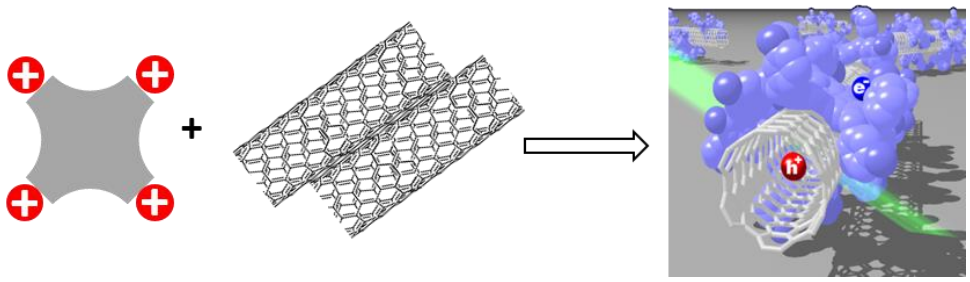

Figure 17. Schematic representation of octacationic ZnPc/SWCNT hybrids, and the charge-transfer process between both photoactive units.

The third section, and therefore the last one of the present thesis deals with the synthesis and characterization of two water-soluble anionic C_{60} fullerenes. These derivatives consist of a tetraanionic monoadduct and a regioisomerically pure octaanionic bisadduct. In aqueous solution, and in combination with a pyrene-containing tetracationic ZnPc synthesized in Chapter 1.3.3, these two fullerenes form a 1:1 and 1:2 strongly-bounded supramolecular complexes, respectively, driven by the synergy of both electrostatic and π-π interaction. Both complexes have demonstrated to produce a photoinduced charge-transfer process in aqueous medium, which is a large step toward the consecution of the first photovoltaic devices based on water-soluble ZnPc/fullerene supramolecular ensembles (Figure 18).[107]

---

[106] E. Anaya-Plaza, M.M. Oliva, A. Kunzmann, C. Romero-Nieto, R.D. Costa, A. de la Escosura, D.M. Guldi and T. Torres, *Adv. Funct. Mat.*, **2015**, *25*, 7418-7427.

[107] E. Anaya-Plaza, M. Sekita, S. Bauroth, A. de la Escosura, D.M. Guldi and T. Torres, *manuscript in preparation*

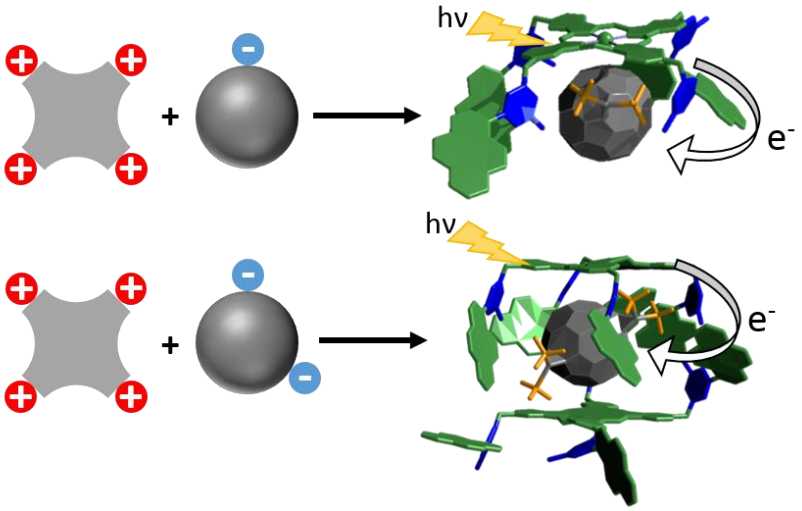

Figure 18. Schematic representation of the two supramolecular complexes triggered by ionic interactions and photoinduced charge-transfer process.

Chapter I:
Synthesis and characterization of water-soluble phthalocyanines

1. Synthesis and characterization of water-soluble zinc phthalocyanines

1.1. Water-soluble phthalocyanines: state of art

The intrinsic aromaticity and planarity of Pcs make them, when unsubstituted, insoluble in most common solvents. Chemical substitution at the periphery or axial positions of the macrocycle allows fine-tuning their solubility, aggregation, and optoelectronic properties. In this regard, aqueous solubility represents a desirable but challenging property for some applications of phthalocyanines that are of biological interest or require environmental friendliness. This is the case of biomedical applications such as PDT,[108] catalysis of reactions in aqueous media,[109] degradation of pollutants,[110] and environmentally friendly processing of photovoltaic devices.[111] At this point, it is important to specify that aqueous solubility also implies buffer solutions, more related to biological media, and the addition of small amounts of polar organic solvents (e.g., DMSO, DMF, methanol, etc.), always less than 10 %.

Taking advantage of the synthetic versatility of Pcs, different patterns of substitution have been developed to render water-soluble derivatives. Indeed, water-soluble Pcs (wsPcs) can be classified according to the nature of the hydrophilic groups involved, independently of their direct attachment to the macrocycle or the existence of spacers.[112] Additionally, a small family of charged wsPcs, bearing cationic and anionic substituents at the same time, has been also reported.[113] Most of those derivatives result from the quaternization of a nitrogen with propanesultone. This reagent bears a hidden sulfonate function that appears after the ring opening of the reactant during the quaternization reaction. This family of Pcs does not present a significant improvement in solubility or properties, compared to purely anion or cationic ones, leading to a low impact in the field.

---

[108] a*)* T. J. Dougherty, C. J. Gomer, B. W. Henderson, G. Jori, D. Kessel, M. Koberlik, J. Moan, Q. Peng, *J. Natl. Cancer Inst.* **1998**, *90*, 889-905; b) S. B. Brown, E. A. Brown, I. Walker, *Lancet Oncol.* **2004**, *5*, 497-508; *c*) D. E. Dolmans, D. Fukumura, R. K. Jain, *Nat. Rev. Cancer* **2003,** *3*, 380-387; d) *Handbook of Photomedicine*, (M. R. Hamblin, Y.Y. Huang Eds), CRC Press, **2012**.

[109] a) D. Wöhrle, O. Suvorova, R. Gerdes, O. Bartels, L. Lapok, N. Baziakina, S. Makarov and A. Slodek, *J. Porphyrins Phthalocyanines,* **2004**, *8*, 1020-1042. b) A. Vashurin, A. Filippova, S. Znoyko, A. Voronina, O. Lefedova, I. Kuzmin, V. Maizlish and O. Koifman, *J. Porphyrins Phthalocyanines*, **2015**, *19*, 983-996.

[110] a) K.T. Ranjit, I. Willner, S. Bossman and A. Braun, *J. Phys. Chem. B*, **1998**, *102*, 9397-9403. b) R. Zugle, E. Antunes, S. Khene and T. Nyokong, *Polyhedron*, **2012**, *33*, 74-81. c) Y. Zhao, L. Yang, Q. Xu, M. Barahman, D. Bartusik, A. Greer and A.M. Lyons, *J. Phys. Chem. A*, **2014**, *118*, 10364-10371.

[111] S. Schumann, R.A. Hatton and T.S. Jones, *J. Phys. Chem. C*, **2011**, *115*, 4916-4921.

[112] F. Dumoulin, M. Durmus, V. Ahsen and T. Nyokong, *Coord. Chem. Rev.*, **2010**, *254*, 2792-2847.

[113] M. Çamur, V. Ahsen and M. Durmus, *J. Photochem. Photobiol. A*, **2011**, *219*, 217-227.

Below, we discuss in detail both anionic and cationic systems.

1.1.1. **Anionic phthalocyanines**

The main anionic functional groups comprise sulfonate-, phosphorus-based and carboxylate functionalities, directly attached to the macrocycle or linked through various spacers. The hydrophilicty provided by these groups is strongly pH-dependant, the conjugate acid forms being not necessarily water-soluble.

(i) Sulfonated Pcs

The synthesis of sulfonated Pcs can follow different pathways like the employment of sulfonated precursors or the introduction of the sulfonate function on the phthalocyanine core. These pathways have been extensively developed by van Lier and his research group,[114] especially those that lead to asymmetrically substituted sulfonated Pcs. The most common methodology consists on the well-known statistical cyclotetramerization of 4-sulfophthalic acid monosodium salt[114b] or 4-sulfophthalonitrile potassium salt,[115] with the desired phthalonitrile in presence of the corresponding metallic salt. An alternative synthetic route consists on the sulfonation of the Pc macrocycle, treating it with concentrated sulfuric acid[116] or fuming sulfuric acid.[117] By this method, a mixture of mono-, di-, tri- and tetrasulfonated phthalocyanines was obtained and separated by column chromatography. Finally, a third possible route is based on the ring expansion reaction of sulfonic subPcs, leading to trisulfonic acid Pcs in elevated yields.[118] Other sulfonated phthalocyanines precursors have been reported, bearing the sulfonic acid moieties in the substituents not directly connected to the macrocycle.[119]

---

[114] a) R. Langlois, H. Ali, N. Brasseur, J.R. Wagner and J.E. van Lier, *Photochem. Photobiol.*, **1986**, *44*, 117-123. b) H. Ali, R. Langlois, J.R. Wagner, N, Brasseur, B. Paquette and J.E. van Lier, *Photochem. Photobiol.*, **1988**, *47*, 713-717. c) R. Edrei, V. Gottfried, J.E. van Lier and S. Kimel, *J. Porphirins Phthalocyanines*, **1998**, *2*, 191-199. d) E. Ranyuk, R. Lebel, Y. Berube-Lauziere, K. Klarskov, R. Lecomte, J.E. van Lier and B. Guerin, *Bioconj. Chem.*, **2013**, *24*, 1624-1633.

[115] Z. Jiang, W. He, H. Yao, J. Wang, N. Chen and J. Huang, *J. Porphirins Phthalocyanines*, **2011**, *15*, 140-148.

[116] N. Brasseur, H. Ali, R. Langlois, R.J. Wagner, J. Rousseau and J.E. van Lier, *Photochem. Photobiol.*, **1987**, *45*, 581-586.

[117] A. Siejak, D. Wróbel, P. Siejak, B. Olejarz and R.M. Ion, *Dyes Pigm.*, **2009**, *83*, 281-290.

[118] a) S.V. Kudrevich, S. Gilbert and J.E. van Lier, *J. Org. Chem.*, **1996**, *61*, 5706-5707. b) S. Kudrevich, N. Brasseur, C. La Madeleine, S. Gilbert and J.E. van Lier, *J. Med. Chem.*, **1997**, *40*, 3897-3904.

[119] a) V.M. Negrimovsky, V.M. Derkacheva, E.A. Luk'yanets, A. Weitemeyer, D. Wöhrle and G. Schneider, *Phosphorus, Sulfur, Silicon Relat. Elem.*, **1995**, *104*, 161-167. b) S. Arslan and I. Yilmaz, *Polyhedron*, **2007**, *26*, 2387-2394.

(ii) Phosphonate-Pc systems

Despite of being a particularly useful kind of substituent, which allows a good adjustment of properties by pH, only a few examples of water-soluble phosphourous-substituted Pcs have been reported. Two different strategies have been followed so far. First, a direct phosphorylation of 4-bromo-[120] or 4-iodophthalonitrile[121] with diethylphosphite and palladium catalyst takes place. The resulting phosphonic ester derivative was later deprotected in acidic medium. The second strategy consist on the inclusion of an aliphatic spacer between the aromatic ring and the phosphonic acid moiety. To this end, phosphorylation of 4-(bromomethyl)phthalonitrile through an Arbuzov's reaction lead to the desired diethyl 3,4-dicyanobenzylphosphonate phthalonitrile.[122] Recently, N. Venkatramaiah *et al.* synthesized zinc and metal-free octaphosphonate-Pc that present no-fluorescence in benefit of an enhanced singlet oxygen generation, along with selectivity to bladder cancerous cells.[123]

(iii) Carboxylated Pcs

Carboxylic acid derivatives show a pH-dependant solubility in water. In general, carboxylated Pcs exhibit high solubility in alkaline media, where they are present as anionic salts. Their solubility in neutral or acidic solutions, on the other hand, strongly depends on the metallic atom and the substitution pattern.

Tetracarboxylic acid-Pcs are obtained by cyclotetramerization of trimellitic acid or anhydride in the presence of urea, ammonium chloride and ammonium molybdate. The resulting tetra amido-Pc is fully hydrolized under harsh alkaline or acid conditions.[124] Octacarboxylic acid Pc is synthesized by cyclotetramerization of pyromellitic dianhydride[125] or 1,2,4,5-tetracyanobenzene[126] in presence of urea, the corresponding metal salt, and DBU or aluminium molybdate, respectively. The resulting tetraimidephthalocyanine is subsequently hydrolized in acid or basic media. The macrocyclation of benzene-1,2,3,5-

---

120 G. Märkl, K. Gschwendner, I. Rötzer and P. Kreitmeier, *Helv. Chim. Acta*, **2004**, *87*, 825-844.

121 W.M. Sharman, S.V. Kudrevich and J.E. van Lier, *Tetrahedron Lett.*, **1996**, *37*, 5831-5834.

122 R.W. Boyle, J.E. van Lier, *Synlett.*, **1993**, *5*, 351-352.

123 N. Venkatramaiah, P.M.R. Pereira, F.A.A. Paz, C.A.F. Ribeiro, R. Fernandes and J.P.C. Tomé, *Chem. Commun.*, **2015**, *51*, 15550-15553.

124 J. Griffiths, J. Schofield, M. Wainwright and S.B. Brown, *Dyes Pigments*, **1997**, *33*, 65-78.

125 K. Sakamoto and E. Ohno, *Prog. Org. Coat.*, **1997**, *31*, 139-145.

126 G.P. Shaposhnikov, V.E. Maizlish and V.P. Kulinich, *Russ. J. Gen. Chem.*, **2005**, *75*, 1480-1488.

tetracarboxylic acid in presence of urea, ammonium molybdate and the corresponding metal salt, followed by hydrolysis leads to a regioisomer mixture of α,β-disubstituted symmetric Pc.[126] In order to avoid the formation of oligomeric species, Zn- and CuPcs have been prepared from diesterified phthalonitrile (obtained in four steps from *o*-xylene) and subsequent hydrolysis.[127] The existing water-soluble asymmetric carboxylated Pcs, in turn, are of the A_3B type, synthesized by crossover statistical condensation. [125,128]

The inclusion of spacers between the Pc core and the carboxylic acid groups lead to the possibility to synthesize carboxylated Pcs from unprotected carboxylic acid phthalonitriles. Different spacers have been employed, such as alkyl chains,[122] aromatic rings,[129] and other moieties.[130] Among the latest, dendritic Pcs bearing carboxylic acids at the dendron shells increases drastically the number of solubilizing moieties, avoiding at the same time aggregation in aqueous media.[130c,131]

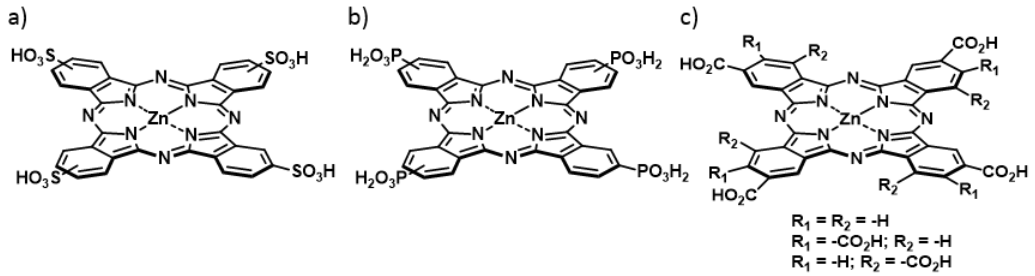

Chart 1. Chemical structures of symmetric derivatives of a) sulfonated, b) phosphonated, and c) carboxilated ZnPcs.

---

[127] D.M. Opris, F. Nüesch, C. Löwe, M. Molberg and M. Nagel, *Chem. Mater.*, **2008**, *20*, 6889-6896.

[128] a) N. Masilela, M. Idowu and T. Nyokong, *J. Photochem. Photobiol. A*, **2009**, *201*, 91-97. b) N. Masilela and T. Nyokong *Dye Pigm.*, **2010**, *84*, 242-248. c) N. Masilela, N. Nombona, T. Loewenstein, T. Nyokong and D. Schlettwein, *J. Porphirins Phthalocyanines*, **2010**, *14*, 985-992.

[129] a) M.D.K. Nazeeruddin, R. Humphry-Baker, M. Grätzel, D. Wöhrle, G. Schnurpfeil, G. Schneider, A. Hirth and N. Trombach, *J. Porphyrins Phthalocyanines*, **1999**, *3*, 230-237. b) C.-F. Choi, P.-T. Tsang, J.-D. Huang, E.Y.M. Chan, W.-H. Ko, W.-P. Fong and D.K.P. Ng, *Chem. Commun.*, **2004**, 2236-. c) W. Liu, T.J. Jensen, F.R. Fronczek, R.P. Hammer, K.M. Smith and M.G.H. Vicente, *J. Med. Chem.*, **2005**, *48*, 1033-.

[130] a) U. Dreschsler, M. Pfaff and M. Hanack, *Eur. J. Org. Chem.*, **1999**, *12*, 3441-3453. b) S.A. Mikhalenko, L.I. Solv'eva and E.A. Luk'yanets, *Russ. J. Gen. Chem.*, **2004**, *74*, 451-459. c) K. Sakamoto, S. Yoshino, M. Takemoto and N. Furuya, *J. Porphirins Phthalocyanines*, **2013**, *17*, 605-627.

[131] a) A.C.H. Ng, X.-Y. Li and D.K.P. Ng, *Macromolecules*, **1999,** *32*, 5292-. b) X.-Y. Li, A.C.H. Ng, C. Wu, D.K.P. Ng, *Macromolecules*, **2000**, *33*, 2119-. c) F. Setaro, R. Ruiz-González, S. Nonell, U. Hahn and T. Torres, *J. Inorg. Biochem.*, **2014**, *136*, 170-176. d) F. Setaro, M. Brasch, U. Hahn, M.S.T. Koay, J.J.L.M. Cornelissen, A. de la Escosura and T. Torres, *Nano Lett.*, **2015**, *15*, 1245-1251.

1.1.2. **Cationic phthalocyanines**

Cationic Pc derivatives can be obtained by quaternization of aliphatic or aromatic nitrogen atoms in their substituents. The quaternization reaction uasually takes place as the last step in the synthetic route, due to the experimental inconvenience of working with pH-independent charged species. This is achieved by several reactants like methyl bromide/iodide and dimethyl sulfate. It is worthy to note that all the methylating agents are recognized carcinogenic agents as they are likely to methylate DNA. For this reason, extreme precautions must be taken when they are handled. Iodoalkanes of various chain lengths and iodo-oligo(ethylene glycol) have also been employed as quaternizing agents, aiming to modulate amphiphilicity of the resulting cationic compounds. Below, most common cationic functional groups employed in synthesis of wsPcs will be discussed, and are summarized in Chart 2.

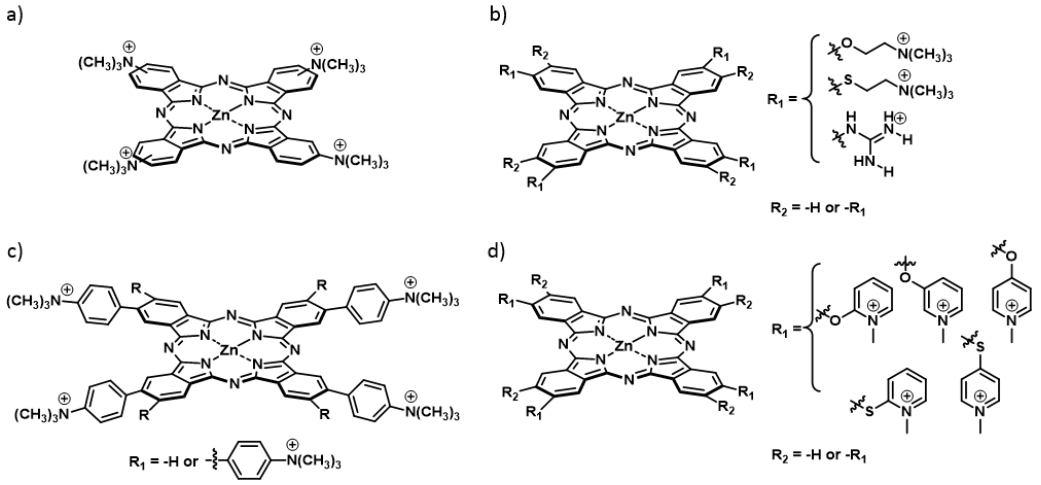

Chart 2. Chemical structures of most commonly employed cationic ZnPc derivatives.

(i) Ammonium derivatives

Trimethylammonium-functionalized Pcs, bearing the ammonium moiety directly bounded to the Pc core, have been described very recently, after dealing with solubility issues of the precursors (Chart 2a). This kind of Pc shows a strong π-π stacking interactions,

despite the "a priori" intense cation-cation repulsion.[132] This family of Pcs have been employed as DNA-labelling molecules, and PDI agents.[133]

Functionalized tertiary amines and their hydrochloride salts have been commonly achieved by grafting 2-(dimethylamino)ethanethiol,[134] 2-(diethylamino)ethanethiol,[135] 1,3-bis(dimethylamino)-2-propanol,[136] 2-(dimethylamino)ethanol,[137] or 3-aminothiophenol,[138] either by ether or thioether linkages, resulting in α and/or β mono- and disubstituted phthalonitriles and subsequent cyclotetramerization and quaternization reactions (Chart 2b). These simple structures and closely related ones have shown efficient telomerasa inhibitors.[139]

More complex spacers such as 2,4,6-tris(*N,N,N*-trimethylaminomethyl)phenol have been employed for antifungal treatments, [140] enabling the inclusion of a higher number of ammonia moieties and reducing, at the same time, the natural trend of these compounds to aggregate.

Guanidinium-substituted Pcs (Chart 2b) have demonstrated high specificity in G-quadruplex binding, thus being employed as telomerasa inhibitors.[141] Oligo(ethylene glycol)

---

[132] a) W. Duan, Z. Wang and M.J. Cook, *J. Porphyrins Phthalocyanines*, **2009**, *13*, 1255-1261. b) H. Yang, L. Chen, M. Guo, Y. Deng, P. Huang and D. Li, *Anal. Sci.*, **2015**, *31*, 543-549.

[133] D.M.G.C. Rocha, N. Venkatramaiah, M.C. Gomes, A. Almeida, M.A.F. Faustino, F.A.A. Paz, A. Cunha and J.P.C. Tomé, *Photochem. Photobiol. Sci.*, **2015**, *14*, 1872-1879.

[134] a) S. Dabak, G. Gümus, A. Gül and Ö. Bekaroglu, *J. Coord. Chem.*, **1996**, *38*, 287-. b) S. Gürsoy, A. Cihan, M.B. Koçak and Ö. Bekaroglu, *Monatsh. Chem.*, **2001**, *132*, 813-. c) Y. Arslanoglu and E. Hamuryudan, *Dyes Pigments*, **2007**, *75*, 150. d) B. Manisova, S. Binder, L. Malina, J. Jiravova, K. Langova and H. Kolarova, *Anticancer Res.*, **2015**, *35*, 3943-3951.

[135] a) M. Idowu and T. Nyokong, *Polyhedron*, **2009**, *28*, 416-. b) M. Machacek, A. Cidlina, V. Novakova, J. Svec, E. Rudolf, M. Miletin, R. Kucera, T. Simunek and P. Zimcik, *J. Med. Chem.*, **2015**, *58*, 1736-1749.

[136] a) M.P. De Filippis, D. Dei, L. Fantetti and G. Roncucci, *Tetrahedron Lett.*, **2000**, *41*, 9143-. b) M. Soncin, C. Fabris, A. Busetti, D. Dei, D. Nistri, G. Roncucci and G. Jori, *Photochem. Photobiol. Sci.*, **2002**, *1*, 815-.

[137] a) K. Kasuga, K. Ohmori, H. Tanaka, M. Handa, T. Sugimori, *Inorg. Chem. Commun.*, **2006**, *9*, 1019-1022. b) Y. Arslanoglu, E. Hayran and E. Hamuryudan, *Dyes Pigments*, **2013**, *97*, 340-346.

[138] F. Giuntini, D. Nistri, G. Chiti, L. Fantetti, G. Jori and G. Roncucci, *Tetrahedron Lett.*, **2003**, *44*, 515-517.

[139] L. Zhang, J. Huang, L. Ren, M. Bai, L. Wu, B. Zhai and X. Zhou, *Bioorg. Med. Chem.*, **2008**, *16*, 303-312.

[140] a) S.B. Sesalan, A. Koca and A. Gül, *Dyes Pigments*, **2008**, *76*, 259-. b) X.-S. Li, J. Guo, J.-J. Zhuang, B.-Y. Zheng, M.-R. Ke and J.-D. Huang, *Bioorg. Med. Chem. Lett.*, **2015**, *25*, 2386-2389.

[141] a) J. Alzeer, B.R. Vummidi, P.J.C. Roth and N.W. Luedtke, *Angew. Chem. Int. Ed.,* **2009**, *48*, 9362-9365. b) A. Membrino, M. Paramasivam, S. Cogoi, J. Alzeer, N.W. Luedtke and L.E. Xodo, *Chem. Commun.*, **2010**, *46*, 625-627. c) J. Alzeer and N.W. Luedtke, *Biochemistry.*, **2010**, *49*, 4339-4348.

(OEG) spacers have been used in some case, showing an increased amphiphilicity[142] or cationic Pc dimers.[143]

(iv) Anilinium derivatives

Anilines present a nitrogen directly bounded to an aromatic ring, conjugating its lone electron pair with the cycle. Despite this particularity, this functional group is suitable to be quaternized in similar conditions to ammonium derivatives. Following such strategy, a Suzuki-Miyaura reaction between 4-(dimethylamino)phenylboronic acid and 4-iodo- or 4,5-dibromophthalonitrile, and subsequent cyclotetramerization and quaternization reactions, leads to rigid tetra- and octacationic Pc derivatives, respectively (Chart 2c).[144] A range of spacers have been employed between the aniline unit and the Pc core, such as ether moieties,[145] OEG chains,[146] and more complex conjugated bridges,[147] yet this is not a broadly employed functionality since present a more challenging synthesis, showing no remarkable advantages in comparison with ammonium derivatives.

(v) Pyridinium derivatives

Pyridine is the most common substituent moiety to synthesize water-soluble Pcs due to its synthetic versatility. This heterocycle provides a lone nitrogen pair not conjugated within the aromatic ring, presenting aromaticity even after quaternization. The linkage of pyridines to phthalonitrile is usually achieved through a ether or thioether bond by nucleophilic substitution reaction of 4- hydroxypyridine,[148] 3-hydroxypyridine,[149] 2-

---

142 Z. Biyiklioglu, M. Durmus and H. Kantekin, *J. Photochem. Photobiol. A*, **2011**, *222*, 87-96.

143 E. Yabas, E. Bagda and E. Bagda, *Dyes Pigments*, **2015**, *120*, 220-227.

144 T. Sugimori, J. Nojima, T. Ozawa, M. Handa and K. Kasuga, *Chem. Lett.*, **2004**, *33*, 1014-1015.

145 B.G. Ongarora, B. Hu, H. Li, F.R. Fronczek and M.G.H. Vicente, *Med. Chem. Comm.*, **2012**, *3*, 19-194.

146 a) D. Çakir, V. Çakir, Z. Biyiklioglu, M. Drumus and H. Kantekin, *J. Organomet. Chem.*, **2013**, *745-746*, 423-431. b) Z. Biyiklioglu, *J. Organomet. Chem.*, **2014**, *752*, 59-66.

147 G.K. Karaoglan, G. Gümrükçü, A. Koca and A. Gül, *Dyes Pigments*, **2011**, *88*, 247-256.

148 a) I. Scalise and E.N. Durantini, *Bioorg. Med. Chem.*, **2005**, *13*, 3037-. b) S. Banfi, E. Caruso, L. Buccafurni, R. Ravizza, M. Gariboldi and E. Monti, *J. Organomet. Chem.*, **2007**, *692*, 1269-. c) M.B. Spesia, D.A. Caminos, P. Pons and E.N. Durantini, *Photodiagn. Photodyn. Ther.*, **2009**, *6*, 52-. d) T.T. Tasso, Y. Yamasaki, T. Furuyama and N. Kobayashi, *Dalton Trans.*, **2014**, *43*, 5886-5892. e) O.J. Achadu, I. Uddin and T. Nyokong, *J. Photochem. Photobiol. A*, **2016**, *317*, 12-25.

149 a) S. Gaspard and T.T. Thi, *J. Chem. Soc., Perkin Trans. II*, **1989**, 383-. b) G. Schneider, D. Wöhrle, W. Spiller, J. Stark and G. Schulz-Ekloff, *Photochem. Photobiol.*, **1994**, *60*, 333-. c) V. Mantareva, D. Petrova, L. Avramov, I. Angelov, E. Borisova, M. Peeva and D. Wöhrle, *J. Porphyrins Phthalocyanines*, **2005**, *9*, 47-. d) M. Durmus and T. Nyokong, *Inorg. Chem. Commun.* **2007**, *10*, 332. e) M. Durmus and T. Nyokong, *Photochem. Photobiol. Sci.*, **2007**, *6*, 659-. f) H. Li, T.J. Jensen, F.R. Fronczek and M.G.H. Vicente, *J. Med. Chem.*, **2008**, *51*, 502-511. g) V. Mantareva, V. Kussovski, I. Angelov, D. Wöhrle, R. Dimitrov, E. Popova and S. Dimitrov, *Photochem. Photobiol. Sci.*, **2011**, *10*, 91-102.

hydroxypyridine,[128b,150] 4-mercaptopyridine[148d,151] and 2-mercaptopyridine[152] with 3- or 4-nitrophthalonitrile (for monosubstituted derivatives)[148-152] or 4,5-dichlorophthalonitrile (for disubstituted ones).[53a]

[150] a) W. Chidawanyika, A. Ogunsipe and T. Nyokong, *New. J. Chem.*, **2007**, *31*, 377-384. b) N. Masilela and T. Nyokong, *J. Lumin.*, **2010**, *130*, 1787-1793. c) R. Zugle and T. Nyokong, *J. Mol. Catal. A*, **2012**, *358*, 49-57.

[151] a) J.B. Pereira, E.F.A. Carvalho, M.A.F. Faustino, R. Fernandes, M.G.P.M.S. Neves, J.A.S. Cavaleiro, N.C.M. Gomes, A. Cunha, A. Almeida and J.P.C. Tomé, *Photochem. Photobiol.*, **2012**, *88*, 537-547.

[152] A) N. Sehlotho, M. Durmus¸ V. Ahsen and T. Nyokong, *Inorg. Chem. Commun*. **2008**, *11*, 479. b) F. Matemadombo, M. Durmus, V. Escriou, S. Griveau, D. Scherman, F. Bedioui and T. Nyokong, *Curr. Anal. Chem.*, **2009**, *5*, 330. c) N. Saydan, M. Durmus, M.G. Dizge, H. Yaman, A.G. Gürek, E. Antunes, T. Nyokong and V. Ahsen, *J. Porphyrins Phthalocyanines*, **2009**, *13*, 681. d) M. Durmus and V. Ahsen, *J. Inorg. Biochem.*, **2010**, *104*, 297. e) M. Durmus and V. Ahsen, *J. Inorg. Biochem.*, **2010**, *104*, 297-309. f) M. Durmus, H. Yaman, C. Göl, V. Ahsen and T. Nyokong, *Dyes Pigments*, **2011**, *91*, 153-163. g) M.A. Idowu, Y. Arslanoglu and T. Nyokong, *Cent. Eur. J. Chem.*, **2014**, *12*, 403-415.

[53] a) I. Sehgal, M. Sibrian-Vazquez and M.G.H. Vicente, *J. Med. Chem.*, **2008**, *51*, 6014-6020.

1.2. Synthesis and properties of anionic Pcs

1.2.1. **Sulfonated Pcs**

1.2.1.1. Synthesis and characterization

As a first goal of this thesis, we decided to synthesize and study symmetrically and assymetrically sulfonated ZnPcs, for their use in SMOCs processed from aqueous solution (see Chapter 3.2.). In order to synthesize the asymmetrically substituted ZnPcs **2** and **3**, a statistical condensation of potassium 4-sulfonatophthalate and phthalic anhydride in a 1:1 ratio was carried out in melted urea as solvent (adapting a method reported by van Lier *et al.*),[114b] in the presence of $Zn(OAc)_2$, ammonium chloride and ammonium molybdate (Scheme 3). ZnPcs **2** and **3** were subsequently separated from the crude mixture by column chromatography, using chromatographic conditions described by Siejak *et al.* (i.e., in silica gel, with ethyl acetate/ethanol/aqueous ammonia 25% (7:4:4) as eluent).[117] Although in this reaction ZnPc **1** is also generated, it was not produced in high ammont (because of the employed ratio of potassium 4-sulfonatophthalate and phthalic anhydride, i.e., 1:1), and it was impossible to elute it from the column due to its extreme polarity. For the synthesis of ZnPc **1** in higher yield, a procedure previously reported in literature was adapted.[153]

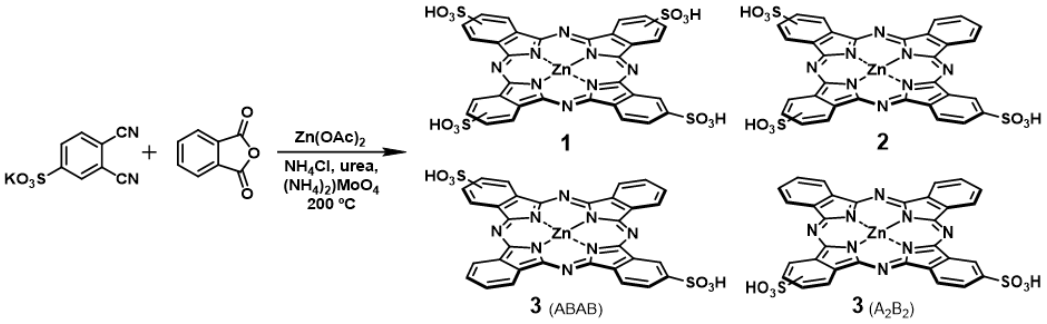

Scheme 3. Synthesis of sulfonated Pcs **1**, **2** and **3**. The latest was obtained as mixture of A_2B_2 and ABAB regioisomers.

The UV-Vis spectra reported by Siejak *et al.* for ZnPcs **1** – **3**, purified under the aforementioned chromatographic conditions, show an unexpected splitting in the ZnPc Q-

[153] V. Derkacheva, S. Mikhalenko, L. Soloveva, V. Alekseeva, L. Marinina, L. Savina, A. Butenin and E. Lukyanets, *Russ. J. Gen. Chem.*, **2007**, *77*, 1117-1125.

Band.[117] They argue the splitting may be due to aggregation, which is quite unlikely in a coordinating solvent as DMSO, or to "the additional energy transition owing to the presence of the sulfo substituents", although such effect has never been described for sulfonated Pcs. In contrast, it is well known that under acidic conditions, the protonation of Pc nitrogen atoms in *meso* positions results in a splitting of the Q-band, with significant bathochromic shifts of the Pc absorption.[153] On these bases, we have reasons to think that during the eluent evaporation (under vacuum) after the column (i.e., ethyl acetate/ethanol/aqueous ammonia 25% (7:4:4)), the occurrence of basic hydrolysis of ethyl acetate (due to heating in the rotavap) and the removal of ammonia when drying under vacuum (which lowers the pH) might result in the roduction of acetic acid to some extent, leading to protonation of the meso positions of the ZnPc Macrocycle. We are not sure whether this might be the reason for Siejak et al.'s observations, or if it influenced their results of photocurrent generation in sulfonated ZnPc thin films, In any case, we did an additional purification step consisting on the re-precipitation of each compound from water/acetone or DMSO/acetone. In this way, the UV-Vis spectra of ZnPc **1** – **3** in DMOS showed in the three cases the non-split Q-band characteristic of neutral metallated Pcs (Figure 19). This additional purification step also allowed removing in its majority the small portion of silica eluted from the column with the different fractions, due to the high polarity of the eluent.

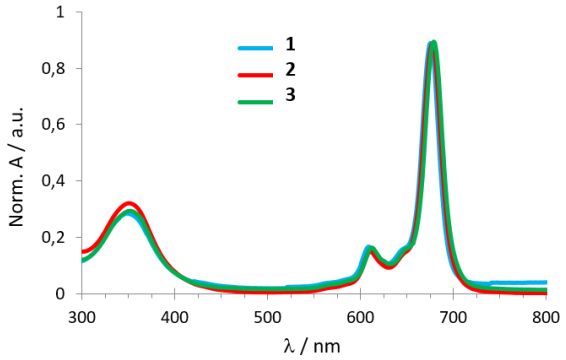

Figure 19. Normalized UV-Vis spectra of **1**, **2** and **3** in DMSO

An exhaustive characterization of the mixture of products obtained in the reaction mixture was carried out by HPLC analysis with the following conditions: the sample was dissolved in sodium phosphate buffer (10 mM, pH = 5, concentration: 10^{-4} M), filtered (0.45 µm pore size, Millipore nylon filters), injected, and eluted from 0% to 95% methanol in

sodium phosphate buffer, with a 50 min linear gradient and a flow rate of 1.0 mL min^{-1}, at 25 ^{o}C. The detection was performed at 680 nm (16 nm band width) and 850 nm (100 nm band width) as reference wavelength. In order to assign the observed HPLC peaks (Figure 20, top) to the different regioisomers of ZnPc **2** and **3**, the dipolar moment of each regioisomer (Figure 20, bottom) was calculated through a semi-empirical procedure at AM1 level, using *Spartan* '02 software for this purpose. These data were in agreement with that the integrals and the statistical distribution of regioisomers in the chromatograms, allowing the assignment of a retention time to each regioisomer at the given conditions. The chromatogram of **2** also shows a small impurity (9%) of **1**, due the difficult chromatographic purification of ionic derivatives. Importantly, the separated ZnPcs **2** and **3** were also characterized by mass spectroscopy (MS) as shown in Figure 21.

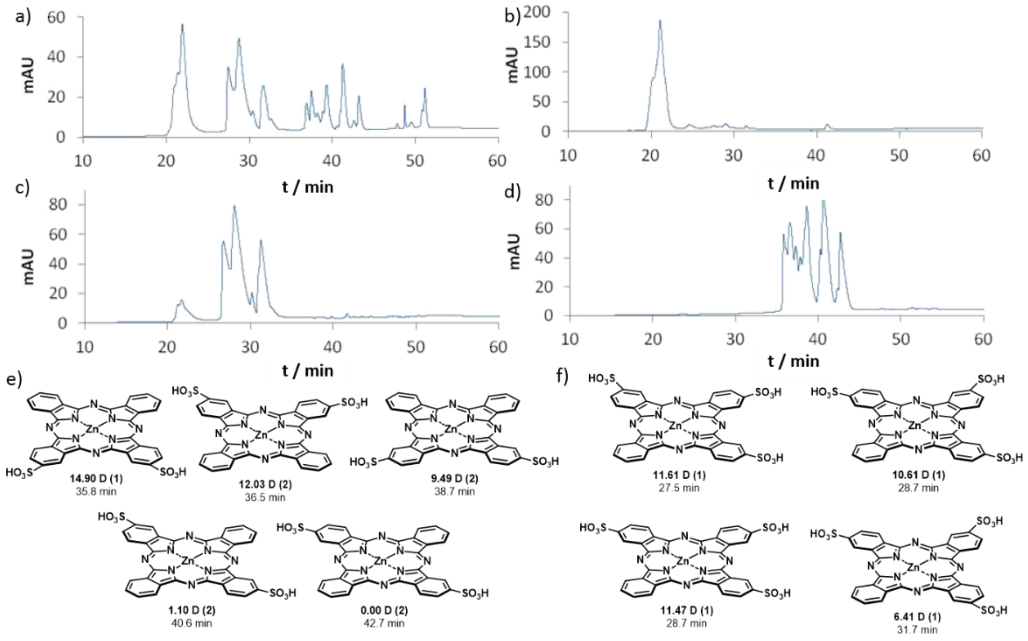

Figure 20. HPLC chromatograms of the crude reaction mixture depicted in Scheme 3 (a), **1** (b), **2** (c), and **3** (d). Regioisomers of **3** (e) and **2** (f) showing the calculated dipolar moment, relative abundance (in brackets) and assigned retention time.

This group of sulfonic Pcs has been employed in the development of water-processed, environmental-friendly solar cells in collaboration with Prof. E. Palomares research group as will be discussed in Chapter 3.2 of the present thesis.

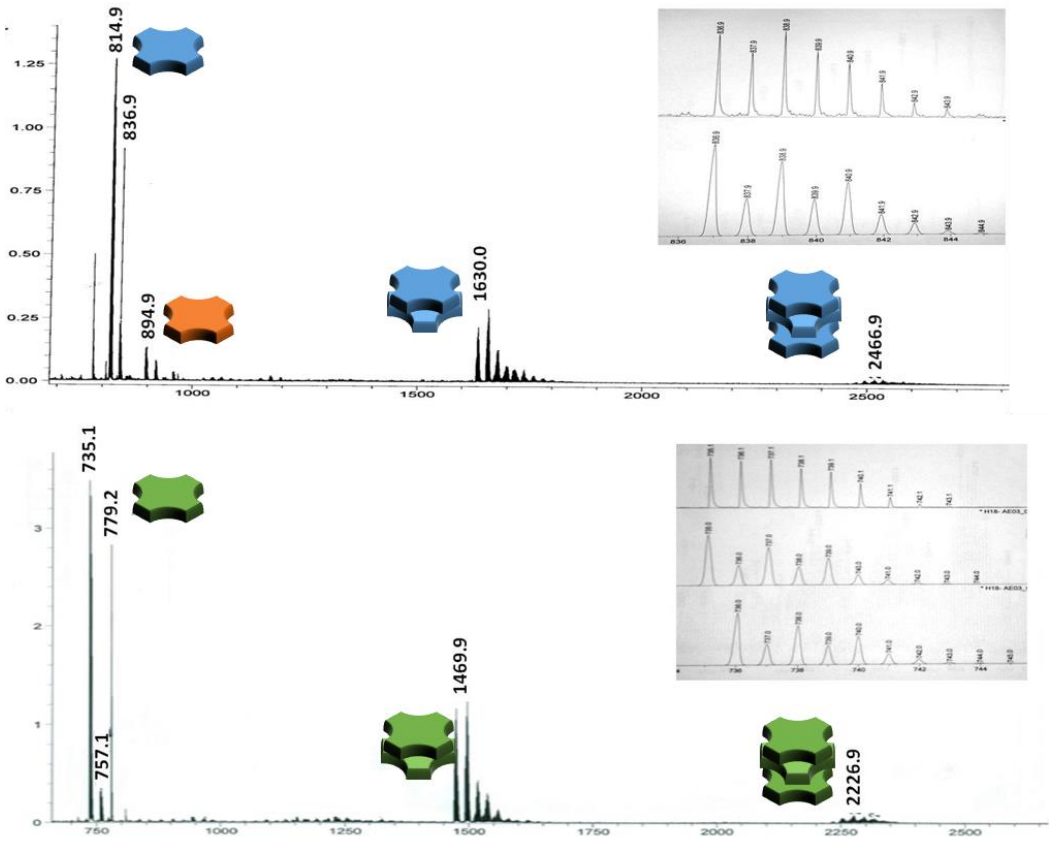

Figure 21. Mass spectra of ZnPc **2** (top) showing traces of ZnPc **1** (orange) and supramolecular dimers and trimers. Mass spectra of ZnPc **3** (bottom) showing signas of supramolecular dimers and trimers. All the signals are shown as acid form and corresponding sodium and potassium salts.

1.3. Synthesis and properties of cationic phthalocyanines

1.3.1. **2-(Trimethylammonium)ethanesulfanyl-ZnPcs**

1.3.1.1. Synthesis and characterization

Amphiphilicity is a desirable property in water-soluble photosensitizers, favouring their insertion in biologically inspired carriers such as micelles and liposomes. Amphiphilicity is achieved by including one or more hydrophilic groups, a charged organic moiety in our case, in a hydrophobic molecule. To this end, a family of symmetric and asymmetric ZnPcs were synthesized by the combination of highly hydrophobic 4-*tert*-butylphthalonitrile and a quaternizable moiety as 4-(2-(dimethylamino)ethylthio)-phthalonitrile. As mentioned before, the synthesis of cationic ZnPcs **4**, **5** and **6** (Chart 3) was achieved by a last quaternization step.

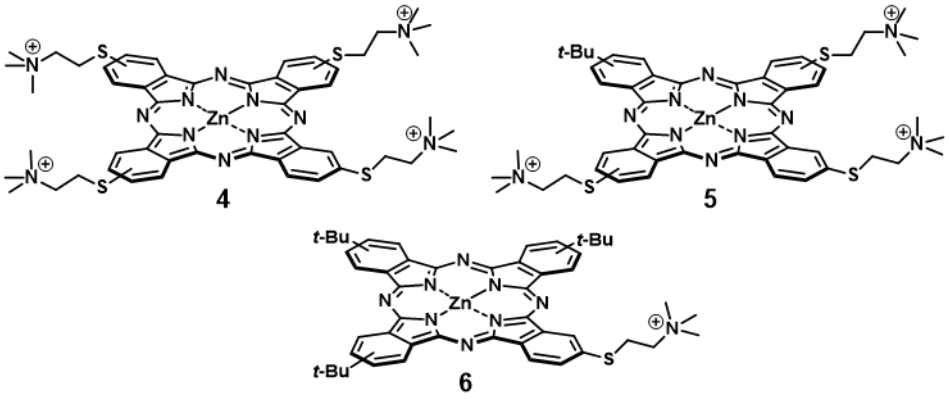

Chart 3. Chemical structure of the peripherally charged ZnPcs **4**, **5** and **6**. Iodine counterions are not depicted for clarity reasons.

The synthesis of this family of ZnPcs described above started with the preparation of phthalonitrile **7**, by adapting a previously described method.[134a] Briefly, 2-dimethylamino-ethanethiol and 4-nitrophthalonitrile underwent a nucleophilic aromatic substitution in the presence of potassium carbonate. To synthesize the symmetrically substituted ZnPc **8**, phthalonitrile **7** underwent cyclotetramerization in presence of zinc acetate and dimethylaminoethanol (DMAE) as solvent, at 140 ^{o}C overnight. The reaction mixture was then dried under reduced pressure, and the resulting solid was dissolved in chloroform and washed with water. To synthesize the asymmetrically substituted ZnPcs **9** and **11,** phthalonitrile **7** and the commercially available 4-*tert*-butylphthalonitrile were reacted in

the presence of zinc acetate in the aforementioned conditions (Scheme 4). Aiming to an efficient synthesis, the ratio between phthalonitriles was optimized depending on the target compound, as well as the eluent for chromatography purification. The ZnPc **9** was obtained from a 3:1 ratio of **7** and 4-*tert*-butylphthalonitrile phthalonitrile ratio and purified using THF/methanol/trimethylamine (10:1:0.1) as eluent. This highly polar eluent is employed due to the high affinity of amino groups with the stationary phase and the symmetric ZnPc **8**, resulting in a low yield (7%). The ZnPc **11**, on the other hand, was obtained in a high yield from a 1:4 ratio of **7** and 4-*tert*-butylphthalonitrile ratio and purified using THF/dioxane (4:1) as eluent, despite the fact that the reaction and purification process must be carried out in the absence of light due to fast photodegradation.

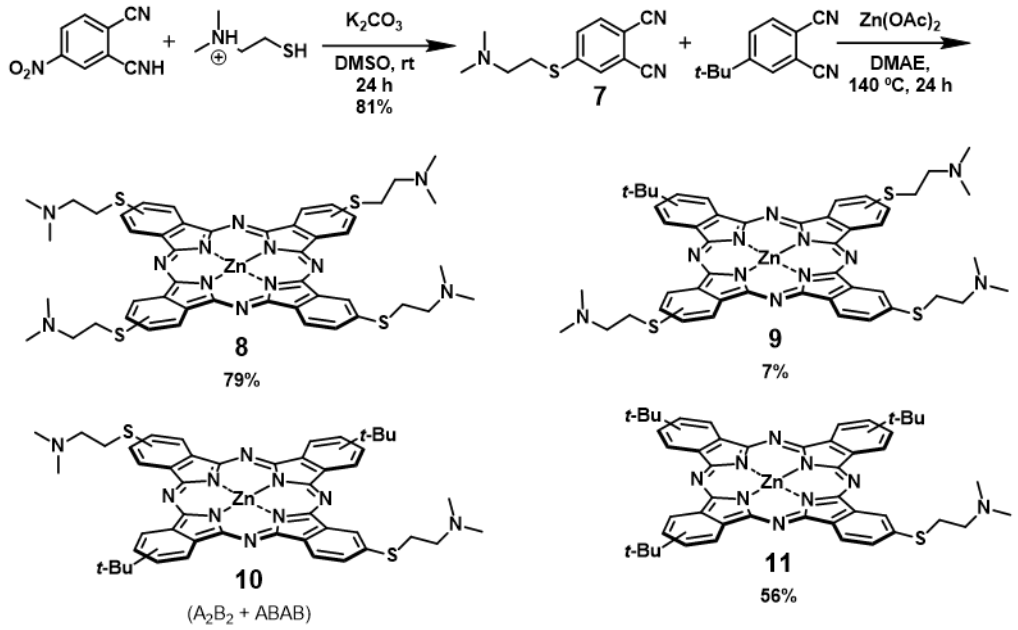

Scheme 4. Synthesis of phthalonitrile **7**, and crossover statistical condensation with 4-*tert*-butylphthalonitrile, to yield the ZnPcs **8** – **11**.

Please note that during the statistical macrocyclation process, the symmetrically substituted ZnPc **8** and the disubstituted ZnPc **10** were also obtained. The first one was obtained in a low yield, with the additional disadvantage of a difficult chromatographic purification, so, when targeted, a non-statistical cyclotetramerization was carried out. The later one, in turn, is presented as a mixture of regioisomers (i.e. ABAB and A_2B_2) that were

unsuccessfully separated. Because of that, further characterization or reactions with these two compounds do not lay in the objectives of the present thesis.

The last step in the synthesis of cationic ZnPcs **4** – **6** consists on the methylation of their precursor ZnPcs, using methyl iodide as thequaternizing agent (Scheme 5), which proceeded in high yields with no synthetic difficulties.

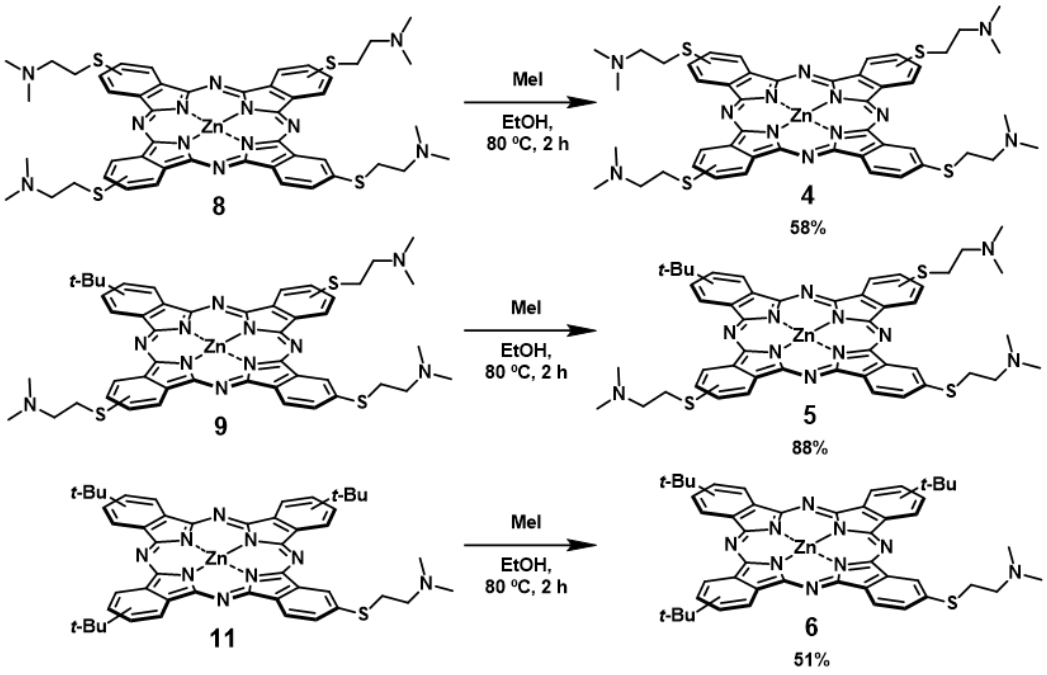

Scheme 5. Synthesis of the quaternized ZnPcs **4**, **5** and **6**.

1.3.1.2. Solubility and aggregation

The aqueous solubility within this series of cationic derivatives depends on the number of charged groups decorating the periphery of the macrocycle. ZnPc **4** is completely soluble in aqueous media, while ZnPcs **5** and **6** need to be first dissolved in a water-miscible organic solvent such as methanol, DMSO or DMF, followed by a rapid injection in water, leading to concentrations of the organic solvent even lower than 1%. The natural trend to aggregate of these compounds in aqueous media is responsible of their broad, absorption spectra with a blue-shifted Q-band centered at 635 nm, assigned to *H*-aggregates. On the other hand, aggregation can be disrupted by increasing the ratio of

organic solvent in the solution, but this has an important drawback: it requires high amounts of such organic solvent (over 70%) turning not compatible with biological media (Figure 22a). Other way to formulate photosensitizer in biologically related media relies on their insertion into micelles. To this end, we evaluated sodium dodecylsulfate (SDS), a surfactant that generates micelles for this purpose. Such proof-of-concept experiment was as follows: 50µL aliquots of ZnPc **6** solution (ca. 1 mg mL^{-1}, in methanol) was added to samples of 5 mL of aqueous SDS in growing concentrations (i.e. 1.0 x 10^{-3}, 1.0 x 10^{-2}, 2.0 x 10^{-2} and 4.0 x 10^{-2} M). These samples were warmed up to 90 ^{o}C for two minutes, and then were left to cool down to room temperature. By this procedure, the preformed micelles of SDS disassemble and by a slow cooling down process they self-assemble again, incorporating the amphiphilic ZnPcs while breaking the aggregation at 4.0 x 10^{-2} M of SDS (i.e. a concentration above the critical aggregation concentration – c.a.c. – of SDS), as shown in Figure 22b. This procedure was employed for the rest of cationic ZnPcs, **4** and **5**, as well as zinc tetra-*tert*-butyl zinc phthalocyanine (**TT0**) as reference compound. In opposition to the very hydrophobic **TT0** derivative, the series of cationic ZnPc show a disaggregating effect by insertion in the SDS micelles (Figure 22c).

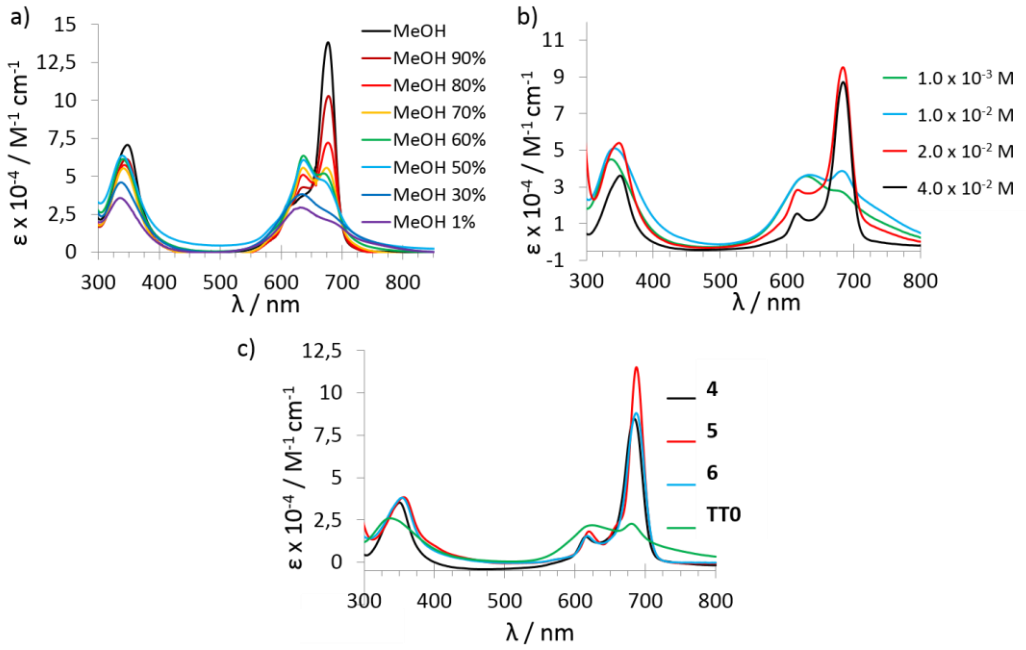

Figure 22. a) Absorption coefficient of **6** at 5.5 x 10^{-6} M in different methanol/water ratios. b) Absorption coefficient of **6** at 5.0 x 10^{-6} M in growing concentrations of SDS. c) Absorption coefficient of ZnPcs **4**-**6** at 5.0 x 10^{-6} M when inserted into SDS micelles

The incorporation of ZnPc **6** into functional micelles has actually been studied as a promising theranostic, multimodal imaging agent in the group of Prof. J.J.L.M. Cornelissen, and will be discussed in detail in Chapter 2.2.

1.3.1.3. Anion exchange and self-aggregation of the amphiphilic ZnPc **6**

Control on aqueous self-aggregation of organic salts offered interesting physicochemical properties. Functional organic nanoparticles (FONs) with a size-dependant spectral properties were first reported by Nakanishi *et al.*[154] This concept was furthermore developed by I.M. Warner research group. Synthesis and study of a group of uniform materials based on organic salts (GUMBOS) and their nanoscale materials (nanoGUMBOS)[155] result in a group of promising candidates for potential applications including biomedical imaging,[155a] antibiotics,[156] cancer therapy,[157] molecular sensing,[158] organic light-emitting diodes[159] and photovoltaics.[160] In most of cases, those organic salts consist on cationic amphiphilic cyanine dyes bearing an amphiphilic counterion. The salt is then dispersed in water following the so-called reprecipitation method that consist in dissolve the salt in a water-soluble organic solvent such as methanol or DMSO and quickly injected in water under sonication.

To synthesize an amphiphilic anion-cation pair, ZnPc **6** undergoes an anion exchange reaction consisting in the solution in dichloromethane with an equimolar amount of

---

154 a) H. Kasai, H. Kamatani, S. Okada, H. Oikawa, H. Mastuda and H. Nakanishi, *Jpn. J. Appl. Phys.*, **1996**, *35*, 221-223. b) H. Kasai, H. Kamatani, Y. Yoshikawa, S. Okada, H. Oikawa, A. Watanabe, O. Ito and H. Nakanishi, *Chem. Lett.*, **1997**, *11*, 1181-1182.

155 a) D.K. Bwambok, B. El-Zahab, S.K. Challa, M. Li, L. Chandler, G.A. Baker and I.M. Warner, *ACS Nano*, **2009**, *3*, 3854-3860. b) S. Das, D. Bwambok, B. El-Zahab, J. Monk, S.L. de Rooy, S. Challa, M. Li, F.R. Hung, G.A. Baker and I.M. Warner, *Langmuir*, **2010**, *26*, 12867-12876.

156 a) M.R. Cole, M. Li, R. Jadeja, B. El-Zahab, D. Hayes, J.A. Hobden, M.E. Janes and I.M. Warner, *J. Antimicrob. Chemother.*, **2013**, *68*, 1312-1318. b) M.R. Cole, M. Li, B. El-Zahab, M.E. Janes, D. Hayes and I.M. Warner, *Chem. Biol. Drug Des.*, **2011**, *78*, 33-41. c) M.R. Cole, J.A. Hobden and I.M. Warner, *Molecules*, **2015**, *20*, 6466-6487.

157 a) P.K.S. Magut, S. Das, V.E. Fernand, J. Losso, K. McDonough, B.M. Naylor, S. Aggarwal and I.M. Warner, *J. Am. Chem. Soc.*, **2013**, *135*, 15873-15879. b) N. Siraj, P.E. Kolic, B.P. Regmi and I.M. Warner, *Chem. Eur. J.*, **2015**, *21*, 14440-14446.

158 a) S. Das, P.K.S. Magut, S.L. de Rooy, F. Hasan and I.M. Warner, *RSC Adv.*, **2013**, *3*, 21054-21061. b) C. Lu, S. Das, P.K.S. Magut, M. Li, B. El-Zahab and I.M. Warner, *Langmuir*, **2012**, *28*, 14415-14423. c) B.P. Regmi, J. Monk, B. El-Zahab, S. Das, F.R. Hung, D.J. Hayes and I.M. Warner, *J. Mater. Chem.*, **2012**, *22*, 13732-13741. d) B.P. Regmi, W.I.S. Galopthdeniya, N. Siraj, M.H. Webb, N.C. Speller and I.M. Warner, *Sensor. Actuat. B*, **2015**, *209*, 172-179.

159 N. Siraj, F. Hasan, S. Das, L.W. Kiruri, K.E. Steege Gall, G.A. Baker and I.M. Warner, *J. Phys. Chem. C*, **2014**, *118*, 2312-2320.

160 a) A.N. Jordan, S. Das, N. Siraj, S.L. de Rooy, M. Li, B. El-Zahab, L. Chandler, G.A. Baker and I.M. Warner, *Nanoscale*, **2012**, *4*, 5031-5038. b) T.E. Karam, N. Siraj, I.M. Warner and L.H. Haber, *J. Phys. Chem. C*, **2015**, *119*, 28206-28213.

sodium docusate and water. After stirring gently for 10 minutes, the organic phase was separated, washed with water and dried under reduced pressure, resulting in the desired product ZnPc **15** as confirmed by ^{1}H-NMR and mass spectrometry (Figure 23).

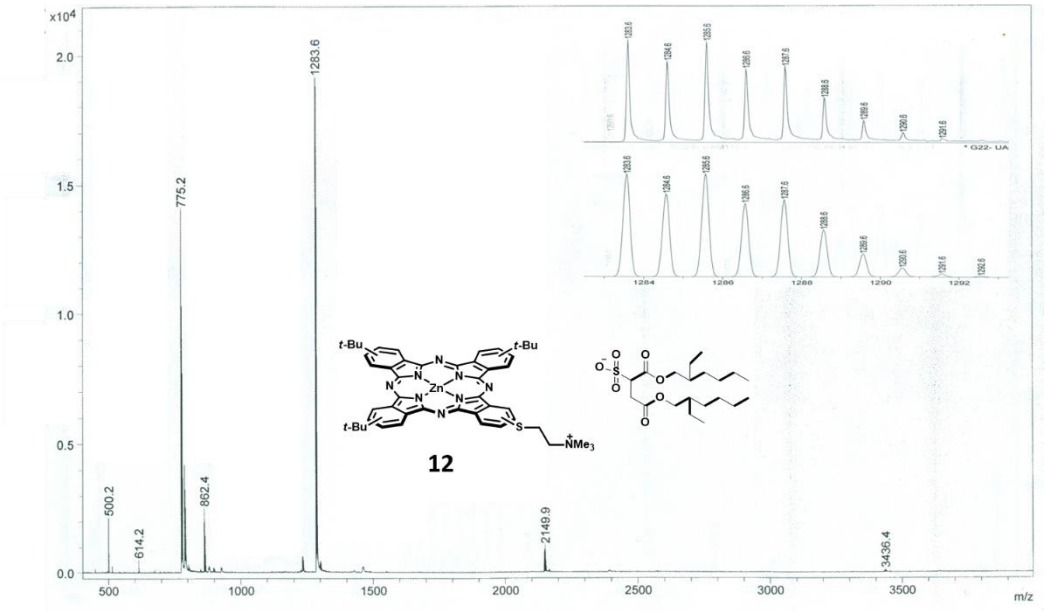

Figure 23. Chemical structure of ZnPc **12** and MALDI mass spectrum showing as major peak the cation of the ionic pair.

Preparation of organic nanoparticles proceed by the previously mentioned reprecipitation method: 0.1 mL of ZnPc **12** in ethanol (1 mM) was quickly injected into 5 mL of milli-Q water under sonication and left for 10 minutes. Dispersion stability was studied by absorption spectroscopy at increasing times after formulation, showing an increase in both absorption at 725 nm and scattering. This phenomena is consecuence of the appearance of large aggregates that precipitates after 48-72 hours (Figure 24a). Broad absorption in the NIR region can be assigned to amorphous aggregation pattern, where *H*-, *J*- and non-aggregated species coexists and fluctuate along time and its contribution can be evaluate by deconvoluting the absorption spectra (Figure 24b). Nevertheless, fresh solution samples (10 minutes of stabilization time) were characterized by TEM (Figure 24c). Samples were prepared by casting 10 µL drop of the solution on a copper/carbon grid for 1 minute, removal of the solution and stain with aqueous uranyl acetate for 1 minute. Groups of circular/spherical aggregates of material were observed, similar of those

described by I.M. Warner research group.[155] Observation of groups instead of isolated spheres can be due to a drying effect or to the incipient solution instability and natural trend to precipitate of ZnPc **12**.

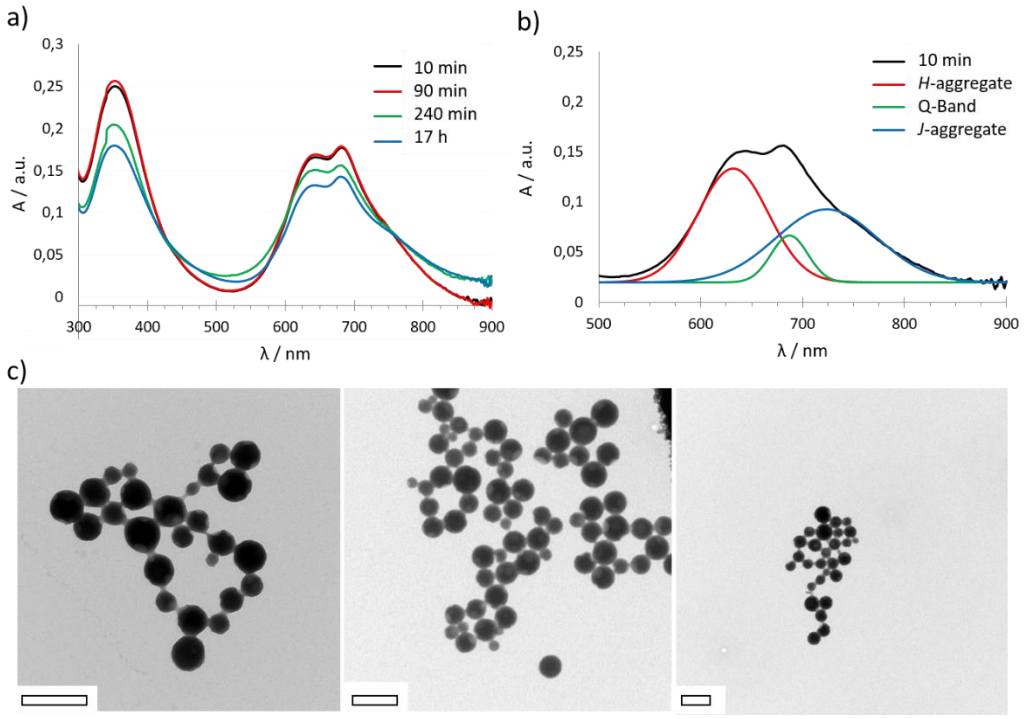

Figure 24. a) Absorption spectra of ZnPc **12** formulated by the reprecipitation method at different stabilization times. b) Deconvolution of the NIR absorption after 10 minutes of stabilization time in the different components (i.e. *H*-aggregate centered at 615 nm, Q-band centered at 680 nm and *J*-aggregate centered at 720 nm). c) Transmission electron images of ZnPc **12** solution after 10 minutes of stabilization time Scale bar: 500 nm.

In conclusion, similar methodology employed for the synthesis of FONs can be applied to amphiphilic Pcs like **12**, successfully obtaining spherical organic nanoparticles. The main drawback of these materials consist in low solution stability, being an issue to tackle before apply this materials.

1.3.1.4. Synthesis of functional, asymmetrically substituted ZnPcs

Synthesis of water-soluble, asymmetric Pcs functionalized with a spacer that can be linked to a targeting molecule such as an antibody or a cell penetrating peptide is of capital interest in drug delivery.[161] To this end and as proof-of-concept, asymmetric ZnPc **13** was synthesize by statistical cyclotetramerization between phthalonitrile **7** and 4-iodophthalonitrile in a 3:1 ratio. Subsequently, ZnPc **13** was reacted with benzyl 4-pentynoate (**14**) through a Shonogashira coupling reaction in standard conditions, resulting in ZnPc **15** (Scheme 6).

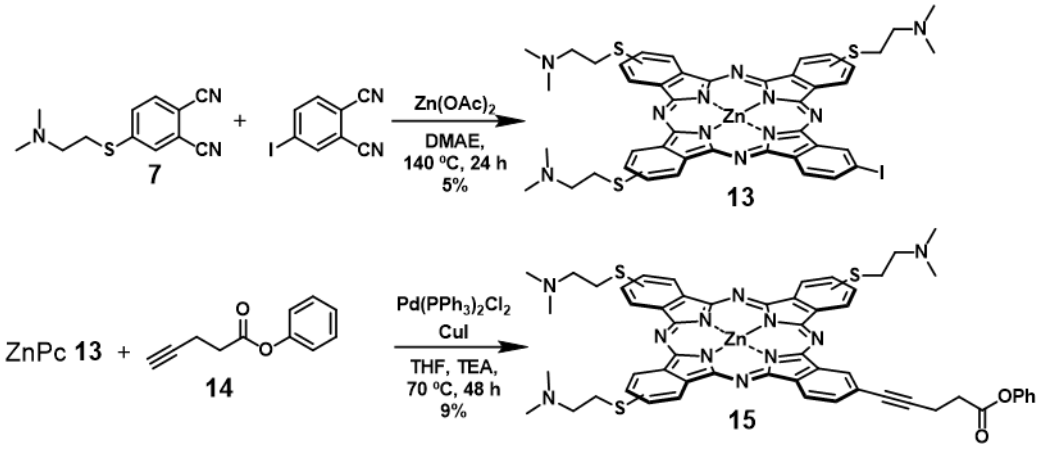

Scheme 6. Synthesis of ZnPc **15**.

As described for ZnPc **9**, low yield was obtained due to an inefficient purification process, enhanced by the need of two purification steps. This low yield means an important drawback in characterization, allowing a few techniques due to the material scarcity as for the practical application. More efficient synthesis or design of easier separation derivatives must be employed in order to apply those derivatives in targeted therapy.

[161] a) M. Mitsunaga, M. Ogawa, N. Kosaka, L.T. Rosenblum, P.L. Choyke and H. Kobayashi, *Nature Med.*, **2011**, *17*, 1685-1691. b) M.-R. Ke *Chem. Eur. J.* **2012**

1.3.2. **Quaternized *tert*-butylphenyl pyridyloxy ZnPcs**

1.3.2.1. Synthesis and characterization

Aiming to synthesize symmetric (ZnPcs **16** and **17**), and asymmetric (ZnPcs **18**, **19**, and **20**) pyridinium-substituted ZnPcs (Chart 4) a bulky aromatic moiety (4-*tert*-butylbenzene) was attached to the pyridyloxy moiety. This group enables an efficient separation from statistical cyclotetramerization reaction mixture by chromatography column.

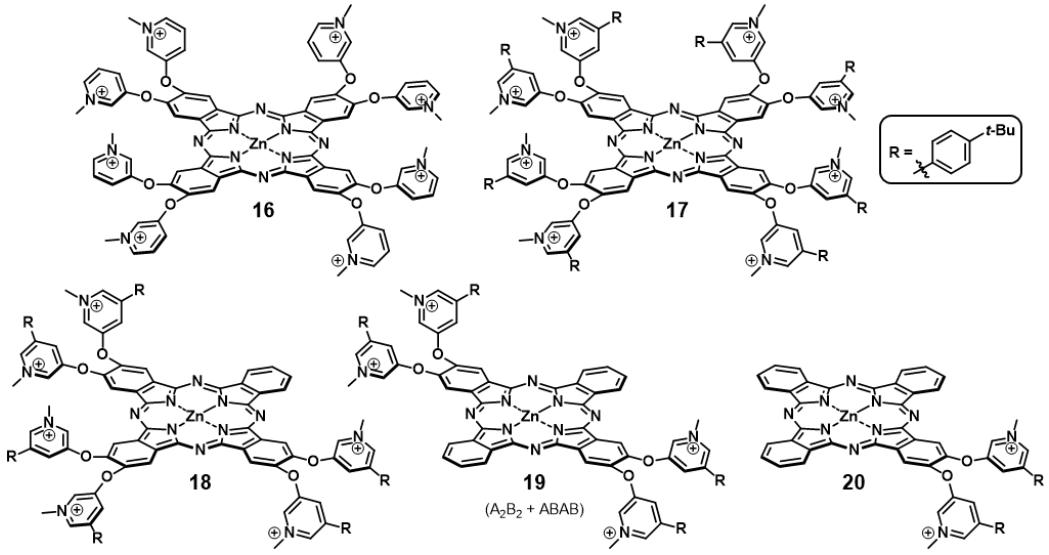

Chart 4**.** Molecular structure of cationic ZnPcs **16** – **20**. Sulfate anions are not represented for clarity porpoises.

ZnPc **16** synthesis was accomplished in a three step, chromatography-free synthetic pathway adapting previously described method.[149f] First step consists in the synthesis of 4,5-bis(pyridyniyl-3-oxy)phthalonitrile (**21**) by nucleophilic aromatic substitution of 4,5-dichlorophthalonitrile with 3-hydroxypyridine in dry DMF in presence of anhydrous potassium carbonate. After purification by recrystallization, phthalonitrile **21** was reacted in typical cyclotetramerization conditions in the presence of anhydrous zinc acetate, resulting in ZnPc **22**. Last step consists in quaternization of pyridyl groups in the presence of dimethylsulfate, resulting in ZnPc **16** (Scheme 7).

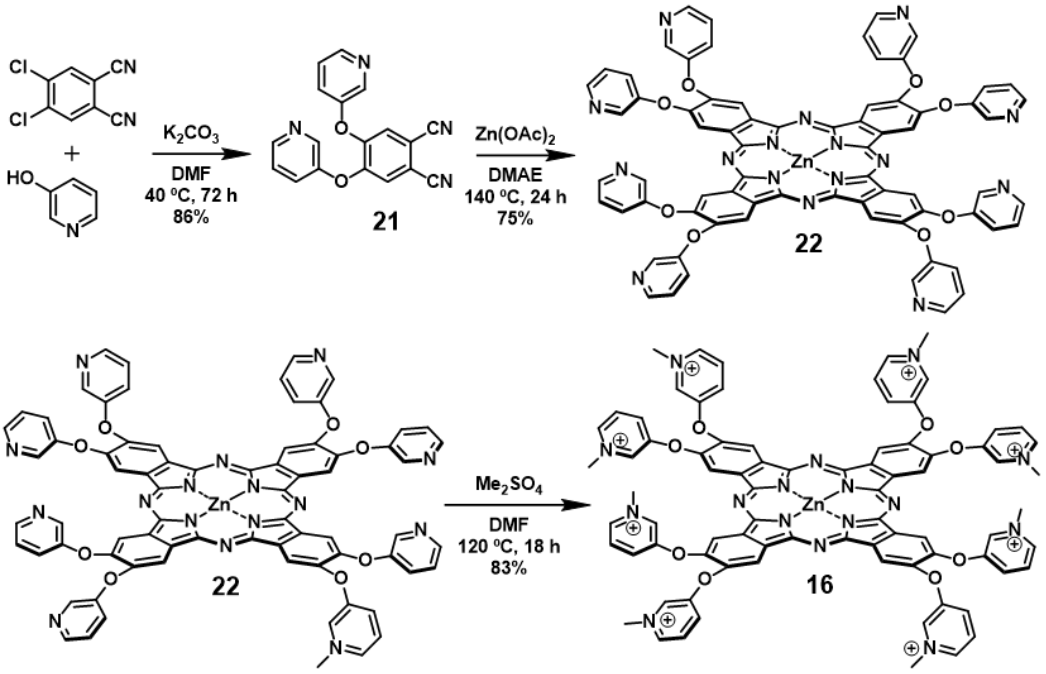

Scheme 7. Synthetic routes of ZnPc **16**. Sulfate anions of the cationic salt are not represented for clarity porpoises.

On the other hand, synthesis of the *tert*-butyphenyl derivatives (ZnPcs **17** – **20**) starts with the preparation of the desired pyridynol derivative. Compound **24** was prepared by Suzuki cross-coupling between 3-bromo-5-methoxypyridine and 4-*tert*-butylphenylboronic acid in the presence of tetrakis(triphenyphospine)palladium (0), resulting into **23,** followed by a demethylation step employing boron tribromide (Scheme 8).

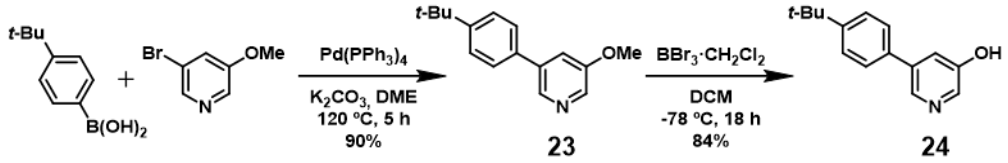

Scheme 8. Synthesis of protected and deprotected pyridine derivatives (**26** and **27** respectively).

Bulky derivatives decreases the reactivity of **24** towards the nucleophilic aromatic substitution of 4,5-dichlorophthalonitrile when reacts in described conditions for phthalonitrile **21**, yielding the product of monosubstitution as main product. Increasing the

reaction time (up to one week) only results in degradation by-products. In order to enhance the reactivity, more energetic conditions are required, achieved by microwave reactor synthesis. In detail, reaction at 100 W and 125 ^{o}C for 30 minutes were found as the optimal conditions, resulting in **25** as major product with traces of monosubstitution or degradation by-products (Scheme 9). Purification step consist in recrystallization in hot ethanol.

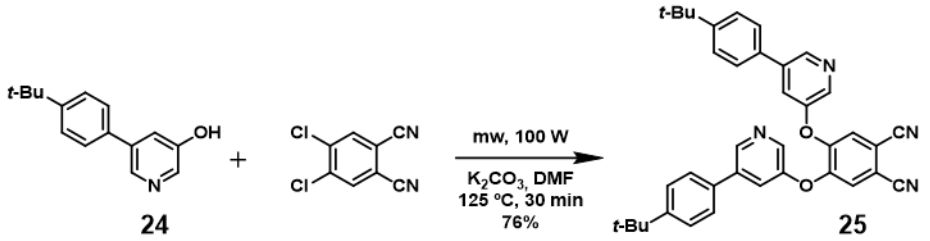

Scheme 9. Synthesis of phthalonitrile **25**.

Symmetrically substituted ZnPc **26** was synthesized by cyclotetramerization of phthalonitrile **25** in the presence of zinc acetate in dimethylaminoethanol, 140 ^{o}C overnight (Scheme 10). Reaction mixture was precipitated in a water/methanol (1:1) mixture and washed with diethylether. Synthesis of asymmetrically substituted ZnPcs **27**, **28**, and **29** was carried out through a statistical cyclotetramerization of a mixture of phthalonitrile 26 and 1,2-dicyanobenzene (1:1) in the aforementioned conditions (Scheme 10). Separation of the species was carried out by chromatography column, using a gradient of toluene/1,4-dioxane (from 5:1 to 2:1, with 1% of pyridine).

Finally, methylation of the peripheral pyridine moieties was carried out following the same methodology as in **16** (see Scheme 7), employing DMF with dimethyl sulfate at 120 ^{o}C, resulting in the targeted permethylated ZnPcs in moderate to good yields (Chart 5).

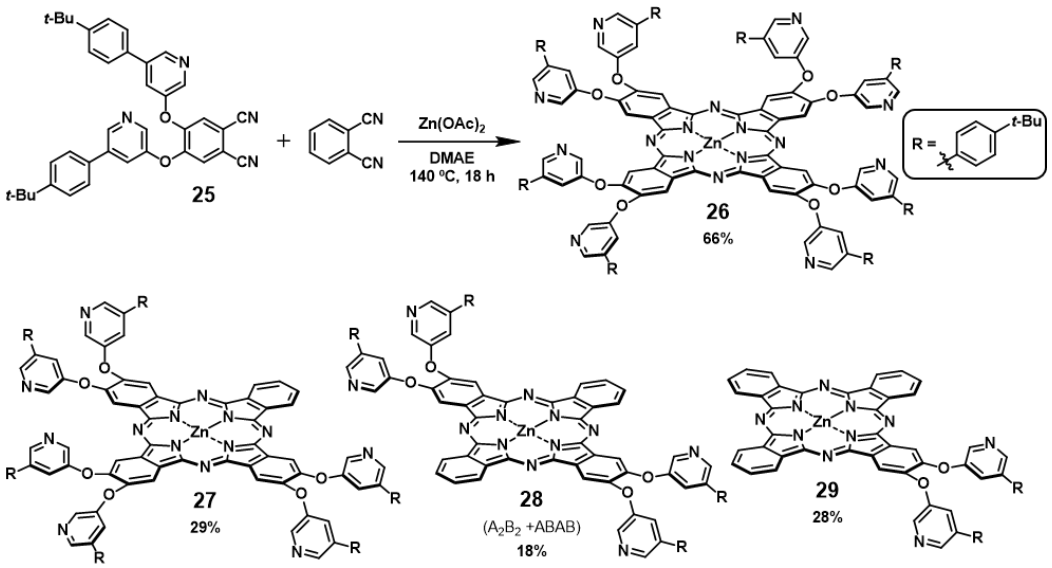

Scheme 10. Synthesis of ZnPcs **26**, **27**, **28**, and **29**.

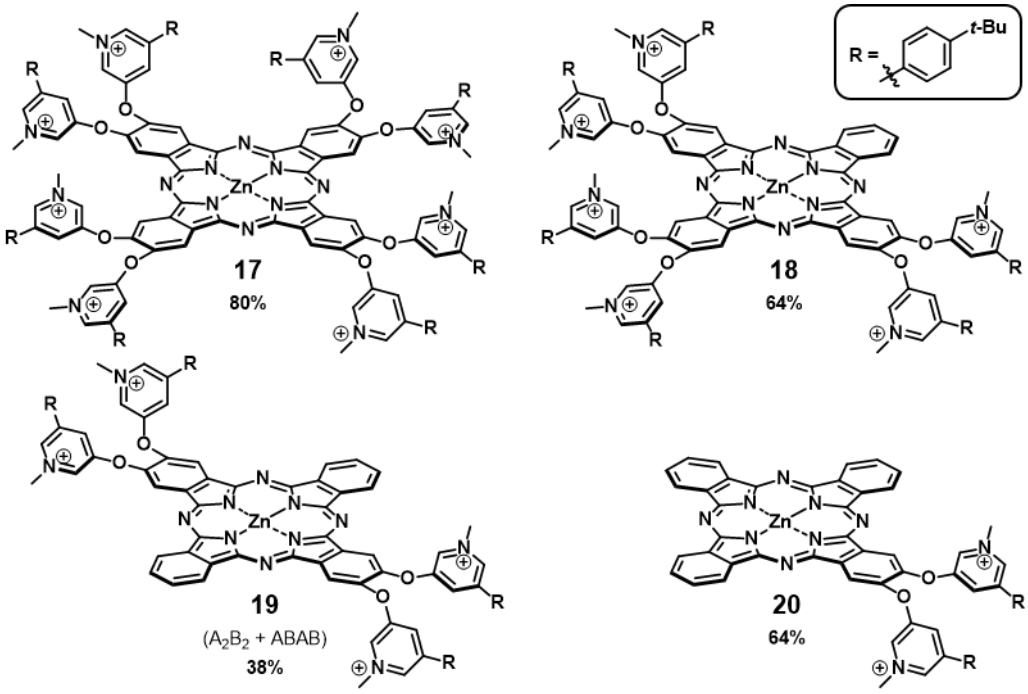

Chart 5. Methylation products and yields.

Control on hydrophilicity of amphiphilic and aggregation of water-soluble ZnPcs can be modulated by the inclusion of triethyleneglycol chains. In particular, inclusion of these hydrophilic chains as quaternizing agents has been employed previously in pyridyl-substituted Pcs.[149f] Synthesis of ZnPc **30**, an analogous of ZnPc **17** quaternized with triethyleneglycol chains instead of methyl groups has been achieved. In detail, ZnPc **26** was dissolved in 2-[2-(2-methoxyethoxy)ethoxy]ethyl iodide, synthesized as detailed in previous methods,[162] and warmed up to 80 ºC (Scheme 11). After 6 days, ZnPc **30** was isolated by precipitation in hexane and purified by size exclusion chromatography using THF as solvent and eluent.

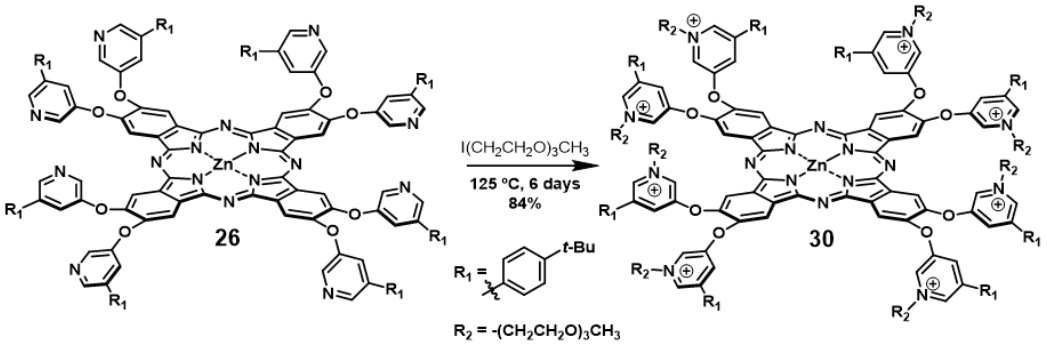

Scheme 11. Synthesis of ZnPc **30**. Iodine anions are not represented for clarity porpoises.

Thoroughly characterization of ZnPc **30** was performed, assuring the complete functionalization of pyridine moieties with triethyleneglycol chains. Of special interest is the mass spectrum obtained by high resolution electrospray, where different cations can be characterized (Figure 25). In detail: $[M+I]^{7+}$ calc. for $[C_{208}H_{256}N_{16}O_{32}ZnI]$ = 525.9609, found; 525.9700. $[M+2I]^{6+}$ calc. for $[C_{208}H_{256}N_{16}O_{32}ZnI_2]$ = 634.7712, found; 634.7778. $[M+3I]^{5+}$ calc. for $[C_{208}H_{256}N_{16}O_{32}ZnI_3]$ = 787.1064, found; 787.1095. $[M+4I]^{4+}$ calc. for $[C_{208}H_{256}N_{16}O_{32}ZnI_2]$ = 1015.3576, found; 1015.3579. In adition, every peak is found with related peaks at M+ n·44.1, corresponding at THF molecules embedded in the triethileneglycol structure.

[162] B.B.-A. Bar-Nir and J.F. Kadla, *Carbohydr. Polym.*, **2009**, *76*, 60-67.

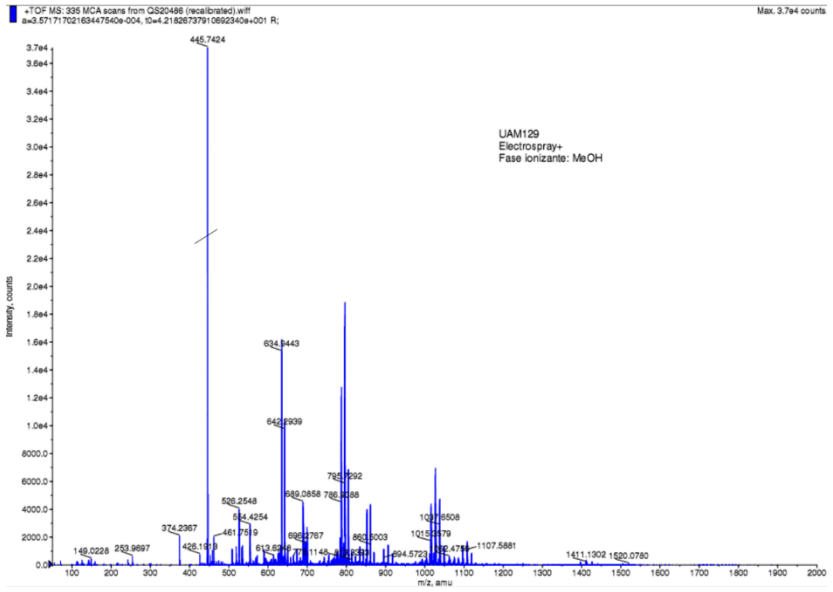

Figure 25. High resolution mass spectra by ESI of ZnPc **30**.

1.3.2.2. Solubility and aggregation

Non-quaternized ZnPcs

Non-quaternized ZnPcs **26** – **29** presents high solubility in common organic solvents and the aggregation depends on its nature. Coordinating solvents such as 1,4-dioxane, DMSO or THF render monomeric molecules as shown in the absorption spectra (Figure 26a). Otherwise, non-coordinating solvents as chloroform, *o*-dichlorobenze or toluene renders *J*-type aggregates as deduced by a bathochromic shift in absorption (Figure 26b). This behaviour is consecuence of the intermolecular pyridine-zinc interaction that triggers a shifted coplanar aggregation. Addition of pyridine disrupt the aggregation, recovering the monomeric absorption thus proving the intermolecular pyridine-zinc as driving force for the aggregation (Figure 26c). Unfortunately, titration of the supramolecular aggregates cannot be fitted to any theoretical model due to the unknown size of the aggregates, precluding to obtain a reliable constant of formation.

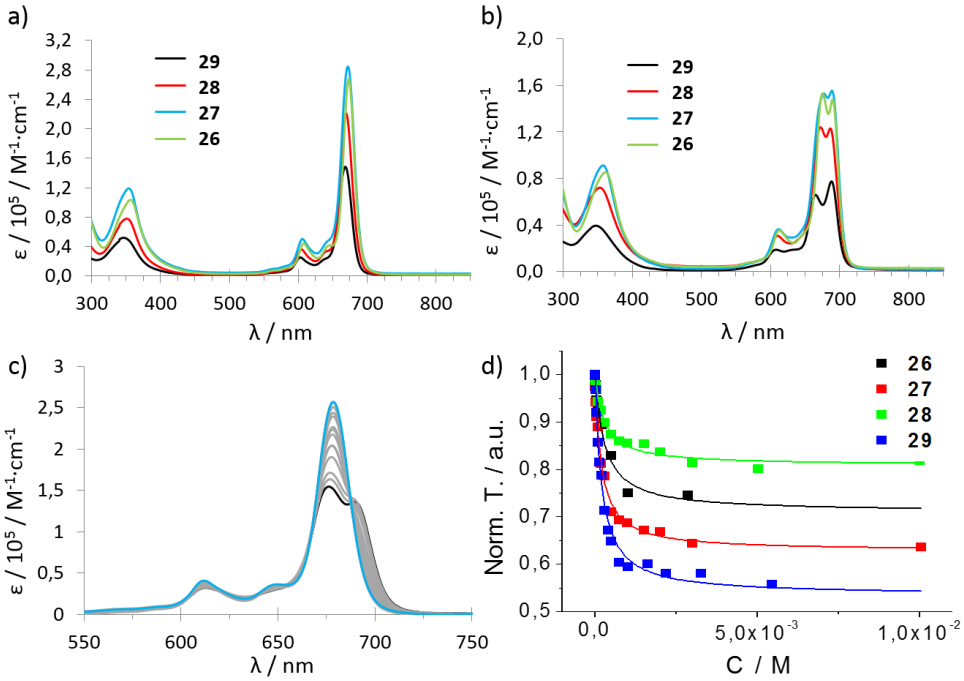

Figure 26. Absorption spectra of ZnPcs **26** – **29** in THF (a) and chloroform (b) at 5.0 x 10^{-6} M. c) Titration of ZnPc **26** in chloroform at 1.0 x 10^{-6} M with growing pyridine equivalents, from 0 (black) to 3000 eq (blue). d) Normalized transmittance at 675 nm *versus* pyridine concentration of titrated ZnPcs **26** – **29** at 1.0 x 10^{-6} M.

Size of the intermolecular aggregates was also evaluated by linear MALDI experiments. This technic, in contrast with standard reflector MALDI, allows to observe larger particles. A solution of ca. 1 mM of the corresponding ZnPc in chloroform was ionized in a DCTB matrix (Figure 27a). This experiment reveals species much larger than dimers, typically observed in MALDI experiments due to π-π interactions. This larger aggregates are caused by the stronger pyridine-zinc interaction.

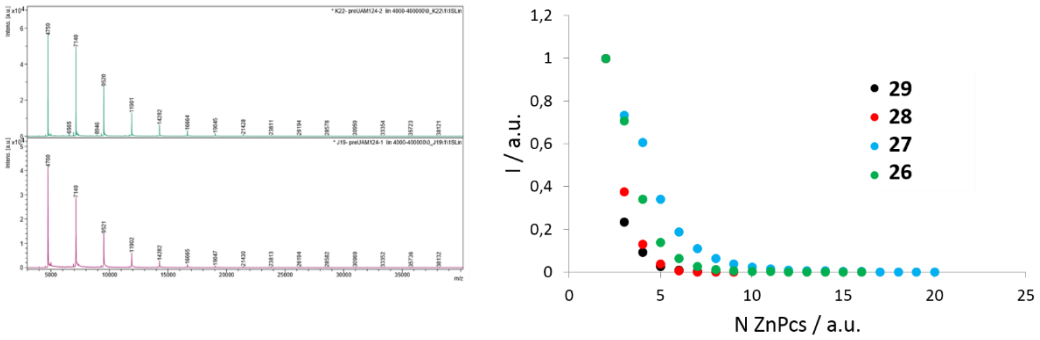

Figure 27. a) Linear MALDI spectrum of ZnPc **26** ionized by DCTB of two different batches showing regular patterns due to +1 ZnPc **26**. b) Normalized intensity of ZnPcs **26** – **29** MALDI experiments *versus* number of ZnPcs per aggregate.

Two antagonist facts affect to the aggregation process: higher the number of pyridyl moieties, larger the possibilities of the molecule to bind to a zinc atom. On the other hand, large presence of bulky groups hinders the approach of other ZnPcs molecules, lowering the efficiency of the bound. Balance of both factors seems to be optimum in ZnPc **27**, showing the larger aggregates thus the most stable bond among the individual molecules.

Quaternized ZnPcs

ZnPcs **16** shows low solubility in most of organic solvents, except in highly polar ones such as DMSO, DMF, and partially in methanol. On the contrary, ZnPc **16** shows high solubility in aqueous media, even in relatively high concentrations (ca. 1 mM) employed for ^{1}H-NMR spectroscopy (Figure 28) and a sharp Q-band in absorption, suggesting a non-aggregated behaviour. Therefore, a possible explanation to that behaviour is the electrostatic repulsion of a crowded charged periphery, that prevents the π-π stacking, Nevertheless, this behaviour disappears in higher ionic strength aqueous solutions, as will be discussed in Chapter 2.3.

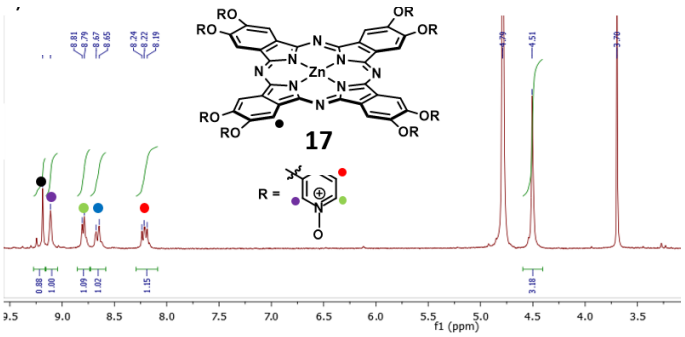

Figure 28. ^{1}H-NMR spectrum of ZnPc **16** in D_2O (ca. 8 mg mL^{-1})

On the other hand, ZnPcs **17** – **20** are not directly soluble in aqueous media but renders very stable solutions, up to months, when dispersed from an organic solvent. In turn, ZnPc 16 shows no aggregationhose ZnPcs displays aggregation patterns strongly dependent on the number of substituents (Figure 29). ZnPc **17** presents low *H*-type aggregation yet do not resemble completely the sharp Q-band of the monomers, indicating a small aggregation degree in opposition to ZnPc **20** that exhibits much higher absorption at 635 nm when compared to the Q-band and lower absorption coefficient. As the number of bulky and solubilizing groups increases the ratio between the Q-band and the *H*-type aggregates band (678 and 635 nm respectively) increases as well, rendering less-aggregated water-soluble ZnPcs. Among these series of quaternized ZnPcs, **17** shows the lower aggregation yet this is not complete.

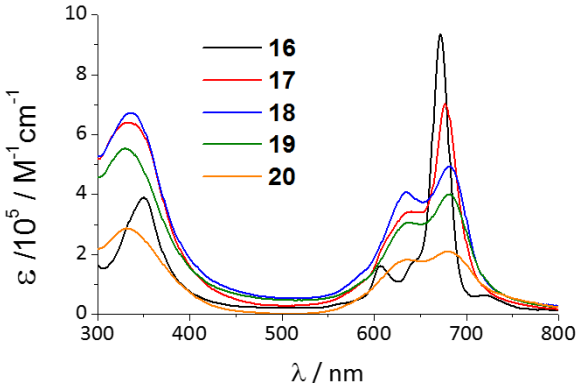

Figure 29. Absorption spectra of cationic ZnPcs **16** – **20** in aqueous media at 5.0 x 10^{-6} M, dispersed from a methanol solution. Final solvent water/methanol (9:1).

In order to achieve a fully non-aggregated ZnPc bearing the *tert*-butylphenyl moiety, a variation of the symmetric ZnPc has been synthesized by quaternizing ZnPc **30** with triethyleneglycol chains as is described previously. Unfortunately, incorporation of the triethyleneglycol chains does not affect drastically, neither in aqueous solubility (yet dispersable from organic solution), nor in the aggregation in aqueous media, showing a similar aggregation degree as previously described methylated analogous ZnPc **17** (Figure 30).

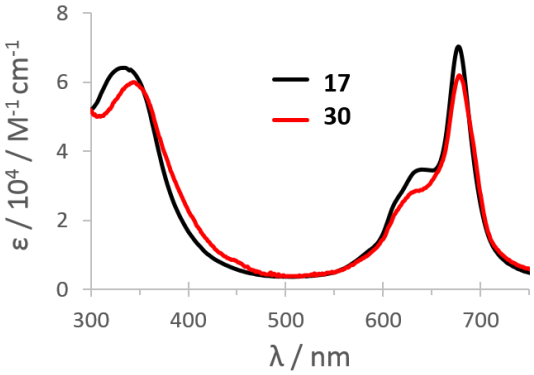

Figure 30. Absorption coefficient of ZnPcs **17** and **30** in water/methanol (90:10).

Nevertheless, other interesting properties arises from the neutral hydrophilic substitution pattern that will be described and exploited in Chapter 2.4.

1.3.3. **Pyrene-containing 3-pyridyloxy-substituted ZnPcs**

1.3.3.1. Synthesis and characterization

In the previous section we have shown that the introduction of tert-butylphenyl substituents at the 5 position of pyridinium moieties allows an easy preparation, purification, and electrochemical characterization (that will be discussed in Chapter 3.3.) of cationic ZnPcs as optoelectronic materials, whose properties and applications are described in Chapter 2 and 3. In this last section of Chapter 1, we describe a parallel synthetic pathway toward a related pyrene-containing a cationic ZnPc derivative (Chart 6). The introduction of pyrene groups pursues enhancing the aggregation and photophysical behaviour of the system, based on their capacity for π-π stacking and excepcional excited state properties. However, the design of compound **31** involves the introduction of four peripheral substituents, instead of eight. The motivation behind this choice was to avoid the steric hindrance that would presumably prevent an easy formation of the octasubstituted compound.

Besides, the properties of ZnPc **31** have been compared to those of the reference compound **32**, synthesized for this purpose and lacking the pyrene units (Chart 6)

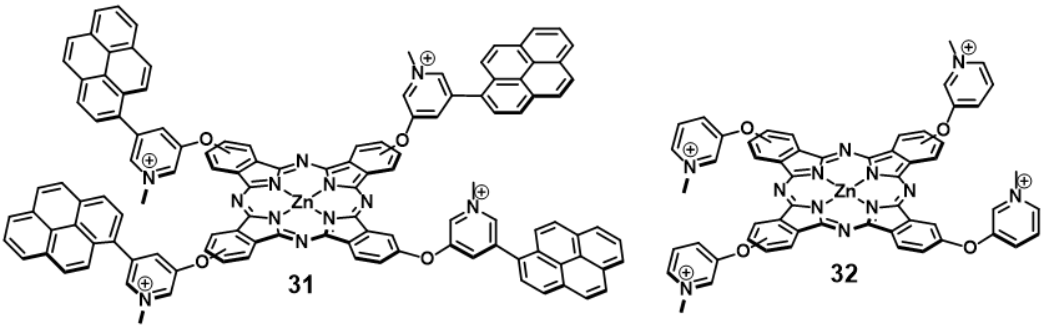

Chart 6. Molecular formula of tetracationic ZnPcs **31** and **32**. Iodine anions are not represented for clarity porpoises

The synthesis of ZnPc **31** was carried out in a similar but optimized way as for ZnPc **17** (Scheme 12). First, pyrene-1-boronic acid pinacol ester (**33**) was synthesized adapting a

previously described method.[163] Briefly, pyrene-1-boronic acid was dissolved in 10 mL of THF and then added to a pinacol solution in diethylether and refluxed for 2.5 hours. The resulting pyrene derivative was reacted with 3-bromo-5-hydroxypyridine *via* Suzuki cross-coupling reaction, obtaining the alcohol **34** in a moderate yield in a single step. In this reaction Pd(dppf)Cl_2 is a much more efficient catalyst than Pd(PPh_4). Phthalonitrile **35** was obtained by nucleophilic aromatic substitution of 4-nitrophthalonitrile with **34**, in anhydrous DMF at room temperature in presence of anhydrous potassium carbonate, and was easily purified by recrystallization. The ZnPc **36** was obtained using typical conditions for cyclotetramerization, employing phthalonitrile **35** in presence of anhydrous zinc acetate, dissolved in DMAE and refluxed overnight. Finally, the tetracationic ZnPc **31** was obtained by methylation in presence of methyl iodide in a sealed tube.

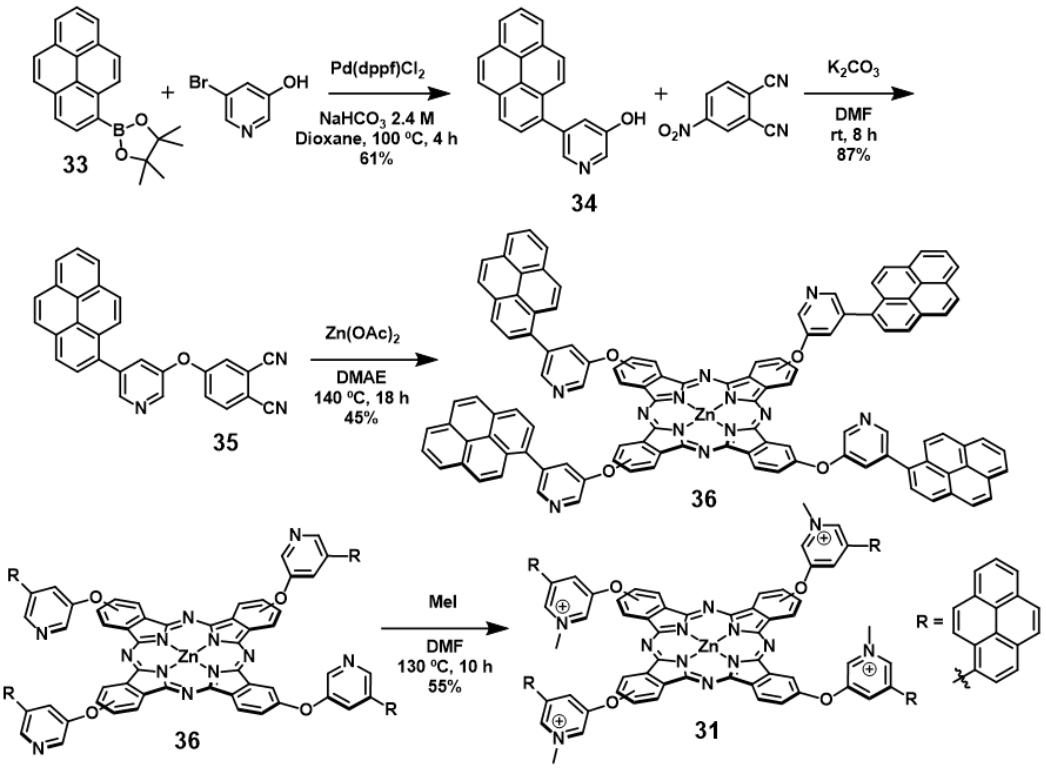

Scheme 12. Synthetic route of ZnPc **31**. Iodine anions are not represented for clarity porpoises

[163] M. Beinhoff, W. Weigel, M. Jurczok, W. Rettig, C. Modrakowski, I. Brüdgam, H. Hartl, A. D. Schlüter, *European J. Org. Chem*,. **2001**, *49*, 3819–3829.

Additionally, ZnPc **32** was synthesized in a three step, chromatography-free synthetic pathway adapting previously described method,[164] in order to be used as reference ZnPc. First step consists in the synthesis of 4-(pyridynyl-3-oxy)phthalonitrile (**37**) by nucleophilic aromatic substitution of 4-nitrophthalonitrile with 3-hydroxypyridine in dry DMF, in presence of anhydrous potassium carbonate. After purification by recrystallization, phthalonitrile **37** was reacted in typical cyclotetramerization conditions in the presence of anhydrous zinc acetate, resulting in ZnPc **38**. Last step consists in quaternization of pyridyl groups in the presence of methyl iodide, resulting in the tetracationic ZnPc **32**.

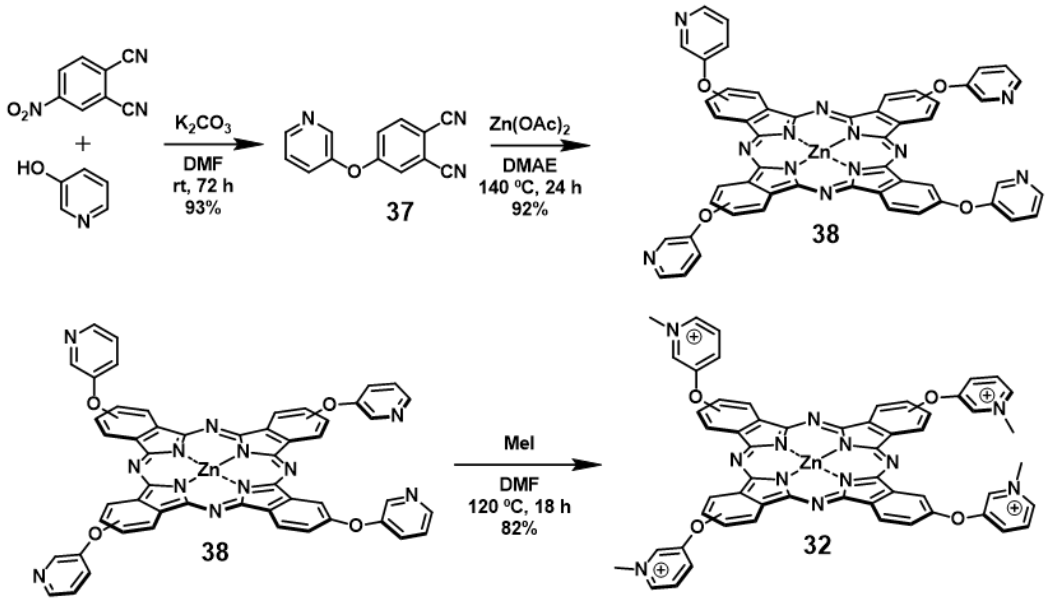

Scheme 13. Synthesis of ZnPc **32**. Iodine anions are not represented for clarity porpoises.

1.3.3.2. Solubility and aggregation

As it was the case for the octacationic ZnPc **17**, derivative **31** also shows no solubility in water, due to the large aromatic pyrene rings decorating the macrocycle`s periphery. Nevertheless, it is dispersible in water from a solution in DMSO, DMF or methanol, leading to a highly stable solution even in organic solvent concentrations lower than 1%. With DMSO, an additional and very interesting effect was observed by UV-Vis and fluorescence

[164] D. Wöhrle, N. Iskander, G. Graschew, H. Sinn, E.A. Friedrich, W. Maier-Borst, J. Stern and P. Schlag, *Photochem. Photobiol.*, *51*, **1990**, 351-356.

spectroscopy: depending on the DMSO proportion in water, different aggregation regimes can occur at the same ZnPc concentration (Figure 31). In pure DMSO (thick red – monomer), **31** shows a sharp absorption band at 678 nm and a high fluorescence emission with maximum at 690 nm, which are characteristic of ZnPcs in their monomeric state. In a mixture of 60% water and 40% DMSO (black – regime A), a decrease in the Q-band intensity and the rise of a band at 635 nm were observed, together with a strong quenching of the emission, indicative of the formation of *H*-type aggregates. Finally, in water with 5% DMSO (bold blue – regime B), **31** shows no *H*-type aggregation band, resembling the Q-band sharpness of the spectrum of monomeric ZnPcs. Surprisingly, the fluorescence spectrum shows no emission recovery, contradicting the first impression of a disaggregated system by UV-Vis spectroscopy.

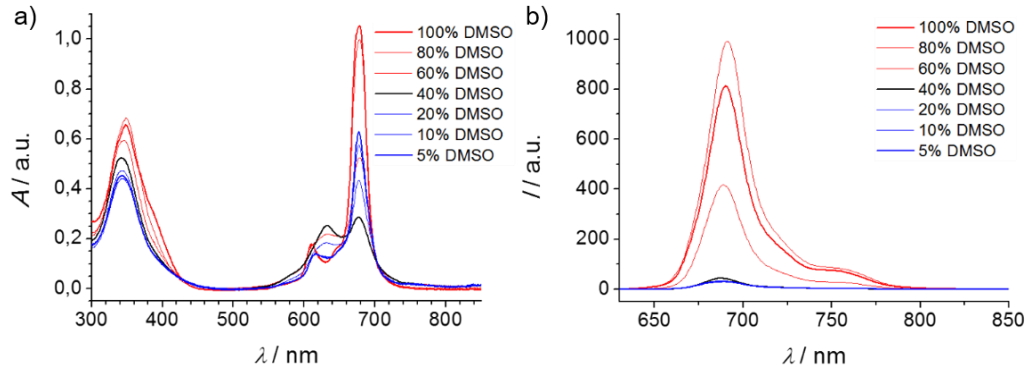

Figure 31. a) Absorption spectra of the ZnPc **31** (5.0 x 10^{-6} M) at different proportions of DMSO in milli-Q water. b) Emission spectra of the ZnPc **31** (5.0 x 10^{-6} M) at different proportions of DMSO in milli-Q water, exciting at 615 nm, 5 nm slit.

Further assesment of the ZnPc **31** aggregation in regime B came out by comparing its absorption extinction coefficient and fluorescence lifetimes with those analogous of ZnPc **32**.[164] As mentioned, the absorption spectrum of **31** in water/DMSO (95:5) presents a sharp absorption band at 678 nm, in opposition to the broad, blue-shifted absorption of *H*-type aggregated ZnPc **32**, also in aqueous solution (Figure 32a). In addition, an intense band at 340 nm is displayed for **31,** corresponding to the combined absorption of the ZnPc Soret band and the pyrene units. The fluorescence lifetime, on the other hand, of ZnPc **31** (313 ps) in aqueous media reveals a strong deactivation of the singlet excited state when compared to the aggregated ZnPc **32** (2.8 ns) in water and with the precursor ZnPc **36** (3.8 ns) in THF (Figure 32b).

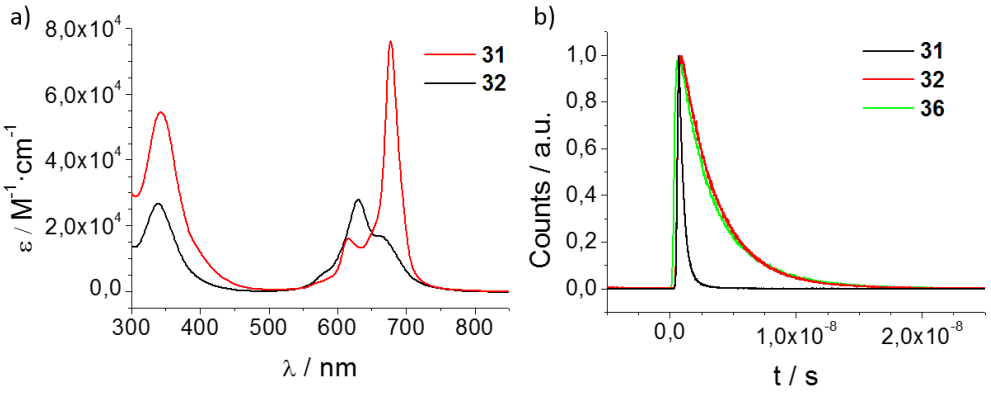

Figure 32. a) Absorption coefficient spectra of ZnPcs **31** and **32** in water with DMSO (1%) and milli-Q water, respectively, both at 5.0 x 10^{-6} M. b) Fluorescence lifetime spectra of ZnPc **31** in water/DMSO (1%), ZnPc **32** in water and ZnPc **36** in THF determined by time-correlated single photon counting (TCSPC) technique.

In sum, the ZnPc **31** in regime A (water/DMSO 60:40) shows *H*-aggregation while regime B (water/DMSO 95:5) shows contradictory spectral features. The absorption spectrum shows a sharp Q-band, yet the quenched emission and short fluorescence lifetime suggest some kind of aggregation. As consequence, we decided to study this strange behaviour in more detail.

1.3.3.3. Supramolecular polymerization

The polymerization mechanisms of self-aggregating molecules have been well studied by the group of E.W. Meijer.[165] Two different mechanisms have been distinguished depending, among others, on the association constant (Ka) of each binding event. The isodesmic model assumes that aggregates are of one dimensional, non-cyclic character. In other words, in this mechanism, the reversible formation of non-covalent bonds presents an identical binding constant for all the events, implying that reactivity of the end groups remains unmodified during chain growth. Thus, the equilibrium constant and Gibbs free energy variations are also equal for each step. On the contrary, the activated or

[165] a) M. M. J. Smulders, M. M. L. Nieuwenhuizen, T. F. a De Greef, P. Van Der Schoot, A. P. H. J. Schenning and E. W. Meijer, *Chem. Eur. J.*, **2010**, *16*, 362–367. b) T.F.A. De Greef, M.M.J. Smulders, M. Wolffs, A.P.H.J. Schenning, R.P. Sijbesma and E.W. Meijer, *Chem. Rev.*, **2009**, *109*, 5687-5754. c) M.J. Mayoral, C. Rest, J. Chellheimer, V. Stepanenko and G. Fernández, *Chem. Eur. J.*, **2012**, *18*, 15607-15611.

cooperative model is based in two different processes (nucleation and elongation), each with different kinetic constants (Figure 33).

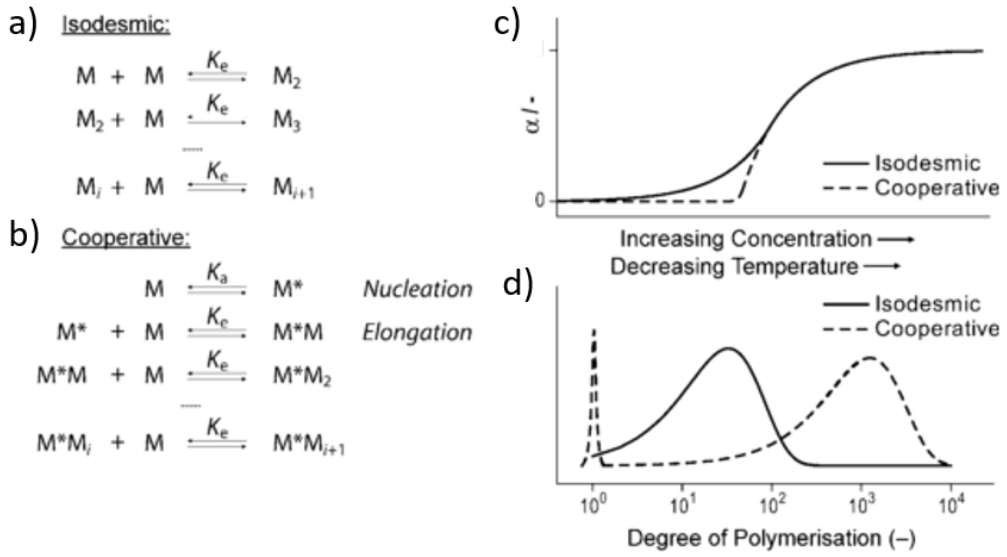

Figure 33. Schematic representantion of the isodesmic (a) and the cooperative (b) mechanism for the supramolecular polymerization of monomers M. c) Schematic representation of the degree of aggregation, *α*, *versus* concentration and temperature for both mechanisms. d) Schematic molecular weight distribution for an isodesmic and a cooperative self-assembly mechanisms. Figure reproduced as shown in ref. 165a.

Since the absorption spectrum of ZnPc **31** in regime B suggests a non-aggregated state and the emission spectrum and lifetime suggests the opposite, a temperature-dependent experiment was performed (Figure 34a). The fluorescence spectra at high temperature showed an emission band at 687 nm, which was gradually quenched and shifted up to 705 nm due to self-aggregation when cooling down. Assuming a two-state equilibrium, the degree of aggregation of the molar fraction of aggregated species *α* is related to temperature by means of a sigmoidal relation. In particular, the degree of aggregation (*α*) was given by the emission at 705 nm, corresponding to the aggregated form, divided by the emission of **31** in its monomeric form, i.e. at 687 nm. The obtained quotient was normalized and fitted to the Boltzmann equation between 0 and 1, suggesting an isodesmic polymerization mechanism (Figure 34b).

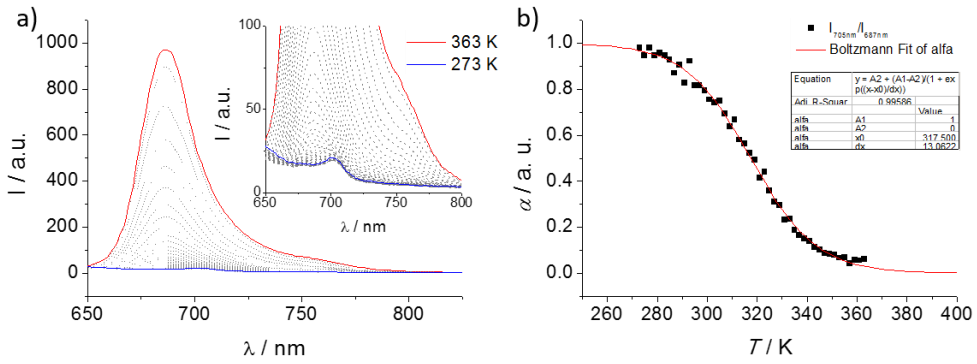

Figure 34. a) Emission spectra of ZnPc **31** (5.0 x 10^{-7} M) in water/DMSO (95:5) at different temperatures (from 273 K to 363 K, each 2 K). b) Fraction of aggregated species *versus* temperature and fitting of the spectral changes (I_{705nm}/I_{687}) to the Boltzmann equation (R^2 = 0.9959).

Following the procedure detailled by M.J. Mayoral *et al.,*[165c] the degree of polymerization (DP_N) and the binding constant for the process was then calculated, the latter being of 8.4 x 10^{-3} M^{-1} (Figure 35).

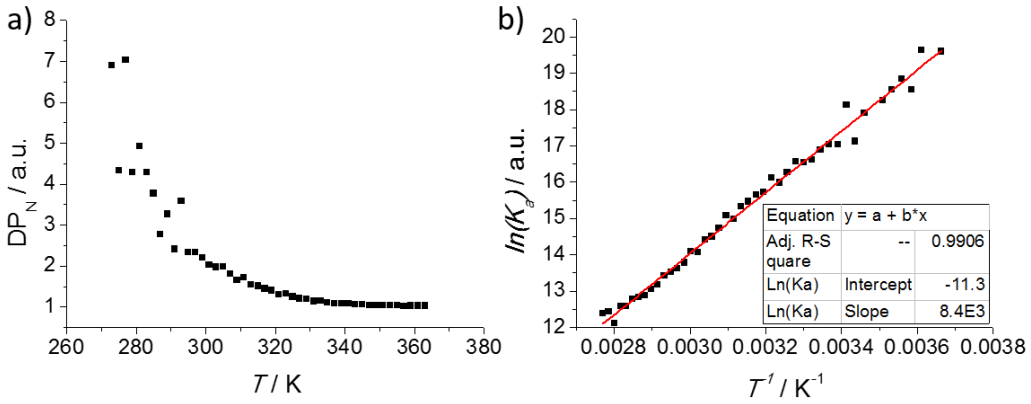

Figure 35. a) Number-averaged degree of polymerization (DP_N) of **31** in water/DMSO (95:5) at different temperatures. b) Van't Hoff plot for the temperature dependence for the aggregation constant *K* of **31** in regime B. R^2 = 0.9906.

Well known *H*-aggregates observed in regime A were also studied following the above methodology in order to compare both regimes. To this end, temperature-dependent experiments were carried out and fitted to an isodesmic model as shown in Figure 36. In detail, a solution of ZnPc **31** (5.0 x 10^{-6} M^{-1}) in water/DMSO (60:40) was subjected to a temperature gradient (Figure 36a) and the normalized transmittance of the

Q-band (λ = 679 nm) was fitted to the Boltzmann equation (Figure 36b). Measuring the emission of **31** at the same conditions, in turn, presented the inconvenience of self-absorption from the Q-band. Lowering the concentration to 1.0 x 10^{-6} M avoided this artefact, enabling an accurate temperature titration and the corresponding fitting to the Boltzman equation (Figure 36c and d, respectively). The most relevant thermodynamic parameters extracted from these temperature-dependent titrations in regimes A and B are summarized in Table 3. As can be observed, a small difference in the melting temperature (T_m) is observed between them. At room temperature (298 K) the number of molecules per aggregate is close to 3 for both regimes.

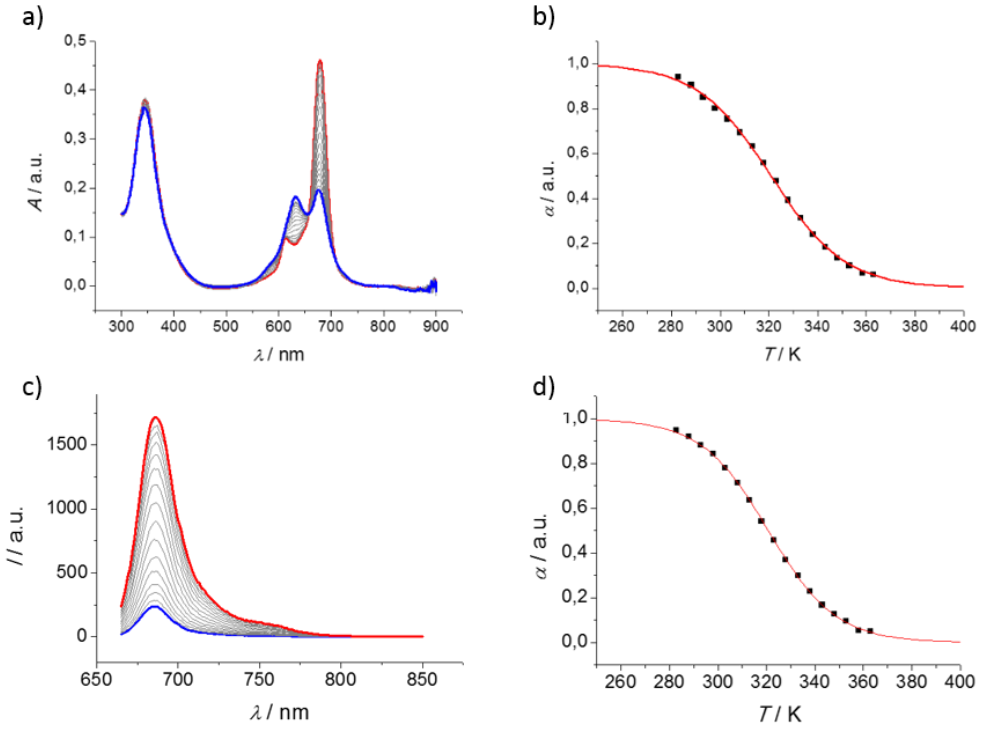

Figure 36. a) Temperature-dependent absorption spectra of ZnPc **31** in water/DMSO (60:40) at 5.0 x 10^{-6} M, from 363 K (red) to 283 K (blue) each 5 K. b) Fraction of aggregated species *versus* temperature and fitting of the spectral changes (transmittance at 679 nm) to the Boltzmann equation (R^2 = 0.9988). c) Temperature-dependent emission spectra of ZnPc **31** in water/DMSO (60:40) at 1.0 x 10^{-6} M, exciting at 615 nm, from 363 K (red) to 283 K (blue) each 5 K. b) Fraction of aggregated species *versus* temperature and fitting of the spectral changes (emission at 686 nm) to the Boltzmann equation (R^2 = 0.9997).

Table 3. Thermodynamic and experimental parameters from temperature-variation experiments of ZnPc **31** in water/DMSO (60:40) (regime B) obtained from absorption and emission from solutions at 5.0 and 1.0 x 10^{-6} M, respectively. Thermodynamic parameters of regime C at 5.0 x 10^{-7} M obtained by emission.

Regime	T_M /K	DP_N	K_a /M^{-1}	$\Delta H^{o[a]}$ /KJ mol^{-1}	$\Delta S^{o[a]}$ /J $mol^{-1}K^{-1}$	ΔG^{o}_{293}[b] /KJ mol^{-1}
B	320.9	2.6	$7.6x10^3$	-63.1	-88.1	-10.3
B	320.8	3.2	$8.0x10^3$	-67.1	-86.4	-41.8
C	317.5	2.9	$8.4x10^3$	-70.1	-93.9	-42.6

[a] Van't Hoff equation: $\ln K = -\frac{\Delta H^0}{RT} + \frac{\Delta S^0}{R}$; R = 8.3144621 J K^{-1} mol^{-1}. [b] Gibb's equation: $\Delta G^0 = \Delta H^0 - T\Delta S^0$.

The magnitude of the association constant in the two aggregation regimes is also very similar (ca. 8 x 10^3 M^{-1}). This fact suggests that they are regulated by the π-π interactions and the differences among them result from a conformational change of **31** due to the proportion of water in the solution. In Figure 37, we present in cartoons hypothetical models to explain these differences in the aggregation mode. *H*-aggregates are well-known to produce a coplanar interaction between adjacent aromatic Pc cores. In regime B, on the other hand, we propose that a reorganization of **31** occurs to maximize both hydrophobic interactions and solvation effects with the pyridinium moieties pointing outwards, and the pyrene rings folded over the Pc core by π-π stacking. This conformation hinders the hydrophobic pyrene from the aqueous medium, and avoids direct Pc-Pc interactions.

Finally, the aggregates formed by ZnPc **31** in regime B conditions were characterized by TEM (Figure 38). The TEM sample was stained with uranyl acetate (2% in water) to enhance the contrast between the grid and the material. Rod-like aggregates (200 x 30 nm size) were found all over the sample, which is in perfect agreement with the previous spectroscopy observations. Rod-like aggregates were observed of and were found all over the sample. We propose the formation of these rod-like structures by a bundling effect of the linear polymers shown in Figure 37. The proposed conformation avoids close contact between the Pc cores, thus showing no effect in the absorption spectrum. The close interaction between ZnPc and pyrene units, on the other hand, could be the cause of the ZnPc excited state deactivation. This unprecedented mode of aggregation, never observed before for ZnPcs or other supramolecular dye optoelctronic materials, actually has unusual

effects on the photophysical behaviour of ZnPc **31**, which was studied during an internship in the group of Prof. Dirk M. Guldi, in Erlangen (Germany), and are carefully described in Chapter 3.4.

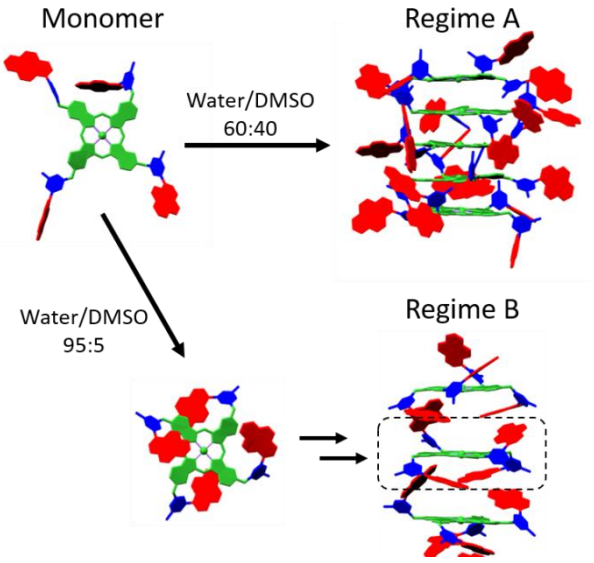

Figure 37. Hypothetical model of the aggregation of **31** in regime A and B.

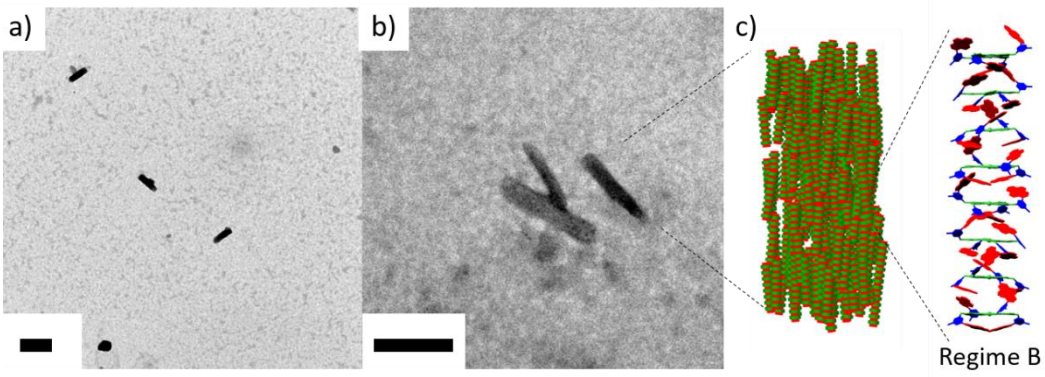

Figure 38. TEM images of ZnPc **31** from a water/DMSO (95:5) solution onto carbon covered copper grids. Aqueous uranyl acetate 2% as stain. Scale bar: 200 nm.

1.4. Conclusions

In the present chapter, the synthesis of both new and previously described water-soluble ZnPc has been tackled, emphasizing in cationic ammonium or pyridinium derivatives. The latter has been the most employed solubilizing group due to its synthetic flexibility prior to quaternization.

First, the synthesis of well-known sulfonated ZnPcs (**1** – **3**) was achieved by combining and adapting different previously described methodologies. A thorough characterization of the regioisomeric content of each ZnPc was performed by combination of HPLC and theoretical calculations of the dipolar moment. Those fully characterized systems has been employed as photoactive material in water-processed organic solar cells in collaboration with Prof. E. Palomares research group as described in Chapter 3.2.[166]

Secondly, previously described ZnPc **4** and its unprecedented asymmetric derivatives **5** and **6** were synthesized and characterized. The ability of the amphiphilic ZnPcs to be inserted in anionic micelles was evaluated, as well as the disaggregating effect that those micelles have in the otherwise strongly aggregated Pcs. In particular, ZnPc **6** was inserted in functional micelles and hierarchically covered by a virus capsid with the collaboration with the group of Prof. Jeroen J.L.M. Cornelissen. This system was proposed as a potential theranostic, multimodal imaging agent and will be described in detail in Chapter 2.2.[167]

In addition, preliminary experiments were performed in order to control the aggregation of ZnPc **6** by anion exchange. By using the reprecipitation method, organic nanoparticles were assembled from the resulting hydrophobic Pc organic salt (ZnPc **12**), yet these nanoparticles presented a reduced stability. Another drawback of the trimethylammonioethylsulfanyl substituents present in compounds **4** – **6** is their difficulty of chromatographic purification, which led us to a change in the design of cationic Pc systems.

Preparation of symmetrically and asymmetrically substituted pyridyl-derivative ZnPcs was achieved in moderate yields incorporating bulky aromatic moieties to the hydroxylpyridine before the conjugation in the macrocycle. Those groups enhances the

---

[166] J.W. Ryan, E. Anaya-Plaza, A. de la Escosura, T. Torres and E. Palomares, *Chem. Commun.*, **2012**, *48*, 6094-6096.

[167] J. G. Millan, M. Brasch, E. Anaya-Plaza, A. de la Escosura, A.H. Velders, D.N. Reinhoudt, T. Torres, M.S.T. Koay and J.J.L.M. Cornelissen, *J. Inorg. Biochem.*, **2014**, *136*, 140-146.

solubility of the derivatives in organic solvents, lowering the aggregation thus enabling an efficient separation from the statistical cyclotetramerization reaction by chromatography column. This strategy rises a series of amphiphilic cationic ZnPcs (**17** – **20**) that exhibits a great electron-acceptor ability. Conjugation of ZnPc **17** with single-walled carbon nanotubes (SWCNTs) was studied as photoactive material in collaboration with the group of Prof. Dirk M. Guldi and detailed in Chapter 3.3.[168] In adition, the synthesis of symmetrically substituted ZnPcs **16** was achieved through an improved synthetic route that, taking advantage of low solubility of the precursors, dispenses chromatography column purification, simplifying otherwise tedious purification. This derivative in particular has been found of special interest as photosensitizer in different biohybrid materials such as protein crystals[169] and cellulose nanocrystals (CNCs),[170] studied in close partnership with Dr. Mauri A. Kostiainen research group. Those works will be exhaustively detailed in Chapter 2.3. and 2.4. of the present thesis, respectively. Other quaternization possibilities has been studied, synthesizing triethyleneglycol-quaternized derivatives (**30**). This derivative present a neutral hydrophilic solvatation sphere that affects the performance of CNCs derivatives as will be exposed in Chapter 2.4.

Finally, conjugation of a photoactive bulky aromatic moiety with the pyridil-3-oxy lead to the synthesis of ZnPc **31**. This Pc exhibits an unprecedented aggregation behaviour in aqueous media, confirmed by the deactivation of the excited estate. Temperature titrations suggests an isodesmic polymerization mechanism, showing a binding constant *K* of 8.4 x10^3 M^{-1}, very similar to the most common *H*-aggregate, also exhibit by this compound in different conditions. The linear polymers trend to bundle in rod-like aggregates as confirmed by TEM imaging and its optoelectronical properties has been studied during a short internship in the group Prof. Dirk M. Guldi.

---

[168] E. Anaya-Plaza, M.M. Oliva, A. Kunzmann, C. Romero-Nieto, R.D. Costa, A. de la Escosura, D.M. Guldi and T. Torres, *Adv. Funct. Mat.*, **2015**, *25*, 7418-7427.

[169] J. Mikkilä, E. Anaya-Plaza, V. Liljeström, J.R. Caston, T. Torres, A. de la Escosura and M.A. Kostiainen, *ACS Nano*, **2016**, *10*, 1565-1571.

[170] E. Anaya-Plaza, E. van de Winckel, J. Mikkilä, J.-M. Malho, O. Ikkala, T. Torres, M.A. Kostiainen and A. de la Escosura, *submitted.*

1.5. Experimental section of Chapter I

1.5.1. **Materials and methods**

In this *Experimental Section* the preparation and characterization of the compounds has been organized following the order as they appear in the text.

Chemical reagents were purchased from Aldrich Chemical Co., Alfa Aesar, Across Organics or Fluka Chemie and were used without further purification. All reactions were performed in standard glassware. Microwave reactions were carried out in a CEM Discovery apparatus. The monitoring of the reactions has been carried out by thin layer chromatography (TLC), employing aluminum sheets coated with silica gel type 60 F_{254} (0.2 mm thick, E. Merck). Purification and separation of the synthesized products was performed by column chromatography, using silica gel (230-400 mesh, 0.040-0.063 mm, Merck). Ionic exchange resin Amberlite IR-120 (plus) was purchased from SUPELCO.

Nuclear magnetic resonance spectra (^{1}H-NMR and ^{13}C-NMR) were recorded on Bruker AM-300 (300 MHz) or AM-500 (500 MHz) instruments, with solvent signal as reference (H_{pc}: Pc protons; H_{py}: pyridine protons; H_{ar}: aromatic protons). The deuterated solvents employed are indicated in parentheses.

UV-Vis spectra were recorded with a JASCO V-660 spectrophotometer. In brackets is expressed the logarithm of the molar absorption coefficient (ε).

Infrared spectra (IR) were recorded on a Bruker Vector 22 spectrophotometer, using solid samples (KBr pellets) or as thin films (film), in the Department of Organic Chemistry (UAM).

Melting points (Mp) were determined in a Buchi 504392-S equipment, in the Department of Organic Chemistry (UAM).

Matrix-assisted laser desorption/ionization time-of-flight (MALDI-TOF) and (MS) and high resolution MS (HRMS) were recorded in the positive ion mode with a Bruker Ultrareflex III TOFTOF spectrometer equipped with a Nd:YAG laser operating at 355. Matrix employed were indicated in parentheses. ESI (electrospray ionization) mass spectra were recorded with an Applied Biosystems QSTAR using as injection system HPLC1100 (Agilent Technologies). FAB (fast atom bombardment) spectra were recorded with a VG AutoSpec

de Waters spectrometer. All MS experiments were carried out at the Servicio Interdepartmental de Investigación (SIdl) of the Universidad Autónoma de Madrid.

HPLC chromatograms were recorded with an Agilent 1290 Infinity LC System (Vacuum degasser, quaternary pump, standard autosampler, termostated column compartment and diode array detector) equipped with an Agilent Eclipse XDB C18 column (4.6 mm ID x 250 mm, 80 Å pore and 5 µm of particle size).

Electrochemical measurements were performed on an Autolab PGStat 30 equipment using a three electrode configuration system. The measurements were carried out using freshly distilled THF or DMSO solutions containing 0.1 M tetrabutylammonium hexafluorophosphate ($TBAPF_6$). A glassy carbon electrode (3 mm diameter) was used as the working electrode, and a platinum wire and an $Ag/AgNO_3$ (in CH_3CN) electrode were employed as the counter and the reference electrodes, respectively. Ferrocene (Fc) was added as an internal reference and all the potentials were given relative to the Fc/Fc^+ couple. Scan rate was 100 mV s^{-1}.

1.5.2. **Synthesis of anionic Pcs**

[2(3),9(10),16(17),23(24)-tetrasulfophthalocyaninato]zinc(II)-N^{29}, N^{30}, N^{31}, N^{32} (**1**)[114b]

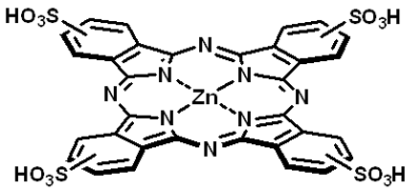

Potassium 4-sulfonatophthalate (10 g, 28 mmol), ammonium chloride (1.94 g, 36.3 mmol), urea (25.4 g, 423 mmol), ammonium molybdate (0.18 g, 0.90 mmol) and anhydrous zinc acetate (1.8 g, 98 mmol) were placed in a round-bottom flask and heated at 170 °C for 30 min. At this point, the solution became light green. The temperature was then raised to 210 °C, and gradually over 6 hours up to 230 °C. After cooling down, the crude black solid was suspended in 10% aqueous HCl saturated with NaCl (200 mL). The precipitate was filtered and subsequently washed with acetone and a mixture of acetone/ethanol/water (10:10:1). A green-black solid was obtained (6.95 g) and further purified by ionic exchange with 55 g of appropriately conditioned ionic exchange resin (Amberlite IR-120 (plus)). A dark-blue solid was collected from the column and subsequently re-precipitated from water/acetone. The re-precipitation process can also be performed from DMSO/acetone, although less crystalline than from the former re-precipitation process. Respective yields: 0.96 g, 15% and 2.97 g, 48%.

Mp: > 250 °C.

^{1}H-NMR (300 MHz, DMSO-d_6): δ (ppm) = 9.65 (d, J = 3.0 Hz, 4H, H_{Pc}), 9.38 (m, 4H, H_{Pc}), 8.48 (dd, J_1 = 7.9 Hz, J_2 = 3.0 Hz, 4H, H_{Pc}).

UV-Vis (DMSO): λ_{max} (nm) (log ε) = 679 (4.93), 612 (4.2), 351 (4.45).

MS (MALDI-TOF, α-cyano-4-hydroxycinnamic acid): *m/z* (%) = 896.9 $[M-H]^-$, 918.9 $[M-2H+Na]^-$, 940.9 896.9 $[M-3H+2Na]^-$.

HPLC (retention time): 21.8 min.

Synthesis of asymmetrically substituted sulfonated Pcs[114b,117]

Potassium 4-sulfonatophthalate (2.5 g, 6.9 mmol), phthalic anhydride (1 g, 7.0 mmol), ammonium chloride (1.0 g, 19 mmol), urea (12.7 g, 211 mmol), ammonium molybdate (0.08 g, 0.4 mmol) and anhydrous zinc acetate (0.9 g, 4.9 mmol) were placed in a 100 mL round-bottomed flask and heated to 170 °C, at which point urea melted and started to decompose into ammonia. The solution gets light green and, after 30 min, the

mixture was heated up to 210 °C and the reaction mixture turned dark blue. The temperature was raised gradually over 6 hours up to 230 °C and finally became solid. After cooling down, the crude black solid was suspended in 10% aqueous HCl saturated with NaCl (200 mL). The precipitate was filtered and subsequently washed with acetone and a mixture of acetone/ethanol/water (10:10:1). The solid was purified by column chromatography, using ethyl acetate/ethanol/aqueous ammonia 25% (7:4:4) as the eluent.

[2(3),9(10),16(17)-trisulfophthalocyaninato]zinc(II)-N^{29}, N^{30}, N^{31}, N^{32} (**2**)

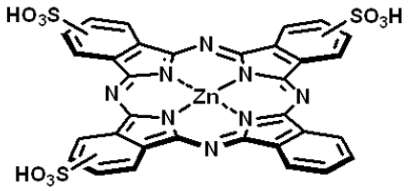

Eluted as the third fraction of the chromatography column. HPLC analysis reveal a 9% of **1** as impurity. The sample was precipitated in acetone from DMSO. Yield: 146.8 mg, 5%.

Mp: > 250 °C.

^{1}H-NMR (300 MHz, DMSO-d_6): δ (ppm) = 8.7-8.3 (m, 2H, H_{Pc}), 8.3-7.5 (m, 4H, H_{Pc}), 7.5-7.2 (m, 2H, H_{Pc}), 7.0-5.9 (m, 7H, H_{Pc}).

UV-Vis (DMSO): λ_{max} (nm) (log ε) = 677 (5.02), 610 (4.26), 350 (4.60).

MS (MALDI, ACC): *m/z* (%) = 816.9 $[M-H]^-$ (100), 838.9 $[M-H+Na]^-$ (76), 897.9 [ZnPc **1**]$^+$ (10), 919.9 [ZnPc **1**-H+Na]$^-$ (1).

HPLC (retention time): 21.8 min (ZnPc **1**, 8.8%); 27.5, 28.7 and 31.7 min for the different regioisomers (91.2%).

[2(3),9(10)(16)(17)-disulfophthalocyaninato]zinc(II)-N^{29}, N^{30}, N^{31}, N^{32} (**3**)

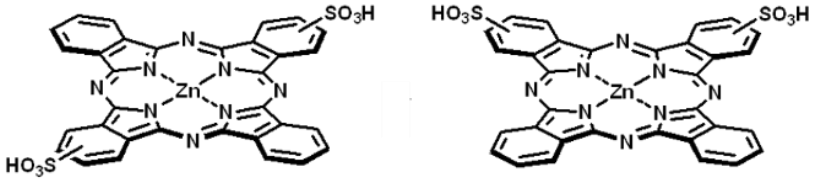

Eluted as the second fraction of the chromatography column. The sample was precipitated in acetone from DMSO. Yield: 411.2 mg, 16%.

Mp: > 250 ^{o}C.
^{1}H-NMR (300 MHz, DMSO-d_6): δ (ppm) = 8.5-8.2 (m, 1H, H_{Pc}), 8.1-7.2 (Ar-H, 5H, m), 7.2-6.1 (Ar-H, 8 H, m).
UV-Vis (DMSO): λ_{max} (nm) (log ε) = 675 (4.99), 609 (4.23), 349 (4.57).
MS (MALDI, ACC): *m/z* (%) = 735.1 $[M-H]^-$, 757.1 $[M-H+Na]^-$, 779.2 $[M-2H+2Na]^-$.
HPLC (retention time): 35.8, 36.5, 38.7, 40.6 and 42.7 min (for the different regioisomers).

1.5.3. **Synthesis of Cationic ZnPcs**

1.5.3.1. Synthesis of 2-(Trimethylammonio)ethanesulfanyl ZnPcs

4-(2-Dimethylaminoethylsulfanyl)phthalonitrile (**7**)[134a]

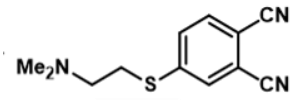

Into a 100 mL two-necked round-bottomed flask 4-nitrophthalonitrile (2.13 g, 12.3 mmol) and 2-(dimethylamino)ethanethiol hydrochloride (1.93 g, 13.7 mmol) was dissolved in freshly distilled DMSO under argon atmosphere. Anhydrous potassium carbonate (2.54 g, 18.4 mmol) was added in small portions for 2 hours at room temperature, turning dark and left stirring overnight. When the reaction is over, 100 mL of water was added and extracted with chloroform (3x50 mL). Combined organic phases were washed with water (2x30 mL), aqueous sodium bicarbonate 5% (2x30 mL) and water (2x20 mL). Resulting solution was dried under reduced pressure. Resulting solid was purified by chromatography column using dichloromethane/methanol (30:1) as eluent. Yield: 2.33 g, 81%.

Mp: 110 ^{o}C.

^{1}H-NMR (300 MHz, $CDCl_3$): δ (ppm) = 7.63 (d, *J* = 8.3 Hz, 1H, H_{ar}); 7.58 (d, *J* = 1.9 Hz, 1H, H_{ar}), 7.51 (dd, J_1 = 8.3, J_2 = 1.9, 1H, H_{ar}), 3.13 (t, *J* = 7.0 Hz, 2H, S-CH_2), 2.62 (t, J = 7.0, 2H, N-CH_2), 2.23 (s, 6H, N-CH_3).

^{13}C-NMR (75,5 MHz, $CDCl_3$): δ (ppm) = 147.3, 133.1, 130.1, 129.9, 116.2, 115.5, 115.1, 110.7, 57.2, 45.2, 30.3.

MS (FAB$^+$, m-NBA): *m/z* (%): 187.0 [M-NMe_2]$^+$ (21), 232.1 [M+H]$^+$ (100), 463.1 [2M+H]$^+$ (18).

FT-IR (KBr), ν (cm^{-1}): 2880-2800 (C-H), 2240 (C≡N), 1600, 1480, 1300, 1020, 900, 820, 520.

[2,(3),9,(10),16,(17),23,(24)-tetrakis-(2-dimethylaminoethylsulfanyl)phthalocyaninato]-zinc(II)-N^{29}, N^{30}, N^{31}, N^{32} (**8**)[134a]

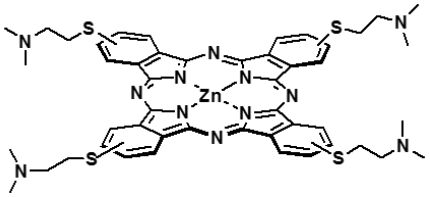

Into a two-necked round-bottomed flask equipped with reflux, phthalonitrile **7** (252.4 mg, 1.08 mmol) and anhydrous zinc acetate (81.2 mg, 0.59 mmol) were dissolved in dimethylaminoethanol under argon atmosphere and was warmed up to 140 °C overnight. The gummy solid formed was dissolved in chloroform (20 mL) and washed with water (3x10 mL). Organic phase was dried under reduced pressure and the resulting green solid was crushed in acetone. Yield: 211 mg, 79%.

Mp: > 250 °C.

^{1}H-NMR (300 MHz, $CDCl_3$): δ (ppm) = 8.5-7.4 (m, 12H, H_{Pc}), 2.39 (m, S-CH_2, 8H), 1.60 (m, 8H, N-CH_2), 1.24 (s, 12H, N-CH_3,).

MS (FAB$^+$): *m/z* (%) = 990 $[M]^+$ (7).

[2,(3)-*tert*-butyl-9,(10),16,(17),23,(24)-tris-(2-dimethylaminoethylsulfanyl)-phthalocyaninato]zinc(II)-N^{29}, N^{30}, N^{31}, N^{32} (**9**)

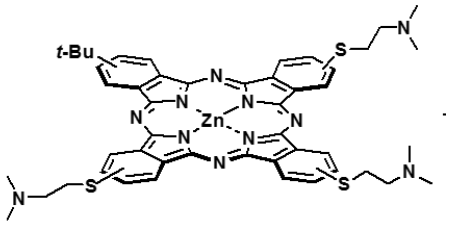

Into a two-necked round-bottomed flask equiped with reflux, phthalonitrile **7** (403.6 mg, 1.74 mmol) and 4-*tert*-butylphthalonitrile (183.1 mg, 0.99 mmol) and anhydrous zinc acetate (127.2 mg, 0.93 mmol) were dissolved in dimethylaminoethanol under argon atmosphere and warmed up to 140 °C overnight. The resulting deep green solution was dried under reduced pressure and the resulting solid was crushed in acetone. The resulting solid was purified by chromatography column with THF/methanol/triethylamine (9:1:0.1) as eluent. Yield: 57 mg, 7%.

Mp: > 250 °C.

^{1}H-NMR (300 MHz, $CDCl_3$): δ (ppm) = 8.9-7.9 (m, 12H, H_{Pc}), 3.58 (t (br), *J* = 6.8 Hz, 6H, S-CH_2), 2.86 (t (br), *J* = 6.6 Hz, 6H, N-CH_2), 2.4 (s (br), 18H, N-CH_3), 1.87 (s (br), 9H, $C(CH_3)_3$).

MS (MALDI-TOF, DCTB): *m/z* (%) = 896.3 $[M\text{-}NMe_2]^+$ (7), 941.3 $[M+1]^+$ (100), 1886.5 $[2M]^+$ (5).

[2,(3),9,(10),16,(17)-tris(*tert*-butyl)-23,(24)-(2-dimethylaminoethylsulfanyl)-phthalocyaninato]zinc(II)-N^{29}, N^{30}, N^{31}, N^{32} (**11**)

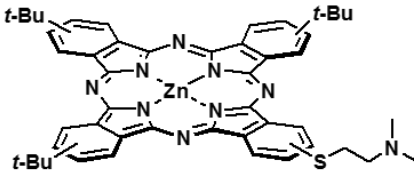

Into a two-necked round-bottomed flask equiped with reflux, phthalonitrile **7** (223.3 mg, 0.97 mmol) and 4-*tert*-butylphthalonitrile (698.1 mg, 3.80 mmol) and anhydrous zinc acetate (299.7 mg, 1.63 mmol) were dissolved in dimethylaminoethanol protected from light, under argon atmosphere and warmed up to 140 °C overnight. The resulting deep green solution was dried under reduced pressure and the resulting solid was crushed in acetone/hexane (1:1). The resulting solid was purified by chromatography column with THF/dioxane (4:1). Yield: 460 mg, 56%.

Mp: > 250 °C

^{1}H-NMR (300 MHz, $CDCl_3$): δ (ppm) = 9.4-9.2 (m, Ar-H, 8H), 8.3 (m, Ar-H, 3H), 8.0 (m, Ar-H, 1H), 3.62 (t(b), S-CH_2, 2H), 2.93 (t(b), N-CH_2, 2H), 2.42 (s(b), N-CH_3, 6H), 1.79 (s(b), $C(CH_3)_3$, 27H).

MS (MALDI, Ditranol): *m/z* (%) = 775.2 [M- NMe_2]$^+$ (14), 847.4 [M]$^+$ (100).

[2,(3),9,(10),16,(17),23,(24)-tetrakis-(2-trimethylammonioethylsulfanyl)phthalocyaninato]-zinc(II)-N^{29}, N^{30}, N^{31}, N^{32}, tetraiodine (**4**)

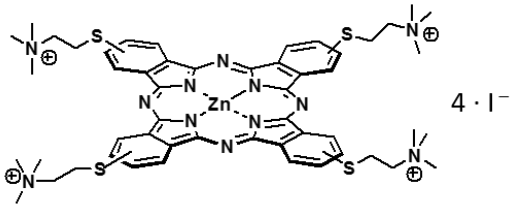

Into a two-necked round bottomed flask equipped with reflux ZnPc **8** (169.2 mg, 0.17 mmol) was dissolved in ethanol (7 mL) under argon atmosphere. The reaction mixture was warmed up to reflux and methyl iodide was added (40 µL, 0.6 mmol) and left for 2 hours. The resulting green solid was washed and crushed with acetone and diethyl ether. Yield: 155.2 mg, 58%.

Mp: > 250 °C.

^{1}H-NMR (300 MHz, DMSO-d_6): δ (ppm) = 9.4 (m, Ar-H, 8H), 8.4 (m, Ar-H, 4H), 4.0 (m, N-CH_2, 8H), 3.9 (m, S-CH_2, 8H), 3.25 (s, N-CH_3).
UV-Vis (MeOH): λ_{max} (nm) (log ε) = 683 (4.94), 611 (4.48), 344 (4.84).
MS (ESI$^+$, ACN): *m/z* (%) = 651.1 $[M-2I]^{+2}$ (100).
FT-IR (KBr), ν (cm^{-1}): 2880-2800 (C-H), 1600, 1460, 1300, 1100, 920, 900, 740.

[2,(3)-*tert*-butyl-9,(10),16,(17),23,(24)-tris-(2-trimethylammonioethylsulfanyl)-phthalocyaninato]zinc(II)-N^{29}, N^{30}, N^{31}, N^{32}, triiodine (**5**)

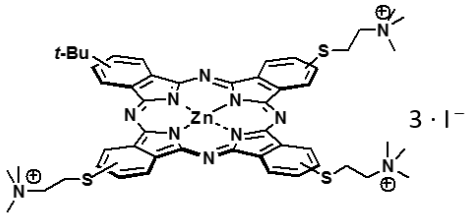

Into a two-necked round bottomed flask equipped with reflux, ZnPc **9** (59.0 mg, 0.063 mmol) was dissolved in ethanol (7 mL) under argon atmosphere. The reaction mixture was warmed up to reflux and methyl iodide was added (10 µL, 0.16 mmol) and left for 2 hours. The resulting green solution was evaporated and the resulting solid was washed and crushed with acetone and diethyl ether. Yield: 75.2 mg, 88%.
Mp: > 250 °C.
^{1}H-NMR (300 MHz, DMSO-d_6): δ (ppm) = 9.3-8.1 (m, 12H, H_{Pc}), 4.0-3.9 (m, 12H, CH_2), 3.36 (s, 27H, N-CH_3), 1.94 (s, 9H, $C(CH_3)_3$).
UV-Vis (MeOH): λ_{max} (nm) (log ε) = 690 (5.06), 614 (4.24), 359 (4.55).
MS (ESI$^+$, MeOH) *m/z* (%) = 328.2 $[M-3I]^{+3}$ (25), 556.5 $[M-2I]^{+2}$ (71).

[2,(3), 9,(10),16,(17)-tris-*tert*-butyl-23,(24)-(2-trimethylammonioethylsulfanyl)-phthalocyaninato]zinc(II)-N^{29}, N^{30}, N^{31}, N^{32} iodine (**6**)

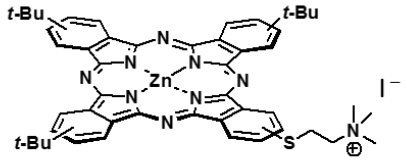

Into a two-necked round bottomed flask equipped with reflux, ZnPc **11** (96.4 mg, 0.11 mmol) was dissolved in ethanol (7 mL) under argon atmosphere. The reaction mixture was warmed up to reflux and methyl iodide was added (10 µL, 0.16 mmol) and left for 2 hours. The resulting green solution was evaporated and the resulting solid was washed and crushed with acetone and diethyl ether. Yield: 57.1 mg, 51%.

Mp: > 250 ^{o}C.

^{1}H-NMR (300 MHz, MeOD-d_4): δ (ppm) = 9.5-7.8 (m, 12H, H_{Pc}), 3.8 (m, 4H, CH_2), 3.3 (s, 9H, NCH_3), 1.94 (m,* $C(CH_3)_3$, 27H).

^{13}C-NMR (75,5 MHz, MeOH-d_4): δ(ppm) = 145.7, 138.8, 136.9, 132.6, 126.2, 124.0, 121.0, 53.9, 36.8.

UV-Vis (MeOH): λ_{max} (nm) (log ε) = 683 (4.94), 611 (4.48), 344 (4.84).

MS (ESI^+, MeOH) *m/z* (%) = 431.7 $[M\text{-}I^-]^{+2}$ (4), 775 $[M\text{-}CH_2CH_2NMe_3I]^+$ (4), 862.3 $[M\text{-}I]^+$ (100%).

* Multiplicity given by the regioisomers mixture.

[2,(3),9,(10),16,(17)-tris-*tert*-butyl-23,(24)-(2-trimethylammonioethylsulfanyl)-phthalocyaninato]zinc(II)-N^{29}, N^{30}, N^{31}, N^{32} docusate (**15**)

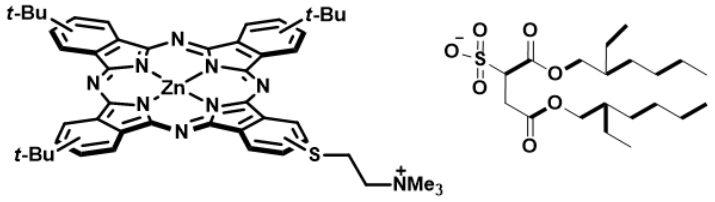

Into a round-bottomed flask, ZnPc **6** (23.7 mg, 0.024 mmol) and sodium docusate (10.8 mg, 0.024 mmol) were dissolved in 10 mL of dichloromethane. After 10 minutes, 5 mL of milli-Q water was added and stirred gently for additional 10 minutes at room temperature, observing a colour transition from green to blue. Organic phase was separated, washed with milli-Q water (3 x 5mL) and dried under reduced pressure. Solid was crushed in hexane and filtered off, resulting in a blue solid. Yield: 28.6 mg, 98%.

Mp: > 250 ^{o}C

^{1}H-NMR (300 MHz, MeOD-d_4): δ (ppm) = 9.3-7.9 (m, 12H, H_{ar}), 3.9 (m, 4H, CH_2), 3.2 (m, 7H, CH_2 and O-CH_2 docusate), 1.92 (s, 27H, $C(CH_3)_3$), 1.3 (m, 14H, CH_2 and CH docusate,) 0.86 (m, 12H, CH_3 docusate).

UV-Vis (MeOH): λ_{max} (nm) (log ε) = 685 (4.90), 611 (4.48), 345 (4.86)

MS (MALDI, DCTB): *m/z* = 775.2 [M-docusate-$CH_2CH_2NMe_3$]$^+$ (75), 862.4 [M-docusate]$^+$ (13), 1283.6 [M]$^+$ (100).

[2,(3)-iodo-9,(10),16,(17),23,(24)-tris-(2-dimethylaminoethylsulfanyl)-phthalocyaninato]-zinc(II)-N^{29}, N^{30}, N^{31}, N^{32} (**13**)

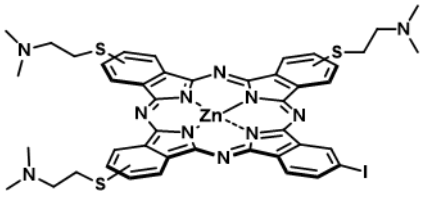

Into a two-necked round-bottomed flask equiped with reflux, phthalonitrile **7** (537.9 mg, 2.32 mmol) and 4-iodophthalonitrile (214.0 mg, 0.85 mmol) and anhydrous zinc acetate (290 mg, 1.57 mmol) were dissolved in dimethylaminoethanol under argon atmosphere and warmed up to 140 ^{o}C overnight. The resulting deep green solution was dried under reduced pressure and the resulting solid was crushed in acetone. The resulting solid was purified by chromatography column with THF/dioxane/TEA (80:20:1) as eluent. Yield: 37 mg, 5%.

Mp: > 250 ^{o}C.

^{1}H-NMR (300 MHz, $CDCl_3$): δ (ppm) = 8.9-7.9 (m, 12H, H_{Pc}), 3.62 (t (br), *J* = 6.8 Hz, 6H, S-CH_2), 2.89 (t (br), *J* = 6.6 Hz, 6H, N-CH_2), 2.35 (s (br), 18H, N-CH_3).

MS (MALDI, DCTB): *m/z* = 986.70 [ZnPc **8**]$^+$ (9), 1009.41 [M$^+$] (67%),

Benzyl 4-pentynoate (**14**)

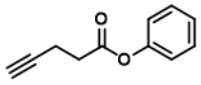

Into a 50 mL round-bottomed flask 4-pentynoic acid (105.3 mg, 1.08 mmol), phenol (103.2 mg, 1.10 mmol), 1-hydroxybenzotriazole (HOBT) (22.3 mmol, 0.17 mmol), and dimethylaminopyridine (37.9 mg, 0.30 mmol) were dissolved in DCM (10 mL) and the resulting solution was cooled down to 0 ^{o}C and 1-ethyl-3-(3-dimethylaminopropyl)-carboiimide (EDC) (216.5 mg, 1.13 mmol) was added. After 20 h at 0 ^{o}C the reaction mixture was evaporated under reduced pressure and the resulting oil was purified by column

chromatography, employing a mixture of hexane/ethyl acetate (10:1) as eluent, resulting as the desired product as a non-colored oil. Yield: 113.6 mg, 61%.

^{1}H-NMR (300 MHz, $CDCl_3$): δ (ppm) = 7.45 (t, *J* = 7.6 Hz, 1H, H_{Ph}), 7.37 (dd, J_1 = 7.7 Hz, J_1 = 7.9 Hz, 1H, H_{Ph}), 7.08 (t, *J* = 8.0 Hz, 1H, H_{Ph}), 2.54-2.51 (m, 2H,CH_2), 2.50-2.46 (m, 2H, CH_2), 1.96 (t, *J* = 2.4 Hz, 1H, -CCH).

[2,(3)-(benzyl 4-pentynoate)-9,(10),16,(17),23,(24)-tris-(2-dimethylaminoethylsulfanyl)-phthalocyaninato]-zinc(II)-N^{29}, N^{30}, N^{31}, N^{32} (**15**)

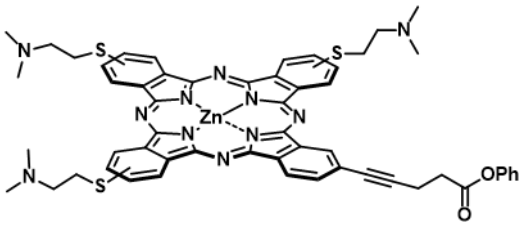

Into a two-necked round-bottomed flask, ZnPc **13** (30.4 mg, 0.030 mmol), $Pd(PPh_3)_2Cl_2$ (6.6 mg, 0.009 mmol), and CuI (8.0 mg, 0.042 mmol) were disolved in THF anhydrous (1.5 mL) and a catalitic ammount of TEA, under argon atmosphere. Subsequently, compound **14** (6.5 mg, 0.037 mmol) was added previously dissolved in 0.5 mL of THF and the reaction mixture was reacted at 80 ^oC for 18 h. The reaction mixture was evaporated and the resulting solid was purified by chromatography column, employing THF/dioxane/TEA (80:20:1). Yield: 3.6 mg, 9%

MS (MALDI, DCTB): *m/z* = 1071.3 [M^+] (100%)

*No spectroscopic measurements has been carried out, due to the low amount of compound obtained and the high aggregation of it,

1.5.3.2. Synthesis of pyridyl-3-oxy substituted ZnPcs

4,5-bis(pyridin-3-yloxy)phthalonitrile (**21**)[53a]

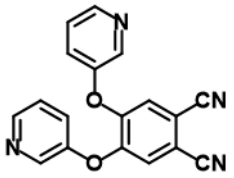

Into a round-bottomed flask 4,5-dichlorophthalonitrile (2.16 g, 10.9 mmol) and 3-pyridynol (2.52 g, 26.5 mmol) were dissolved in 15 mL of freshly distilled DMF under argon atmosphere. Reaction mixture was warmed up to 40 °C and anhydrous potassium carbonate was added in portions (15.0 g, 110 mmol). After 72 hours the reaction is over and was poured into 100 mL and left precipitate at 4 °C. The solid was filtered off and purified by dissolving it in chloroform and adding hot ethanol until appearance of cloudy solution. After the solution is cooled down, the resulting white solid was filtered off. Yield: 2.91 g, 86%.

Mp: > 250 °C.

^{1}H-NMR (300 MHz, $CDCl_3$): δ (ppm) = 8.54 (dd, J_1 = 3.8, J_2 = 2.2 Hz, 2H, H_{Py}), 8.43 (m, 2H, H_{Py}), 7.40 (m, 2H, H_{Py}), 7.39 (m, 2H, H_{Py}), 7.29 (s, 2H, H_{Ar}).

[2,3,9,10,16,17,23,24-octakis(pyridyl-3-oxy)phthalocyaninato]zinc(II)-N^{29}, N^{30}, N^{31}, N^{32} (**22**)[53a]

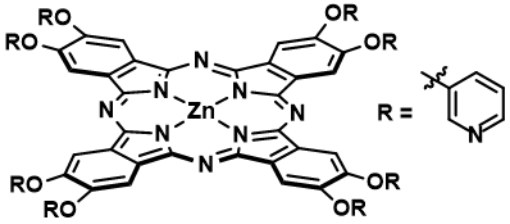

Into a round-bottomed flask equipped with reflux, phthalonitrile **21** (348.2 mg, 1.11 mmol) and anhydrous zinc acetate (107.3 mg, 0.58) were dissolved in dimethylaminoethanol (5 mL) under argon atmosphere and warmed up to 140 °C. After 16 hours the reaction is cooled down to room temperature and poured into water. The green

precipitate was filtered off and washed with acetone and dichloromethane. Yield: 274.3 mg, 75%.

Mp: >250 °C.

^{1}H-NMR (300 MHz, TFA-d): δ (ppm) = 9.60 (s (br), 8H, H_{Pc}), 9.00 (s (br), 8H, H_{Py}), 8.81 (s (br), 8H, H_{Py}), 8.62 (s (br), 8H, H_{Pc}), 8.29 (s (br), 8H, H_{Py}).

UV-Vis (DMSO): λ_{max} (nm) (log ε) = 677 (4.92), 610 (4.15), 361 (4.52).

[2,3,9,10,16,17,23,24-octakis(N-methylpyridinium-3-oxy)phthalocyaninato]zinc(II)-N^{29}, N^{30}, N^{31}, N^{32} tetrasulfate (**16**)

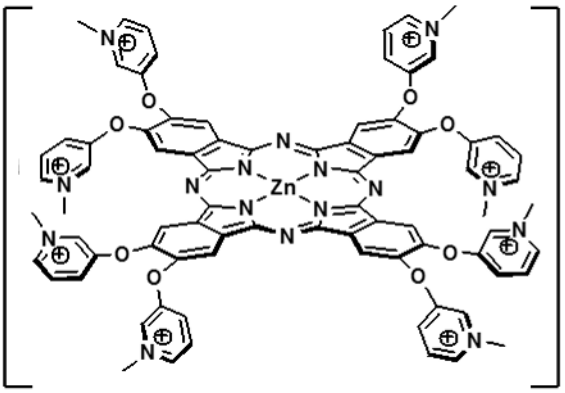

Into a round-bottomed flask ZnPc **22** (100.2 mg, 0.075 mmol) was dissolved in dry DMF (5 mL) and the reaction mixture was warmed up to 120 °C. Then dimethylsulfate (0.2 mL, 2.1 mmol) was added and left reacting overnight. Hot ethanol was added and the resulting green precipitate was filtered off and washed with hot ethanol, ethyl acetate, chloroform, hexane and diethyl ether. Yield: 115.0 mg, 83%.

Mp: >250 °C.

^{1}H-NMR (300 MHz, D_2O): δ (ppm) = 9.19 (s, 8H, H_{Pc}), 9.11 (s, 8H, H_{Py}), 8.80 (d, *J* = 5.9 Hz, 8H, H_{Py}), 8.66 (d, *J* = 6.9 Hz, 8H, H_{Py}), 8.21 (dd, J_1 = 5.9, J_2 = 6.9 Hz, 8H, H_{Py}), 4.51 (s, 24H, CH_3).

UV-Vis (H_2O): λ_{max} (nm) (log ε) = 672 (4.92), 607 (4.13), 350 (4.53).

3-(4-tert-butylphenyl)-5-methoxypyridine (**23**)

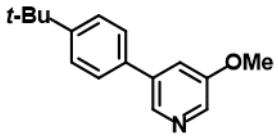

Into a 50 mL two-neck round-bottom flask, equipped with a reflux condenser, 3-bromo-5-methoxypyridine (2.05 g, 10.9 mmol) and 4-(*tert*-butyl)phenylboronic acid (1.90 g, 10.6 mmol) were dissolved in dimethoxyethane under argon atmosphere. Tetrakis(triphenylphosphine)palladium(0) (120 mg, 0.10 mol) was added and the mixture was stirred for 30 min. Previously deoxygenated aqueous potassium carbonate (5 g in 15 mL) was then added and warmed up at 90 ^{o}C for 5 h. After reaction completion, the mixture was dried under vacuum and extracted with diethyl ether and water. The organic phase was separated and the aqueous layer was washed twice more with diethyl ether (2 x 10 mL). the combined organic extracts were dried over anhydrous magnesium sulfate and dried under vacuum. The resulting yellowish solid was purified through column chromatography column, using hexane/ethyl acetate (8:3) as eluent. Yield: 2.30 g, 90%.

Mp: 100 ^{o}C.

^{1}H-NMR (300 MHz, $CDCl_3$): δ (ppm) = 8.47 (d, *J* = 1.8 Hz, 1H; H_{Py}), 8.28 (d, *J* = 2.6 Hz, 1H, H_{Py}), 7.52 (d, *J* = 2.6 Hz, 4H, H_{Ar}), 7.37 (dd, J_1 = 2.6, J_2 = 1.8 Hz, 1H, H_{Py}), 3.91 (s, 3H, CH_3), 1.37 (s, 9H, $C(CH_3)_3$).

^{13}C-NMR (76 MHz, $CDCl_3$): δ (ppm) = 155.8, 151.5, 140.8, 137.3, 135.9, 134.9, 127.1, 126.2, 119.1, 55.7, 34.8, 31.4.

^{13}C-DEPT-135 (76 MHz, $CDCl_3$): δ (ppm) = 140.7, 135.8, 126.9, 126.0, 119.0, 55.6, 31.3.

3-(4-tert-butylphenyl)-5-hydroxypyridine (**24**)

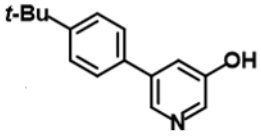

Into a 50 mL round-bottom flask, compound **23** (1.94 g, 8.05 mmol) was dissolved in 7 mL of dichloromethane under argon atmosphere and was cooled down to -78 ^{o}C. A commercial boron tribromide solution (1M, 15 mL, 15.0 mmol) was added dropwise. When the addition was completed, the temperature was raised to room temperature and was the

mixture was left stirring overnight. The reaction was quenched by the addition of saturated sodium bicarbonate. The phases were separated and the aqueous phase was washed with ethyl acetate (3 x 10 mL). The combined organic extracts were dried over anhydrous magnesium sulfate and dried under vacuum. The dark brown solid obtained was purified by crystallization from ethanol. Yield: 1.54g, 84%.

Mp: Decompose 163-165 °C.

^{1}H-NMR (300 MHz, DMSO-d_6): δ (ppm) = 11.5 (s, 1H; OH), 8.68 (s, 1H, H_{Py}), 8.33 (s, 1H, H_{Py}), 8.07 (s, 1H, H_{Py}), 7.73 (d, *J* = 8.2 Hz, 2H, H_{Ar}), 7.58 (d, *J* = 8.4 Hz, 2H, H_{Ar}), 1.33 (s, 9H, $C(CH_3)_3$).

^{13}C-NMR (76 MHz, DMSO-d_6): δ (ppm) = 156.0, 152.3, 139.4, 132.0, 131.3, 129.4, 127.5, 127.0, 126.1, 34.5, 30.9.

4,5-bis(5-tert-butylphenyl-3-pyridyloxy)phthalonitrile (**25**)

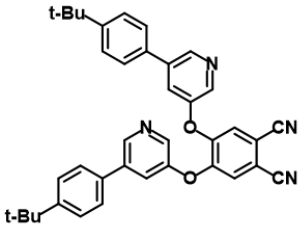

Into a 10 mL round-bottom flask, compound **24** (270.6 mg, 1.19 mmol), 4,5-dichlorophthalonitrile (104.8 mg, 0.532 mmol) and anhydrous potassium carbonate (780 mg, 5.67 mmol) were dissolved into 5 mL of anhydrous DMF. The mixture was reacted in a microwave reactor for 30 min at 125 °C and 100 W. The reaction was followed by TLC using dichloromethane/methanol (20:1) as eluent. The solvent was then evaporated under vacuum, the crude solid was extracted with water/dichloromethane (1:1, 10 mL) and the aqueous phase washed with dichloromethane (2 x 5 mL). The combined organic phases were dried over anhydrous magnesium sulfate and then dried under vacuum. The resulting yellowish solid was dissolved in the minimum amount of hot chloroform and precipitated over hot ethanol. Yield: 194 mg, 76%.

Mp: 223-224 °C.

^{1}H NMR (300 MHz, DMSO-d_6): δ (ppm) = 8.70 (d, *J* = 1.6 Hz, 2H, H_{Py}), 8.41 (d, *J* = 2.6 Hz, 2H, H_{Py}), 8.17 (s, 2H, H_{Ar}), 7.83 (m, 2H, H_{Py}), 7.61 (d, *J* = 8.4 Hz, 4H, H_{Ar}), 7.46 (d, *J* = 8.4 Hz, 4H, H_{Ar}), 1.31 (s, 9H, $C(CH_3)_3$).

^{13}C-NMR (76 MHz, DMSO-d_6): δ (ppm) = 152.2, 151.1, 150.3, 143.6, 138.8, 136.9, 133.0, 126.9, 126.7, 125.8, 122.7, 122.3, 111.9, 34.3, 30.9.
^{13}C-DEPT-135 (76 MHz, DMSO-d_6): δ (ppm) = 143.3, 138.8, 126.6, 126.4, 125.5, 122.5, 30.7.

[2,3,9,10,17,18,23,24-octakis- (5-tert-butylphenyl-3-pyridyloxy)phthalocyaninato]zinc(II)-N^{29}, N^{30}, N^{31}, N^{32} (**26**)

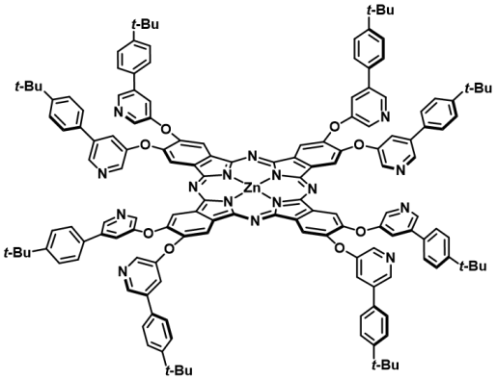

Into a 25 mL round-bottom flask, phthalonitrile **25** (194.4 mg, 0.406 mmol) and anhydrous zinc acetate (30.3 mg, 0,165 mmol) were dissolved in 5 mL of dimethylaminoethanol (DMAE) under argon atmosphere and warmed up to 140 °C overnight. The resulting green solution was poured into a mixture water/methanol (1:1), forming a green precipitate that was filtered off through celite and washed with acetone and diethyl ether. This solid was extracted with THF, leading to a green solid product. Yield: 132.5 mg, 66%.
Mp: >250 °C
^{1}H-NMR (300 MHz, $CDCl_3$ (TFA 5%)): δ (ppm) = 9.38 (s, 8H, H_{Pc}), 8.83 (s, 8H, H_{Py}), 8.73 (s, 8H, H_{Py}), 8.46 (s, 8H, H_{Py}), 7.53 (m, 32H, H_{Ar}), 1.30 (s, 72H; $C(CH_3)_3$).
UV-Vis (THF): λ_{max} (log ε) = 674 (5.43), 608 (4.64), 357 (5.01).
MS (MALDI, DCTB): *m/z* (%) = 2154.9 [M-$C_{15}H_{16}NO$]$^+$ (1), 2379.0 [M^+] (100), 4534.0 [2M-$C_{15}H_{16}NO$]$^+$ (1), 4759.2 [2M]$^+$ (71).
HRMS (MALDI, DCTB) *m/z*: [M]$^+$ calcd for $C_{152}H_{136}N_{16}O_8Zn$, 2377.0013; found, 2377.0071.

General procedure for the synthesis of ZnPcs **27** - **29**:

Into a 25 mL round-bottom flask, phthalonitrile **25** (623.7 mg, 1.08 mmol), 1,2-dicyanobenzene (133.3 mg, 1.04 mmol) and anhydrous zinc acetate (156.0 mg, 0.85 mmol) were dissolved in 5 mL of DMAE under argon atmosphere and subsequently warmed up at 140 °C overnight. The reaction mixture was dried under vacuum, dissolved in 5 mL of THF, precipitated in 100 mL of methanol/water (1:1), and filtered over celite. The obtained blue solid was purified by column chromatography using a toluene/dioxane/pyridine (80:19:1) mixture as eluent. Different fractions were collected and further characterized as **29**, **28**, and **27** in elution order. Yields: **27**: 201.8 mg, 29%. **28**: 139.6 mg, 18%. **29**: 98.2 mg, 28%.

[2,3,9,10,17,18-Hexakis(5-tert-butylphenyl-3-pyridyloxy)phthalocyaninato]zinc(II)-N^{29}, N^{30}, N^{31}, N^{32} (**27**)

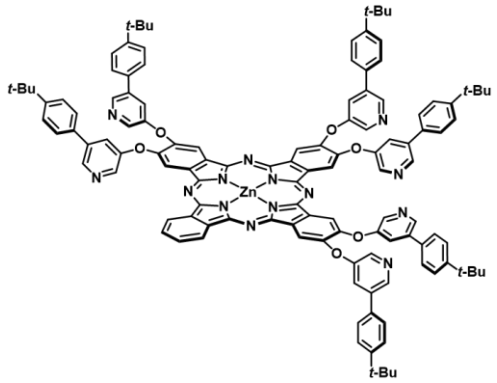

Mp: >250 °C.

^{1}H-NMR (300 MHz, $CDCl_3$ (TFA 5%)): δ (ppm) = 9.45 (s, 2H, H_{Pc}), 9.38 (s, 2H, H_{Pc}), 9.35 (s, 2H, H_{Pc}), 9.34 (m, 2H, H_{Pc}) 8.83 (m, 6H, H_{Py}), 8.56 (s, 2H, H_{Py}), 8.50 (s, 2H, H_{Py}), 8.47 (s, 2H, H_{Py}), 8.92 (m, 4H, H_{Py}), 8.72 (m, 2H, H_{Py}), 8.27 (s, 2H, H_{Pc}), 7.59 (m, 24H, H_{Ar}), 1.32 (s, 18H; $C(CH_3)_3$), 1.31 (s, 18H; $C(CH_3)_3$) 1.30 (s, 18H; $C(CH_3)_3$).

UV-Vis (THF): λ_{max} (log ε) = 672 (5.45), 606 (4.68), 354 (5.07).

MS (MALDI, DCTB): *m/z* (%) = 1478.5 $[M-(C_{15}H_{16}NO)_2]^+$ (3), 1928.7 $[M^+]$ (100), , 3408.6 $[2M-(C_{15}H_{16}NO)_2]^+$ (1), 3859.2 $[2M]^+$ (48).

HRMS (MALDI, DCTB) *m/z*: $[M]^+$ calcd for $C_{122}H_{106}N_{14}O_6Zn$, 1926.7706; found, 1926.7711.

[2,3,9,10,(17,18)-Tetrakis(5-tert-butylphenyl-3-pyridyloxy) phthalocyaninato]zinc(II)-N^{29}, N^{30}, N^{31}, N^{32} (**28**)

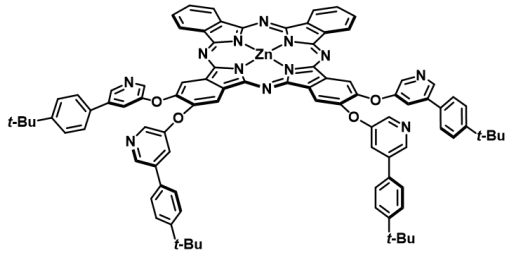

Mp: >250 °C.

^{1}H-NMR (300 MHz, $CDCl_3$ (TFA 5%)): δ (ppm) = 9.43-9.29 (m, 8H, H_{Pc}), 8.90 (m, 4H, H_{Py}), 8.82 (m, 4H, H_{Py}), 8.72 (s, 2H, H_{Py}), 8.56 (s, 2H, H_{Py}), 8.29 (m, 4H, H_{Pc}), 7.59 (m, 16H, H_{Ar}), 1.31 (m, 36H, $C(CH_3)_3$).

UV-Vis (THF): λ_{max} (log ε) = 670 (5.32), 605 (4.34), 351 (4.81).

MS (MALDI, DCTB) *m/z* (%): 1478.5 $[M^+]$ (100), 2958.1 $[2M]^+$ (18), 4437.7 $[3M]^+$ (2).

HRMS (MALDI, DCTB) *m/z*: $[M]^+$ calcd for $C_{92}H7_6N_{12}O_4Zn$, 1476.5398; found, 1476.5387.

[2,3-Bis(5-tert-butylphenyl-3-pyridyloxy) phthalocyaninato]zinc(II)-N^{29}, N^{30}, N^{31}, N^{32} (**29**)

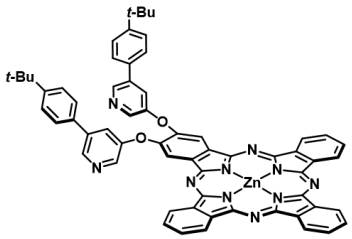

Mp: >250 °C.

^{1}H-NMR (300 MHz, $CDCl_3$ (TFA 5%)): δ (ppm) = 9.44-9.26 (m, 8H, H_{Pc}), 8.92 (m, 2H, H_{Py}), 8.60 (m, 4H, H_{Py}), 8.30 (m, 4H, H_{Pc}), 7,88 (s, 2H, H_{Py}), 7.59 (m, 8H, H_{Ar}), 1.32 (s, 18H, $C(CH_3)_3$).

UV-Vis (THF): λ_{max} (log ε) = 669 (5.12), 603 (4.00), 347 nm (4.57).

MS (MALDI, DCTB) *m/z* (%): 1026.3 $[M^+]$ (100), 2056.5 $[2M]^+$ (5).

HRMS (MALDI, DCTB) *m/z*: $[M]^+$ calcd for $C_{62}H_{46}N_{10}O_2Zn$, 1026.3091; found, 1026.3093.

[2,3,9,10,17,18,23,24-octakis(5-tert-butylphenyl-1-methyl-3-pyridiniumoxy)-phthalocyaninato]zinc(II)-N^{29}, N^{30}, N^{31}, N^{32}, tetrasulfate (**17**)

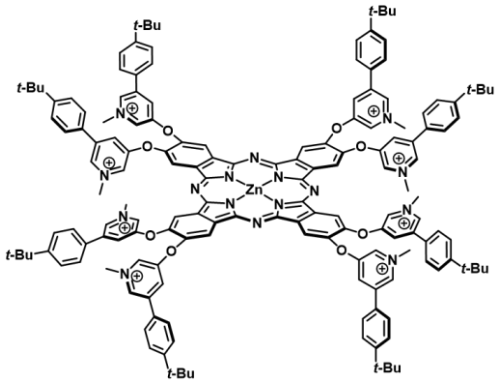

Into a 50 mL two-neck round-bottom flask, compound **26** (95.3 mg, 0.04 mmol) was dissolved in 5 mL of anhydrous DMF and warmed up to 120 °C. Dimethyl sulfate (0.1 mL, 1.1 mmol) was then added. After 24 hours, 10 mL of water were added and the solvent was dried under vacuum. The green solid was solubilized in the minimum amount of hot methanol, precipitated with water and isolated by centrifugation. Yield: 93.2 mg, 80%.

Mp: >250 °C.

^{1}H-NMR (300 MHz, DMSO-d_6): δ (ppm) = 9.53 (s, 8H, H_{Pc}), 9.27 (s, 8H, H_{Py}), 9.23 (s, 8H, H_{Py}), 8.88 (s, 8H, H_{Py}), 7.79 (d, *J* = 8.0 Hz, 16H, H_{Ar}), 7.50 (d, *J* = 8.0 Hz, 16H, H_{Ar}), 4.40 (s, 24H, CH_3), 1.25 (s, 56H, $C(CH_3)_3$).

UV-Vis (methanol/water (1:9)): λ_{max} (nm) (log ε) = 677 (4.84), 640 (4.53), 335 (4.80).

General procedure for the quaternarization of asymmetrically substituted ZnPcs:

Into a 50 mL two-neck round-bottom flask, the corresponding ZnPc precursor was dissolved in 5 mL of anhydrous DMF and warmed up to 120 °C. Dimethylsulfate (30 eq.) was then added. After 24 hours, 10 mL of water were added and the solvent was dried under vacuum. The resulting solid residue was dissolved in hot methanol and precipitated with water. The green precipitate was isolated by centrifugation.

[2,3,9,10,17,18-hexakis(5-tert-butylphenyl-1-methyl-3-pyridiniumoxy)-phthalocyaninato]zinc(II)-N^{29}, N^{30}, N^{31}, N^{32}, trisulfate (**18**)

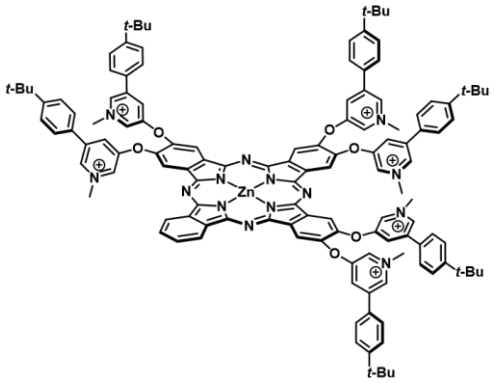

ZnPc **27** (103.2 mg, 0.053 mmol) was used as the starting material. Yield: 78.3 mg, 64%.

Mp: >250 °C.

^{1}H-NMR (300 MHz, DMSO-d_6): δ (ppm) = 9.55 (s, 6H, H_{Py}), 9.40 (s, 2H, H_{Pc}), 9.30 (s, 6H, H_{Py}), 9.27 (s, 6H, H_{Pc}), 8.97 (s, 3H, H_{Py}), 8.90 (s, 3H, H_{Py}), 8.28 (m, 2H, H_{Pc}), 7.83 (m, 12H, H_{Ar}), 7.54 (m, 12H, H_{Ar}), 4.44 (s, 6H; CH_3), 4.41(s, 12H, CH_3), 1.27 (s, 54H, $C(CH_3)_3$).

UV-Vis (methanol/water (1:9)): λ_{max} (nm) (log ε) = 682 (4.72), 634 (4.64), 336 (4.84).

[2,3,9,10,(17,18)-tetrakis(5-tert-butylphenyl-1-methyl-3-pyridiniumoxy) phthalocyaninato]zinc(II)-N^{29}, N^{30}, N^{31}, N^{32}, disulfate (**19**)

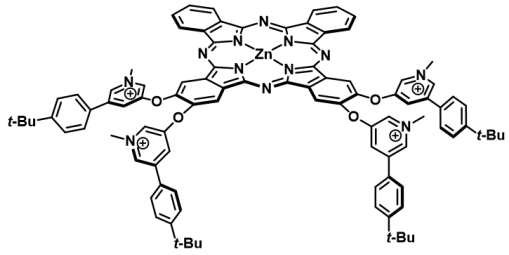

ZnPc **28** (78.2 mg, 0.053 mmol) was used as the starting material. Yield: 35.0 mg, 38%.

Mp: >250 °C.

^{1}H-NMR (300 MHz, DMSO-d_6): δ (ppm) = 9.26 (m, 12H, H_{Py}), 8.95 (s, 2H, H_{Pc}), 8.85 (s, 1H, H_{Pc}), 8.26 (s, 3H, H_{Pc}), 7.81 (m, 18H, H_{Ar}), 7.55 (m, 12H, H_{Ar}), 4.44 (m, 12H; CH_3), 1.27 (m, 36H; $C(CH_3)_3$).
UV-Vis (methanol/water (1:9)): λ_{max} (nm) (log ε) = 681 (4.63), 637 (4.53), 329 (4.76).

[2,3-bis(5-tert-butylphenyl-1-methyl-3-pyridiniumoxy)phthalocyaninato]zinc(II)-N^{29}, N^{30}, N^{31}, N^{32}, sulfate (**20**)

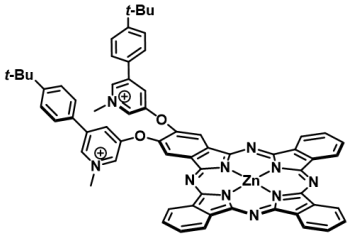

ZnPc **29** (16.8 mg, 0.016 mmol) was used as the starting material. Yield: 11.9 mg, 64%.
Mp: >250 °C.
^{1}H-NMR (300 MHz, DMSO-d_6): δ (ppm) = 9.48 (m, 6H, H_{Pc}), 9.37 (m, 2H, H_{Pc}), 9.34 (s, 2H, H_{Pc}), 9.28 (s, 2H, H_{Py}), 8.96 (s, 2H, H_{Py}), 8.27 (m, 6H, H_{Pc}), 7.83 (d, 4H, *J* = 8.5 Hz, H_{Ar}), 7.54 (d, 4H, *J* = 8.5 Hz, H_{Ar}), 4.45 (s, 6H, CH_3), 1.27 (s, 18H, $C(CH_3)_3$).
UV-Vis (methanol/water (1:9)): λ_{max} (nm) (log ε) = 680 (4.31), 636 (4.26), 331 (4.45).
MS (ESI^+) *m/z* (%): 528.2 [M^{2+}] (100).

[2,3,9,10,17,18,23,24-octakis(5-tert-butylphenyl-1-[2-(2-(2-methoxyethoxy)ethoxy)ethyl]-3-pyridiniumoxy)-phthalocyaninato]zinc(II)-N^{29}, N^{30}, N^{31}, N^{32}, octaiodine (**30**)

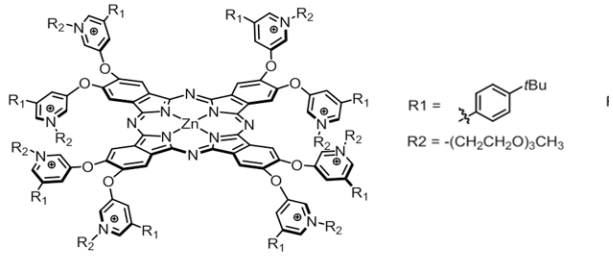

In a 10 mL sealed tube, ZnPc **26** (30.1 mg, 12.6 µmol) was dissolved in 2-[2-(2-methoxyethoxy)ethoxy]ethyl iodide[162] (1.0 g, 3.65 mmol) and warmed up to 80 °C for 6

days under argon atmosphere. The reaction mixture was then poured in hexane. The obtained precipitate was filtered through cellite and collected with THF. After evaporation of the solvent under reduced pressure, the resultant solid was purified by size exclusion chromatography (Sephadex®) using THF as eluent. The product was obtained as a green solid. Yield: 49.5 mg, 84%.

Mp: 182-184 ^{o}C.

^{1}H-NMR (500 MHz, DMSO-d_6): δ (ppm) = 9.50 (s, 8H, H_{Pc}), 9.30 (s, 8H, H_{Py}), 9.25 (s, 8H, H_{Py}), 8.93 (s, 8H, H_{Py}), 7.78 (d, *J* = 8.4 Hz, 16H, H_{Ar}), 7.50 (d, *J* = 8.4 Hz, 16H, H_{Ar}), 4.84 (s (br), 16H, CH_2), 3.96 (s(br),16H, CH_2), 3.56 (m, 16H, CH_2), 3.42 (m, 16H, CH_2), 3.30 (m, 16H, CH_2), 3.17 (m, 16H, CH_2), 3.02 (s, 24H, CH_3), 1.25 (s, 56H, $C(CH_3)_3$).

^{13}C-NMR (126 MHz, DMSO-d_6): δ (ppm) = 156.9, 153.9, 153.3, 147.2, 141.3, 139.3, 138.0, 137.4, 134.6, 134.5, 133.8, 130.1, 130.0, 128.4, 128.0, 126.6, 125.9, 117.4, 71.5, 70.1, 70.0, 69.9, 69.0, 61.4, 58.4, 35.01, 31.28.

UV-Vis (DMSO): λ_{max} (nm) (log ε) = 679 (5.23), 657 (4.62), 614 (4.42), 335 (4.81).

HRMS (ESI^{+}): *m/z* = $[M+I]^{7+}$ calc. for $[C_{208}H_{256}N_{16}O_{32}ZnI]$ = 525.9609, found; 525.9700. $[M+2I]^{6+}$ calc. for $[C_{208}H_{256}N_{16}O_{32}ZnI_2]$ = 634.7712, found; 634.7778. $[M+3I]^{5+}$ calc. for $[C_{208}H_{256}N_{16}O_{32}ZnI_3]$ = 787.1064, found; 787.1095. $[M+4I]^{4+}$ calc. for $[C_{208}H_{256}N_{16}O_{32}ZnI_2]$ = 1015.3576, found; 1015.3579.

1.5.3.3. Synthesis of pyrene-pyridyl-3-oxy substituted ZnPc

1-pyrenylboronic acid pinacol ester (**33**)

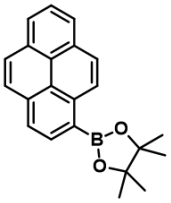

Into a round-bottomed flask 1-pyrenylboronic acid (1.94 g, 7.88 mmol) and pynacol (2.84 g, 24.00 mmol) were placed and dissolved in 10 mL of THF and 40 mL of diethylether and was warmed up to reflux. After 3 hours reaction mixture was dried under reduced pressure and purified by chromatography column, using heptane/ethylacetate (20:1) as eluent. Product was obtained as a white solid. Yield: 2.39 g, 92%.

Mp: 120 ^{o}C.

^{1}H-NMR (300 MHz, DMSO-d_6): δ (ppm) = 8.97 (d, *J* = 9.2 Hz, 1H, H_{Ar}), 8.45 (d, *J* = 7.7 Hz, 1H, H_{Ar}), 8.32 (d, *J* = 7.7 Hz, 2H, H_{Ar}), 8.27-8.23 (m, 3H, H_{Ar}), 8.18 (d, *J* = 8.9 Hz, 1H, H_{Ar}), 8.08 (t, *J* = 7.6 Hz, 1H, H_{Ar}), 1.43 (s, 12H, CH_3).

^{13}C-RMN (76 MHz, DMSO-d_6): δ (ppm) = 135.6, 133.7, 132.9, 130.6, 130.1, 128.7, 127.8, 127.4, 126.2, 125.6, 124.2, 123.7, 123.6, 83.8, 24.8.

3-hydroxy-5-(1-pyrenyl)pyridine (**34**)

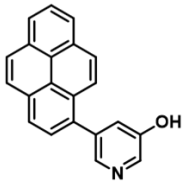

Into a round-bottomed flask **33** (2.39 g, 7.27 mmol) and 3-bromo-5-hydroxypyridine (1.24 g, 7.10 mmol) was dissolved in 90 mL of 1,4-dioxane under argon atmosphere. Pd(dppf)Cl_2·CH_2Cl_2 (340 mg, 0.42 mmol) was then dissolved and 80 mL of previously deoxygenated aqueous sodium carbonate (2.4 M) was added. Reaction mixture was warmed up to 100 ^{o}C for 4 hours. After cooling down, both phases were separated and the aqueous was washed with THF (3x10 mL). Combined organic phases were dried over anhydrous Mg_2SO_4 and dried under reduced pressure. Solid residue was purified by

chromatography column, using hexane/ethyl acetate (3:2) as eluent. Product was obtained as a white solid. Yield: 1.28 g, 61%.

Mp: >250 °C.

^{1}H-NMR (300 MHz, DMSO-d_6): δ (ppm) = 10.23 (s, 1H, OH), 8.39 (d, *J* = 7.9 Hz, 1H, H_{Ar}), 8.36 (d, *J* = 6.9 Hz, 1H, H_{Ar}), 8.32 (d, *J* = 7.8 Hz, 1H, H_{Ar}), 8.29 (d, *J* = 4.3, 1H, H_{Py}), 8.29 (d, *J* = 4.2, 1H, H_{Py}), 8.26 (s, 2H), 8.22 (d, *J* = 9.4 Hz, 1H), 8.13 (d, *J* = 7.6 Hz, 1H), 8.08 (d, J = 6.9 Hz, 1H, H_{Ar}), 8.04 (d, J = 7.4 Hz, 1H, H_{Ar}), 7.40 (t, J = 4.3 Hz, 1H, H_{Py}).

*Furthermore characterization was not possible to conduct due to solubility issues.

4-(5-(1-pyrenyl)pyridin-3-yloxy) phthalonitrile (**35**)

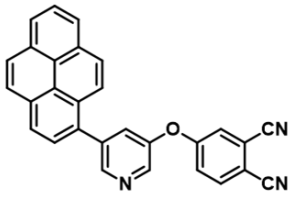

Into a round-bottomed flask **34** (493.8 mg, 1.67 mmol) and 4-nitrophthalonitrile (323.1 mg, 1.87 mmol) were dissolved in DMF (20 mL) under argon atmosphere. Anhydrous potassium carbonate (1.0 g, 7.24 mmol) was then added in portions and was stirred at room temperature for 8 hours. The reaction was poured over water-ice mixture and the precipitate was filtered off and purified by crystallization hot ethanol. Product was obtained as a white solid. Yield: 612.4 mg, 87%.

Mp: 92 °C.

^{1}H-NMR (300 MHz, DMSO-d_6): δ (ppm) = 8.77 (s (br), 1H, H_{Py}), 8.66 (d, *J* = 2.5 Hz, 1H, H_{Py}), 8.38 (d, *J* = 8.0 Hz, 1H, H_{Ar}), 8.34 (d, *J* = 7.9 Hz, 1H H_{Ar}), 8.30 (d, *J* = 7.9 Hz, 1H, H_{Ar}), 8.23 (s, 2H), 8.21 (d, *J* = 9.3 Hz, 1H, H_{Ar}), 8.17-8.01 (m, 5H, H_{Ar}), 7.96 (s (br), 1H, H_{Py}), 7.67 (dd, J_1 = 8.7 Hz, J_2 = 2.4 Hz, 1H, H_{Ar}).

^{13}C-RMN (76 MHz, DMSO-d_6): δ (ppm) = 160.4, 150.8, 147.4, 140.9, 137.6, 136.3, 131.9, 130.8, 130.3, 129.1, 128.3, 128, 127.9, 127.2, 126.5, 125.7, 125.3, 124.9, 124.1, 124, 123.8, 123.1, 122.8, 116.8, 115.8, 115.3, 108.9.

^{13}C-DEPT-135: (76 MHz, DMSO-d_6): δ (ppm) =147.4, 140.9, 136.3, 129.1, 128.3, 127.9, 127.2, 126.5.

[2,(3),9,(10),16,(17),23,(24)-tetrakis-(5-(1-pyrenyl)pyridin-3-yloxy) phthalocyaninato]-zinc(II)-N^{29}, N^{30}, N^{31}, N^{32} (**36**)

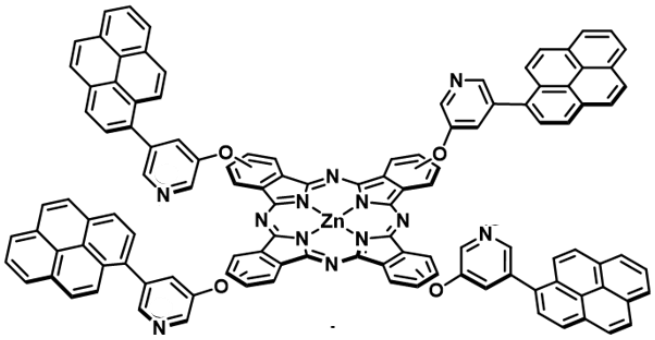

Into a sealed tube phthalonitrile **35** (346 mg, 0.82 mmol) and anhydrous zinc acetate (75 mg, 0.41 mmol) were dissolved in dimethylaminoethanol (5 mL) under argon atmosphere. Reaction was warmed up to 150 ^{o}C for 24 hours. Reaction mixture was poured over water/methanol (1:1) mixture and the blue precipitate was filtered off. Green solid was purified by chromatography column using toluene/1,4-dioxane/pyridine (40:10:1) as eluent. Product was obtained as a green solid (162 mg, 45%).

Mp: > 250 ^{o}C

^{1}H-NMR (300 MHz, THF-d_8 (TFA (5%)): δ (ppm) = 12.39 (TFA), 9.2-7.6 (m).*

UV-Vis (THF): λ_{max} (nm) (log ε) = 673 (5.24), 608 (4.48), 346 (5.16).

MS (MALDI-TOF, DCTB): *m/z* (%) = 1750.4 [M^+] (100), 3500.9 [$2M^+$] (4).

HRMS (MALDI-TOF, DCTB+PPGNa2000) m/z: exp. Mass = 1748.4179 calc. Mass = 1748.4146.

*Due to extremely low solubility and regioisomeric mixture characterization by NMR spectroscopy was imposible to determine.

[2,(3),9,(10),16,(17),23,(24)-tetrakis- (N-methyl-5-(1-pyrenyl)pyridinium-3-yloxy)phthalocyaninato]zinc(II)-N^{29}, N^{30}, N^{31}, N^{32}, tetraiodine (**31**)

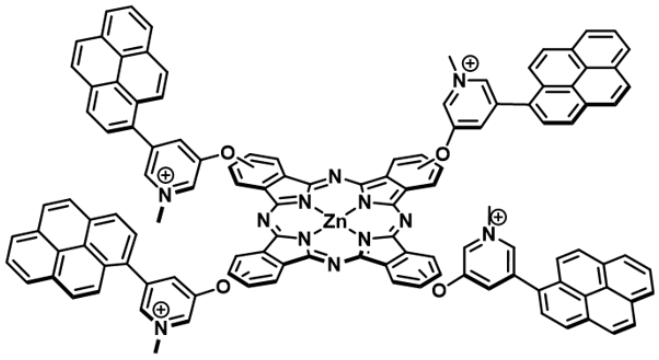

Into a sealed tube ZnPc **36** (58 mg, 33 µmol) was dissolved in DMF (2 mL) under argon atmosphere and methyliodide (0.15 mL, 2.4 mmol) was added and warmed up to 130 ^{o}C. After 10 hours reaction mixture was poured onto diethyl ether. Resulting precipitate was isolated by centrifugation and washed with diethyl ether (3x5 mL), water (3x5 mL) and acetone (1x5 mL). Product was obtained as a green solid. Yield: 42.2 mg, 55%.

Mp: > 250 ^{o}C

^{1}H-NMR (500 MHz, DMSO-d_6): δ (ppm)* = 9.59 (m, 4H, H_{Pc}), 9.50 (m, 8H, H_{Py}+H_{Pc}), 9.40 (2s, 4H, H_{Py}), 9.04 – 8.86 (4s (br), 4H, H_{Py}), 8.51 – 8.42 (m, 4H, H_{Ar}), 8.42 – 7.91 (m, 36H, H_{Ar}+H_{Pc}), 4.59 (2s, 12H).

^{13}C-DEPT-135 (126 MHz,DMSO-d_6): δ (ppm)** = 142.4, 136.2, 135.4, 129.2, 127.6, 127.1, 126.6, 125.9, 125.5, 124.1, 113.9, 49.0.

UV-Vis (DMSO): λ_{max} (nm) (log ε) = 679 nm (5.20), 611 nm (4.44), 348 nm (5.00).

MS (ESI^{+}, methanol) = 452.13 $[M]^{+4}$ (100).

*Multiplicity of the multiplets is given by regioisomers mixture.

**Due to low solubility and regioisomeric mixture ^{13}C-NMR characterization was impossible to determine.

4-(pyridin-3-yloxy)phthalonitrile (**37**)

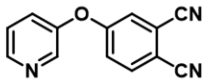

Into a round-bottomed flask 3-hydroxypyridine (1.47 g, 15.4 mmol) and 4-nitrophthalonitrile (2.04 g, 11.8 mmol) were dissolved into 30 mL of dry DMF under argon atmosphere. Anhydrous K_2CO_3 (16 g, 116 mmol) was added in portions and left for 72 hours at room temperature. Reaction mixture was poured over water and resulting precipitate was filtered off and purified by recrystallization in hot ethanol, resulting in a crystalline white solid. Yield: 2.42 g, 93%.

Mp: 120 °C

^{1}H-NMR (300 MHz, DMSO-d_6): δ (ppm) = 7.28 (d, *J* = 2.6 Hz, 1H, H_{Py}), 7.34-7.31 (m, 1H, H_{Py}), 7.46-7.41 (m, 2H, H_{Ar}), 7.80-7.74 (m, 1H, H_{Ar}), 8.48 (t, J=1.8 Hz, 1H, H_{Py}), 8.60 (t, J=3.1 Hz, 1H, H_{Py}).

[2,(3),9,(10),16,(17),23,(24)-tetrakis(pyridyl-3-oxy)phthalocyaninato]zinc(II)-N^{29}, N^{30}, N^{31}, N^{32} (**38**)

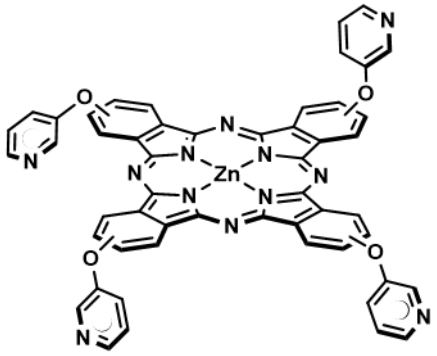

Into a round-bottomed flask phthalonitrile **18** (1.23 g, 5.54 mmol) and anhydrous zinc acetate (0.54 g, 2.94 mmol) were dissolved in dimethylaminoethanol (5 mL) under argon atmosphere and the solution was warmed up to 140 °C overnight. Reaction mixture was poured over water/methanol (1:1) mixture and the blue precipitate was filtered off. Green solid was purified by hot methanol washing, resulting in a green solid. Yield: 1.2 g, 92%.

Mp: >250 °C.

^{1}H NMR (300 MHz, DMSO-d_6 (TFA 10%)): δ ppm = 9.17-9.13 (m, 4H, H_{Py}), 8.93-8.70 (m, 9H, H_{Pc}), 8.10-8.20 (m, 4H, H_{Pc}), 8.55-8.60 (m, 8H), 7.89-7.95 (m, 4H, H_{Py}).

UV-Vis (THF): λ_{max} (nm) (log ε) = 672 (5.05), 607 (4.34), 351 (4.69).

[2,(3),9,(10),16,(17),23,(24)-tetrakis(N-methylpyridynium-3-oxy)phthalocyaninato]zinc(II)-N^{29}, N^{30}, N^{31}, N^{32} (**32**)

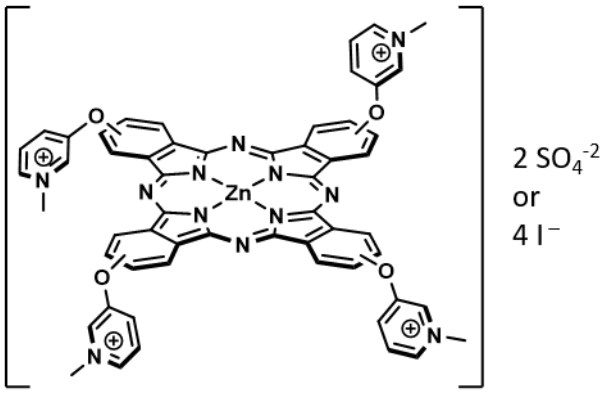

Into a sealed tube ZnPc **38** (309.4 mg, 326 µmol) was dissolved in DMF (7 mL) under argon atmosphere and iodomethane (0.12 mL, 1.93 mmol) was added and warmed up to 130 °C. After 10 hours reaction mixture was poured onto diethyl ether. Resulting precipitate was isolated by centrifugation and washed with diethyl ether (3x25 mL) and acetone (3x15 mL). Product was obtained as a deep blue solid. Yield: 385.1 mg, 82%.

Mp: > 250 °C

^{1}H-NMR (300 MHz, DMSO-d_6): δ (ppm) = 9.38 (s (br), 4H, H_{Py}), 9.34 – 9.18 (m, 4H, H_{Pc}), 8.97 (m, 8H, H_{Pc}+H_{Py}), 8.67 (t (br), J = 9.7 Hz, 4H, H_{Py}), 8.41 – 8.24 (m, 4H, H_{Py}), 8.17 – 8.04 (m, 4H, H_{Pc}), 4.51 (s, 12H, CH_3).

^{13}C-NMR (76 MHz,DMSO-d_6): δ (ppm) = 156.2, 156.2, 151.6, 140.9, 139.7, 139.6, 137.3, 137.3, 134.9, 134.7, 134.0, 129.0, 124.6, 121.5, 113.0, 54.4, 54.4, 54.3.

UV-Vis (DMSO): λ_{max} (nm) (log) = 677 (5.12), 610 (4.38), 349 (4.65).

Chapter II: Phthalocyanine Biohybrid Materials as Singlet Oxygen Generation Platforms

2. Chapter II: ZnPc biohybrid materials as singlet oxygen generation platform

2.1. Introduction

2.1.1. **Phthalocyanine-based biohybrid materials**

One of the most appealing possibilities of uses of Pcs is as biohybrid materials for different biomedical applications. This strategy consist in the incorporation of Pcs into the various available biological nanostructures. In the following paragraphs we summarize and discuss the most relevant Pc-based biohybrid materials developed up to now.

(i) Pc-Protein

i. Pc-peptide

Covalently linked Pc-peptide photodynamic agents have been synthesized taking advantage of mild synthetic organic methodologies such as Pd-catalized cross coupling,[171] via "click-chemistry"[172] or solid-phase conjugation.[173] Hydrophylic and hydrophobic Pcs have been conjugated to selected peptides, varying the formulation of the PS. In particular, M.-R. Ke *et al.* synthesized amphiphilic moieties where the presence of the targeting peptide enhances the PDT effect by increasing the cellular uptake both in vitro and *in vivo* experiments.[172a,b]

Supramolecular conjugation also takes place in self-assembled peptide nanofibers,[174] vesicles,[175] or thin-films,[176] being the latest employed as biosensors. A remarkable example

---

[171] a) H. Ali, S. Ait-Mohand, S. Gosselin, J.E. van Lier and B. Guérin, *J. Org. Chem.*, **2011**, *76*, 1887-1890. b) E. Ranyuk, N. Cauchon, K. Klarskov, B. Guerin and J.E. van Lier, *J. Med. Chem.*, **2013**, *56*, 1520-1534.

[172] a) M. Mudyiwa, M.W. Ndinguri, S.A. Soper and R.P. Hammer, *J. Porphyrins Phthalocyanines*, **2010**, *14*, 891-903. b) M.-R. Ke, S.-L. Yeung, W.-P. Fong, D.K.P. Ng and P.-C. Lo, *Chem. Eur. J.*, **2012**, *18*, 4225-4233. c) M.-R. Ke, D.K.P. Ng and P.-C. Lo, *Chem. Asian J.*, **2014**, *9*, 554-561.

[173] a) M. Sibrian-Vazquez, J. Ortiz, I.V. Nesterova, F. Fernández-Lázaro, A. Sastre-Santos, S.A. Soper and M.G.H. Vicente, *Bioconjugate Chem.*, **2007**, *18*, 410-420. b) B.G. Ongarora, K.R. Fontenot, X. H, I. Sehgal, S.D. Satyanarayana-Jois and M.G.H. Vicente, *J. Med. Chem.*, **2012**, *55*, 3725-3738.

[174] a) X. Mao, C. Wang, X. Ma, M. Zang, L. Liu, L. Zhang, L. Niu, Q. Zeng, Y. Yang and C. Wang, *Nanoscale*, **2011**, *3*, 1592-1599. b) R. Garifullin, T.S. Erkal, S. Tekin, B. Ortaç, A.G. Gürek, V. Ahsen, H.G. Yaglioglu, A. Elmali and M.O. Guler, *J. Mater. Chem.*, **2012**, *22*, 2553-2559.

[175] A.J. van Hell, M.M. Fretz, D.J.A. Crommelin, W.E. Hennik and E. Mastrobattista, *J. Control. Release*¸**2010**, *141*, 347-353.

of *in vitro* Pc-polypeptide binding has been reported by S. Tabassum *et al.*,[177] where an octacarboxylic ZnPc sodium salt recognizes and inhibits growth of amyloid β, a polypeptide deposited as fibrils in Alzheimer's disease brain cells, opening new possibilities to face this disease.

ii. Pc-antibody systems

Conjugation of antibodies (Abs) with chromophores have raised a completely new field called photoinmunotherapy (PIT). This moieties has been described from 90's decade as a potential targeting molecule with high affinity for selected cells.[178] First example of this application was reported by M. Carcenac *et al.*,[179] describing an enhanced PDT effect of alluminum phthalocyanines (AlPcs) antibody conjugates. Since them, only few examples of directly bounded Pc-antibody has been reported,[180] in favour of ternary higher structures that combine more than two therapeutical moieties. Surprisingly, Pc-Ab moieties have become of growing interest since Dr. H. Kobayashi research group describe deep tumoral penetration and fluorescence *in vivo* imaging of a SiPc-Ab (Figure 39) that presents localized photothermal effect dominating over singlet oxygen generation.[181,182]

---

[176] M.F. Zampa, I.M.S. Araujo, J.R.S. dos Santos Junior, V. Zucolotto, J.R.S.A. Leite and C. Eiras, *Int. J. Anal. Chem.*, **2012**, *2012*,1-7.

[177] S. Tabassum, A.M. Sheikh, S. Yano, T. Ikeue, M. Handa and A. Nagai, *FEBS J.*, **2015**, *282*, 463-476.

[178] A.P. Savitsky, K.V. Lopatin, N.A. Golubeva, M.Yu. Poroshina, E.B. Chernyaeva, N.V. Stepanova, L.I. Solovieva and E.A. Lukyanets, *J. Photochem. Photobiol. B*, **1992**, *13*, 327-333.

[179] a) M. carcenac, C. Larroque, R. Langlois, J.E. van Lier, J.-C. Artus and A. Pelegrin, *Photochem. Photobiol.*, **1999**, *70*, 930-936. b) M. Carcenac, M. Dorvillius, V. Garambois, F. Glaussel, Ch. Larroque, R. Langlois, N.E. Hynes, J.E. van Lier and A. Pelegrin, *Brit. J. Cancer*, **2001**, *85*, 1787-1793.

[180] a) M.B. Vrouenraets, G.W.M. Visser, M. Stigter, H. Oppelaar, G.B. Snow and G.A.M.S. van Dongen, *Cancer Res.*, **2001**, *61*, 1970-1975. b) M.B. Vrouenraets, G.W.M. Visser, M. Stigter, H. Oppelaar, G.B. Snow and G.A.M.S. van Dongen, *Int. J. Cancer*, **2002**, *98*, 793-798.

[181] M. Mitsunaga, M. Ogawa, N. Kosaka, L.T. Rosenblum, P.L Choyke and H. Kobayashi, *Nature Med.*, **2011**, *17*, 1685-1691.

[182] a) M. Mitsunaga, T. Nakajima, K. Sano, P.L. Choyke and H. Kobayashi, *Bioconjugate Chem.*, **2012**, *23*, 604-609. b) M. Mitsunaga, T. Nakajima, K. Sano, G. Kramer-Marek, P.L. Choyke and H. Kobayashi, *BMC Cancer*, **2012**, *12*, 345-352. c) T. Nakajima, K. Sano, M. Mitsunaga, P.L. Choyke and H. Kobayashi, *Cancer Res.*, **2012**, *72*, 4622-4628. d) I. Sehgal, H. Li, B. Ongarora, D. Devillier and M.G.H. Vicente, *J. Porphyrins Phthalocyanines*, **2013**, *17*, 150-156. e) S. Kishimoto, M. Bernardo, K. Saito, S. Koyasu, J.B. Mitchel, P.L. Choyke and M.C. Krishna, *Free Radical Bio. Med.*, **2015**, *85*, 24-32. f) K. Sato, T. Nagaya, M. Mitsunaga, P.L. Choyke and H. Kobayashi, *Cancer Lett.*, **2015**, *365*, 112-121. g) K. Sato, T. Nakajima, P.L. Choyke and H. Kobayashi, *RSC Adv.*, **2015**, *5*, 25105-25114. h) K. Sato, T. Nagaya, P.L. Choyke and H. Kobayashi, *Theranostics*, **2015**, *5*, 698-709. i) H. Hanaoka, T. Nakajima, K. Sato, R. Watanabe, Y. Phung, W. Gao, T. Harada, I. Kim, C.H. Paik, P.L. Choyke, M. Ho and H. Kobayashi, *Nanomedicine*, **2015**, *10*, 1139-1147.

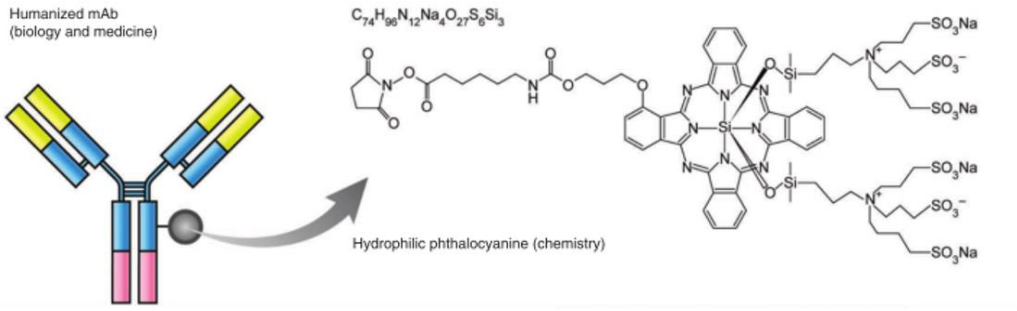

Figure 39. Schematic representation of IR700-mAB (SiPc-Ab) PIT agent, as shown in ref.181

iii. Protein cage-Pc systems

Hollow protein scaffolds such as ferritin and virus-like particles have been employed as nanocarriers or nanoreactors due to its ability to accommodate polymers, enzymes or other biologically relevant materials inside the hollow structure.[55d,183] Despite a few examples of surface modification, incorporation of photosensitizers, more precisely Pcs within the cage is a field exploited almost exclusively by our group. M. Brasch, A. de la Escosura *et al*.[184] first described loading of ZnPc aggregates inside previously emptied cowpea chlorotic mottle virus (CCMV) native assemblies, known as T=3, at pH = 5. Drawback of this methodology consist in a slowly loss of photosensitizer by diffusion through protein porous. This problem was overcame by basifying the media or ensembling the virus at pH = 7.5, producing a smaller, non-porous capsid known as T=1, now suitable for PDT application. Described loaded virus-like particles were studied by cryo-electron microscopy three dimensional reconstruction and AFM, concluding that for T=3 particles ZnPcs are localized over the porous of the protein cage and, on the contrary, T=1 particles present a well-packed ZnPc nanoparticle consisting in 180 ZnPcs ordered in 18 decamers stacks (Figure 40).[185] This starting point expands the possibilities of nanocarried photosensitizer options to be applied in phototherapy and have been recently exploited.[186]

---

[183] R.M. Putri, J.J.L.M. Cornelissen and M.S.T. Koay, *ChemPhysChem*, **2015**, *16*, 911-918.

[184] M. Brasch, A. de la Escosura, Y. Ma, C. Uetrecht, A.J.R. Heck, T. Torres and J.J.L.M. Cornelissen, *J. Am. Chem. Soc.*, **2011**, *133*, 6878-6881..

[185] D. Luque, A. de la Escosura, J. Snijder, M. Brasch, R.J. Burnley, M.S.T. Koay, J.L. Carrascosa, G.J.L. Wuite, W.H. Roos, A.J.R. Heck, J.J.L.M Cornelissen, T. Torres and J.R. Castón, *Chem. Sci.*, **2014**, *5*, 575-581.

[186] a) F. Setaro, M. Brasch, U. Hahn, M.S.T. Koay, J.J.L.M. Cornelissen, A. de la Escosura and T. Torres, *Nano Lett.*, **2015**, *15*, 1245-1251. b) E. de los Pinos, J.T. Schiller, R.C. Kines and J. MacDougall, US. Pat. 056412, **2014**.

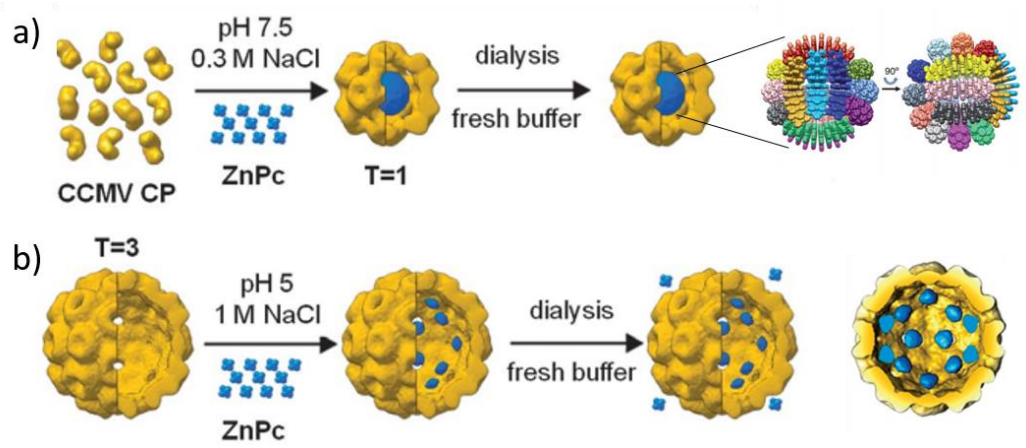

Figure 40. a) Self-assembly conditions of 10 nm ZnPc nanospheres within T=1 CCMV virus-like particle (diameter: 20 nm) and cryo-EM 3D reconstruction. b) Encapsulation conditions of ZnPc inside T=3 CCMV virus-like particles and cryo-EM 3D reconstruction. Reproduced with permission of ref.

(vi) Pc-Nucleic acid systems

Only a few examples of Pc-DNA/RNA covalent conjugates have been described, aiming DNA/RNA recognition and their application in sensors.[187] Nevertheless, gene therapy and RNA interference, based in the delivery of a selected nucleic acid sequence that supress the expression of a target gene is a suitable and powerful strategy. A recent trend in this field, known as photoinmunotherapy, photorelease and assisted transfection of siRNA or DNA has been found to enhance therapeutical effectiveness,[188] generally employing a dendritic Pc[189] as soft nanocarrier that bounds to neoplasic cells and delivers the genetic cargo upon light irradiation.[190] Nishiyama *et al.* developed a supramolecular

[187] a) A.A. Chernonosov, N.A. Kuznetsov, V.V. Koval, D.V. Pyshnyi, N.M. Derkacheva, E.A. Lukyanets and O.S. Fedorova, *Nucleos. Nucleot. Nucl.*, **2004**, *23*, 983-987. b) A.A. Kuznetsova, L.I. Soloveva and O.S. Fedorova, *Russ. J. Bioorg. Chem.*, **2008**, *34*, 613-624. c) A.A. Kuznetsova, E.A. Lukyanets, L.I. Solovyeva, D.G. Knorre and O.S. Fedorova, *J. Biolomol. Struct. Dyn.*, **2009**, *26*, 307-319.

[188] a) L. Prasmickaite, A. Høgset and K. Berg, *Photochem. Photobiol.*, **2001**, *73*, 388-395. b) D. Separovic, P. Breen, N. Joseph, J. Bielawski, J.S. Pierce, E. van Buren and T.I. Gudz, *Anticancer Res.*, **2012**, *32*, 2479-2486. c) D. Separovic, P. Breen, N. Joseph, J. Bielawski, J.S. Pierce, E. van Buren and T.I. Gudz, *Anticancer Res.*, **2012**, *32*, 753-760.

[189] W.-S. Li and T. Aida, *Chem. Rev.*, **2009**, *109*, 6047-6076.

[190] a) N. Nishiyama, W.-D. Jang and K. Kataoka, *New J. Chem.*, **2007**, *31*, 1074-1082. b) Y. Tamaki, *Nanomedicine*, **2009**, *4*, 341-352. c) W.-D. Jang and W.-G. Koh in *Nanobiomaterials*, ed. D.-K. Yi and G.C. Papaefthymiou, CRC Press, Boca Raton, Florida, US, **2014**, *3*, 81-108. d) C. Schuman, O. Taratula, O. Khalimonchuk, A.L. Palmer, L.M. Cronk, C.V. Jones, C.A. Escalante and O. Taratula, *Nanomed. Nanotechnol.*, **2015**, *11*, 1961-1970.

gene-peptide-dendritic ZnPc moiety that, under laser irradiation, trigger gene transfection in the specifically bounded cells. [191]

Supramolecular recognition between charged Pcs and nucleotide sequences has been described thoroughly and can be easily monitored by fluorescence spectroscopy.[192] In particular, interaction of charged Pcs with G-quadruplets (i.e. aminoacid sequences that promotes a DNA folding motif), involved in telomere stability, regulation of promoters and viral integration and recombination are of capital interest as cancer growth inhibition strategy.[193] Alzeer *et al.* described specific binding of charged ZnPc seems to disrupt the folded configuration of G-quadruplets, triggering a telomerasa inhibition and, therefore, knocking-down RNA expression while a real-time imaging by Pc fluorescence was performed.[141a]

(vii) Liposomes

Encapsulation of highly hydrophobic Pcs in liposomes present several advantages. First, there is no need in include any hydrophilic group in the Pc due to the intrinsic amphiphilic nature of the liposomes. Second, Pcs shows no aggregation, maintaining the photophysical properties like ROS generation and fluorescence. Third, a lower amount liposomal-PS moiety has to be administered to the patient, due to the high payload of the liposomes and enhanced intratumoral PS delivery. Finally, the possibility of conjugate other pharmacological compounds, leading to more complex and specific drugs.[60d] Actual trends in liposomal-Pc conjugates are directed toward multifunctional moieties. Pc-liposome conjugates have been successfully employed in clinical applications, including the treatment of leishmaniasis,[194] artherosclerosis,[195] and as antineoplasic agents[196] even in

---

[191] N. Nishiyama, A. Iriyama, W.-D. Jang, K. Miyata, K. Itaka, Y. Inoue, H. Takahashi, Y. Yanagi, Y. Tamaki, H. Koyama and K. Kataoka, *Nature Mat.*¸ **2005**, *4*, 934-941.

[192] a) H. Dezhampanah, T. Darvishzad and M. Aghazadeh, *Spectroscopy*, **2011**, *26*, 357-365. b) M. Özçesmeci, Ö.B. Ecevit, S. Sürgün and E. Hamuryudan, *Dyes Pigm.*, **2013**, *96*¸52-58. c) N.C.L. Zeballos, G.A. Gauna, M.C.G. Vior, J. Awruch and L.E. Dicelio, *J. Photochem. Photobiol. B*, **2014**, *136*, 29-33. d) Ö. Kurt, I. Özésmeci, B.S. Sesalan and M.B. Koçak, *New J. Chem.*, **2015**, *39*, 5767-5775. e) E. Yabas, E. Bagda and E. Bagda, *Dyes Pigm.*, **2015**, *120*, 220-227.

[193] a) A. Membrino, M. Paramasivam, S. Cogoi, J. Alzeer, N.W. Luedtke and L.E. Xodo, *Chem. Commun.*, **2010**, *46*, 625-627. c) H. Yaku, T. Murashima, D. Miyoshi and N. Sugimoto, *Chem. Commun.*, **2010**, *46*, 5740-5742. d) H. Yaku, T. Murashima, D. Miyoshi and N. Sugimoto, *Molecules*, **2012**, *17*, 10586-10613.

[60d] R. Weijer, M. Broekgaarden, M. Kos, R. van Vught, E.A.J. Rauws, E. Breukink, T.M. van Gulik, G. Storm and M. Heger, *J. Photochem. Photobiol. C*, **2015**, 103-131.

[194] a) J. Montanari, C. Maidana, M.I. Esteva, C. Salomon, M.J. Morilla and E.L. Romero, *J. Control. Release*, **2010**, *147*, 368-376. b) J.B.P. Ribeiro, A.L. Miranda-Vilela, D. Graziani, M.R.A. Gomes, A.A.S. Amorim, R.D. García, J.S. Filho, A.C. Tedesco, F.L. Primo, J.R. Moreira, A.V. Lima and R.N.R. Sampaio, *Photodiagn. Photodyn.*, **2015,** *in press*. c) L. E. S.

clinical trials.[197] Due to the broadness of this field and because it lies off the general topic of the present thesis is not going to be discussed.

(viii) Carbohydrates

Synthesis of glycosylated Pcs has been achieved following different strategies. (i) sugar-substitution of phthalonitriles in α, β or both positions leads from mono- to tetrasubstituted phthalonitriles. Subsequent cyclotetramerization leads to symmetric and asymmetric glycosylated Pcs. Moreover, a different strategy can be followed, by performing axial substitution in silicon phthalocyanines.[66,198] A particular case of functional sugars are cyclodextrines (i.e. barrel-shaped cyclic oligosaccharide), that presents interesting properties as host of hydrophobic or amphiphilic molecules in aqueous media. This particular moiety has been employed along with Pcs[199] as drug delivery system due to its high biocompatibility[200] or as recognition motif to create supramolecular photoactive species.[201]

Polysaccharides in conjugation with Pcs are of particular interest in non-medical technologies such as detectors, catalysis and environmental science. To those ends chitosan,[202] cellulose[203] and more recently cellulose nanocrystals (CNCs)[204] acted as insoluble scaffold where immobilize the photoactive Pcs.

Contreras, J. Zirzlmeier, S.V. Kirner, F. Setaro, F. Martínez, S. Lozada, P. Escobar, U. Hahn, D.M. Guldi and T. Torres, *J. Porphyrins Phathalocyanines*, **2015**, *19*, 320-328.

[195] A. Visona and G. Jori, *Artherosclerosis,* **1993**, *100*, 213-222.

[196] a) E. Reddi, G. Locastro, R. Biolo and G. Jori, *Br. J. Cancer*, **1987**, *56*, 597-600. b) W.G. Love, S. Duk, R. Biolo, G. Jori and P.W. Taylor, *Photochem. Photobiol*., **1996**, *63*, 656-661.

[197] M. Ochsner, *J. Photochem. Photobiol. B*, **1996**, *32*, 3-9.

[198] S. Singh, A. Aggarwal, N.V.S.D.K. Bhupathiraju, G. Arianna, K. Tiwari and C.M. Drain, *Chem. Rev.*, **2015**, *115*, 10261-10306.

[199] M. Kryjewski, T. Goslinski and J. Mielcarek, *Coord. Chem. Rev.*, **2015**, *300*, 101-120.

[200] a) A.O. Ribeiro, J.P.C. Tomé, M.G.P.M.S. Neves, A.C. Tomé, J.A.S. Cavaleiro, O.A. Serra and T. Torres, *Tetrahedron Lett.*, **2006**, *47*, 6129-6132. b) J.T.F. Lau, P.-C. Lo, Y.-M. Tsang, W.-P. Fong and D.K.P. Ng, *Chem. Commun.*, **2011**, *47*, 9657-9659. c) L.M.O. Lourenço, P.M.R. Pereira, E. Maciel, M. Válega, F.M.J. Domingues, M.R.M. Domingues, M.G.P.M.S. Neves, J.A.S. Cavaleiro, R. Fernandes and J.P.C. Tomé, *Chem. Commun.*, **2014**, *50*, 8363-8366. d) S. Lu, Y.J. Ma, H.Y. Xuan, A. Wang, B. Zhao, X.D. Li, J.H. Zhou, Y. Lin, L. Zhou and S.H. Wei, *RSC Adv.*, **2014**, *4*, 59759-59763. e) C. Conte, A. Scala, G. Siracusano, N. Leone, S. Patane, F. Ungaro, A. Miro, M.T. Sciortino, F. Quaglia and A. Mazzaglia, *RSC Adv.*, **2014**, *4*, 43903-43911.

[201] a) X. Leng, C.-F. Choi, P.-C. Lo and D.K.P. Ng, *Org. Lett.*, **2007**, *9*, 231-234. b) E.A. Ermilov, R. Menting, J.T.F. Lau, X. Leng, B. Röder and D.K.P. Ng, *Phys. Chem. Chem. Phys.*, **2011**, *13*, 17633-17641.

[202] a) R. Bonnett, M.A. Krysteva, I.G. Lalov and S.V. Artarsky, *Water Res.*, **2006**, *40*, 1269-1275. b) P. Khoza and T. Nyokong, *J. Molecul. Cat. A*, **2015**, *399*, 25-32. c) S. Meenakshi, K. Pandian, L.S. Jayakumari and S. Inbasekaran, *Mat. Sci. Eng. C*, **2016**, 136-144.

Based on the previously prepared systems, in the present chapter three photoactive biohybrid materials will be presented, employing aqueous cationic ZnPcs as chromophores and three different biologically related nanostructures: micelles contained by CCMV-based VLPs, the apoferritin protein cage and cellulose nanocrystals.

2.1.2. **Phthalocyanines as photosensitizers**

Singlet oxygen ($^1O_2$) is the lowest excited electronic state of molecular oxygen, resulting in a highly reactive molecule. The particular physicochemical properties of this species has been widely studied in diverse scientific fields.[205] In fact, presents high reactivity towards organic substrate as oxidizing agent, being involved as intermediate in many biological oxidation events. Furthermore, most promising nanotechnology applications takes advantage of the high reactivity of this species in technologies like photodynamic therapy (PDT) for cancer treatment, photodynamic inactivation (PDI) for bacteria and fungi inactivation, water treatments by oxidation of organic pollutants, diagnostic arrays and as an oxidant in organic synthesis.

2.1.2.1. Chromophore photophysics

Mechanism of $^1O_2$ generation can undergoes both physical and chemical methods. We will focus on the generation through electron or charge transfer from the excited state of a chromophore to the molecular oxygen (O_2) present in the media. Two main aspects of this process, that is light absorption and energy/electron transfer process itself, are described in Figure 41. Herein, a modified Jablonsky energy diagram outlines the characteristic possible radiative and non-radiative processes between the electronic states of the chromophore, i.e. photon absorption, internal conversion, fluorescence, intersystem crossing and phosphorescence. Each electronic state noted have vibrational levels associated.

---

[203] a) H. Hayatsu, *J. Chromatogr. A*, **1992**, *597*, 37-56. b) S. Chen, Y. Huang, *Mat. Lett.*, **2015**, *142*, 235-237.

[204] P. Chauhan and N. Yan, *RSC Adv.*, **2015**, *5*, 37517-37520.

[205] a) M. C. De Rosa and R. J. Crutchley, *Coord. Chem. Rev*. **2002**, *233*, 351-371. b) P. R. Ogilby, *Chem. Soc. Rev*. **2010**, *39*, 3181-3209. c) M. Ethirajan, Y. Chen, P. Joshi and R. K. Pandey, *Chem. Soc. Rev*. **2011**, *40*, 340-362. d) K. Ishii, *Coord. Chem. Rev*. **2012**, *256*, 1556-1568.

The ground state (S_0) of the chromophore present two electrons of opposite spins. Upon illumination, the chromophore absorbs one photon of the corresponding energy and one of the electrons is promoted into an orbital of higher energy, maintaining the initial spin. The transition to the first excited state (S_1) leads to the formation of the short-lived singlet excited state, in the range of the nanoseconds. Excitation to more energetic levels (S_n) is followed by a fast internal conversion (IC) leading to the more stable excited state S_1. The energy of the excited state can be dissipated by restoring the chromophore ground state through two main pathways. First, thermal decay (TD), i.e. dissipation of the energy by non-radiative transition between two electronic states. Second, emission or fluorescence (F), i.e. spontaneous emission of photons upon transition between two electronic states. Both pathways occurs between two states of the same spin multiplicity. Regarding the emitted photon, is less energetic than the absorbed one due to vibrational, non-radiative relaxation processes. Moreover, the vibrational profile of the ground and excited state are similar. For this reason, the fluorescence spectrum is most often a mirror image of the absorption. The gap between the maximum absorption of the two bands is called "Stokes Shift".[206]

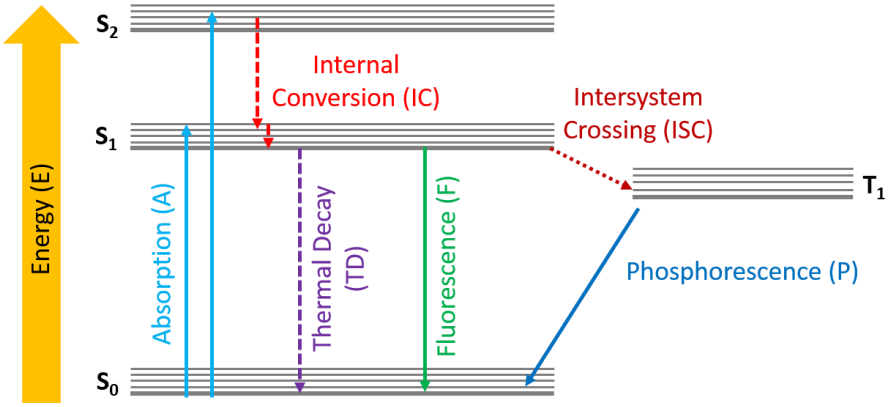

Figure 41. Modified Jablonsky energy diagram showing the various modes of excitation and relaxation occurring in PS: absorption (A), internal conversion (IC), fluorescence (F), intersystem crossing (ISC) and phosphorescence (P).

[206] a) B. Valeur, in *Molecular Fluorescence: Principles and Applications*, (Wiley-VCH) New York 2001. b) V. Ramamurthy, K. S. Schanze, in *Organic Photochemistry and Photophysics*, (CRC Press Taylor & Francis Group) New York, 2006

The singlet state S_1 can undergo a spin inversion of the excited electron through a process call Intersystem Crossing (ISC). Resulting triplet excited state (T_1) is a long-living state (in the order of microseconds) that can dissipate energy by relaxing to the ground state emitting a photon. This process, called phosphorescence (P) occur between two electronic states with different spin multiplicity. This factor explains long life of the triplet excited state since the $T_1 \rightarrow S_0$ transition is forbidden. The P spectrum is located at higher wavelength than the F spectrum, as the energy of the lowest vibrational level of the triplet excited state is significantly lower than that of the singlet excited state.

Interaction between a triplet excited state chromophore and a molecular oxygen molecule leads to an electron or energy transfer between both molecules. Due to this, a long-living triplet excited state is a desirable property when designing a photosensitizer (PS). Thus, efficient chromophore ISC from the singlet excited state to the triplet excited state is of capital interest in $^1O_2$ generation process. Because this spin-forbidden process is promoted by spin-orbit coupling, which is a function of Z^4 (where Z is the atomic number), heavy atoms should increase the triplet excited state lifetime. This is known as the heavy-atom effect.[206,207]

Triplet excited state chromophore undergoes two kind of reactions in the presence of O_2, named as Type I and Type II photoreactions.[208]

Type I photoreactions

$$^3PS^* + S \rightarrow PS^{\cdot-} + S^{\cdot+}$$
$$^3PS^* + {}^3O_2 \rightarrow PS + O_2^{\cdot-}$$
$$PS^{\cdot} + {}^3O_2 \rightarrow PS^{\cdot+} + O_2^{\cdot-}$$
$$S^{\cdot+} + {}^3O_2 \rightarrow \text{oxidative damage}$$
$$S^{\cdot} + O_2^{\cdot-} \rightarrow \text{oxidative damage}$$

Type II photoreactions

$$^3PS^* + {}^3O_2 \rightarrow PS + {}^1O_2$$
$$^1O_2 + S \rightarrow \text{oxidative damage}$$

Figure 42. Overview of Type I and Type II photoreactions during PDT. Energy transfer to biological substrates (S) and molecular oxygen ($^3O_2$) causes production of reactive oxygen species (ROS) and dose-dependent damage.

---

[207] a) J. C. Kozian and D. O. Cowan, A*cc. Chem. Res.* **1978**, *11*, 334-341. b) M. R. Detty and P. B. Merkel, *J. Am. Chem. Soc.* **1990**, *112*, 3845-3855. c) N. J. Turro In *Modern Molecular Photochemistry*, (Sausalito) University Science Books, CA, 1991, pp. 191-195. d) A. Gorman, J. Killoran, C. O'Shea, T. Kenna, W. M. Gallagher and D. F. O'Shea, *J. Am. Chem. Soc*. **2004**, *126*, 10619-10631

[208] C. S. Foote, *Photochem Photobiol*. **1991**, *54*, 659-668.

Type I photoreactions proceed by an electron and/or proton transfer, where the triplet excited state chromophore interacts directly with the cellular substrate (i.e. lipids, proteins, nucleic acids, etc.). The generated radicals react with molecular oxygen, yielding several oxygen intermediates (i.e. superoxide anion – $O_2^{\cdot -}$, hydroxyl radical – $OH^{\cdot}$ and hydrogen peroxide – H_2O_2), collectively called reactive oxygen species (ROS)[209]. Alternatively, Type II photoreactions proceed by energy (not electron) transfer from chromophore T_1 to oxygen ground state ($^3O_2$), generating the aforementioned $^1O_2$.

2.1.2.2. Singlet oxygen photophysics

Molecular oxygen (O_2) present an unusual electronic structure with a triplet ground state. After collision with a triplet excited state chromophore a process of triplet-triplet energy transfer takes place. In singlet oxygen, the two highest energy electrons lie together in the same anti-bonding orbital with opposite spin (Figure 43). The electronic configuration of this species explains its high reactivity towards electron rich organic moieties such as aromatic rings, amines and thioethers.[205,210]

---

[209] H. Shibaguchi, in *Reactive Oxygen species in non-invasive cancer therapy*, from *Handbook on Reactive Oxygen Species (ROS)*, (Eds. M. Suzuki, S. Yamamoto), Nova Science Publishers, Inc. Hauppauge, N.Y, 2014, 279-302.

[210] a) M. Wainwright, *J. Antimicrob. Chemother.* **1998**, *42,* 13-28. b) C. M. Bergamini, S. Gambetti, A. Dondi and C. Cervellati, *Curr. Pharm. Des.* **2004**, *10*, 1611-1626. c) C. Schweitzer and R. Schmidt, *Chem. Rev.* **2003***, 103*, 1685-1758. d) R. Schmidt, *Photochem. Photobiol*. **2006**, *82*, 1161-1177. f) L. B. Josefsen, R. W. Boyle, *Met.-Based Drugs*, **2008**, 276109.

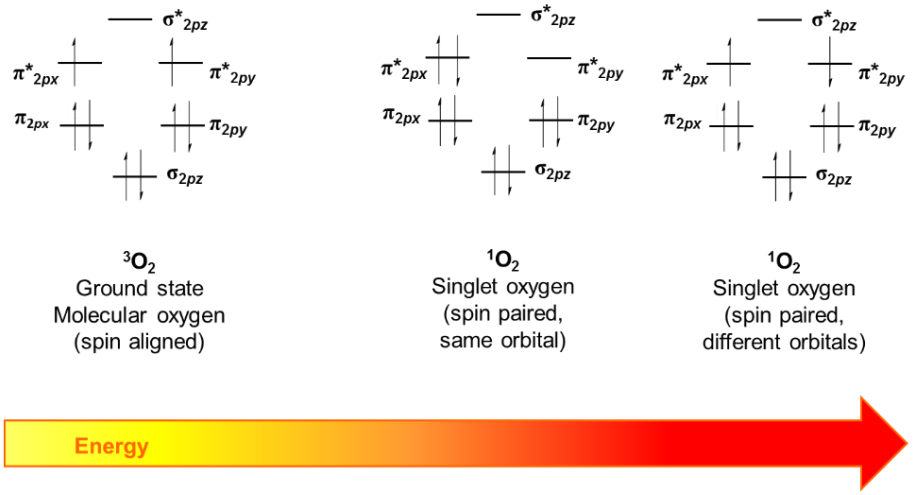

Figure 43. Molecular orbital diagram of oxygen.

Singlet oxygen deactivates by transferring its electronic energy to solvent vibrations. Due to this, $^1O_2$ lifetime strongly depends on the solvent in which it is generated.[211] In most organic solvents, this lifetime is around 10-100 µs, while the shortest values are found in water (3-4 µs) due to the strong OH vibration. In deuterated solvents, the corresponding vibrations shift to lower frequencies, resulting in a drastic increase (over one order of magnitude) in the lifetime (up to 65 µs for D_2O).

Due to its inherent reactiveness and short half life, $^1O_2$ has to be generated *in situ* and in close contact to the substrate. Under physiological conditions (i.e. for PDT) a substantially shorter lifetime (100-250 ns) leads to a small diffusion rate, predicted to be of ca. 45 nm, smaller distance than a single cell.

2.1.2.3. Design of singlet oxygen generation nanoplatform

Taking into account the aforementioned properties of both chromophore and singlet oxygen, design of an effective singlet oxygen generator requires both optimum photosensitizer and the proper delivery vehicle or nanostructured platform that maintain the photophysical properties of the selected dye.

---

[211] F. Wilkinson, W. P. Helman and A. B. Ross, *J. Phys. Chem. Ref. Data* **1995**, *24*, 663-1021.

Concerning the first point, hundred of natural and synthetic dyes have been evaluated primarily as Ps for PDT. Optimal features listed below can be extent to other chromophores involved in $^1O_2$ dependant technologies.

(i) Be a single and pure substance, with a known and stable composition.
(ii) Have minimum dark toxicity and negligible cytotoxicity in the absence of light.
(iii) Should not yield toxic metabolites.
(iv) Present optimal absorption, distribution, metabolism and excretion properties.
(v) Exhibit greater retention in target tissue/cells over healthy ones.
(vi) Have high molar extinction coefficients, with high absorbance, particularly in the red and near infrared UV-Vis spectral regions (600-800 nm range), for a maximum light penetration and minimum light scattering with the "therapeutic window".
(vii) Have high triplet-state quantum yields ($\phi_T \geq 0.5$), lifetimes (μs range) and sufficiently energetic (≥ 94 Kj mol^{-1}). This photophysical parameters leads to high $^1O_2$ production (i.e. $^1O_2$ quantum yield – $\phi_\Delta \geq 0.5$).
(viii) Have a short, inexpensive and high-yield synthetic route, with easy translation into multigram-scale reactions.

Taking into account the aforementioned requirements, in the present chapter three photoactive biohybrid materials will be presented. All of them have been prepared employing cationic water-soluble ZnPcs as chromophores and three different biological units: micelles contained by CCMV virus capsid, apoferritin protein in crystalline phase and cellulose nanocrystals.

2.2. Protein cage nanoparticles containing ZnPc-paramagnetic micelles as potential multimodal imaging and therapy agent.

Well-defined nanostructured materials represent a very important breakthrough in a broad range of biomedical technologies such as imaging, diagnostics and therapy. Moreover, biggest impact on this particular area lies in the integration of various functional component in the same agent, turning into a multifunctional agent for different imaging modalities (multimodal imaging) or both therapy and diagnosis (theranostic agent).

Bioinspired containers such as coat proteins (CPs) of virus capsids has been increasingly employed as suitable nanocarriers for a great variety of purposes.[212] In the particular case of MRI, widely studied paramagnetic NPs are produced through inhomogeneous formulations due to the inherent stochastic nature of the synthetic process. Therefore, VLPs present an optimal scaffold to prepare homogenous and monodisperse contrast agents such as iron oxide or Gd^{3+} derivatives,[213] being chelates of the later the predominantly used moiety.[214] Other contrast agents, suitable for complementary imaging techniques like fluorescence has been also incorporated to

---

[212] a) M. Comellas-Aragones, H. Engelkamp, V.I. Claessen, N.A.J.M. Sommerdijk, A.E. Rowan, P.C.M. Christianen, J.C. Maan, B.J.M. Verduin, J.J.L.M. Cornelissen and R.J.M. Nolte, *Nat. Nanotech.*, **2007**, *2*, 635-639. b) A. de la Escosura, R.J.M. Nolte and J.J.L.M. Cornelissen, *J. Mater. Chem.*, **2009**, *19*, 2274-2278. c) T. Douglas and M. Young, *Science*, **2006**, *312*, 873-875. d) A. Ghasparian, T. Riedel, J. Koomullil, K. Moehle, C. Gorba, D.I. Svergun, A.W. Perriman, S. Mann, M. Tamborrini, G. Pluschke and J.A. Robinson, *Chem BioChem.*, **2011**, *12*, 100-109. e) Z. Liu, J. Qiao, Z. Niu and Q. Wang, *Chem. Soc. Rev.*, **2012**, *41*, 6178-6194. f) Q. Wang, T. Lin, L. Tang, J.E. Johnson and M.G. Finn, *Angew. Chem. Int. Ed.*, **2002**, *41*, 459-462.

[213] a) D.E. Prasuhn Jr., R.M. Yeh, A. Obenaus, M. Manchester and M.G. Finn, *Chem. Commun.*, **2007**, *12*, 1269-1271. b) A.G. Malyutin, R. Easterday, Y. Lozovyy, A. Spilotros, H. Cheng, O.R. Sanchez-Felix, B.D. Stein, D.G. Morgan, D.I. Svergun, B. Dragnea and L.M. Bronstein, *Chem. Mat.*, **2015**, *27*, 327-335. c) S. Shukla and N.F. Steinmetz, *WIRES Nanomed. Nanobiotechnol.*, **2015**, *7*, 708-721.

[214] a) P. Caravan, J.J. Elison, T.J. McMurry and R.B. Lauffer, *Chem. Rev.*, **1999**, *99*, 2293-2352. b) M. Allen, J.W.M. Bulte, L. Liepold, G. Basu, H.A. Zywicke, J.A. Frank, M. Young and T. Douglas, *Magn. Reson. Med.*, **2005**, *54*, 807-812. c) E.A. Anderson, S. Isaacman, D.S. Peabody, E.Y. Wang, J.W. Canary and K. Kirshenbaum, *Nano. Lett.*, **2006**, *6*, 1160-1164. d) L. Liepold, S. Anderson, D. Willits, L. Oltrogge, J.A. Frank, T. Douglas and M. Young, *Magn. Reson. Med.*, **2007**, *58*, 871-879. e) A. Datta, J.M. Hooker, M. Botta, M.B. Francis, S. Aime and K.N. Raymond, *J. Am. Chem. Soc.*, **2008**, *130*, 2546-2552. f) L.Liepold, M.J. Abedin, E.D. Buckhouse, J.A. Frank, M.J. Young and T. Douglas, *Nano Lett.*, **2009**, *9*, 4520-4526. g) J.K. Pokorski, K. Breitenkamp, L. Liepold, S. Qazi and M.G. Finn, *J. Am. Chem. Soc.*, **2011**, *133*, 9242-9245. h) P.D. Garimella, A. Datta, D.W. Romanini, K.N. Raymond and M.B. Francis, *J. Am. Chem. Soc.*, **2011**, *133*, 14704-14709. i) J. Lucon, S. Qazi, M. Uchida, G.J. Bedwell, B. LaFrance, P.E. Prevelige and T. Douglas, *Nat. Chem.*, **2012**, *4*, 781-788. j) S. Qazi, L. Liepold, M.J. Abedin, B. Johnson, P. Prevelige, J.A. Frank and T. Douglas, *Mol. Pharmaceutics*, **2013**, *10*, 11-17. k) M. A. Bruckman, S. Hern, K. Jiang, C.A. Flask, X. Yu and N.F. Steinmetz, *J. Mater. Chem. B*, **2013**, *1*, 1482-1490. l) Y. Song, Y.J. Kang, H. Jung, H. Kim, S. Kang and H. Cho, *Sci. Rep.,* **2015**, *5*, 15656-15665.

previously mentioned virus-like nanoparticles.[215] Porphyrinoids, in particular Pcs present the added value of being good candidates not only for imaging but as $^1O_2$ generators. Most important drawback of the previous Pc-functionalized virus cages lies in the inherent aggregation of the chromophore, quenching any excited-state related event such as fluorescence or singlet oxygen generation.[184,185]

Herein, we describe a straightforward method for the incorporation of amphiphilic ZnPc **6** into amphiphilic Gd^{3+} chelates that generates functional micelles in aqueous dispersion. Named micelles triggers the hierarchical, self-assembling process of CCMV CPs into a multifunctional system developed in collaboration with Prof. Cornelissen research group. This approach tackles several disadvantages found in previously described systems like a long and expensive modification of the CPs by a supramolecular self-assembly process, increased stability of Gd^{3+} micelles by the encapsulation in the protein coat and avoid of the chromophore aggregation, preserving its monomeric photophysical properties.

2.2.1. **Micelles: synthesis and characterization**

Preparation of the multifunctional micelles started with the synthesis of the amphiphilic ligand 1,4,7,10-tetraaza-1-(1-carboxymethylundecane)-4,7,10-triacetic acid cyclododecane (DOTAC10) and its Gd^{3+} complex (Gd-DOTAC10) as described previously.[216] Then, preparation of the corresponding micelles was accomplished by dissolving the corresponding compounds in mili-Q water to a final concentration of 40 mM (5.5 times the critical aggregation concentration - Figure 44).[216] Optically active micelles ZnPc **6**/DOTAC10 and ZnPc **6**/Gd-DOTAC10 were prepared adapting the methodology described in Chapter 1.3.1.2. In detail, 50 µL of a solution of ZnPc **6** in methanol (5.5×10^{-5} M) was added dropwise to 1mL of the corresponding micellar solution (DOTAC10 and Gd-DOTAC10 - Figure 44a and b, respectively) in the aforementioned conditions. The resulting solution was warmed up to 80 ^oC for two minutes and then allowed to cool down to room

---

[215] a) D.E. Prasuhn Jr., J. Kuzelka, E. Strable, A.K. Udit, S.-H. Cho, G.C. Lander, J.D. Quispe, J.R. Diers, D.F. Bocian, C. Potter, B. Carragher and M.G. Finn, *Chem. Biol.*, **2008**, *15*, 513-519. b) N. Stephanopoulos, Z.M. Carrico and M.B. Francis, *Angew. Chem. Int. Ed.*, **2009**, *48*, 9498-9502. c) N. Stephanopoulos, G.J. Tong, S.C. Hsiao and M.B. Francis, *ACS Nano*, **2010**, *4*, 6014-6020. d) J.-K. Rhee, M. Baksh, C. Nycholat, J.C. Paulson, H. Kitagishi and M.G. Finn, *Biomacromolecules*, **2012**, *13*, 2333-2338. e) S. Qazi, M. Uchida, R. Usselman, R. Shearer, E. Edwards and T. Douglas, *J. Biol. Inorg. Chem.*, **2014**, *19*, 237-246.

[216] G.M. Nicolle, É. Tóth, K.-P. Eisenwiener, H.R. Mäcke and A.E. Merbach, *J. Biol. Inorg. Chem.*, **2002**, *7*, 757-769.

temperature. Finally, milli-Q water was added to the solution up to 1 mL in order to control the final concentration.

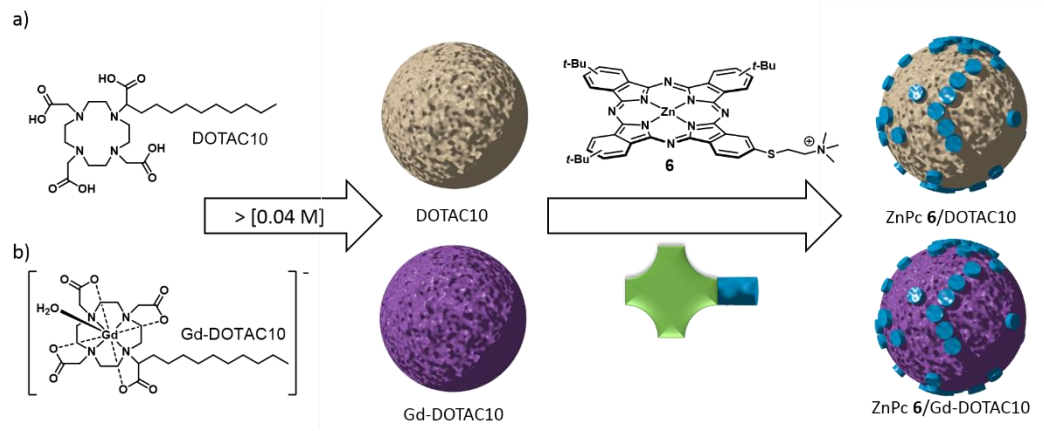

Figure 44. a) Chemical structure of amphiphilic ligand DOTAC10 and the schematic representation of the micelles formed spontaneously and after insertion of ZnPc **6**. b) Chemical structure of the anionic complex Gd-DOTAC10 and the schematic representation of the micelles formed spontaneously and after inclusion of ZnPc **6.**

Absorption spectra of the optically active micelles confirm the insertion of ZnPc **6** within the micellar structure of dual micelle **6**/DOTAC10. This interaction, triggered by hydrophobic-hydrophobid interaction and cation-anion recognition, leads to a complete disaggregation of the chromophore in aqueous media (Figure 45), in a similar way as in SDS micelles described in Chapter 1.3.1.2.

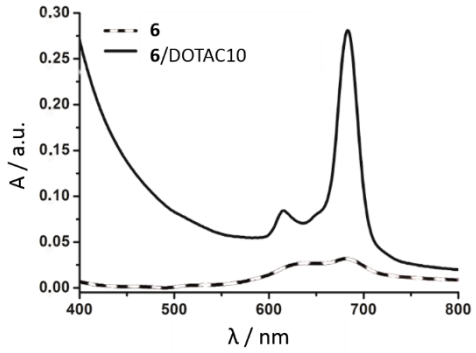

Figure 45. Absorption spectra of ZnPc **6** and optically active micelle **6**/DOTAC10 at the same chromophore concentration (2.75 x 10^{-6} M).

Subsequent encapsulation by CCMV was accomplished by self-assembly of the previously isolated of the corresponding CPs, [212a] leading into a nanostructured multimodal agent as described in following section.

2.2.2. **Hierarchical encapsulation of multifunctional micelles within protein-nanoparticles**

At first glance, MRI active micelles Gd-DOTAC10 and **6**/Gd-DOTAC10 were subjected to encapsulation process. Self-assembly of purified CPs has been found to undergoes through a template effect, based in the electronical interaction of polyanionic template and positively charged residues from the CP.[217] To successfully encapsulate the micelles, 1 mL of the CCMV CP solution (0.4 mM, pH 7.5, 50 mM Tris, 300 mM NaCl, 1mM dithiothreitol) was mixed with 1 mL of the corresponding micellar solution. The mixtures were incubated at pH 7.5 and 4 ^{o}C for 30 minutes. Non-encapsulated micelles building blocks were subsequently removed by dialysis against pH 5 buffer (50 mM sodium acetate, 1 M NaCl, 1 mM NaN_3) for 12 h at the same temperature. On the other hand, blue precipitate corresponding to non-conjugated ZnPc **6** was removed from solution by centrifugation. The assembled protein NPs were then purified by means of size exclusion chromatography, in particular fast protein liquid chromatography (FPLC) and monitored at 280 and 682 nm, being the absorption maxima of CPs and ZnPc **6**, respectively (Figure 46).

In detail, FPLC chromatogram of Gd-DOTAC10/CCMV (Figure 46a) reveals both assembled VLPs (eluted at 1.3 mL) and unassembled CP (eluted at 2.3 mL) when monitored at 280 nm. On the other hand, absorption at 682 nm reveals no relevant feature as consequence of the absence of any absorbing chromophore. In a parallel characterization methodology, FPLC chromatogram of **6**/DOTAC10/CCMV (Figure 46b) reveals similar features, addressable to the aforementioned species. Moreover, absorption at 682 nm reveals the presence of ZnPc **6** in the protein NPs, proving the successfully encapsulation of **6**/DOTAC10 within the VLPs.

---

[217] a) A. de la Escosura, P.G.A. Janssen, A.P.H.J. Schenning, R.J.M. Nolte and J.J.L.M. Cornelissen, *Angew. Chem. Int. Ed.*, **2010**, *49*, 5335-5338. b) I.J. Minten, Y.Ma, M.A. Hempenius, G.J. Vancso, R.J.M. Nolte and J.J.L.M. Cornelissen, *Org. Biomol. Chem.*, **2009**, *7*, 4685–4688. c) F.D. Sikkema, M. Comellas-Aragones, R.G. Fokkink, B.J.M. Verduin, J.J.L.M. Cornelissen and R.J.M. Nolte, *Org. Biomol. Chem.*, **2007**, *5*, 54–57. d) M. Kwak, I.J. Minten, D.-M. Anaya, A.J. Musser, M. Brasch, R.J.M. Nolte, K. Müllen, J.J.L.M. Cornelissen and A. Herrmann, *J. Am. Chem. Soc.*, **2010**, *132*, 7834–7835.

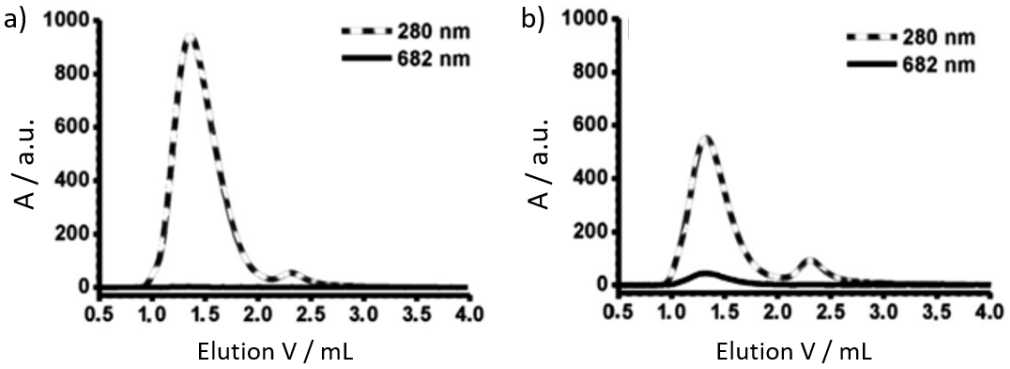

Figure 46. Size exclusion (FPLC) chromatograms of a) Gd-DOTAC10/CCMV and b) **6**/DOTAC10/CCMV. Dashed trace is characteristic of the CP (monitored at 280 nm), whereas the solid trace is characteristic of the ZnPc **6** (monitored at 682 nm).

In addition, TXRF measurements further confirmed the presence of Gd^{3+} and Zn^{2+} in the Gd-DOTAC10/CCMV and **6**/DOTAC10/CCMV species, respectively. However, accurate quantification of the Gd^{3+} of the former ones was not possible. Although TXRF data confirm the presence of Gd^{3+}, its concentration was shown to be substantially below the reported limit of quantification (LOQ) for comparable, organic matrix-based samples (167 µg L^{-1} *versus* LOQ = 330 µg L^{-1}).[218] Such low concentration of Gd^{3+} is probably related to the low stability of Gd-DOTAC10/CCMV (as their high critical concentration suggests). In addition, the possibility that the micelles diffuses out of the CCMV NP upon the dialysis purification step cannot be discarded.

The formation of VLPs were further confirmed by TEM. In particular, the obtained images were used to determine the size distribution of the newly formed cages (Figure 47). Mean diameter values of 24.8 ± 3, 24.6 ± 3 and 24.3 ± 3 nm were found for the DOTAC10/CCMV, Gd-DOTAC10/CCMV and **6**/DOTAC10/CCMV, respectively. All three means present a comparable value and smaller than the diameter of empty T = 3 capsids *(*i.e. 28 nm).[219] Notably, the observed diameter distributions are broad, with particles

---

[218] L. Telgmann, M. Holtkamp, J. Kunnemeyer, C. Gelhard, M. Hartmann, A. Klose, M. Sperling and U. Karst, *Metallomics*, **2011**, *3*, 1035–1040.

[219] a) V.S. Reddy, P. Natarajan, B. Okerberg, K. Li, K.V. Damodaran, R.T.Morton, C.L. Brooks and J.E. Johnson, *J. Virol.*, **2001**, *75*, 11943–11947. b) J.A. Speir, S. Munshi, G.Wang, T.S. Baker and J.E. Johnson, *Structure*, **1995**, *3*, 63–78.

ranging from 20 nm (T = 2)[217d,220] to 28 nm (T = 3). This variability of capsid's size upon encapsulation of a polyaionic core has been shown previously for CCMV CPs loaded with anionic polymers or gold nanoparticles bearing carboxylated polyethylene glycol chains.[217a,220] In our particular case, the experimentally broad diameter distributions may be explained by the different templating efficiencies of the unstable micelles.

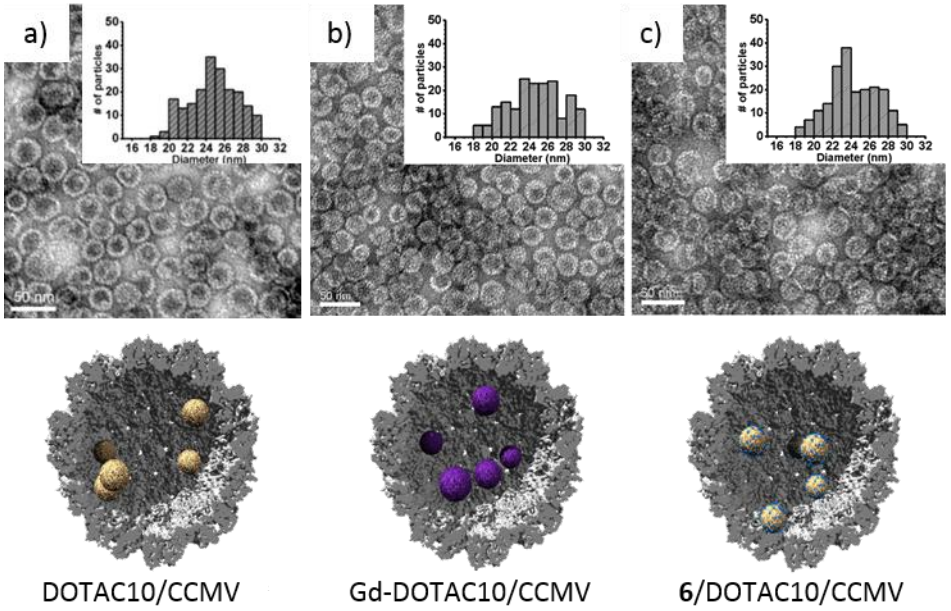

Figure 47. TEM micrographs of DOTAC10/CCMV (a), Gd-DOTAC10/CCMV (b) and **6**/DOTAC10/CCMV (c) and the corresponding schematic representation. Inset: histograms showing the respective diameter distribution of capsids. Scale bar: 50 nm.

The low stability, therefore the non-effective template effect toward the CCMV CP self-assembly process of the proposed micelles composed by DOTAC10, Gd-DOTAC10, and **6**/DOTAC10 was overcome by the encapsulation of the optically active and paramagnetic micelle **6**/Gd-DOTAC10. This was successfully achieved following the same synthesis and purification protocol of the aforementioned species Gd-DOTAC10/CCMV and **6**/DOTAC10/CCMV. Characterization of the self-assembled **6**/Gd-DOTAC10/CCMV (Figure

[220] a) S.E. Aniagyei, C.J. Kennedy, B. Stein, D.A. Willits, T. Douglas,M.J. Young,M. De, V.M. Rotello, D. Srisathiyanarayanan, C.C. Kao and B. Dragnea, *Nano Lett.*, **2009**, *9*, 393–398. b) R.D. Cadena-Nava, Y. Hu, R.F. Garmann, B. Ng, A.N. Zelikin, C.M. Knobler and W.M. Gelbart, *J. Phys. Chem. B*, **2011**, *115*, 2386–2391.

48a) by FPLC confirmed the formation of protein cages eluting at 1.3 mL, with the low but appreciable absorption at 682 nm due to the ZnPc **6** (Figure 48b). TEM micrograph analysis reveals an average mean diameter of 22.4 ± 2 nm (Figure 48c). This value is smaller than those obtained for the capsids containing DOTAC10, Gd-DOTAC10, and **6**/DOTAC10 micelles. In fact, **6**/Gd-DOTAC10/CCMV VLPs are only slightly larger than those with T = 2 architecture (i.e. 20 ± 2 nm), meaning that a higher proportion of the latest is being obtained in this case.

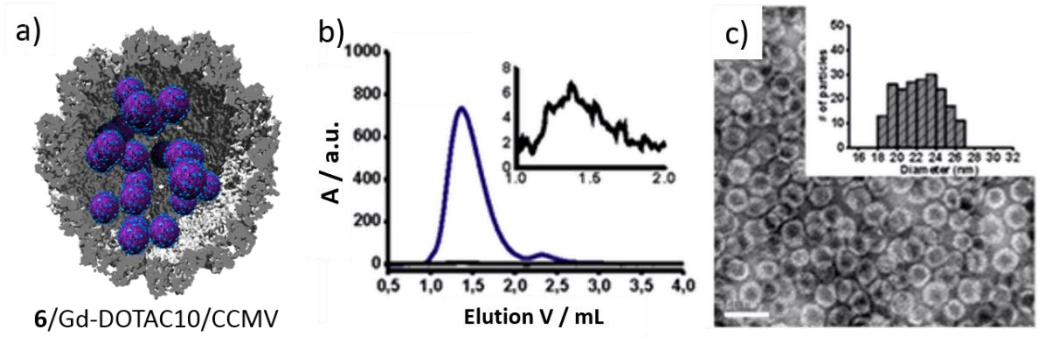

6/Gd-DOTAC10/CCMV

Figure 48. a) Schematic representation of **6**/Gd-DOTAC10/CCMV. b) Size exclusion (FPLC) chromatogram of **6**/Gd-DOTAC10/CCMV, showing the characteristics of the CP (monitored at 280 nm, blue) and the ZnPc **6** (monitored at 682 nm, black). Inset: Black trace zoom. c) TEM micrography of **6**/Gd-DOTAC10/CCMV. Inset: histogram showing the diameter distribution of the capsids. Scale bar: 50 nm.

TXRF measurements reveals a higher micellar cargo than those obtained for previously characterized systems (Table 4). In this particular system, an average payload of 15 ZnPc **6** molecules and 350 Gd^{3+} ions were found per CCMV protein NP in comparison with the measurable yet non-quantificable value for Gd^{3+} and 3 ZnPcs for Gd-DOTAC10/CCMV and **6**/Gd-DOTAC10/CCMV, respectively. Assuming that the micelles formed consists of at least 15 amphiphilic Gd-DOTAC monomers (as previously reported for Gd-DOTAC14 micelles),[216] a maximum value of 23 micelles encapsulated per capsid is obtained.

Both experimental techniques (TXRF and TEM) suggests a significant stabilization and change in the overall surface charge of the micelle by incorporating the amphiphilic ZnPc ZnPc **6**. Moreover, more efficient micelle-templated self-assembly of the protein cages was achieved by encapsulation of micelle **6**/Gd-DOTAC10.

Table 4. Capsid, Zn^{2+} and Gd^{3+} concentration of Gd-DOTAC10/CCMV, **6**/DOTAC10/CCMV and **6**/Gd-DOTAC10/CCMV. Data extracted from TXRF analysis.

	[CCMV NP] / nM	[Zn^{2+}] – [Gd^{3+}] / mg L^{-1}	Zn^{2+} atoms/capsid ([Zn^{2+}] / mM)	Gd^{3+} atom/capsid - [Gd^{3+}] / mM
Gd-DOTAC10/ CCMV	364	0.000 – 0.167	---	---[b]
6/DOTAC10/CCMV	125	0.026[a] – 0.000	3 (3.975x10^{-4})	---
6/Gd-DOTAC10/ CCMV (non diluted)	1022	0.990[a] – 56.471	15 (0.015)	350 (0.359)
6/Gd-DOTAC10/ CCMV (diluted)	128	0.124 – 7.059	15 (1.9x10^{-3})	350 (0.0449)

[a] Values corrected, subtracting the background Zn^{2+} signal from the saline buffer. [b] Values below the LOQ limit.[218]

2.2.3. **Multifunctional protein nanoparticles theranostic potential**

In order to test the potential interest of the systems previously synthesized, both the $^1O_2$ production and the MRI properties were evaluated. The former was quantified indirectly by measuring the corresponding ϕ_Δ in DMSO by the so-called *relative method*, [221] that consists in the photodegradation of 1,3-diphenylisobenzofuran (DPBF), a $^1O_2$ scavenger (see Experimental section for details). ZnPc **6** present a noticeable high value of ϕ_Δ = 0.68, referred to unsubstituted ZnPc (ϕ_Δ = 0.67).[222] This excellent value, even measured in an organic solvent, suggests in a first approach that ZnPc **6** is a suitable chromophore for PDT application.

The MRI properties, on the other hand, were also studied by determining their relaxation efficiency. The longitudinal relaxation times (T_1) is related to the Gd^{3+} concentration and the species relaxivity (r_1) by Equation 1:

$$\left(\frac{1}{T_1}\right)_{obs} = \left(\frac{1}{T_1}\right)_{d} + r_1[Gd^{3+}] \qquad (1)$$

[221] S. Makhseed, A. Tuhl, J. Samuel, P. Zimcik, N. Al-Awadi, V. Novakova, *Dyes Pigments*, **2012**, *95*, 351-357.

[222] N, Kuznetsova, N.S. Gretsova, E.A. Kalmykova, E.A. Makarova, S.N. Dashkevic, V.M. Negrimovskii, O.L. Kaliya and E.A. Lukyanets, *Russ. J. Gen. Chem.*, **2000**, *70*, 133-140.

Here, T_1 of a series of dilutions of known Gd^{3+} and capsid concentrations were measured by means of a standard saturation recovery experiment at 600 MHz (14.1 T). By plotting the measured $1/T_1$ values as a function of Gd^{3+}, the r_1 was obtained as the slope of the curve (Figure 49). Increased value of **6**/Gd-DOTAC10/CCMV (3.9 mM^{-1} s^{-1}) in comparison with the Gd-DOTAC10 compound (2.5 mM^{-1} s^{-1}) suggest a decrease in the tumbling rate (τ_R) of the complex due to micellization inside the protein NP.[216,223] Relaxivity observed in **6**/Gd-DOTAC10/CCMV is comparable to previously described Gd-DOTA complexes covalently linked to wild-type CCMV cages (i.e. 3-4.4 mM^{-1} s^{-1} at 500 MHz),[213] suggesting a similar τ_R stabilization achieved by supramolecular immobilization.

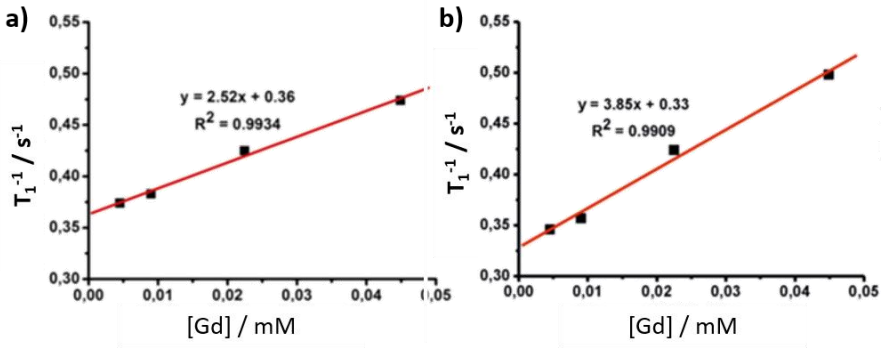

Figure 49. Relaxivity plots of a) complex Gd-DOTAC10 (r_1 = 2.52 mM^{-1} s^{-1}) and b) **6**/Gd-DOTAC10/CCMV VLPs (r_1 = 3.85 mM^{-1} s^{-1}) at 600 MHz, 25 °C.

The possible use of **6**/Gd-DOTAC10/CCMV as MRI contrast agent is illustrated by T_1-weighted MR image (Figure 50). Self-assembly of **6**/Gd-DOTAC10 micelles inside capsids results in a substantially higher contrast compared to that observed for the non-micellar compound Gd-DOTAC10 at the same Gd^{3+} concentration (45 µM, far below the micelles critical concentration). Aggregation, due to self-assembly of the micelles and the stabilization achieved by their inclusion within the capsids results in a substantially higher contrast when compared to the response of compound Gd-DOTAC10 in the same conditions. The absence of ZnPc **6** led to a less efficient encapsulation, precluding Gd^{3+} quantification thus making the study of T_1-weighted of Gd-DOTAC10/CCMV meaningless.

---

[223] A. Accardo, D. Tesauro, L. Aloj, C. Pedone and G. Morelli, *Coord. Chem. Rev.*, **2009**, *253*, 2193-2213. b) W.J.M. Mulder, G.J. Strijkers, G.A.F van Tilborg, A.W. Griffioen and K. Nicolay, *NMR Biomed.*, **2006**, *19*, 142-164.

Figure 50. T_1-weighted MR image of capsid buffer (a), compound **40** (b) and CCMV-**42** (c). Conditions: $[Gd^{3+}]$ = 45 μM. Images at 600 MHz (14.1 T, TE = 6 ms, TR = 500 ms).

In summary, a multifunctional nanostructured system has been described as promising theranostic agent. A novel and straightforward preparation method is reported, based in the hierarchically self-assembly of stable CCMV protein NPs, triggered by co-assembling of anionic paramagnetic micelles (Gd-DOTAC10) and amphiphilic ZnPc **6**. Phototoxicity of the chromophore has been quantified (ϕ_Δ, = 0.68) along with the MR imaging performance. Encapsulation of the multifunctional micelles into the protein NP increases its stability leading into improved r_1, thus showing better MRI signal. Even though the present system need to be further studied, concomitance of both enhanced MR imaging and promising therapeutical projection represent a first step towards the use of self-assembled protein cages for multimodal imaging and therapy.

2.3. Photoactive biohybrid crystals: hierarchical co-crystallization of protein cages and phthalocyanine-pyrene supramolecular moiety.

Among the biohybrid materials, protein cages such as virus capsids and apoferritin (**aFt**)[224] are very promising biological building blocks to be organized into higher-order superlattices, taking advantage of the loading ability within their inner cavity of a variety of organic and inorganic materials.[212b,225] However, crystalline coassemblies of protein cages and functional synthetic components are rare.[226] Moreover, the development of photoactive biohybrid crystal is a highly desirable, yet unaccomplished goal within the field.

In the following chapter, developed in collaboration with Prof. M.A. Kostiainen research group in Aalto University, the preparation of an organic dye/protein cage crystalline structure will be described for the first time. This structure has been prepared by the combination of previously synthesized octacationic ZnPc **16** and commercially available 1,3,6,8-pyrenetetrasulfonic acid (PTSA), resulting in the supramolecular (1:1) complex **16-PTSA**, which act as a molecular glue that allows further crystallization along with **aFt** (p*I* ~ 4.5 – Figure 51). Tetracationic complex **16-PTSA** triggers the hierarchical self-assembly process, driven by electrostatic interactions with the exterior negatively charged patches of the **aFt** cage, resulting in optically active and robust ternary face-centered cubic (fcc) packed crystals. Furthermore, resulting crystals can be disassembled by increasing the electrolyte concentration of the surrounding solution, representing the first case of a stimuli-responsive photosensitizing crystalline phase. Finally, $^1O_2$ production has been evaluated, leading into long-range nanoscale photoactive material with potential applications in PDT, diagnostic arrays and water treatments.[227]

---

[224] G. Jutz, P. van Rijn, B.Santos Miranda and A. Böker, *Chem. Rev.*, **2015**, *115*, 1653-1701.

[225] a) J.-W. Yoo, D.J. Irvine, D.E. Discher and S. Mitragotri, *Nat. Rev. Drug Discovery*, **2011**, *10*, 521-535. b) Y. Ma, R.J.M. Nolte and J.J.L.M. Cornelissen, *Adv. Drug Delivery Rev.*, **2012**, *64*, 811-825. c) Q. Zeng, H. Wen, Q. Wen, X. Chen, Y. Wang, W. Xuan, J. Liang and S. Wan, *Biomaterials*, **2013**, *34*, 4632-4642.

[226] a) J. Mikkilä, H. Rosilo, S. Nummelin, J. Seitsonen, J. Ruokolainen and M.A. Kostiainen, *ACS Macro Lett.*, **2013**, *2*, 720-724. b) V. Liljeström, J. Mikkilä and M.A. Kostiainen, *Nat. Commun.*, **2014**, *5*, 4445. c) S. Välimäki, J. Mikkilä, V. Liljeström, H. Rosilo, A. Ora and M.A. Kostiainen, *Int. J. Mol. Sci.*, **2015**, *16*, 10201-10213.

[227] a) M.C. DeRosa and R.J. Crutchley, *Coord. Chem. Rev.*, **2002**, *233-234*, 351-371. b) D. Ashen-Garry and M. Selke, *Photochem. Photobiol.*, **2014**, *90*, 257-274.

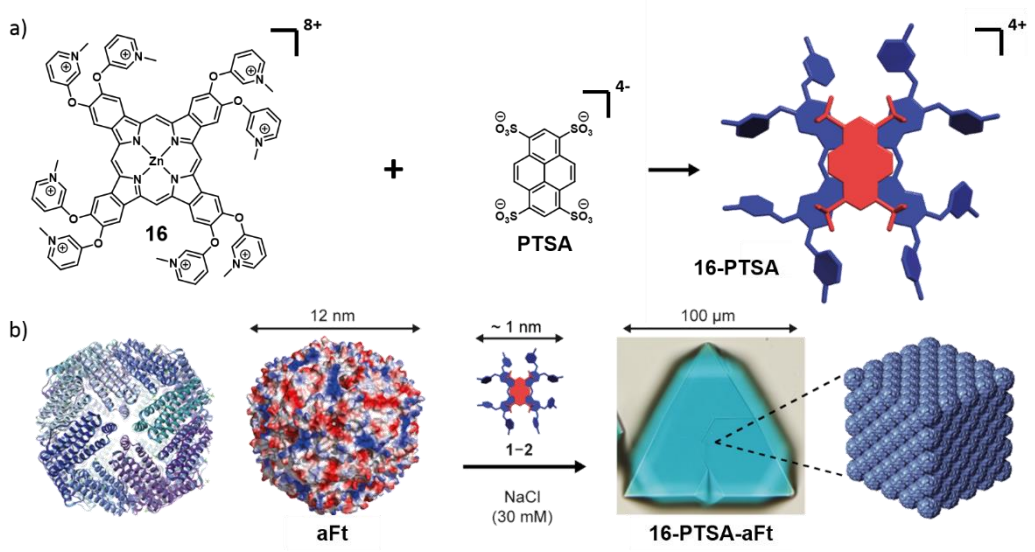

Figure 51. Scheme of the followed hierarchical strategy toward photoactive biohybrid crystals (**16-PTSA-aFt**). a) Chemical structures of **16**, PTSA, and corresponding counterions and the self-assembly of tetracationic **16-PTSA** supramolecular complex. b) Illustrations of the 12 nm sized **aFt** cage and its further co-crystallization with **16-PTSA** complex driven by electrostatic interactions. Illustrations of **aFt** show the folded protein subunits (left) and the calculated electrostatic surface potential (right) with negatively charged patches (in red) covering the cage surface. Note that the cartoons of **16-PTSA**, **aFt** and the crystals are not in the same scale. Counterions of the molecules are not shown for clarity propoises.

2.3.1. **Synthesis and characterization**

2.3.1.1. Supramolecular complex **16-PTSA** characterization

In order to tackle these synthetic challenges, we decided to study the octacationic ZnPc **16**, taking advantage of its aqueous solubility and the ability bind to the negative domains on the exterior surface of **aFt** (Figure 51b). As for most Pcs, the UV-Vis spectrum of **16** in phosphate buffered saline (PBS) solution, containing 187 mM NaCl to mimic physiological conditions, reveals the formation of aggregates (Figure 52). This can be observed as the broadness and strong splitting of the ZnPc Q-band, with an intense absorption at 635 that is characteristic of *H*-type aggregation. The non-covalent complexation of ZnPc **16** with tetraanionic **PTSA** was subsequently proved in the same buffer conditions, rationalizing that in a 1:1 stoichiometry the complex would still leave 4 positive charges for further binding to **aFt**. Interestingly, the addition of **PTSA** to **16**, up to a 1:1 molar ratio, increased the Q-band intensity and shifted its maximum from 669 to 680

nm, while no absorption peak due to the ZnPc *H*-type aggregates was remaining. Further additions of **PTSA** caused only minor changes in the absorption spectra.

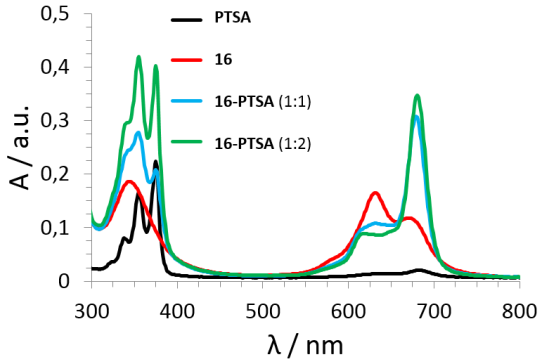

Figure 52. UV–Vis spectra of **16** (5.0 x 10^{-6} M), **PTSA** (5.0 x 10^{-6} M) and the **16-PTSA** complex at 5.0 x 10^{-6} M of ZnPc **16** in PBS buffer. Note that absorption at 600-700 nm of **PTSA** is due to a contamination that has been substracted in the other spectra.

Aforementioned results were taken as an indication of ZnPc-PTSA complexation and Job plot method was performed in order to determine the stoichiometry of the complex (Figure 53a), resulting into a 1:1 ratio (Figure 53b).

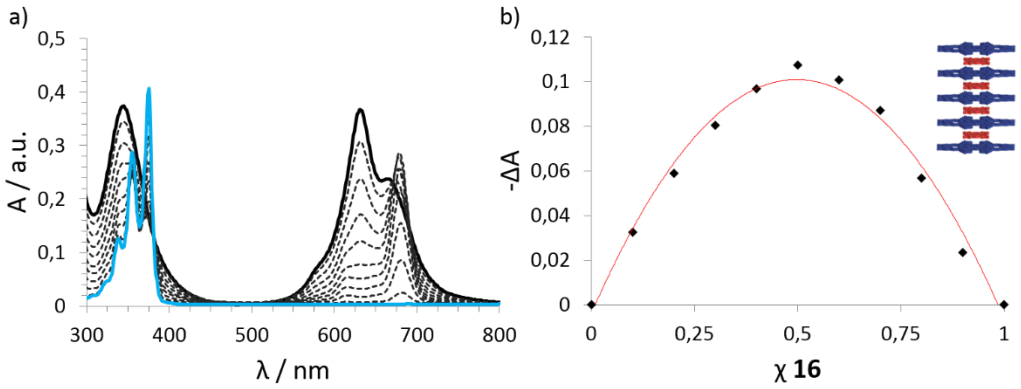

Figure 53. a) UV-Vis spectra of all **16-PTSA** samples measured for the Job's plot experiment. Samples were prepared in PBS buffer. Molar rations of **16** and **PTSA** range from 10:0 (black line) to 0:10 (blue line), while the overall concentration stays constant (1.0 x 10^{-5} M) in all samples. b) Job plot diagram derived from measurements presented in (a) confirms that **16** and **PTSA** self-assemble into complex **16-PTSA** with a stoichiometric 1:1 ratio schematically depicted in the inset.

Absorption titration was conducted, aiming to determine the association constant of the complex formation. To this end, a solution of **16** (5.0 x 10^{-6} M) in PBS was titrated with increasing amounts of **PTSA** (from 0.0 to 1.0 x 10^{-5} M), remaining constant buffer and **16** initial concentrations (Figure 54a). Association constant of **16-PTSA** complex, as well as self-aggregation constant of **16** in PBS buffer were evaluated by Reactlab™ Equilibria software (Figure 54b). Complex formation constant was found to be (1.73 ± 0.03) × 10^{6} M^{-1}, value in good agreement to typical electrostatic driven interactions. On the other hand, self-aggregation constant was found to be of (5.43 ± 0.06) x 10^{4} M^{-1}, value in good agreement with the π-π supramolecular complexes.

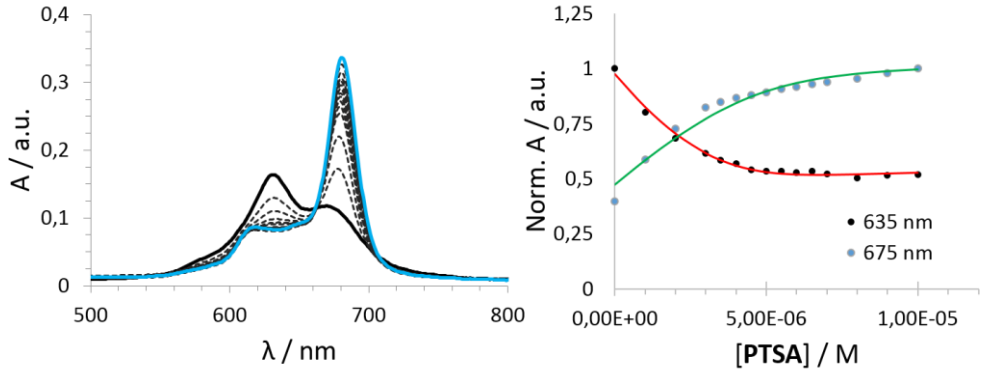

Figure 54. a) UV-Vis titration of **16** (5.0 x 10^{-6} M) with **PTSA** from 0.0 (black line) to 1.0 x 10^{-5} M (blue line) in PBS buffer. b) Normalized absorption at 635 (*H*-aggregates) and 675 nm (monomer) and fitted curves resulting from the titration and fitting.

Selected optical window from 450 to 850 nm was selected, in order to avoid absorption due to **PTSA**. Titration of the Q-band was then adjusted to the following model, where the aggregates are assumed to be dimers:

$$2\ H \leftrightarrow H_2;\ K_{H\text{-}H} = [H_2] / [H]^2$$

$$H+G \leftrightarrow HG;\ K_{H\text{-}G} = [HG] / [H][G]$$

where H, H_2 and G stand for ZnPc **16**, ZnPc **16** dimer and **PTSA** respectively. $K_{H\text{-}H}$ and $K_{H\text{-}G}$ correspond to self-association constant and complex formation binding constants, respectively. Values in brackets denotes concentration.

Furthermore, fluorescence titration showed a significant recovery of the ZnPc emission upon complexation, supporting that self-quenching of the excited state is not taking place in the complex. Overall, these studies proved the strong binding between **16** and **PTSA**, even in relatively high electrolyte concentration, and the concomitant recovery of the pristine ZnPc photochemical properties, otherwise lost in PBS solution.

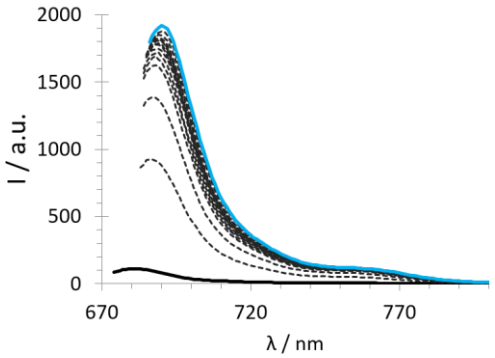

Figure 55. Fluorescence titration of **16** (5.0 x 10^{-6} M) with **PTSA** from 0.0 (black line) to 1.0 x 10^{-5} M (blue line) in PBS buffer. Samples were excited at 669–681 nm wavelength depending on the maximum observed in the excitation spectra measured in advance.

2.3.1.2. **16-PTSA** Complex – apoferritin co-crystallization

Next step in the crystal formation from **16-PTSA** complexes and **aFt** from *Pyrococcus furiosus* has been studied. Spherical and hollow **aFt** has been chosen because it can be used to store for example small molecules or noble metal nanoparticles inside the 8 nm sized inner cavity, and therefore, it offers a flexible platform for designing multifunctional protein complexes.[228] The outer diameter of **aFt** is 12 nm and the cage consists of 24 protein subunits (Figure 51b). We thus combined and mixed **16**, **PTSA**, as well as **aFt** in a buffer solution containing 5 mM Tris (pH 8.5) and 0–200 mM NaCl to tune the electrostatic interactions. Samples were left overnight into a fridge (+7 °C) resulting in ternary **16-PTSA-aFt** crystals. The stoichiometric ratio of **16**/**PTSA**/**aFt** in the sample solutions was 100:100:1.

---

[228] a) N.D. Chasteen and P.M. Harrison, *J. Struct. Biol.*, **1999**, *126*, 182-194. b) J. Tatur, W.R. Hagen and P.M. Matias, *J. Biol. Inorg. Chem.*, **2007**, *12*, 315-630. c) O. Kasyutich, A. Ilari, A. Fiorillo, D. Tatchev, A. Hoell and P. Ceci, *J. Am. Chem. Soc.*, **2010**, *132*, 3621-3627. d) M. Kim, Y. Rho, K.S. Jin, B. Ahn, S. Jung, H. Kim and M. Ree, *Biomacromolecules*, **2011**, *12*, 1629-1640. e) Z. Zhen, W. Tang, H. Chen, X. Lin, T. Todd, G. Wang, T. Cowger, X. Chen and J. Xie, *ACS Nano*, **2013**, *7*, 4830-4837.

The crystals were first studied with an optical microscope (Figure 56). In the samples with 0 mM NaCl mostly poorly defined amorphous complexes were assembled, but in 30 mM NaCl concentration large, up to 100 µm sized, **16-PTSA** -**aFt** crystals were observed. The crystals have clearly visible faceting and overall uniform octahedral crystal habit. The shorter Debye screening length caused by higher electrolyte concentration helps to avoid kinetically trapped structures and promotes the formation of larger crystal domains. In the samples with 40 mM or higher NaCl concentration only loose aggregates were present, which implies that at these conditions the electrostatic interactions between **16-PTSA** complexes and **aFt** are strongly interfered. Increasing the NaCl concentration to 100 mM in samples with preformed large crystals rapidly disassembled them. We also found that the crystals could be removed from the solvent and dried to yield free-standing crystals. As a reference, we prepared samples where only **16** and **aFt** were combined, without **PTSA** In general, the samples behaved in similar manner, although the observed crystals were less defined at 40 mM or higher NaCl concentration.

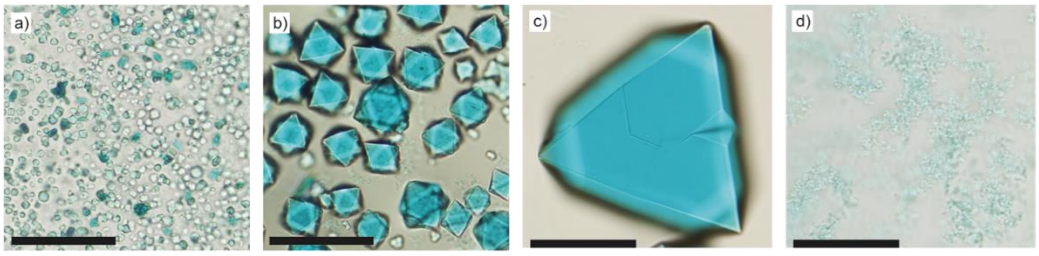

Figure 56. **16-PTSA**-**aFt** crystals self-assembled in a) 0 mM, b) 20 mM, c) 30 mM, d) 40 mM NaCl solutions. Scale bars in all images are 50 µm. All the samples were prepared in Tris buffer (pH = 8.5).

The **16-PTSA**-**aFt** crystals were further studied by small-angle X-ray scattering (SAXS) (Figure 57a), in order to characterize the crystal symmetry and lattice spacing. The SAXS data for crystals formed in 20 mM NaCl concentration is dominated by intensive diffraction peaks, which fit to a face-centered cubic (fcc) crystal structure. The four first diffraction peaks ((hkl) = (111), (200), (220), (311); q:q^* = 1, √(4/3), √(8/3), √(11/3)) of the fcc structure (space group $Fm\bar{3}m$; number 225) are unambiguously identified at q = (0.056, 0.065, 0.091, 0.105) Å^{-1}. It is known that **aFt** protein cages alone tend to form an fcc structure (a = 18.3-18.5 nm) upon crystallization[229] and that the crystallization proceeds by growing fastest in

[229] a) D.M. Lawson, P.J. Artymiuk, S.J. Yewdall, J.M.A. Smith, J.C. Livingstone, A. Treffry, A. Luzzago, S. Levi, P. Arosio, G. Cesareni, C.D. Thomas, W.V. Shaw and P.M. Harrison, *Nature*, **1991**, *349*, 541-544. b) P.D. Hempstead, S.J. Yewdall,

the direction of the hexagonally patterned {111} planes,[230] giving rise to an octahedral crystal habit. We postulate that the crystal growth in our system proceeds in analogous manner to yield the observed regular octahedron shape of the crystals (Figure 57b). Measured lattice constant a_{SAXS} was 19.6 nm (for cubic phases $a = 2\pi\sqrt{(h_2+k_2+l_2)}/q_{(hkl)}$) and the center-to-center distance d_{cc} between **aFt** units was 13.8 nm. The d_{cc} corresponds well to the dimensions of **aFt** (12 nm) coated with **16-PTSA** complexes.

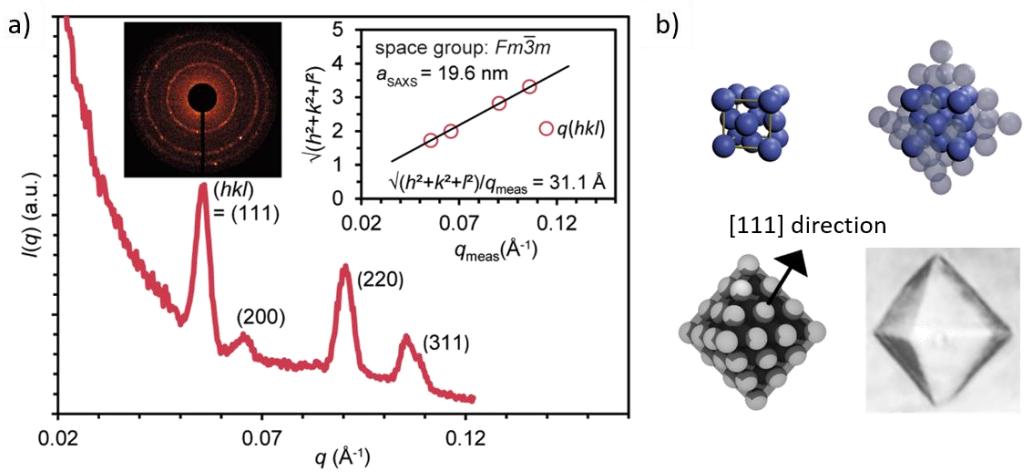

Figure 57. a) SAXS data from **16-PTSA**-**aFt** crystals in 20 mM NaCl concentration indicates a face-centered-cubic crystal structure for the **16-PTSA**-**aFt** crystals. Top left inset shows the 2D scattering pattern and top right inset shows the Quadratic Miller indices of assigned reflections for $Fm\bar{3}m$ structure *versus* measured q-vector positions. Solid line presents a linear fit, which yields the lattice constant a_{SAXS} and the **aFt** center-to-center distance d_{cc}. b) Schematic presentation of the suggested **16-PTSA**-**aFt** crystal formation and regular octahedron shape observed in optical microscopy (bottom-right).

In order to probe the potential applicability of the presented biohybrid crystals, we studied whether the crystal formation with **aFt** affects the optical properties of the **16-PTSA** complex. The absorption spectrum of the ternary assemblies, in presence of 30 mM NaCl concentration, was measured (Figure 58a). By comparison to the reference samples, i.e., **16**, **PTSA**, and **16-PTSA** in the same conditions as for the **16-PTSA**-**aFt** crystals, we could infer that the binding between **16** and **PTSA** is not broken in the crystalline structure,

---

A.R. Fernie, D.M. Lawson, P.J. Artymiuk, D.W. Rice, G.C. Ford and P.M. Harrison, *J. Mol. Biol.*, **1997**, *268*, 424-448. c) B. Tomas, D. Carter and F. Rosenberger, *J. Cryst. Growth*, **1998**, *187*, 499-510.

[230] a) S.-T. Yau and P.G. Vekilov, *Nature*, **2000**, *406*, 494-497. b) S.-T. Yau and P.G. Vekilov, *J. Am. Chem. Soc.*, **2001**, *123*, 1080-1089.

having similar absorption features for the **16-PTSA** complex. As an additional control, the spectrum of **16** combined with only **aFt** was also recorded, showing that the protein cage in absence of **PTSA** is not able to break the ZnPc aggregates

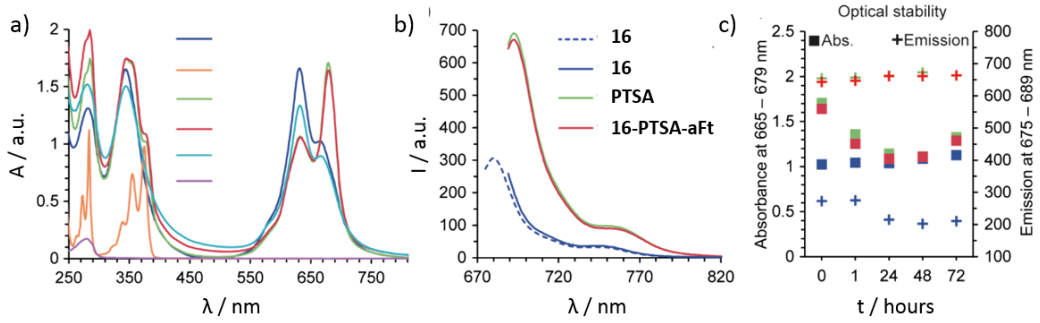

Figure 58. a) Absorption spectrum of **16**, **PTSA**, **16-PTSA**, **16-PTSA-aFt**, and **aFt**, from top to bottom. **16-PTSA**-**aFt** crystals self-assembled in 30 mM NaCl (5 mM Tris buffer, pH 8.5) and the reference samples. ZnPc **16** remains constant at 5.0 x 10^{-4} M. b) Fluorescence emission of **16** (λ_{exc} = 665 - dashed and 679 nm - solid), **16-PTSA** and the **16-PTSA**-**aFt** crystals (λ_{exc} = 679 nm), with excitation wavelengths adjusted according to the corresponding excitation spectra. c) Absorbance and fluorescence of **16-PTSA**-**aFt** (red symbols) and reference samples (**16**, blue symbols; **16-PTSA**, green symbols) measured over time. Left y-axis shows the absorbance at the absorption maxima at 665 nm (**17**) or at 679 nm (**16-PTSA** and **16-PTSA**-**aFt**). Right y-axis shows the fluorescence intensity at 675 nm (**16**, λ_{exc} = 665 nm) or at 689 nm (**16-PTSA** and **16-PTSA**, λ_{exc} = 679 nm).

A similar experiment was conducted by fluorescence spectroscopy (Figure 58b). Excitation took place at the wavelength that maximizes emission, i.e., at 665 nm for **16** and at 679 nm for **16-PTSA** and the **16-PTSA-aFt** crystals, according to the corresponding excitation spectra. Solution of **16** was excited also at 679 nm to make the comparison of the samples more profound. The concentration of the ZnPc in all samples was adjusted to 5.0 x 10^{-6} M by dilution. Interestingly, the emission profile of the **16-PTSA** and **16-PTSA**-**aFt** samples had a similar shape and their intensities more than doubled that of **16** alone, when exciting with the given wavelengths. Again, this result indicates that crystallization does not alter the optical properties of the **16-PTSA** complex. The remarkable fluorescence properties of the crystals at the NIR spectral region may be of utility in biomedical technologies that involve an optical imaging step. Finally, Figure 58c shows that all samples were stable over time, as no major changes occurred in their absorption or fluorescence after the complexes had formed.

Demonstrating that the photosensitizer complex retains its excited state features like fluorescence even in the crystalline phase, $^1O_2$ generation will be evaluated in the following subsection, demonstrating the potential of the nanoscale arrays in aforementioned applications involving reactive oxygen species.

2.3.1.3. Singlet oxygen generation

Considering the multiple applications that photoinduced $^1O_2$ presents, showing the functional photosensitizing properties of the biohybrid crystals is critically important. Φ_Δ of **17** was determined in DMSO using the *relative method*, as explained in the experimental section. The employment of DMSO, as a coordinating solvent, disrupts the aggregation of **17** by coordination to the zinc metal center, resulting in a Φ_Δ value of 0.72 (non-substituted ZnPc was taken as reference – $\Phi_{\Delta(DMSO)} = 0.67$),[222] which indicates the excellent photosensitizing ability of **16** when it does not self-quench its excited state.

For measuring complex **16-PTSA** and the **16-PTSA**-**aFt** crystals, in turn, aqueous solubility of the scavenger was required. DPBF was then dispersed, from a concentrated solution in DMSO (ca. 1 mM), into a solution of the common neutral pharmaceutical solubilizer Cremophor EL (0.5 % w/w) in the 5 mM Tris buffer, together with the corresponding photosensitizing system (i.e., **16**, **16-PTSA** or **16-PTSA**-**aFt** and previously disassembled crystals in the presence of 500 mM of NaCl – **16-PTSA**-**aFt** NaCl). The absorbance of all samples at the Q-band maximum wavelength was adjusted to 0.1, to ensure that the concentration of PS was approximately equal in all samples. Decay of the scavenger absorption for the crystalline system **16-PTSA-aFt** during these experiments is shown in Figure 59a. Decrease in Q-band intensity or appearance of new bands were not observed in any case, confirming the photosensitizing system integrity over the whole experiment. Under these circumstances, dependence of $\ln(A_0/A_t)$ against irradiation time (t) (with A_0 and A_t being the respective scavenger absorbance values at the monitoring wavelength before and after the irradiation time t) was plotted, affording a straight line whose slope reflects the PS efficacy to generate $^1O_2$ (Figure 59b). A dark control was performed, showing that none of the samples induced DPBF bleaching in the absence of irradiation. Importantly, the **16-PTSA** complex photogenerates $^1O_2$ almost as efficiently as **16**, especially when it is co-crystallized with **aFt**. We can consequently conclude that **16-PTSA**-**aFt** represents the very first case of a highly efficient photosensitizing crystalline structure.

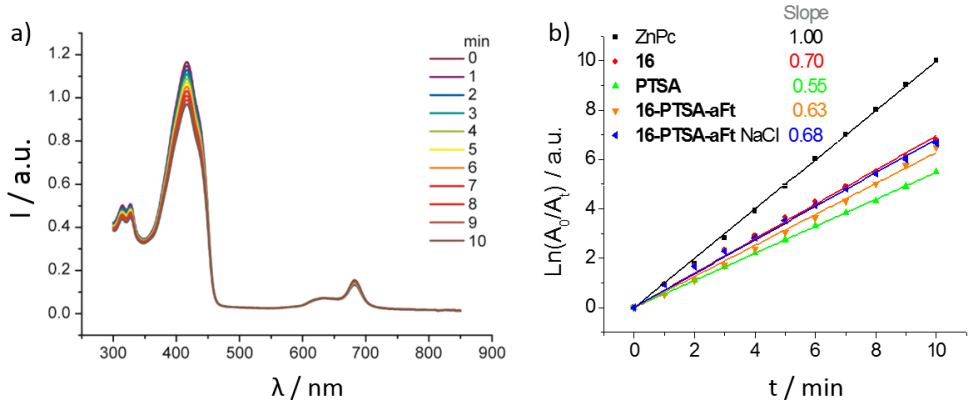

Figure 59. a) Plot of the DPBF absorption decay in the Tris buffer with Cremophor EL (0.5 % w/w) for **16-PTSA-aFt** sample. b) Normalized absorption ($\ln(A_0/A_t)$) of DPBF over time, showing its photodegradation rate in the presence of different PS. Solid lines present linear fits from which the slope is directly proportional to the photoinduced generation of $^1O_2$. ZnPc accounts for the non-substituted derivative used as reference compound. ZnPc stands for unsubstituted zinc phthalocyanine, employed as reference.

Finally, photodamage to **aFt** during irradiation of the **16-PTSA-aFt** crystals has been also evaluated (Figure 59). This has been carried out by irradiating the crystals over different periods of time in the same experimental conditions previously mentioned, long enough to entirely bleach the scavenger. The experiment was monitored by UV-Vis spectroscopy and SDS-PAGE after each irradiation period. Overall, no degradation of **aFt** was observed, indicating that the protein cage is resistant to $^1O_2$ and therefore the present crystalline platform is a sufficiently robust PS system for practical applications.

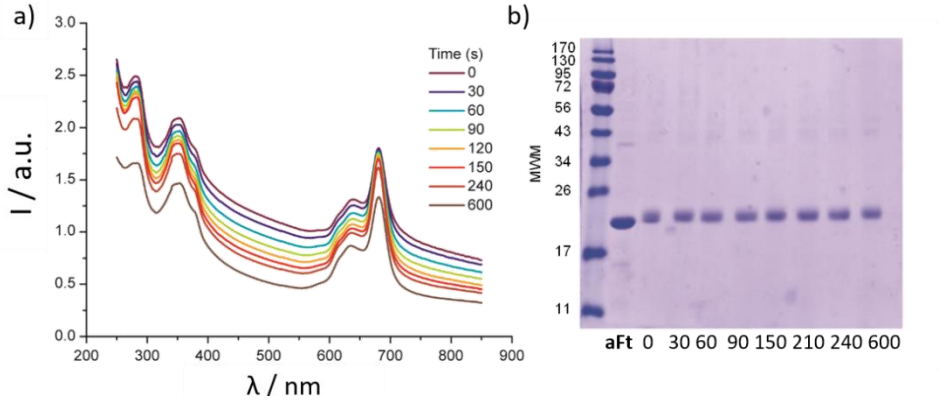

Figure 60. a) UV-Vis spectra of **16-PTSA-aFt** after each irradiation step. b) SDS-PAGE gel, showing **aFt** stability along irradiation time. 50 µL aliquots were then taken after each irradiation step. Molecular weigth markers (MWM) are given on the left (kDa).

In summary a hierarchical protocol to organize organic dyes and protein cages into functional ternary superlattices has been developed, based on the formation of a supramolecular complex between octacationic ZnPc **16** and tetraanionic pyrene derivatives **PTSA**. Formation of complex **16-PTSA** is driven by electrostatic and π-π interactions, which in turn binds to the negatively charged patches in the **aFt** protein cage exterior surface, acting as a molecular glue that induces co-crystallization. The resulting crystals are photoactive and robust biohybrid materials that emit fluorescence and can generate highly reactive $^1O_2$ without self-degradation upon irradiation. Moreover, such fcc-packed crystals, with diameters up to 100 μm, can be disassembled by increasing the electrolyte concentration. We envision that this kind of functional, highly ordered systems could be utilized, for example, to develop recyclable and environmentally benign water treatment agents, diagnostic arrays or photocatalytic crystals (e.g., of oxidation processes). Furthermore, the supramolecular approach is fully modular and can be easily extended to other cationic organic dyes that present different optoelectronic properties or **aFt** loaded with functional materials.

2.4. Photoactive cellulose nanocrystals by supramolecular surface immobilization of phthalocyanine photosensitizers

Cellulose represent the most abundant biopolymer produced in the biosphere and has been industrially processed and used for nearly 150 years. Actually, cellulose-related materials has been employed in nanoscience in the last two decades, resulting into environmental-friendly, high-end derivatives. In particular, rod-shaped cellulose nanocrystals (CNCs) have attracted growing attention due to their extraordinary mechanical properties, high aspect ratio and surface area, colloidal stability, biocompatible sugar-based chemical structure and cheap processing for a well-defined nanomaterial.[231] Main synthetic procedure to isolation of CNCs from cellulose fibbers is based on acid hydrolysis, cleaving the cellulose fibres transversely. The amorphous regions localized surrounding the microfibrils and embebed within the cellulose strands acts as structural defects that are removed upon hydrolysis, leaving the rod-shaped crystalline segments intact. Size and aspect ratio of the resulting CNCs strongly depends on the cellulose origin, with lengths from 70 nm (cotton) to few µm (*Valonia*).[231c] Moreover, different chemical modification procedures of the CNC surface has been described, being responsible of important modifications in their properties and, consequently, applications.[232] Only few examples has been described previously of chromophores in conjugation with CNCs like perylenes,[233] ruthenium complexes[234] and porphyrinoids.[235] In particular, Pcs remains

---

[231] a) M. Pääkkö, J. Vapaavuori, R. Silvennoinen, H. Kosonen, M. Ankerfors, T. Lindström, L.A. Berglund and O. Ikkala, *Soft Matter*, **2008**, *4*, 2492-2499. b) S.J. Eichhorn, A. Dufresne, M. Aranguren, N.E. Marcovich, J.R. Capadona, S.J. Rowan, C. Weder, W. Thielemans, M. Roman, S. Renneckar, W. Gindl, S. Veigel, J. Keckes, H. Yano, K. Abe, M. Nogi, A.N. Nakagaito, A. Mangalam, J. Simonsen, A.S. Benight, A. Bismarck, L.A. Berglund and T. Peijs, *J. Mater. Sci.*, **2010**, *45*, 1-33. c) Y. Habibi, L.A. Lucia and O.J. Rojas, *Chem. Rev.*, **2010**, *110*, 3479-3500. d) R.J. Moon, A. Martini, J. Nairn, J. Simonsen and J. Youngblood, *Chem. Soc. Rev.*, **2011,** *40*, 3941-3994. e) H. Rosilo, E. Kontturi, J. Seitsonen, E. Kolehmainen and O. Ikkala, *Biomacromolecules*, **2013**, *14*, 1547-1554. f) J.R. McKee, E.A. Appel, J. Seitsonen, E. Kontturi, O.A. Scherman and O. Ikkala, *Adv. Funct. Mater.*, **2014**, *43*, 2706-2713. g) M. Giese, L.K. Blusch, M.K. Khan and M.J. MacLachlan, *Angew. Chem. Int. Ed.*, **2015**, *54*, 2888-2910. h) A. Boujemaoui, S. Mongkhontreerat, E. Malmström and A. Carlmark, *Carbohydr. Polym.*, **2015**, *115*, 457-464.

[232] a) Y. Habibi, *Chem. Soc. Rev.*, **2014**, *43*, 1519-1542. b) S. Eyley and W. Thielemans, *Nanoscale*, **2014**, *6*, 7764-7779. c) J. Zoppe, L. Johansson and J. Seppälä, *Carbohydr. Polym.*, **2015**, *126*, 23-31.

[233] M.L. Hassan, C.M. Moorefield, H.S. Elbatal, G.R. Newkome, D.A. Modarelli and N.C. Romano, *Mat. Sci. Eng. B*, **2012**, *177*, 350-358.

[234] M.L. Hassan, C.M. Moorefield, H.S. Elbatal and G.R. Newkome, *J. Macromol. Sci. A*, **2012**, *49*, 298-305.

[235] a) E. Feese, H. Sadeghifar, H.S. Gracz, D.S. Argyropoulos and R.A. Ghiladi, *Biomacromolecules*, **2011**, *12*, 3528-3539. b) N. Drogat, R. Granet, C. Le Morvan, G. Begaud-Grimaud, P. Krausz and V. Sol, *Bioorg. Med. Chem. Lett.*, **2012**, *22*, 3648-3652.

almost unexplored, being only previously described by P. Chauhan and N. Yang as oxidant of aqueous chemicals.[236]

Aqueous formulation of the hydrophobic ZnPcs described in the first chapter of the present thesis is an important prerequisite for most of the applications described. Moreover, lack of aggregation, especially in high concentrations or in biologically related buffer solutions turns of capital interest, aiming to an efficient $^1O_2$ production. To this end, two cationic ZnPcs-CNC systems has been prepared by immobilization of cationic ZnPcs **17** and **33** to the surface of sulfated CNC through an easy, non-covalent approach, avoiding tedious chemical modification of the CNCs in collaboration with Prof. M.A. Kostiainen research group. The anionic ZnPc **1** was also employed as negative control, showing no functionalization of the CNC. In addition, $^1O_2$ production has been evaluated, proving the potential applicability of these complexes to be applied in biomedical, environmental or chemical applications.

2.4.1. **Synthesis and characterization**

Preparation of the functionalized CNCs (Figure 61) was accomplished as follows: pristine CNCs, synthesized following a previously described method,[237] were dissolved in milli-Q water (3 mL, 5 mg mL^{-1}) and were subsequently added to a solution of the corresponding ZnPc **1** and **16** (12 mL, ca. 0.1 mM) and sonicated for 90 minutes. In the case of ZnPc **30**, for the previous dissolution in aqueous medium, it had to be first dissolved in a concentrated solution in DMSO (ca. 10 mM) and then rapidly injected into water, with a final DMSO proportion of less than 1%. After sonication of the mixture, the resulting dispersion was centrifuged at 10000 rpm (9391 rfc) for 10 minutes. Colored supernatant was then removed and the pellet was washed by adding 10 mL of milli-Q water, re-dispersed by 2 minutes sonication and centrifuged for 10 extra minutes at 10000 rpm (9391 rfc). This procedure was repeated 5 times until no color was observed in the supernatant. In the case of ZnPc **1**, the pellet was shown as a white solid in contrast of ZnPcs **16** and **30** that were presented as blue solid.

---

[236] P. Chauhan and N. Yan, *RSC Adv.*, **2015**, *5*, 37517-37520.

[237] H. Rosilo, J. McKee, E. Konturi, T. Koho, V. Hyrtönen, O. Ikkala and M.A. Kostiainen, *Nanoscale*, **2014**, *6*, 11871-11881.

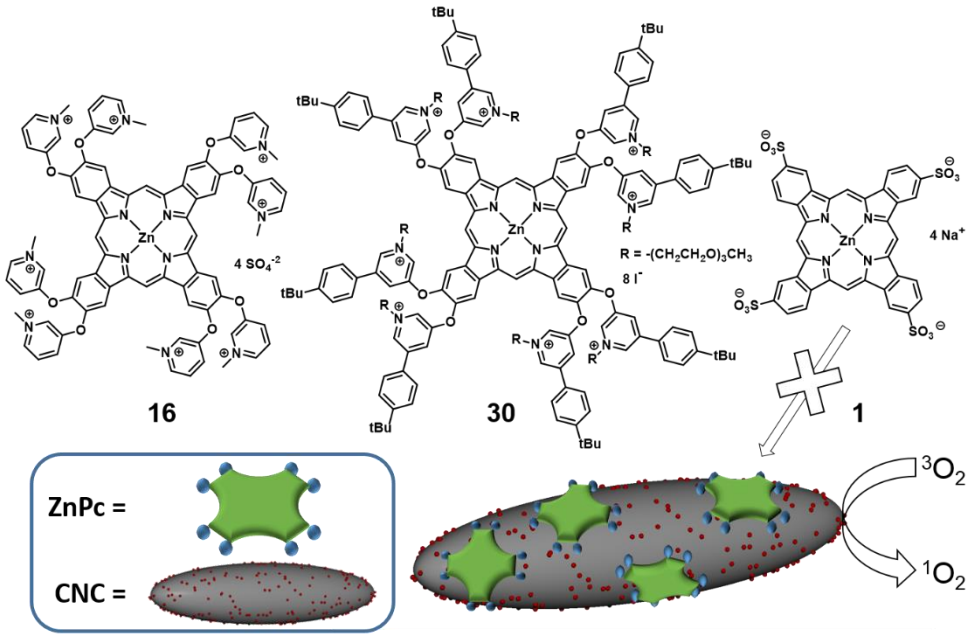

Figure 61. Chemical structures of ZnPcs **1** (negative control), **16** and **30**. Schematic representation of ZnPc immobilized supramolecularly onto the surface of sulfate-decorated CNC.

The ZnPc payload in the hybrids was determined through elemental analysis of lyophilized **16-CNC** (C, 43.0; H, 6.2; N, 0.23%) and **30-CNC** (C, 43.6; H, 6.14; N, 0.36%). By comparison with the molecular formulae of pristine CNC ($C_6H_{10}O_5)_n$, **16** ($C_{80}H_{64}O_{24}N_{16}S_4Zn$) and **30** ($C_{208}H_{256}O_{32}N_{16}I_8Zn$), combined in different ratios, the ZnPc payload in **16-CNC** and **30-CNC** was calculated to be 1.0 x 10^{-5} and 1.7 x 10^{-5} mol of ZnPc per gram of CNC respectively, as detailed in the experimental section. The binding efficiency was then evaluated for **16-CNC** (13.5%) and **30-CNC** (22.2% of sulfate groups neutralized by the ZnPc cationic charges) by comparing the ZnPc payload and the sulfate ester degree of substitution, previously determined as 0.1.[237] The robustness of the present non-covalent ZnPc-CNC hybrids was also evaluated by thermogravimetric analysis (Figure 62a). Pristine CNC start to decompose above 200 °C, owing to a catalytic effect that was previously assigned to the surface sulfate groups.[232c] On the other hand, decomposition of **16-CNC** and **30-CNC** only starts above 300 °C, suggesting that the catalytic effect is hindered in the hybrids, and further highlighting the interaction between sulfate moieties and cationic ZnPc as the binding driving force. Aggregation of ZnPcs **1**, **16** and **30**, has been studied by UV-Vis spectroscopy both in solution and bound onto the CNC (Figure 62b). At relatively high

concentration in water (0.1 mM), compounds **1** and **16** showed a strong absorption band at 635 nm, not present when the spectra were recorded in a coordinating solvent like DMSO, which is taken as an indication of *H*-type ZnPc aggregation. In the case of **30**, aggregation is partially prevented due to the presence of bulky groups. The absorption spectra of the ZnPc-CNC hybrids **16-CNC** and **30-CNC**, on the other hand, show the characteristics of non-aggregated ZnPc, as well as the typical scattering from CNC. On the contrary, the spectrum of **1-CNC** shows no ZnPc absorption features, indicating the absence of non-specific binding and proving cation-anion recognition as the driving force of the supramolecular immobilization process. Furthermore, binding to the CNC disrupts the ZnPc stacking, as observed by the absence of the 635 nm absorption band. This indicates that self-quenching has been avoided and the photosensitizing properties of the complex can be significantly improved.[14]

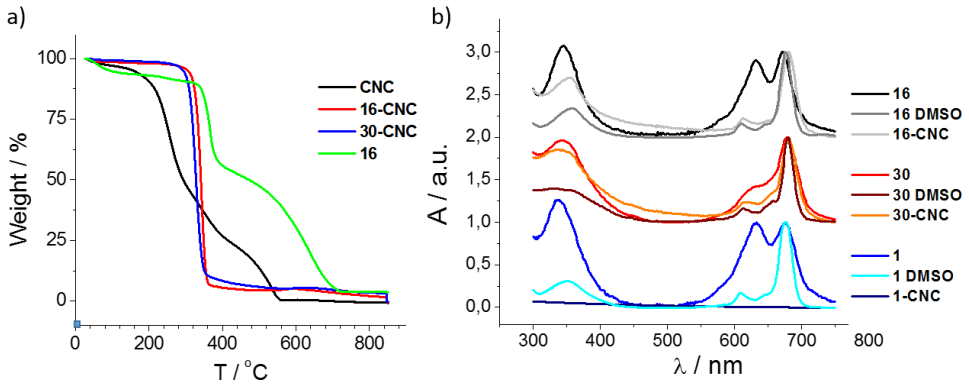

Figure 62. a) Thermogravimetric analysis of pristine CNCs, ZnPc **16** and composites **16-CNC** and **30-CNC**. Temperature increment of 20 °C/minute. b) Normalized to Q-band absorption spectra of compounds **16**, **30** and **1** in water and DMSO, as compared to those of hybrids **16-CNC**, **30-CNC** and **1-CNC**.

Dynamic light scattering (DLS) was then used to estimate the hydrodynamic diameter of pristine CNC (128 ± 8 nm), **16-CNC** (234 ± 17 nm) and **30-CNC** (216 ± 17 nm), at low concentration (0.05 mg mL^{-1}) to minimize the absorption of the ZnPc (Figure 63a). A significant increase in size can be observed for the complexes in comparison to non-modified CNC (Table 5). We ascribe this increase in size to a slight CNC aggregation and electrostatic cross-linking induced by the immobilized ZnPc. Yet the particle sizes still remain in the range of a few hundreds of nanometres and have moderate polydispersity index (PDI) values. The electric double layer of the system was evaluated by measuring the electrophoretic mobility (Table 5) and ζ-potentials (Figure 63b) of the hybrid particles at

0.05 mg mL^{-1}. The value found for **16-CNC** (-3.20 x 10^{-8} m^2 V^{-1} s^{-1}) closely resembles that of the pristine CNC (-3.23 x 10^{-8} m^2 V^{-1} s^{-1}), as a consequence of the low percentage of interacting sulfate esters (13.5%) in **16-CNC**, which leaves the electrostatic surface of the particles very similar to that in the absence of ZnPc. On the contrary, the electrophoretic mobility of **30-CNC** (-0.93 x 10^{-8} m^2 V^{-1} s^{-1}) drops drastically, as compared to pristine CNC, revealing neutral colloidal stabilization of the particle surface rendered by the methoxy(triethylenoxy) chains.

Table 5. Z-average size and PDI from DLS, mobility and ζ-potential measurements of CNC, **16-CNC** and **30-CNC**.

	Z-avg. / nm	PDI	Mobility / 10^{-8} $m^2 \cdot V^{-1} \cdot s^{-1}$	ζ-Pot. / mV
CNC	128±8	0.18	-3.23±0.04	-41.3±5.5
16-CNC	234±17	0.34	-3.20±0.2	-40.4±2.3
30-CNC	216±17	0.24	-0.93±0.12	-12.0±1.5

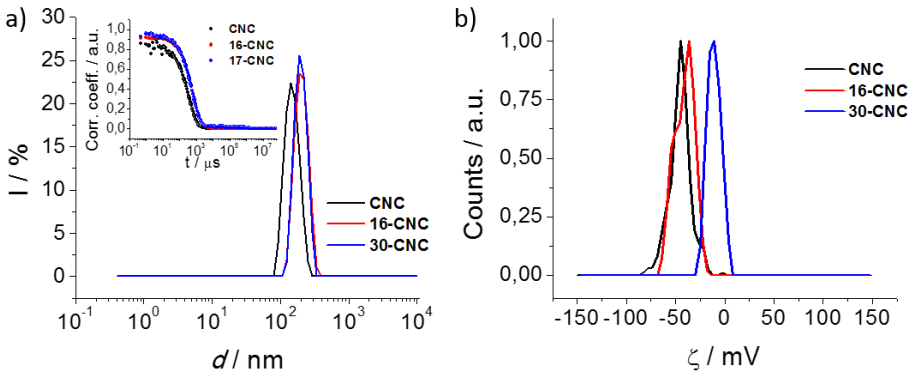

Figure 63. a) DLS results showing the increase in intensity-averaged size distribution when CNC are coated with **16** (**16-CNC**) and **30** (**30-CNC**) in 5 µg L^{-1} solutions. *Inset*: correlograms of selected spectra. b) ζ-potential of CNC showing no variation in **16-CNC** and a decrease of 29.3 mV in absolute value for **30-CNC**.

In order to characterize aggregation of the ZnPc-decorated CNCs, suggested above by DLS data, electron microscopy studies were also conducted. Cryogenic transmission electron microscopy (cryo-TEM) images of **16-CNC** (Figure 64a) show clusters of slightly

aggregated rod-shaped nanocrystals in different orientations. This behaviour differs from **30-CNC** (Figure 64b) where all the nanocrystals are shown in flat, highly orientated, well-packed sheets. We ascribe these differences to the presence of PEG chains in the chemical structure of **30** that hinder the binding to the CNC, yielding thermodynamically favored closed-packed assemblies. In opposition, **16** binds faster due to the exposed cationic surface, yielding kinetically trapped amorphous aggregates.

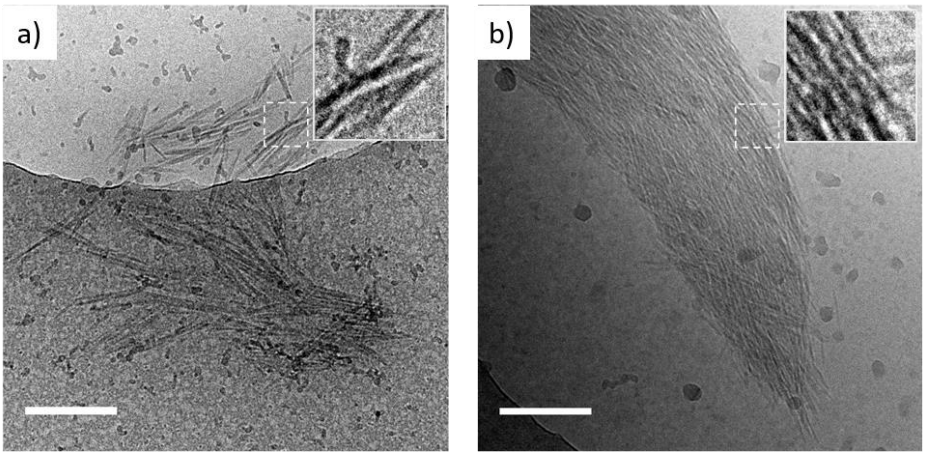

Figure 64. Cryo-TEM image of (c) **16-CNC** and (d) **30-CNC** at 0.5mg mL^{-1} in water. Scale bars: 200 nm. Insets show magnifications of the areas marked by dashed lines.

2.4.2. **Singlet oxygen generation**

To demonstrate the photosensitizing ability of the ZnPc-CNC complexes, we proceeded to study their efficacy for photoinduced $^1O_2$ production and to compare it with that of the corresponding free ZnPc derivative (Table 2, left column). Φ_Δ values for **16**, **30**, **16-CNC** and **30-CNC** were first determined in DMSO using the *relative method*, as explained in the experimental section. As a consequence, the four samples showed similar and very high Φ_Δ values, which correlates well with compounds **16** and **30** having a similar electronic structure and existing in their monomer form both in solution and onto the CNC.

For measuring in aqueous solution, i.e., in conditions much closer to the biological medium, DPBF had to be dispersed from a concentrated solution in DMSO (ca. 1 mM) into a solution of the common neutral pharmaceutical solubilizer Cremophor EL (0.5 % w/w) in

milli-Q water, together with the photosensitizing system (i.e. **16**, **30**, **16-CNC** and **30-CNC**). In this case, the presence of Cremophor EL does not allow determining absolute values for Φ_{Δ}, but plotting the dependence of $\ln(A_0/A_t)/A_{Q\text{-band}}$ against irradiation time (t) affords a straight line whose slope reflects the PS efficacy to generate $^1O_2$. Here A_0 and A_t are the respective scavenger absorbance values at the monitored wavelength (414 nm) before and after the irradiation time t. $A_{Q\text{-band}}$ is a normalization factor that, assuming ε as a constant in all samples, is proportional to and thus accounts for the PS concentration. then represents the scavenger photo-degradation profiles induced by **16**, **30**, **16-CNC** and **30-CNC**, revealing that the immobilization of **16** on the CNC surface enhances $^1O_2$ production over 30% (Table 6, right column), while the photosensitizing ability of **30** decreases to approximately 40% when present onto the CNC, always in comparison to the corresponding PS molecules in solution.

Table 6. $^1O_2$ quantum yield (Φ_{Δ}) values determined in DMSO (left column) and relative $^1O_2$ generation in 5% Cremophor EL aqueous solution (with **16** being taken as the reference), obtained from the normalized DPBF absorption decay sensitized by **16**, **30**, **16-CNC** and **30-CNC** (right column). All Φ_{Δ} values were determined as the average of three different measurements.

	Φ_{Δ} [DMSO]	**Relative $^1O_2$ production**
16	0.72	1.00
16-CNC	0.69	1.34
30	0.69	1.05
30-CNC	0.60	0.41

Importantly, these results can be rationalized based on the different modes of packing occurring for the two ZnPc-CNC hybrids (see cryo-TEM results above). **30-CNC** is a tightly packed system, limiting diffusion of molecular O_2 through the CNC bundles,[238] for which only the PS molecules in close contact with the solvent (i.e. located in the surface of those bundles) can effectively produce $^1O_2$. For **16-CNC**, the open amorphous CNC structure ensures contact of a higher fraction of PS molecules with the oxygenated solvent,

[238] A.J. Svagan, C.B. Koch, M.S. Hedenqvist, F. Nilsson, G. Glasser, S. Baluschev and M.L. Andersen, *Carbohydr. Polym.*, **2016**, *136*, 292-299.

which together with the observed negligible ZnPc stacking results in a highly efficient composite photosensitizing system.

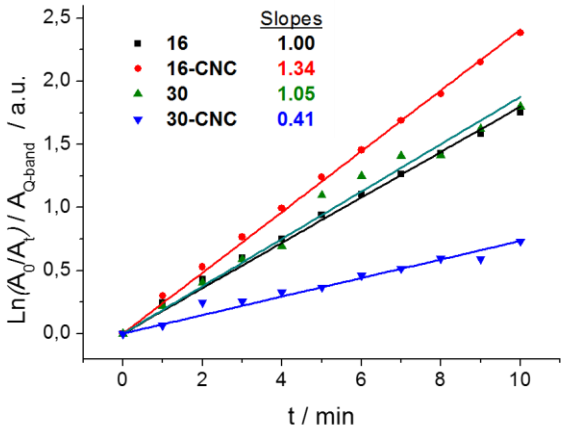

Figure 65. Normalized absorption profiles of DPBF in 5% Cremophor EL aqueous solution over time, showing its photo-degradation rate sensitized by **16**, **30**, **16-CNC** and **30-CNC**. The slope of each line denotes the relative capacity of the corresponding PS system for $^1O_2$ production, with **16** being taken as the reference.

In summary, supramolecular complexes of Pc molecules and nano-crystalline cellulose has been studied as a novel class of nano-structured chromophores for $^1O_2$ photo-generation. The immobilization strategy relies on electrostatic recognition between cationic ZnPc derivatives and unmodified CNC through an easy and straightforward non-covalent methodology. The resulting hybrids have been characterized by UV-Vis spectroscopy, DLS and cryo-TEM, proving that ZnPc stacking and CNC clustering are key processes that need to be prevented for an optimal $^1O_2$ production. As a result of their optimization, **16-CNC** represents a highly efficient photosensitizing system. Importantly, $^1O_2$ is a key species in therapeutic modalities such as PDT and PDI, as well as in water treatments, diagnostic arrays and photocatalytic technologies. The hybrids developed herein are therefore very promising photoactive biomaterials, which may find useful applications in biomedicine and nanotechnology.

2.5. Conclusions

In the present chapter three different biohybrid materials has been prepared by the combination of water-soluble cationic ZnPcs and affordable biomolecules. These carriers has been carefully selected in order to maintain or highlight the already outstanding properties of Pcs by disrupting typical aggregation of these hydrophobic macrocycles in aqueous media. The employment of biomolecules such as virus capsids, protein NPs or CNCs in combination with water soluble ZnPcs means taking advantage of biocompatible, water-formulated homogeneous nanocarriers that leads into well-defined nanostructured photoactive moieties. Moreover, a supramolecular approach has been employed in each example, resulting into challenging yet straight-forward methodology that avoids long or complex synthetic routes, lowering expenses thus making them more suitable to be applied.

First example consists in a ternary multifunctional system with potential applications in nanomedicine as multimodal imaging and theranostic agent. This nanoparticle consists in a protein coat from CCM virus hierarchically self-ensembled by the templating effect of previously self-ensembled Gd^{3+}-containing micelles, bearing amphiphilic ZnPc **6**. Stability of the mentioned multifunctional micelles was concomitantly increased by confining them within the virus-like NP. Moreover, characterization of the system has been carried out by different experimental techniques such as FPLC, TEM and TRXF. Resulting MRI enhanced response, along with the well know potential of non-aggregated ZnPcs role as fluorescence contrast agent and its high ϕ_Δ of 0.68 leads into an optimized yet in development nanomedicine multimodal agent.

Secondly, in collaboration with Prof. M.A. Kostiainen research group, a hierarchical protocol to organize organic dyes and protein cages into functional ternary superlattices has been developed. This nanoscale arrays are based on the formation of a supramolecular complex between ZnPc **16** and tetraanionic pyrene derivative **PTSA**. Tetracationic complex **16-PTSA** act as molecular glue, inducing co-crystalization of the **aFt** by binding to its negatively charged patches. Both **16-PTSA** complex and crystalline lattices has been thoroughly characterized by absorption, fluorescence, optical microscopy and SAXS. This results in the first example of crystalline arrays that emit fluorescence and can generate $^1O_2$ to be applied in environmentally benign water treatment agents, diagnostic arrays or photocatalytic crystals.

Finally, and during an internship in the group of Prof. Mauri A. Kostiainen, a novel class of nano-structured chromophores for $^1O_2$ photogeneration has been developed by grafting cationic ZnPcs **16** and **30** onto unmodified negatively charged CNCs. This functionalization relies on electrostatic interactions, resulting into fully disaggregated ZnPcs. Resulting nano-structured chromophores has been deeply characterized by absorption, elemental analysis, DLS, ζ-potential and cryo-TEM. Moreover, bundling behavior of CNCs in suspension has been found of capital importance for an optimal $^1O_2$ production. As a result of their optimization, **16-CNC** represents a highly efficient photosensitizing system to be employed in therapeutic modalities such as PDT and PDI, as well as in water treatments, diagnostic arrays and photocatalytic technologies.

2.6. Experimental Section

2.6.1. **Materials and methods**

All reagents were commercially available and used without any further purification. The water used in all procedures was Milli-Q purified. Phosphate-buffered saline (PBS buffer, 10 mM Na_2HPO_4, 2.7 mM KCl, 187 mM NaCl, pH 7.4) or Tris buffer (20 mM Tris, pH 8.5) has been prepared by solution of commercially available salts in milli-Q water. Apoferritin (**aFt**) from *Pyrococcus furiosus* was ordered from Molirom and it was delivered as a 10 mg mL^{-1} water solution. **aFt** is a 12 nm spherical protein cage with an inner cavity of 8 nm in diameter.[2,3] The protein shell consists of 24 protein subunits that each have a molecular weight of 20 kDa. **aFt** can withstand high pH (8.5–9) and temperature (85–90 °C).

Optical microscopy was performed on a marienfeld-superior microscope slide ($76 \times 26 \times 1.35$ mm with a round cavity of 15-18 mm diameter and 0.6-0.8 mm depth) and a cover glass was placed on the sample. Samples of 20 µL were imaged with Leica DM4500 P optical microscope equipped with Canon EOS 60D camera using transmission mode. A ruler at the sample position was imaged to calibrate the scale of the images.

SAXS measurements were carried out using a rotating anode Bruker Microstar microfocus X-ray source (Cu Kα radiation, λ = 1.54 Å). The X-ray beam was monochromated and focused by a Montel multilayer focusing monochromator (Incoatec). The beam was further collimated by four slits (JJ X-Ray) resulting in a beam size of less than 1 mm at the sample position. The scattering was collected using Hi-Star 2D area detector (Bruker). The used sample-to-detector distance was 1.59 m, and silver behenate standard sample was used to calibrate the q-range. One-dimensional SAXS data were obtained by azimuthally averaging the 2D scattering data. The magnitude of the scattering vector q is given by $q = 4\pi \sin\vartheta/\lambda$, where 2ϑ is the scattering angle. The samples were measured as is: i.e. 10 µL of **44**-**aFt** crystal sample solution was sealed in a metal ring using Kapton tape. Sample thickness was approximately 0.9 mm. The sample environment was evacuated during the measurements to avoid scattering from air. SAXS measurements from non-powder-like samples with large crystals, (i.e. crystals formed in 30 mM NaCl concentration) were unsuccessful due to the fast sedimentation of large crystals and possible instability of the crystals in the X-ray beam.

SDS-PAGE gels was performed as follows: fractions containing irradiated **16-PTSA**-**aFt** crystals for different times (30 s – 6 min) were added to Laemmli simple buffer to a 1x

final concentration (62.5 mM Tris–HCl, 2% SDS, 5% glycerol, 0.012% bromophenol blue, 2 mM dithiothreitol, pH 6.8), heated (3 min, 100 °C), and resolved in 14% polyacrylamide gels at 20 °C until the dye reached the gel bottom. Samples were visualized by Coomassie blue staining.

The FPLC was equipped with a Superose 6 size exclusion column 10/100 GL (GE Healthcare) with a bed volume of 2.4 mL. Injection volume: 100 µL. The capsid concentration in each sample used for further elemental analysis was determined by measuring its UV absorbance at 280 nm, using a ε_{CP}= 24080M^{-1} cm^{-1}.

TXRF measurements were performed by a Bruker S2 Picofox apparatus (Bruker AXS GmbH, Karlsruhe, Germany) portable system. The primary X-rays were generated by an air-cooled lowpower X-ray tube using a molybdenum anode. The excitation settings were 50 kV and 750 mA. Measurements were performed by signal integration over 1500 s. Quartz glass disks were used as sample carriers, which were previously cleaned in 1 N nitric acid followed by flushing in water for 1 h at 80 °C. They were subsequently dried, coated with silicon solution for better wettability and dried again. Samples for TXRF analysis were prepared by adding equal amounts of the gallium internal standard (10 mg L^{-1}) and the sample to be analyzed (volume). After vortexing, a drop of the solution was placed on the quartz disk and dried under vacuum for 15 min. For control purposes, elemental analysis of the empty capsid (in buffer) was conducted and the obtained values for each sample were corrected. The quantification is performed by the Bruker S2 Picofox TXRF software (Spectra,Version 6.1.5.0), based on the known quantity of the gallium internal standard added.

Transmission electron microscopy (TEM) images were obtained using analytical TEM FEI instruments. Samples were preparated by dropping 5 µL of the desired sample onto Formvar-carbon coated grids (from Electron Microscopy Sciences). The sample was left for 1 minute and the excess of liquid was removed using a piece of filter paper. Uranyl acetate (5 µL, 1% w/v) was then applied and the drying procedure was repeated. The particle size distribution of the newly formed assemblies (after purification by FPLC) was determined by analyzing over 200 particles observed in TEM images.

Cryo-TEM images were carried out with JEOL JEM-3200FSC equipment. Vitrification of samples was done with a Vitrobot in a saturated water vapor environment. A drop (3 µL) of freshly sonicated ZnPc-CNC solution (ca. 0.5 mg·mL^{-1} of CNC) was deposit on Quantifoil R2/1 grid and the excess sample was blotted away with filter paper. Blot and drain times

were 2 and 0.5 s, respectively. Grids were plunged into liquid ethane/propane (1:1) solution that was cooled with liquid nitrogen surrounding the ethane/propane container.

MRI experiments were carried out on a 14.1 T (600MHz) Avance II NMR Spectrometer from Bruker (Karlsruhe, Germany), equipped with a vertical narrow bore magnet (14.1 T), a great B_0 compensation unit (BGU-II) and 3 great 1/60 amplifier units (X, Y and Z) also from Bruker. A micro 5 imaging probe, equipped with a 10mm diameter saddle coil insert from Bruker (Karlsruhe, Germany) was used. The maximum gradient strength was 4.8 G cm^{-1} A^{-1} and the temperature inside the probe was kept at ~25 ^{o}C by a gradient water cooling unit BCU20 from Bruker. Experiments (acquisition and processing) were carried out using Paravision (v. 4.0)/Top Spin (v. 1.5). All NMR/MRI tubes (5/10 mm diameter) were purchased from Wilmad Labglass (New Jersey, U.S.A.). Glass capillary tubes (melting point tubes, inner diameter 1mm) used for MRI were purchased from VWR, Germany.

T_1 measurements were performed in a 1 cm (outer diameter) glasstube as follows: stock solutions of the Gd-DOTAC10 complex and the encapsulated Gd-DOTAC10/ZnPc micelles (with known concentrations of Gd^{3+} and capsid) were diluted 2, 5 and 10 times. For each experiment, capillary tubes of 1mm inner diameterwere filled with these solutions, placed in a custom-made Kel-F capillary holder and subsequently introduced in the 1 cm tube for imaging. Longitudinal relaxation timeswere measured using a saturation recovery pulse sequence with static TE (echo time) = 6 ms and 16 TR (repetition time) values, namely 100, 150, 200, 350, 500, 600, 700, 800, 1000, 1500, 2000, 3000, 4000, 6000, 8000 and 10000 ms. The measurements were done on 5 subsequent axial slices of 1mm, with a field of view of 10mm × 10 mm, a matrix size of 128 × 128 and 2 averages. T1 values were obtained by mono- exponentially fitting the intensities of selected regions of interest for each axial slice using the image sequence analysis tool in Paravision 4.0 software. T_1-weighted images were obtained using a spin echo sequence with the following parameters: TR = 500 ms, TE = 6 ms, 1 axial slice of 6mmthickness, field of view=10mm× 10mm, matrix size = 256 × 256 and 10 averages. The longitudinal relaxivity r_1 (in mM^{-1} s^{-1}) was obtained as the slope of the plot $1/T_1$ vs. Gd^{3+}.

A Zetasizer Nano ZS90 analyzer (Malvern Instruments) with a He–Ne laser of 633 nm was used for measuring the particle size distributions, electrophoretic mobilities and ζ-potentials of pristine CNC, **16-CNC** and **30-CNC** at a 90° scattering angle. Disposable PMMA cuvettes (Plastibrand) were used for DLS measurements and Universal 'Dip' cell (ZEN1002) for ζ-potential measurements. CNC (0.5 mg mL^{-1} in Milli-Q water), **16-CNC** and **30-CNC**

(0.05 mg mL^{-1} in Milli-Q water) were sonicated and filtered through 0.45 mm filters (Corning) immediately before measuring at 25 °C. DLS results are an average of three measurements with 10 measurement runs of 10 seconds each. Mobility values were converted to ζ-potentials using the Smoluchowski equation and reported values are an average of four measurements with 50 measurement runs.

2.6.2. **Singlet oxygen quantum yield**

Singlet oxygen quantum yield (Φ_Δ) was calculated through Equation 2:

$$\Phi_\Delta^S = \Phi_\Delta^R \frac{k^S I_{aT}^R}{k^R I_{aT}^S} \quad (2)$$

where k is the slope of a plot of ln (A_0/A_t) *versus* irradiation time t, with A_0 and A_t being the absorbance of chemical trap at the monitored wavelength before and after irradiation time t, respectively. I_{aT} is the total amount of light absorbed by the dye. Superscripts *R* and *S* indicate reference and sample, respectively. I_{aT} is calculated as a sum of intensities of the absorbed light I_a at wavelengths (DMSO : from 506 nm to 800 nm; H_2O : from 455 to 800 nm; step 0.5 nm). Light under 506 or 455 nm is completely filtered off by a filter, while light above 800 nm is not absorbed by the dye. I_a at given wavelength is calculated using Beer's law (Equation 3):

$$I_a = I_0(1 - e^{-2.3A}) \quad (3)$$

Where transmittance of the filter at a given wavelength stays for I_0 and the absorbance of the dye at this wavelength stays for A.

In detail the procedure was as follows:

The measurements were performed in DMSO and D_2O, using as standard reference non-substituted ZnPc and Eosin Y, and as chemical scavenger 1,3-diphenylisobenzofuran (DPBF) and anthracene-9,10-diyl-bis-methylmalonate (ADMA), respectively.All experiments were performed three times (unless noted otherwise) and the obtained data represents a mean value of these three experiments. The estimated error is ± 10%. 1.8 mL of a stock solution of DPBF (with an absorbance of ca. 1) in DMSO was transferred into a 1 x 1 cm quartz optical cell and bubbled with oxygen for 1 min. Concentrated stock solution of the reference was added in a defined amount to reach an absorbance of the final solution in

the Q-band maximum of about 0.1. Same procedure was follow with the sample, approaching the absorbance maximum of the Q-band to 0.1. The solution was then stirred for 1 min and irradiated for defined time intervals using a halogen lamp of 300 W. Incident light was filtered through a water filter to remove heat and an orange HOYA G (DMSO) or MS filter to remove light under 530 and 455 nm, respectively. Decrease of the scavenger concentration with irradiation time was monitored at 414 nm and 377 nm in the case of DPBF and ADMA, respectively. No significant changes in Q-band shape or intensity indicates no decomposition or aggregation of the chromophore within the experimental period.

2.6.3. **Job's plot method**

Eleven 3 mL samples with different portions of **1** and **2** in PBS buffer were prepared and their UV–Vis absorption was measured for the job plot experiment (Figure S2). Measurements were carried out using a JASCO V-660 spectrophotometer and a Hellma QS quartz cuvette with a 1 cm light path at room temperature. Absorption spectra were scanned with 1 nm resolution. The concentration of both components in different samples varied from 10 to 0 µM so that the overall concentration was always 10 µM.

An equimolar job plot diagram was derived from the UV–Vis spectra shown. Δ*A* (A_{exp} - A_0) was calculated for each sample, for the job plot diagram at 631 nm using the following equation

$$A_0 = \varepsilon_{\mathbf{1}} x c_0 + \varepsilon_{\mathbf{2}}(1-x)C_0$$

where $\varepsilon_{\mathbf{1}}$ and $\varepsilon_{\mathbf{2}}$ are the molar extinction coefficients of **1** and **2**, x is the molar fraction of **1** and C_0 is the total concentration of both components in the solution. -Δ*A* was presented as a function of the molar fraction of **1**, and the highest point occurred at x = 0.5 (Figure S2b), which corresponds to a 1:1 stoichiometry of **1** and **2**.

2.6.4. **ZnPc-CNC load determination**

Elemental analysis was carried out in a LECO CHNS-932 analyser.

Nitrogen percentage ($\%_N$) of the ZnPc-CNC composites is given by the following formula:

$$\%_N = \frac{M_N}{M_C + M_H + M_O + M_N + M_{Zn} + M_I + M_S}$$

where *M* is the elemental mass and the element is denoted in the corresponding subindex. The elemental mass of nitrogen and, likewise, the rest of elements were calculated through the following formula:

$$M_N = mw_N\,(aN_{ZnPc} + bN_{CNC})$$

where *mw* is the molecular weight of the element, N_{ZnPc} and N_{CNC} are the number of nitrogen atoms of the ZnPc and the CNC respectively. Parameters *a* and *b* denote the relative ratio between ZnPc and CNC. Applying both formulas to composites **16-CNC** and **30-CNC**:

16-CNC:

$$0.0023 = \frac{14.01 \cdot (16a)}{12.01 \cdot (80a + 6b) + 1.01 \cdot (64a + 10b) + 16 \cdot (24a + 5b) + 14.01 \cdot (16a) + 65.34a + 32.06 \cdot (4a)}$$

If *a* = 1, *b* = 589.75 or, what is the same, 589.75 mol of glucose monomers per ZnPc **1** mol. Multiplying this value by the molecular weight of glucose gives 1 ZnPc **1** mol per 95633 g of CNC or, otherwise, 1.05×10^{-5} mol of ZnPc **1** per gram of CNC.

30-CNC

$$0.0036 = \frac{14.01 \cdot (16a)}{12.01 \cdot (208a + 6b) + 1.01 \cdot (256a + 10b) + 16 \cdot (32a + 5b) + 14.01 \cdot 16a + 65.34a + 126.9 \cdot 8a}$$

If *a* = 1, *b* = 355.78 or, what is the same, 355.78 mol of glucose monomers per ZnPc **16** mol. Multiplying this value by the molecular weight of glucose gives 1 ZnPc **30** mol per 57693 g of CNC or, otherwise, 1.73×10^{-5} mol of ZnPc **30** per gram of CNC.

Sulfate ester degree of substitution has been previously quantified as 0.1 so 1 of each 10 glucose monomers presents a sulfate ester. Using data obtained from elemental analysis, the number of sulfate esters interacting with ZnPc charges has been estimated.

Table 7. Coverage data extracted from elemental analysis.

	Glucose units per ZnPc	**Sulfate esters per ZnPc**	**Charges ratio (ZnPc:CNC)**	**%**
16-CNC	589.75	59.0	8 : 59	13.5 %
30-CNC	355.78	35.6	8 : 36	22.2 %

Chapter III: Aqueous phthalocyanine systems for energy conversion

3. Chapter III: aqueous phthalocyanines for energy conversion

3.1. Introduction to photovoltaic processes and devices

3.1.1. Characteristic parameters of solar cells

The properties of photovoltaic devices can be characterized by plotting the measured current density output (*J*) of the cell *versus* the voltage output (*V*) of the cell (*J-V* graph). In the dark, this *J-V* curve passes through the origin, since at that moment no current is flowing through the device and no potential is present. By exposing the photovoltaic device to the light, the *J-V* curve shifts down due to the generated photocurrent (Figure 66). The most important parameters extracted from this plot are the following:

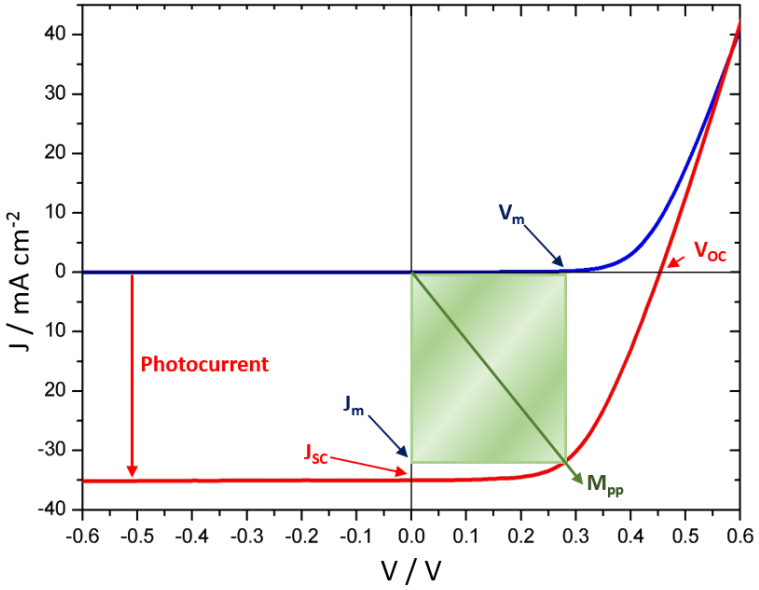

Figure 66. Typical J-V curve for any type of solar cell in the dark (blue) and under illumination (red). The most important photovoltaic parameters are indicated.

(ix) Short-circuit current (I_{SC})

It is the current that flows through an illuminated solar cell when there is no external resistance (i.e. the electrodes are simply connected or short-circuited). I_{SC} is the maximum current that a photovoltaic device is able to produce. The short-circuit current depends on

a number of factors, such as the area of the solar cell. Due to this and to remove the dependence of the solar cell area, it is more common to list the short-circuit current density (J_{SC} in mA cm^{-2}), rather than the short circuit current (I_{SC} in mA).

(x) Open circuit voltage (V_{OC})

It is the maximum possible voltage across a photovoltaic device. This is the voltage across the cell, under illumination, when no current is flowing through the device.

(xi) Maximum power point (Mpp)

This magnitude makes reference to the point (V_m, J_m) on the *J-V* curve at which the maximum power is produced. Power is the product of current *J* and *V*. On the graph, it is represented as the rectangle formed between the point on the *J-V* illuminated graph and the axes where the area is maximum.

(xii) Fill Factor (FF):

This magnitude represent the ratio of its actual maximum power to its theoretical power output, if its *J* and k would be at their maxima (i.e. J_{SC} and V_{OC}, respectively). The more "square" the graph, the better FF. This is a very important property used to measure the photovoltaic device performance and can be written down as follows (Eq. 1):

$$FF = \frac{J_m \times V_m}{J_{SC} \times V_{OC}} \qquad \text{Eq. 1}$$

(xiii) Power Conversion Efficiency (PCE or η)

This is the most general way to define the efficiency of a photovoltaic device and correspond to the ratio of power output (P_{out}) to power input (P_{in}). PCE measures the amount of power produced by a photovoltaic device relative to the power available in the incident solar radiation. P_{in} is the sum over all wavelengths of the incident light, which usually has a value of 100 mW cm^{-2} when solar simulators are used. PCE can be written down as follows (Eq. 3):

$$PCE\ (\eta) = \frac{P_{out}}{P_{in}} \times 100\% = \frac{J_m x V_m}{P_{in}} \times 100\% = \frac{J_{SC} x V_{OC} x FF}{P_{in}} \times 100\% \qquad \text{Eq. 3}$$

PCE is one of the most important parameter to characterise solar cell performances. In order to compare results from various devices, regardless of the design and active material, photovoltaic cells are all subject to the same standard test conditions. The cells are typically illuminated at a constant density of ca. 100 mW cm^{-2}, which is the defined as the standard "1 Sun" value, with a spectrum consistent to an air-mass global value of 1.5

(AM 1.5G), at a temperature of 25 ^{o}C. Air mass describes the spectrum of radiation and can be defined as the amount of atmosphere trough sunlight has to pass to reach the Earth's surface. This is the abbreviated as AM x, in which x is the inverse of the cosine of the zenith angle of the sun. The above mentioned AM 1.5G conditions, taken as standard, correspond to the spectrum and irradiance of sunlight incident with a zenith angle of 48.2^{o}.

(xiv) External quantum efficiency (EQE)

Also known as IPCE, is another important parameter for solar cell characterization. It is calculated by the number of electrons extracted in an external circuit, divided by the number of incident photons at a certain wavelength under short-circuit condition. IPCE can be written down as follows (Eq. 4).

$$IPCE = \frac{number\ of\ electrons}{number\ of\ incident\ photons} = \frac{J_{SC}(\lambda)/e}{P_{in}(\lambda)/(hc/\lambda)} = \frac{J_{SC}(\lambda)hc}{P_{in}(\lambda)e\lambda} \qquad \text{Eq.4}$$

where λ is the wavelength, *e* is the elementary charge, *h* is the Planck constant and *c* is the speed of light in vacuum.

3.1.2. **Small-molecules for planar heterojunction solar cells**

Among the different types of organic solar cells (OSCs) overviewed in the introduction of the present thesis, next subsections are focused in planar heterojunction solar cells composed by small-molecules in order to introduce in detail the devices described in the present chapter. Other compositions or architectures will not be discussed as a matter of extension.

In general terms, the photovoltaic process for solar cells[239] is triggered by the absorption of light by the active layer, exciting an electron from the higher electronically occupied band to the lower unoccupied band (i.e. HOMO to LUMO in organic solar cells and valence to conduction bands in semiconductors), subsequently generating an exciton (i.e. electron-hole pair). In the case of the semiconductors, the absorption of photons with energies greater than the bandgap of the semiconductor results in the direct generation of free charge carriers (electron and holes) that are able to diffuse under an externally applied

[239] a) T.M. Clarke and J.R. Durrant, *Chem. Rev.*, **2010**, *110*, 6736-6767. b) X. Liu, H. Chen and S. Tan, *Renew. Sust. Energ Rev.*, **2015**, *52*, 1527-1538.

electric field to their respective electrodes. On the other hand, organic materials characteristically have a much lower dielectric constant than their inorganic counterparts, resulting in the generation of tightly coulombically bounded exciton pairs, with a binding energy range that lies from 0.1 to 0.5 eV.[239] In addition, organic semiconductors do not exhibit band-like transport behaviour, rather than moving along by a hopping mechanism between localized states.[240] The charge-carriers mobility in organic semiconductors are, therefore, inherently low, with typical values less than 10^{-2} cm^2 V^{-1} s^{-1}. Aforementioned differences between inorganic and organic semiconductors drive the structural design of organic solar cells.

3.1.2.1. Planar heterojunction devices

As previously discussed, in 1986 Tang boosted the organic photovoltaic (OPV) performance, using a two component donor:acceptor active layer, consisting of a copper Pc (CuPc – donor) and a perylene derivative (acceptor), in a planar heterojunction device.[ref] The general principle ruling the heterojunction devices is to use two organic materials with different electron affinities and ionization potentials. In this manner, exciton dissociation at the heterojunction's interface of the two components will be favoured by the electron withdrawing from the organic material with the largest electron affinity. Moreover, the hole remains in the component with the lowest ionization potential.

In a typical heterojunction photovoltaic device, four main processes occur during the conversion of solar into electrical energy (Figure 67). Induced by light absorption, an electron is promoted from the HOMO to the LUMO of the photoactive specie, forming an exciton (step 1; photoinduced exciton generation). This formed exciton moves towards a donor/acceptor interface *via* chemical potential gradient (step 2; exciton diffusion to the interface) where the electron can transfer to the LUMO of the acceptor material, forming a charge transfer complex. This complex is favourable to occur when the energy difference between the LUMO of the donor (blue) and acceptor (red) is greater than the binding energy of the exciton. This energy difference is typically on the order of a couple hundred meV, depending on the materials employed. Any energy excess absorbed by this exciton is lost in the systems. Despite the localization of the electron and hole in different materials, they still remains strongly bounded by coulombic interactions. The charge transfer state then becomes a charge separated state, or free charge carriers (step 3; exciton

[240] V. Coropceanu, J. Cornil, D.A.S. Filho, Y. Oliver, R. Silbey and J.-L. Bredas, *Chem. Rev.*, **2007**, *107*, 926-952.

dissociation) if the distance between the electron and hole becomes greater than the coulomb capture radius (i.e. the mutual separation of two charges at which the Coulombic attraction is less than κT). Any dissociated charge is then transported through p-type or n-type domains to the electrodes (step 4; charge collection), with holes being collected at the anode (usually a transparent electrode such as ITO) and electrons being collected at the cathode (usually a low work function metal like aluminium). Moreover, other elements are usually employed in the construction of PHJ devices in order to enhance its performance. As most employed example, ITO anode is usually coated with an interfacial hole blocking layer like poly(3,4-ethylenedioxythiophene):poly(styrenesulfonate) (PEDOT:PSS) in order smoothens out the ITO surface, seals the active layer from oxygen and prevents the diffusion of ITO into the active layer.

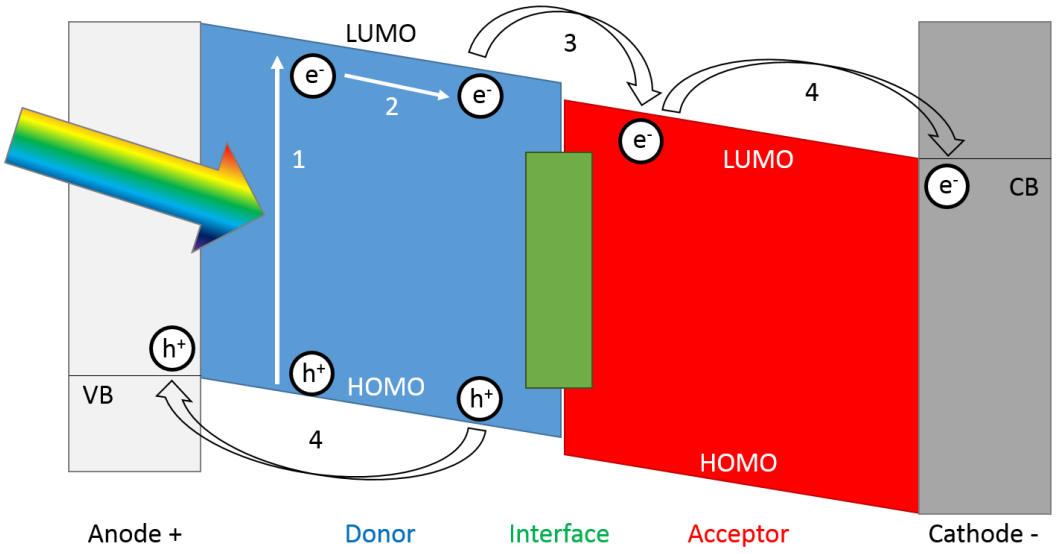

Figure 67. Schematic representation of the operating principles of organic photovoltaic (OPV) devices, highlighting the desired transport of charge pairs generated at interface (green) through the donor (blue) and acceptor (red) materials. CB and VB denotes conduction and valence band respectively.

Unfortunately, not all the incident light is converted into photocurrent. There is some undesired side-processes that limits the efficiency of a device.[241] For example, not all

[241] a) D. Veldman, S.C.J. Meskers and R.A.J. Janssen, *Adv. Funct. Mater.*, **2009**, *19*, 1939-1948. b) C.W. Schlenker and M.E. Thompson, *Chem. Commun.*, **2011**, *47*, 3702-3716. c) U. Hormann, J. Kraus, M. Gruber, C. Schuhmair, T. Linderl, S. Grob, S. Kapfinger, K. Klein, M. Stutzman, H.J. Krenner and W. Brutting, *Phys. Rev. B*, **2013**, *88*, 235307-

the incoming photons are absorbed by the active layer. This is a result of the limited bandgap and thickness of the active layer, thus a highly absorbing, panchromatic dye is desirable. In addition, excitons which are created too far from the donor/acceptor interface (exciton diffusion length is limited to 5-10 nm),[242] are not able to dissociate into free charge pairs within the lifetime of the exciton, resulting into undesired by-processes, which make the exciton decay back to its ground state. Other loss mechanisms are the recombination of the hole-electron pair across the donor/acceptor interface (referred to as geminate recombination) and recombination of free charges during transportation to the electrodes. All these energy losses have a direct bearing on the solar cell efficiency and characteristic parameters such as J_{SC}, V_{OC} and FF are also impacted. For instance, the Incident Photon to Current Efficiency (ICPE), which describes the overall efficiency of the four main processes of the photovoltaic process in OPVs can be described as follows (Eq. 1)

$$ICPE = \eta_{abs}(\lambda) \times \eta_{diff}(\lambda) \times \eta_{ct}(\lambda) \times \eta_{coll}(\lambda) \qquad \text{Eq. 2}$$

where η_{abs} is the photoabsorption efficiency, η_{diff} is the exciton diffusion efficiency to the donor/acceptor interface, η_{ct} is the charge transfer efficiency,[243] η_{coll} is the charge collection efficiency, and λ is the wavelength of intereste. ICPE values close to 1 for a specified wavelength indicate efficient current generation for light absorbed at that wavelength with limited recombination losses. The J_{SC} is dependent on efficient light-harvesting, carrier generation and mobility, while the V_{OC} is proportional to the energy difference between the HOMO of the donor and the LUMO of the acceptor.[244] In this respect, molecular orbital levels, absorption coefficients, morphology of the layers and molecular diffusion length are the main factors that control the final result. Research in the field during the last decade, based in rational design of new optimized materials has led to power conversion efficiencies (PCEs) of 11.0.[245]

23531867. d) W. Li, K.H. Hendriks, A. Furlan, M.M. Wienk and R.A.J. Janssen, *J. Am. Chem. Soc.*, **2015**, *137*, 2231-2234.

[242] Y. Wang, H. Benten, S. Ohara, D. Kawamura, H. Ohkita and S. Ito, *ACS Appl. Mater. Interfaces*, **2014**, *6*, 14108-14115.

[243] H. Bässler and A. Köhler, *Phys. Chem. Chem. Phys.*, **2015**, *17*, 28451-28462.

[244] a) C.J. Brabec, A. Cravino, D. Meissner, N.S. Sariciftci, T. Fromherz, M.T. Rispen, L. Sanchez and J.C. Hummelen, *Adv. Funct. Mater.*, **2011**, *11*, 374-380. b) B. Qi and J. Wang, *J. Mater. Chem.*, **2012**, *22*, 24315-24325.

[245] M.A. Green, K. Emery, Y. Hishikawa, W. Warta and E.D. Dunlop, *Prog. Photov.*, **2015**, *23*, 805-812.

3.1.2.2. Small molecules-based solar cells

First examples of SMOSCs were built in PHJ arquitectures by high vacuum evaporation techniques of chromophores such as Pcs, PDIs and C_{60} fullerenes among others.[246] This technique limits the range of chromophores employed to those stable under the harsh evaporation conditions. Search for alternatives lead into small conjugated molecules solution processed devices as most promising technique. This research was initiated by J. Roncali *et al.* in 2006,[247] and since then the use of many classes of chromophores, such as oligothiophenes, triphenylamines, BODIPYs, diketopyrrolopyrroles, and other π-conjugated molecules has been employed. Different solution processing techniques (spin-coating, inkjet printing, dip-coating and spraying) has been employed, giving rise to a vast number of successful configurations.[248]

However, to date, the range of efficient small molecule donors described in the literature is quite limited due to the difficulty in first synthesising a soluble molecule with semiconductor properties followed by a successfully retention of its optoelectronic properties when incorporated into a device. On this behalf, Pcs are preferred chromophores,[249] not only for their unique optical and electronic properties, allowing a strong light absorption even in thin films but for their robustness to be incorporated by vacuum-sublimation techniques. Additionally, suitable functionalization allows a fine tuning in solubility, aggregation, optical and electronic properties resulting into optimized derivatives for a broad range of requirements.[250]

---

[246] a) D. Wynands, M. Levichkova, K. Leo, C. Uhrich, G. Schwartz, D. Hildebrandt, M. Pfeiffer and M. Riede, *Appl. Phys. Lett.*, **2009**, *97*, 073503. b) G.D. Wei, R.R. Lunt, K. Sun, S.Y. Wang, M.E. Thompson and S.R. Forrest, *Nano Lett.*, **2010**, *10*, 3555-3559.

[247] J. Roncali, P. Frere, P. Blanchard, R. de Bettignies, M. Turbiez, S. Roquet, P. Leriche and Y. Nicolas, *Thin Solid Films*, **2006**, *511-512*, 567-570.

[248] a) B. Walker, C. Kim and T.-Q. Nguyen, *Chem. Mater.*, **2011**, *23*, 470-482. b) A. Mishra and P. Bauerle, *Angew. Chem. Int. Ed.*, **2012**, *51*, 2020-2067. b) Y. Lin, Y. Li and X. Zhan, *Chem. Soc. Rev.*, **2012**, *41*, 4245-4272. c) Y. Chen, X. Wan and G. Long, *Acc. Chem. Res.*, **2013**, *46*, 2645-2655. d) W. Ni, X. Wan, M. Li, Y. Wang and Y. Chen, *Chem. Commun.*, **2015**, *51*, 4936-4950.

[249] a) M.V. Martínez-Diaz and T. Torres, in *Handbook of Porphyrin Science* (Eds.: K. Kadish, K.M. Smith and R. Guilard, World Scientific Press, Singapur, **2010**, Vol. 10, Chapter 45. b) M.G. Walter, A.B. Rudine and C.C. Wamser, *J. Porphyrins Phthalocyanines*, **2010**, *14*, 759-792. c) H. Imahori, T. Umeyama, K. Kurotobi and Y. Takano, *Chem. Commun.*, **2012**, *48*, 4032-4045.

[250] a) T.B. Fleetham, N. Bakkan, J.P. Mudrick, J.D. Myers, V.D. Cassidy, J. Cui, J. Xue and J. Li, *J. Mater. Sci.*, **2013**, *48*, 7104-7114. b) B.H. Lesard, T.M. Grant, R. White, E. Thibau, Z.-H. Lu and T.P. Bender, *J. Mat. Chem. A*, **2015**, *3*, 24512-24524.

In the present chapter, three different systems will be studied, aiming towards the development of candidates for water-processed photovoltaic devices. First, water-soluble ZnPcs **1-3** has been employed as suitable chromophores in the development of aqueous-processed photovoltaic devices where the active role in the generated photocurrent has been studied. In these devices the donor photoactive layer (i.e. ZnPc) was deposited by the sping-coating technique and the electron acceptor (i.e. C_{60} fullerene) by classical vapour deposition technique. Aiming to develop a fully aqueous processed photovoltaic device, supramolecular complexes between ZnPcs **16** or ZnPc **17** and single-walled carbon nanotubes (SWCNTs) has been prepared. The photophysical features of corresponding aqueous dispersions has been studied, arising the uncommon property of charge transfer from the SWCNT to the ZnPc upon photoexcitation, switching the classical role of the resulting supramolecular hybrids. The capacity for energy conversion of the new water-soluble electron donor-acceptor moieties has been presented in a fully water-processed proof-of-concept demonstration. Finally, supramolecular complexes of ZnPc **31** and water-soluble fullerenes has been characterized in both organic and aqueous solvents. Photophysical studies of the resulting complexes revealed a charge transfer process from the ZnPc towards the fullerene in what represents a first step into the design of a more realistic photoactive center in artificial photosynthesis.

3.2. Small molecule solar cells based on anionic water-soluble zinc phthalocyanines donors

SMOCS have made great strides in recent years,[251] especially in the case of solution processed devices,[252] with record efficiency of 6.7 %.[253] Within this field, Pc donors have been shown to produce relatively efficient SMOSC,[254] with solution processed small molecule bulk heterojunctions utilising Pc donos showing efficiencies of 0.8 % using a ZnPc derivative and 1.6 % with a ruthenium Pc (RuPc) oligothiophene complex.[255] Pcs are ideal sensitizers, with outstanding absorption in the near IR region, yet their use in SMOSC, as with any efficient SMOSC, has involved organic chlorinated solvents to perform the deposition of the active layers. Ideally, organic films fabricated using solution process techniques should avoid the use of environmentally inconvenient solvents, such as chlorinated solvents (e.g. chlorobenzene, dichloromethane, *o*-dichlorobenzene, etc.) to reduce health risks and become even more environmentally friendly.[256]

Based on these factors, Jones and co-workers reported a significant finding based on a water-soluble tetrasulfonated copper Pc (CuPc) that provides a route to removing chlorinated solvents in the fabrication of a SMOSCs.[257] Thus, the production of devices has been shown, where part of the active layers have been prepared from aqueous solution of CuPc as electron donor and the acceptor layer of C_{60} fullerene being prepared using moderate-vacuum deposition techniques. The devices have shown a light-to-energy conversion under standard conditions of 0.32%. Interestingly in the work mentioned above, there was no contribution of photocurrent from the CuPc donor, which severly limited the the device J_{SC} and in turn the power η. Considering this lack of photocurrent, it seems obvious that a significant margin for improvement in device performance exists.

---

[251] a) D. Wynands, M. Levichkova, K. Leo, C. Uhrich, G. Schwartz, D. Hildebrandt, M. Pfeiffer and M. Riede, *Appl. Phys. Lett,* **2009**, *97*, 073503. b)

[252] B. Walker, C. Kim and T.-Q. Nguyen, *Chem. Mater.*, **2011**, *23*, 470-482.

[253] Y. Sun, G.C. Welch, W.L. Leong, C.J. Takacs, G.C. Bazan and A.J. Heeger, *Nat. Mater.*, **2012**, *11*, 44-48.

[254] a) M.V. Martinez-Diaz, G. de la Torre and T. Torres, *Chem. Commun.*, **2010**, *46*, 7090-7108. b) G. Bottari, G. de la Torre, D.M. Guldi and T. Torres, *Chem. Rev.*, **2011**, *110*, 6768-6816.

[255] a) M.K.R. Fischer, I. Lopez-Duarte, M.M. Wienk, M.V. Martinez-Diaz, R.A.J. Janssen, P. Bauerle and T.Torres, *J. Am. Chem. Soc.*, **2009**, *131*, 8669-8676. b) A. Sanchez-Diaz, R. Pacios, U. Muñecas, T. Torres and E. Palomares, *Org. Electron.*, **2011**, *12*, 329-335.

[256] a) S. Hellweg, U. Fischer, M. Scheringer and K. Hungerbuhler, *Green Chem.*, **2004**, *6*, 418-427. b) A.M. Ruder, *Ann. N. Y. Acad. Sci.*, **2006**, *1076*, 207-227.

[257] S. Schumann, R.A. Hatton and T.S. Jones, *J. Phys. Chem. C*, **2011**, *115*, 4916-4921.

Following the pioneering work of Jones, the series of anionic ZnPcs **1 – 3** has been employed as active layer in water-processed SMOSCs. Variation in the numbers of sulfonate substituents at the periphery of the macrocycle produces a shift into the frontier orbital energies, significantly altering the device characteristics. First of all, absence of photocurrent of tetrasulfonate ZnPc **1** akin to the CuPc behaviour described by Jones was found. Nonetheless, by decreasing the number of substituents (i.e. ZnPcs **2** and **3**) photocurrent of the corresponding device is increased due to the contribution of the chromophore. This increase in J_{SC} is accompanied by a noticeable decrease in the V_{OC}. The best donor molecule is shown to be ZnPc **3**, recording a modest efficiency of up to 0.46% at 1 sun, which represents a significant improvement in the field.

3.2.1. **Results and discussion**

The ZnPc sulfonated derivatives **1**, **2** and **3** synthesis was described in Chapter 1.2.1. The devices were fabricated by spin coating a 10 mg mL^{-1} sulfonated ZnPc solution directly onto UV/O_3 treated ITO (2000 rpm, 1 min, ca. 13 nm thick),[117] followed by the evaporation of C_{60} fullerene (40 nm), bathocuproine (BCP – 10 nm), and Al (100 nm), with devices having an active area of 0.09 cm^2. All devices were studied under standard conditions (A.M 1.5 G solar spectrum, 100 mW cm^{-2}). The *J-V* curves for the respective devices differ significantly (Figure 68a), resulting in very different V_{OC} and J_{SC} values. The standout result is the significant increase in photocurrent with decreasing number of sulfonate substituents. The device comprising of ZnPc **1** shows similar characteristics to those of the CuPc analogue investigated by Jones and co-workers.[257] (i.e. relatively high V_{OC} and very low J_{SC}), due to the inability of the device to extract the photogenerated charges from the donor layer. However, upon decreasing the number of substituents the photocurrent increases. The origin of the increase in photocurrent is clearly depicted in the IPCE spectra (Figure 68b). For devices where ZnPc **1** was employed the IPCE spectra show no photogenerated current in the spectral region where it absorbs. The ZnPcs **2** and **3** do however show a contribution to the device photocurrent. A similar effect of the degree of zinc Pors sulfonation on photocurrent has been previously described for photoelectrochemical cells.[258]

---

[117] A. Siejak, D. Wróbel, P. Siejak, B. Olejarz and R.M. Ion, *Dyes Pigm.*, **2009**, *83*, 281-290.

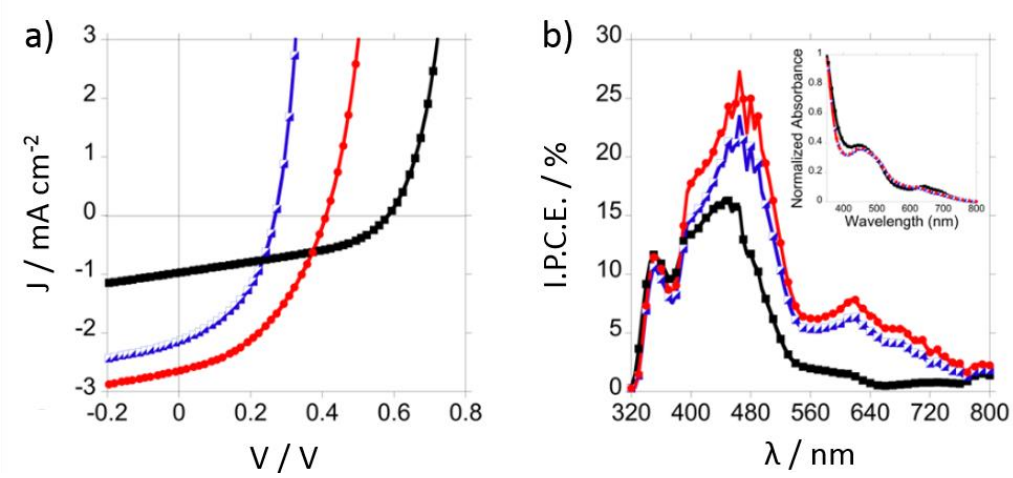

Figure 68. a) *J-V* curves of devices comprising of ITO/ZnPcs **1**-**3**/C_{60}/BCP/Al (black, blue and red respectively). b) IPCE spectra for above described devices. *Inset*: corresponding absorption spectra of the ZnPc thin films.

One probable explanation for the lack of photocurrent from ZnPc **1** arises from the small difference in energy between the LUMO of the ZnPc and the C_{60}. In OSCs the photogenerated exciton is bound by a Coulombic force, which is on the order of 0.3 eV. In order to separate charges, the general process requires excitons to travel to the donor-acceptor interface where the difference in donor and acceptor LUMO levels must exceed the Coulombic attraction force, i.e., the difference in donor and acceptor LUMO levels (ΔE_{LUMO}) has to exceed 0.3 eV. In this case, the LUMO energy is -3.3 eV, whereas ZnPc **2** and **3** both have LUMO energies of -3.2 eV (Table 8). Comparison of these values with the energy of the C_{60} LUMO, -3.5 eV,[259] shows that the photocurrent differences observed may simply be explained by a lack of free energy at the ZnPc **1**-C_{60} interface. However, the values presented for the LUMO energies are for isolated molecules in solution, which do not represent the interfacial electronic interactions present in the device.[260] A more detailed study on each ZnPc-C_{60} interface is therefore required to confirm this hypothesis.

[259] R. Schwedhelm, L. Kipp, A. Dallmeyer and M. Skibowski, *Phys. Rev. B.*, **1998**, *58*, 13176.

[260] H. Ishii, K. Sugiyama, E. Ito and K. Seki, *Adv. Mater.*, **1999**, *11*, 605-625.

Table 8. Energy levels and device performances for the series of water-soluble sensitizers ZnPc **1-3**. Device area and architectures all equal, with the structure ITO/ZnPc/C_{60}/BCP/Al.

Molecule	HOMO/eV[a]	LUMO/eV[a]	V_{OC}/V	J_{SC}/mA cm^{-2}	FF	η / %
ZnPc **1**	-5.1	-3.3	0.57	0.97	0.40	0.22
ZnPc **2**	-5.0	-3.2	0.27	2.11	0.43	0.25
ZnPc **3**	-5.0	-3.2	0.46	2.66	0.42	0.46

[a] HOMO and LUMO energies have been determined from differential pulse voltammetry experiments. See Experimental section.

Studying the morphology of the ZnPcs films using AFM (Figure 69) provides further insights into the role that sulfonation plays in controlling device performance. A clear difference between the morphology of ZnPc **1** and ZnPc **2** and **3** films is seen, with the former one creating large crystalline domains, as opposed to the more "grainy" morphology of the other two thin films. The roughness of the former is also much lower, with a route-mean square roughness (RMS) of 3.0 nm as opposed to 9.3 and 5.8 for ZnPc **2** and **3**, respectively. The high RMS of ZnPc **2** films may explain the low V_{OC} as they are on the order of the film thickness and may lead to contact between ITO and C_{60}.

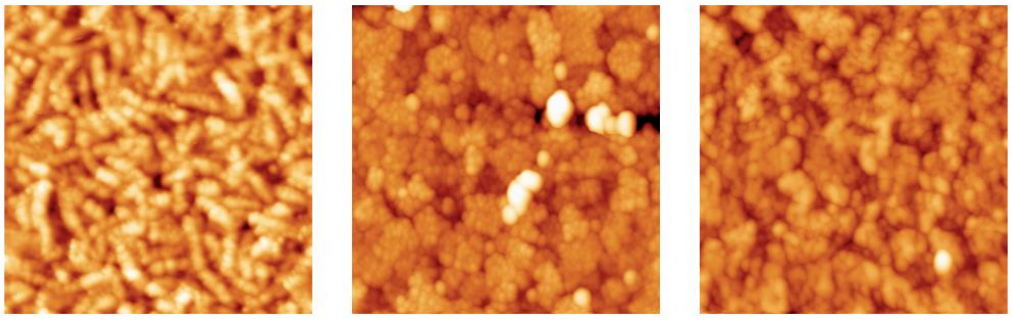

Figure 69. AFM images (2 x 2 μm) for ZnPc **1**, **2** and **3** (from left to right) thin films on ITO with RMS values of 3.0, 9.3 and 5.8 nm and Z-scale of 20, 50 and 50 nm, respectively.

The trends made here regarding morphology correlate well with the device performance values (Table 8), suggesting that morphology plays a key role in determining the photocurrent in these devices, as well as the photovoltage. The morphology of the

thin-films may also affect the interfacial electronic interactions with C_{60}, which would tie in with the previously depicted hypothesis that the problem with photocurrent generation in ZnPc **1** is a thermodynamic one. Is worthy to remark that increasing the thickness of the ZnPc layers led to a decrease in performance (data not shown) in agreement with the case of the CuPc derivative,[257] suggesting a low exciton diffusion length for free carriers in these devices.

Turning to the relationship between the degree of sulfonation and the device V_{OC}, it is important to note that it is not directly related with the degree of sulfonation, being highest for ZnPc **1**, lowes for ZnPc **2** and ZnPc **3** having a value in between. It is worth mentioning that the 100 mV difference in energy between the HOMO of ZnPc **2** and **3** does correspond well to the 110 mV difference in V_{OC} (Table 8). Nonetheless, the origin of the device V_{OC} is still under active debate, with many attempts at understanding it being reported.[261] In general, the device V_{OC} is proportional to the difference in energy between the HOMO of the donor and the LUMO of the acceptor (ΔE_{DA}), yet the molecules used all posses very similar HOMO energies. In this respect we would expect the device V_{OC} to be lowest for ZnPc **3**, as it possesses the lowest ΔE_{DA}. Therefore, we speculate several loss processes to exist that lead to the lower device V_{OC} observed for ZnPc **2** and **3**, especially considering the very different morphologies observed with the AFM study.

In conclusion, the role of the substituents in ZnPc molecules have been shown, being paramount for tuning the performance of OSCs based on water-soluble pcs. This finding has led to a significant improvement in device performance by tuning the energy levels of the donor ZnPc to achieve a more energetically favourable photooxidation of the C_{60} acceptor layer, resulting in maximum efficiencies of 0.46 under standard conditions. Also, the number of substituents controls the morphology of the thin films which in turn affects device performance. Having successfully demonstrated the first goal, further research will focus into develop a water-soluble acceptor molecule, in order to provide both an environmentally friendly and an inexpensive route towards functional OSCs.

Having successfully incorporated three ZnPc derivatives as photoactive layer in SMOSCs processed from aqueous solution, the first step towards the development of

---

[261] a) A. Maurano, R. Hamilton, C.G. Shuttle, A.M. Ballantyne, J. Nelson, B. O'Regan, W. Zhang, I. McCulloch, H. Azimi, M. Morana, C.J. Brabec and J.R. Durrant, *Adv. Mater.*, **2010**, *22*, 4987-4992. b) C. Deibel, T. Strobel and V. Dyakonov, *Adv. Mater.*, **2010**, 22, 4097-4111. c) C.W. Schlenker and M.E. Thompson, *Chem. Commun.*, **2011**, *47*, 3702-3716. d) J. Bisquert and G. Garcia-Belmonte, *J. Phys. Chem. Lett.*, **2011**, *2*, 1950-1964.

water-processed solar cells has been demonstrated. Moreover, the next step will be to develop a water-soluble acceptor molecule or water-soluble donor-acceptor system, in order to provide both an environmentally friendly and an inexpensive route towards functional OSCS.

3.3. Water-soluble zinc phthalocyanine/electron donor carbon nanotubes as unprecedented supramolecular materials for energy conversion

A fundamental aspect of innovation in materials science relates to the exploration of new properties in known materials, sometimes even achieving behaviours that are opposite to those traditionally encountered, which expands the scope of the corresponding research areas. In the field of energy conversion the development of organic photovoltaic materials processed from aqueous solution would, for example, reduce health risks and results in environmentally friendlier devices.[262] Hydrophilic photoactive building blocks featuring either electron-donating or electron-accepting characteristics have been much less studied than their hydrophobic analogues.[263] Indeed, taking photovoltaic components into aqueous media should bring new capacities of those components as described in the previous section.[REF] Herein, we have extended this approach to an entirely water-soluble system through the noncovalent immobilization of cationic ZnPcs **16** and **17** onto CoMoCAT single wall carbon nanotubes (SWCNTs) - Figure 70. Such strategy affords water-soluble, hydrophilic photosynthetic reaction centres – SWCNT/ZnPc – in which ZnPc acts as electron-acceptor and SWCNT serves as electron-donor. The latter contrast with the commonly encountered functions, in which ZnPc and SWCNT play the role of electron donor and electron acceptor, respectively. The novel SWCNT/ZnPc hybrids were probed as active materials for photovoltaic applications.

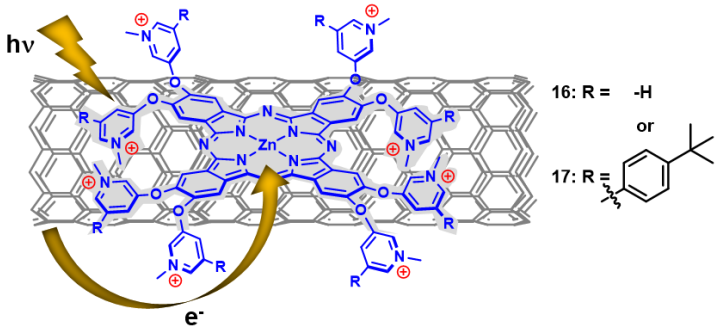

Figure 70. Schematic representation of the described aqueous SWCNT/ZnPcs supramolecular hybrids.

---

[262] a) S. Hellweg, U. Fischer, M. Scheringer and K. Hungerbuhler, *Green Chem.*, **2004**, *6*, 418-427. b) A.M. Ruder, *Ann. N. Y. Sci.*, **2006**, *1076*, 207-227.

[263] Y. Huang, E.J. Kramer, A.J. Heeger and G.C. Bazan, *Chem. Rev.*, **2014**, *114*, 7006-7043.

Pcs are unique electron-donors due to their high thermal and photostability, and because of their intense absorption in the red/near-infrared (NIR) region of the solar spectrum, as has been extensively discussed previously. Such remarkable features render Pcs excellent antennas that, on one hand, harvest light and, on the other hand, transfer the absorbed energy in form of energy or electrons, to suitable acceptors. To date, a number of hydrophobic Pcs have been implemented into artificial photosynthetic systems in combination with different carbon nanostructures as electron-accepting materials, giving rise to long-lived charge-separated states. On the contrary, Pcs with electron accepting character are rather scarce.[264] For this purpose, they need to bear highly electron-withdrawing substituents.[265]

SWCNTs are considered key materials in nanotechnology as a result of their nanometer-scale size and their extraordinary chemical, mechanical, thermal, and electronic properties.[266] A great number of covalent[267] and noncovalent[268] strategies have been developed in recent years to functionalize SWCNTs with photoactive units, which upon photoexcitation give rise to intramolecular energy and electron transfer events. Noncovalent methodologies do not affect the electronic structure of SWCNTs and are simpler form a synthetic point of view. Any of such strategies to decorate SWCNTs with Pcs afford SWCNT/Pc conjugates and/or hybrids, in which the Pcs normally function as electron donating materials.[269] The role of SWCNTs in terms of electron accepting *versus* electron

---

[264] M.-E. Ragoussi, J.-J. Cid, J.-H. Yum, G. de la Torre, D. Di Censo, M. Grätzel, M.K. Nazeeruddin and T. Torres, *Angew. Chem. Int. Ed.*, **2012**, *51*, 4375-4378.

[265] a) M.V. Martinez-Díaz, S. Esperanza, A. de la Escosura, M. Catellani, S. Yunus, S. Luzzati and T. Torres, *Tetrahedron Lett.*, **2003**, *44*, 8475-8478. b) R.A. Hatton, N.P. Blanchard, V. Stolojan, A.J. Miller and S.R.P. Silva, *Langmuir*, **2007**, *23*, 6424-6430. c) Q.L. Song, H.B. Yang, Y. Gan, C. Gong and C.M. Li, *J. Am. Chem. Soc.*, **2010**, *132*, 4554-4555. d) Y. Zhang, P. Ma, P. Zhu, X. Zhang, Y. Gao, D. Qui, Y. Bian, N. Kobayashi and J. Jiang, *J. Mater. Chem.*, **2011**, *21*, 6515-6524. e) M.-E. Ragoussi, G. Katsukis, A. Roth, J. Malig, G. de la Torre, D.M. Guldi and T. Torres, *J. Am. Chem. Soc.*, **2014**, *136*, 4593-4598.

[266] a) S. Reich, C. Thomsen and J. Maultzsch in *Carbon Nanotubes: Basic Concepts and Physical Properties*, Willey-VCH, Weinheim, Germany **2004**. b) V.N. Popov and P. Lambin, *Carbon Nanotubes*, Springer, Dordrecht, Netherlands **2006**. c) S. Fukuzumi and T. Kojima, *J. Mater. Chem.*, **2008**, *18*, 1427-1439. d) D.M. Guldi and N. Martin, *Carbon Nanotubes and Related Structures*, Willey-VCH, Weinheim, Germany, **2010**.

[267] A. Hirsch, *Angew. Chem. Int. Ed.*, **2002**, *41*, 1853-1859

[268] a) D.I. Schuster and J.D. Megiatto, *Nat. Chem.*, **2009**, *1*, 182-183. b) G. Bottari, J.A. Suanzes, O. Trukhina and T. Torres, *J. Phys. Chem. Lett.*, **2011**, *2*, 905-913. c) C. Romero-Nieto, R. Garcia, M.A. Herranz, C. Ehli, M. Ruppert, A. Hirsch, D.M. Guldi and N. Martin, *J. Am. Chem. Soc.*, **2012**, *134*, 9183-9192.

[269] a) F. D'Souza and O. Ito, *Chem. Soc. Rev.*, **2012**, *41*, 86-96. b) F. D'Souza, A.S.D. Sandanayaka and O. Ito in *Organic Nanomaterials: Synthesis, Characterization, and Device Applications*, ed. G. Bottari and T. Torres, John Wiley & Sons, Inc., Hoboken, NJ, USA, **2013**. c) G. Bottari, O. Trukhina, M. Ince and T. Torres, *Coord. Chem. Rev.*, **2012**, *256*, 2453-2477. d) K. Dirian, M.A. herranz, G. Katsukins, J. Malig, L. Rodriguez-Perez, C. Romero-Nieto, V. Strauss, N.

donating is however exchangeable. Up to now, electron donor SWCNTs were only realized when confronted with strong electron-acceptors such as fullerenes and perylenes.[270]

Taking the aforementioned into account, ZnPcs with hydrophilic and strongly electron-withdrawing peripheral substituents are required to guarantee solubility in aqueous media and to invert electron transfer performance of SWCNTs. Achieving water-soluble Pcs constitutes a demanding synthetic challenge. Pcs that are symmetrically substituted with eight quaternizable pyridyloxy substituents (ZnPc **16**), for example, are highly insoluble in most solvents, rendering not only their preparation but also their spectroscopic characterization nearly impossible. On the same note, asymmetric Pcs containing those substituents are unknown, despite the fact that tailoring the number of pyridyloxy motieties at the Pc ring would be a useful approach to tune the Pc features.

3.3.1. **Results and discussion**

3.3.1.1. Electrochemical characterization

In light of the above limitations, the novel series ZnPc **17**-**20** has been employed in the present application. Most importantly, increasing the number of pyridyloxy substituents in this series gradually increases their electron-accepting nature (-1.00 and -1.02 V *versus* Fc/Fc^+ for ZnPc **16** and **17**, respectively), yielding first reduction potentials comparable to those of fullerenes (-1.09 V *versus* Fc/Fc^+)) and fullerene derivatives (-1.17 V *versus* Fc/Fc^+).[271] The symmetrical ZnPcs **16** and **17** were probed as dispersants for CoMoCAT SWCNTs in aqueous media. This choice has been reasoned based on the strength of their electron-accepting character. In the resulting CoMoCAT SWCNT/**16** and CoMoCAT SWCNT/**17** hybrids, the electron transfer from SWCNT to ZnPc has been demonstrated upon photoexcitation. The latter and the unique stability of CoMoCAT SWCNT/**16** and CoMoCAT SWCNT/**17** encouraged their integration into solar energy conversion schemes.

Martin and D.M. Guldi, *Chem. Sci.*, **2013**, *4*, 4335-4353. d) G. Bottari, G. de la Torre and T. Torres, *Acc. Chem. Res.*, **2015**, *48*, 900-910.

[270] F. D'Souza, R. Chitta, A.S.D. Sandanayaka, N.K. Subbaiyan, L. D'Souza, Y. Araki and O. Ito, *J. Am. Chem. Soc.*, **2007**, *129*, 15865-15871. b) U. Hahn, S. Engmann, C. Oelsner, C. Ehli, D.M. Guldi and T. Torres, *J. Am. Chem. Soc.*, **2010**, *132*, 6392-6401.

[271] M. Murata, Y. Murata and K. Komatsu, in *Organic Nanomaterials: Synthesis, Characterization, and Device Applications*, ed. G. Bottari and T. Torres, John Wiley & Sons, Hoboken, NJ, USA, **2013**, p. 225.

To characterize the electron donor or acceptor nature of ZnPcs with pyridyloxy peripheral substituents, electrochemical studies using cyclic voltammetry (CV) and Osteryoung square wave voltammetry (OSWV) were conducted for cationic ZnPcs **17** and **22** – **25** and non-quaternized ZnPcs **29** – **32**. Here, the well-studied tetra-*tert*-butyl-ZnPc (TT0) was used as a reference.[272] Notably, the electrochemical features of ZnPc **21** could be tested due to their lack of solubility in solvents commonly employed for these techniques. For the rest of them the redox potentials could be characterized owing to their better solubility as a consequence of having *tert*-butylphenyl groups in the pyridyloxy substituents, and are presented in Table 9 with the corresponding voltammograms shown in Figure 71.

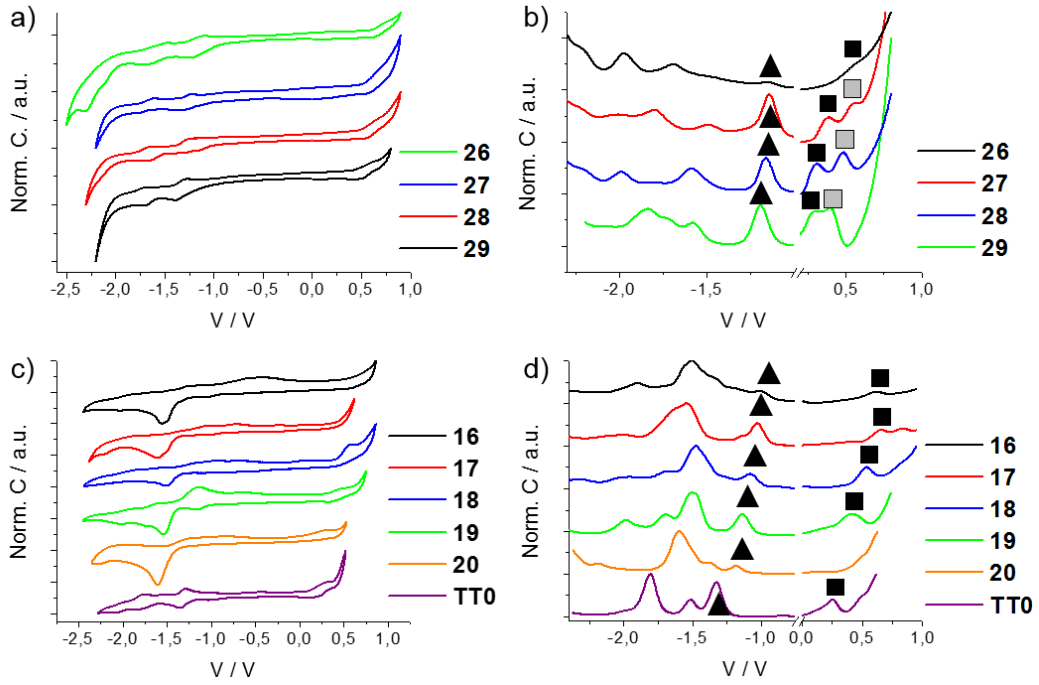

Figure 71. Electrochemical characterization of ZnPcs **26** – **29** by circular voltamperometry (a) and OSWV (b) in anhydrous THF. Electrochemical characterization of cationic ZnPcs **16** – **20** and reference **TT0** by circular voltamperometry (c) and OSWV (d) in freshly distilled DMSO.

[272] A. Gouloumis, S. G. Liu, A. Sastre, P. Vazquez, L. Echegoyen and T. Torres, *Chem. Eur. J.*, **2000**, *6*, 3600

From the voltammograms of **26 – 29** in THF (Figure 71a and b) a clear trend as a function of the number of ZnPc pyridyloxy groups is derived. Increasing the number of pyridyloxy groups results in a slight decrease of the first reduction, that is, from -1.19 V for **29** to -1.14 V for **26**, and a substantial increase of the first oxidation, that is, from +0.29 V for **29** to +0.57 V for **26**, suggesting an electron-withdrawing effect of the aforementioned functional groups. This effect is magnified when the pyridyloxy groups are methylated enhancing the electron-withdrawing character of these groups as can be observed for ZnPcs **16 – 20** (comparing results of Figure 71 and Table 9).

Table 9. Electrochemical data for compounds **17 – 20**, **26 – 29**, and **TT0** reference, determined by OSWV.

ZnPc	E_{red3}	E_{red2}	E_{red1}	E_{ox1}	E_{ox2}
16[a)]	-1.50	-	-1.00	0.61	-
17[a)]	-1.53	-1.12	-1.02	0.65	0.83
18[a)]	-1.47	-1.26	-1.07	0.53	-
19[a)]	-1.49	-	-1.13	0.41	-
20[a)]	-1.59	-1.36	-1.18	0.31[c)]	-
TT0[a)]	-1.81	-1.51	-1.32	0.25	0.50
26[b)]	-1.69	-	-1.14	0.57	-
27[b)]	-1.80	-1.48	-1.14	0.38	0.55
28[b)]	-	-1.59	-1.16	0.31	0.48
29[b)]	-1.83	-1.58	-1.19	0.29	0.40

[a)] $TBAPF_6$ 0.1M in freshly distilled DMSO. [b)] $TBAPF_6$ 0.1M in freshly distilled THF.
[c)] Data extracted from Cyclic Voltametry (CV).

For **17 – 20**, the irreversible reduction at around -1.6 V increases in intensity as the number of pyridinium groups increases. In other words, the latter groups impact the electrochemical potentials of the Pcs, yet the first reductions could be identified in OSWVs for all the cationic ZnPcs. The corresponding values range from -1.18 V in **20** to -1.02 V in **17** and are in all cases less negative than those observed for the non-quaternized ZnPcs **26 – 30**, indicating the stronger electron accepting nature of the pyridyloxy units once they are

quaternized. A similar effect is seen in the anodic scans, with first oxidations ranging from +0.31 V in **20** to +0.65 V in **17** as the number of cationic substituents increases. In sum, incorporating *tert*-butylphenyl groups in **17** - **20** is key to document, for the first time, that quaternized pyridyloxy ZnPcs are excellent electron-acceptors. Moreover, symmetrically substituted ZnPcs **16** and **17** are by far the best electron-acceptors within the whole series. They were therefore chosen as the main target compounds to be immobilized onto SWCNTs, for which the following studies were focused on their full photophysical characterization and application as photoactive material in organic solar cells.

3.3.1.2. Noncovalent immobilization of ZnPcs **16** and **17** onto SWCNTs

Key toward testing interactions in CoMoCAT SWCNT/ZnPc hybrids is the preparation of suspensions from CoMoCAT SWCNTs in D_2O or D_2O/MeOH (9:1 v/v). The latter were prepared following previously described procedures.[273] In detail, ZnPc **16** was dissolved in D_2O (ca. 10^{-3} M). On the other hand, ZnPcs **17** was dissolved in MeOH and subsequently poured over D_2O, to a final ZnPc concentration of ~ 10^{-3} M in a D_2O/MeOH ratio of 9:1. The suspensions of CoMoCAT SWCNT/**16** and CoMoCAT SWCNT/**17** hybrids were prepared in pure D_2O and D_2O/methanol (9:1), respectively, by means of repeating several cycles, which include vigorous stirring, ultrasounds for 30 min at 20 ^oC, and ultracentrifugation. This protocol rendered suspensions that were suitably stabile for the spectroscopic characterization. In both cases, interactions with CoMoCAT SWCNTs are discernible. For example, in the visible region, the ZnPc Q-band absorption shift from 673 to 690 nm for **16**, and from 677 to 692 nm for **17** (Figure 72). In the NIR region, the CoMoCAT SWCNT absorptions also reveals a redshift.

[273] a) J. Bartelmess, C. Ehli, J.-J. Cid, M. García-Iglesias, P. Vázquez, T. Torres and D.M. Guldi, *Chem. Sci.*, **2011**, *2*, 652-660. b) J. Bartelmess, B. Ballesteros, G. de la Torre, D. Kiessling, S. Campidelli, M. Prato, T. Torres and D.M. Guldi, *J. Am. Chem. Soc.*, **2010**, *132*, 16202-16211.

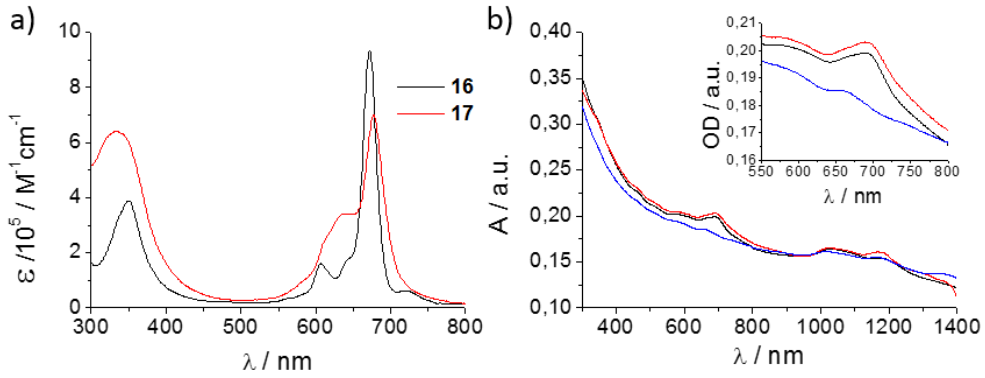

Figure 72. a) UV-Vis spectra of ZnPc **16** and **17** in D_2O and D_2O/methanol (9:1), respectively. b) Absorption spectra of CoMoCAT SWCNT (blue), CoMoCAT SWCNT/**16** (black), and CoMoCAT SWCNT/**17** (red) suspensions in D_2O and D_2O/methanol (9:1), respectively.

To complement the absorption assays, CoMoCAT SWCNT/ZnPc hybrids were subjected to emission measurements upon excitation in the area from 600 to 800 nm (Figure 73b). The results were compared to CoMoCAT SWCNT suspended with a standard surfactant, that is, sodium dodecylbenzenesulfonate (SDBS), in D_2O. All suspensions were prepared with comparable absorption throughout the excitation area. For CoMoCAT SWCNT/SDBS, emission maxima at 961, 1028, 1125, and 1250 nm were measured, which correspond to SWCNT with chirality (6,5), (7,5), (7,6), and (10,5), respectively.[274] For CoMoCAT SWCNT/ZnPc hybrids, a similar but bathochromically shifted emission pattern was found. Importantly, the emission intensities of CoMoCAT SWCNT/ZnPc are dramatically quenched when compared to CoMoCAT SWCNT/SDBS (Figure 73c). This observation goes hand in hand with an immobilization of **16** and **17** onto CoMoCAT SWCNTs.

[274] S.M. Bachilo, M.S. Strano, C. Kittrell, R.H. Hauge, R.E. Smalley and R.B. Weisman, *Science*, **2002**, *298*, 2361-2366.

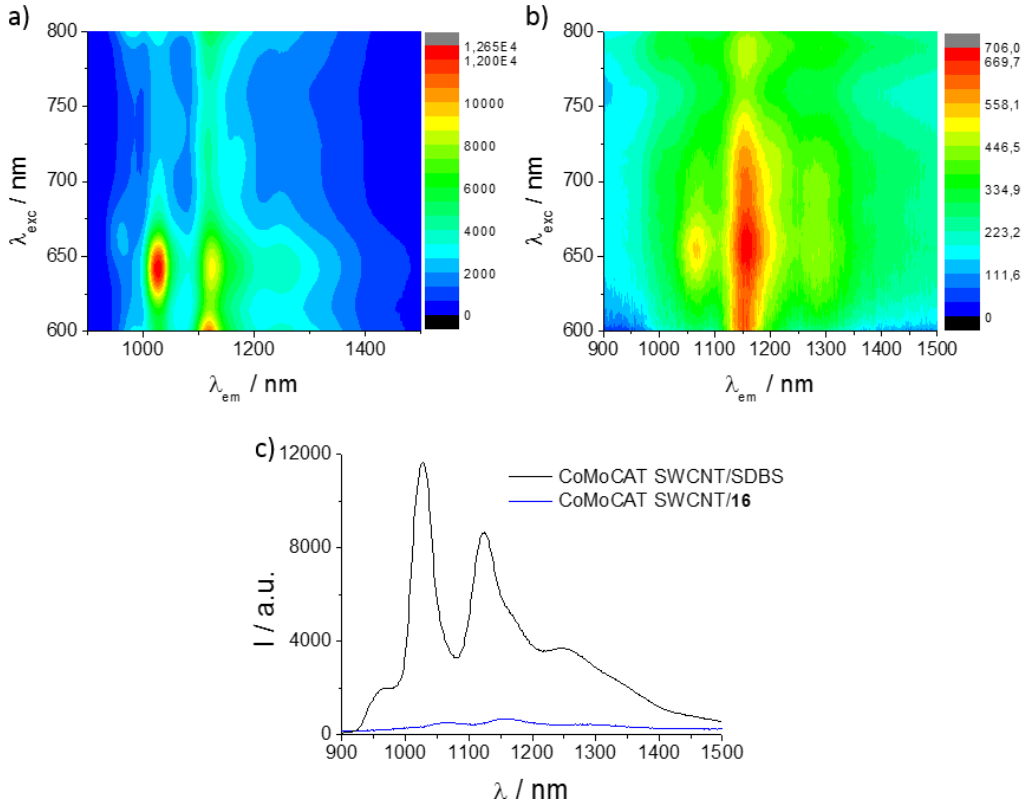

Figure 73. Steady-state 3D NIR fluorescence spectra of CoMoCAT SWCNT/SDBS (a) and CoMoCAT SWCNT/**16** (b) in D_2O. c) Comparison of the NIR fluorescence spectra with comparable absorptions, exciting at 650 nm.

Additional insights into structural and electronic characteristic of the hybrids were derived from solid-state Raman experiments with 1064 nm excitation.[275] Figure 74 illustrates all the important signatures of CoMoCAT SWCNTs, that is, their radial breathing mode (RBM-), D-, and G-modes, together with the 2D-mode. The D-band in CoMoCAT SWCNT/ZnPc hybrids at 1285 ± 2 cm^{-1}, as the reflection of structural damages in CoMoCAT SWCNTs,[276] increases slightly when compared to CoMoCAT SWCNT/SDBS. Likewise, no changes evolved for the G-band in CoMoCAT SWCNT/ZnPc hybrids. The 2D-mode, in turn,

[275] a) R. Graupner, *J. Raman Spectrosc.*, **2007**, *38*, 673-683. b) M.S. Dresselhaus, G. Dresselhaus, A. Jorio, A.G.S. Filho, M.A. Pimenta and R. Saito, *Acc. Chem. Res.*, **2002**, *35*, 1070-1078.

[276] S. Lefrant, I. Baltog and M. Baibarac, *Synth. Met.*, **2009**, *159*, 2173-2176.

shifts from 2548 ± 2 cm^{-1} for CoMoCAT SWCNT/SDBS to 2555 ± 2 cm^{-1} for CoMoCAT SWCNT/**16** and for CoMoCAT SWCNT/**17**. Finally, the RBM-modes reveal also upshifts. Altogether, this indicates that π-π interactions are operative between for CoMoCAT SWCNTs and ZnPcs.

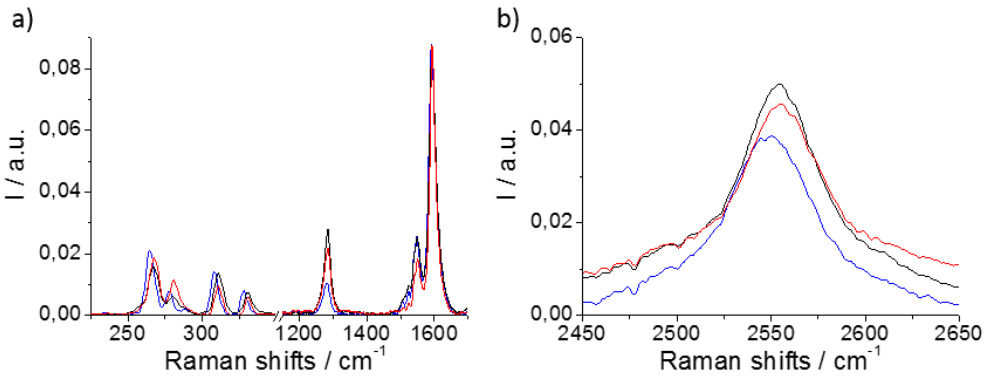

Figure 74. FT-Raman spectra of CoMoCAT SWCNT/SDBS (blue), CoMoCAT SWCNT/**16** (black), and CoMoCAT SWCNT/**17** (red) in the solid state – 1064 nm excitation. b) Detail of the 2D-mode.

Finally, the nature of the excited-state interactions between for CoMoCAT SWCNTs and ZnPcs have been proved by means of transient absorption measurements. Upon excitation of for CoMoCAT SWCNT/SDBS in D_2O at either 387 or 660 nm, the instantaneous bleaching of for CoMoCAT SWCNT-centered transitions was noted. These are exact mirror images of the ground state absorption (Figure 75a). In particular, bleaching of the CoMoCAT SWCNT van Hove singularities evolves in the form of minima at 1031, 1128, and 1256 nm, as well as a shoulder at 986 nm. Upon photoexciting CoMoCAT SWCNT/**16** and CoMoCAT SWCNT/**17** at 387 nm, spectroscopic and kinetic differences are discernible. In the NIR region, minima appear at 1110 and 1204 nm for CoMoCAT SWCNT/**16**, and at 1076 and 1200 nm for CoMoCAT SWCNT/**17**. The redshift of the CoMoCAT SWCNT absortption features indicates the formation of charge transfer product, that is, oxidized CoMoCAT SWCNT and reduced ZnPc. In terms of kinetics, the excited state decay processes for the CoMoCAT SWCNT/**ZnPc** hybrids are faster, that is, 0.6 and 45 ps for CoMoCAT SWCNT/**16** and 0.5 and 14 ps CoMoCAT SWCNT/**17**, when compared to 0.9 and 215 ps seen for CoMoCAT SWCNT/SDBS (Figure 75d).

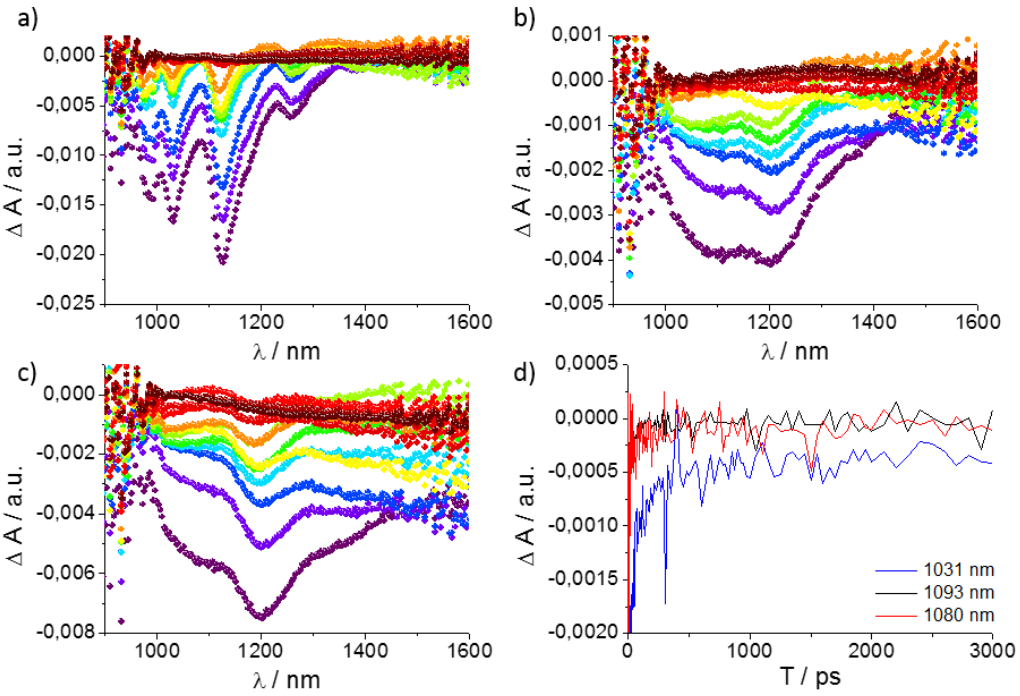

Figure 75. Differential absorption spectra (extended NIR) obtained upon femtosecond pump probe experiments (387 nm) of a) CoMoCAT SWCNT/SDBS, b) CoMoCAT SWCNT/**16**, and c) CoMoCAT SWCNT/**17** in D_2O and D_2O/MeOH (9:1), respectively, with several time delays between 1 (purple) and 7500 ps (dark red), at room temperature. d) Time absorption profiles obtained upon femtosecond pump probe experiments (387 nm) of CoMoCAT SWCNT (blue), CoMoCAT SWCNT/**16** (black) and CoMoCAT SWCNT/**17** (red) in D_2O and D_2O/MeOH (9:1), respectively.

Moreover, the visible range is dominated by transient maxima and minima in the 550 to 700 nm range (Figure 76a and b). Interestingly, the new maximum at 585 nm correlates well with the one-electron reduced ZnPc, as corroborated in spectroelectrochemical experiments (Figure 76c and d). Another important feature is the minimum around 690 nm, which resembles ZnPc immobilized onto CoMoCAT SWCNTs.

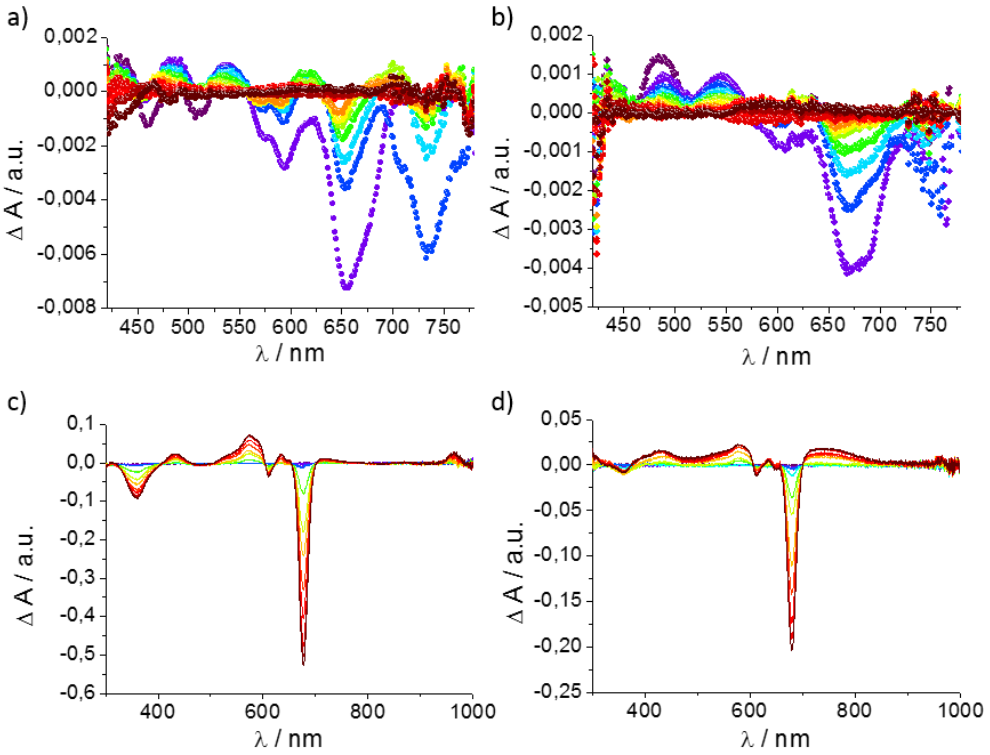

Figure 76. Differential absorption spectra (visible) obtained upon femtosecond pump probe experiments (387 nm) of a) CoMoCAT SWCNT/SDBS and b) CoMoCAT SWCNT/**16** in D_2O, with several time delays between 1 (purple) and 7500 ps (dark red), at room temperature. Differential absorption spectra (visible and NIR obtained upon spectroelectrochemical reduction of **16** (c) and **17** (d) in DMSO at variable potential ranging from 0.0 V (purple) to -1.2 V (dark red).

3.3.1.3. Photovoltaic devices

Encouraged by the photophysical behaviour of CoMoCAT SWCNT/ZnPc hybrids, the fabrication of SWCNT-based photovoltaic cells processed from aqueous solution was undertaken. ZnPc **16** was chosen to build our prototype device, since it provides the highest solubility in water. First of all, films of different thicknesses were prepared by spraying varying amounts of a CoMoCAT SWCNT/**16** D_2O solution on precleaned fluorine-doped tin oxide (FTO) substrates, placed onto a 200 ^oC heating plate. The resulting photoelectrodes were probed by absorption spectroscopy, four-point probe resistivity measurements, and profilometry. The latter is an alpha-step technique to monitor both the film thickness and roughness upon spray deposition. Importantly, the use of the spray

pyrolysis technique enables homogeneous film formation (Figure 77a). Scanning electron microcopy (SEM) images, for example, corroborate that the FTO surface is completely covered by a homogeneous film, where the structure of SWCNTs is preserved (Figure 77b). Moreover, the film thickness could be easily controlled by spraying different amounts of the initial solution, as confirmed by both absorption spectroscopy and profilometry. For example, the absorption features at 650-700 nm, related to the presence of **16** in the hybrid, rise in intensity from 0.3 to 0.6 and to 1.0 when increasing the film thickness from 90 to 250 and 700 nm, respectively. Accordingly, the bulk electrical resistance of the films also increases with thickness, featuring 9-18 $\Omega\ \square^{-1}$ values, which are close to that of bare FTO. Such characteristics underline the potential of CoMoCAT SWCNT/**16** hybrid films as novel photoelectrodes for solar energy conversion. The devices were completed by using an equimolar 3 M Na_2/S/NaOH electrolyte and a Cu_2S-based counter-electrode (see experimental section for more details). Figure 77c shows the photocurrent generated under one sun illumination at AM 1.5 conditions by devices with photoelectrodes featuring different thicknesses. Table 10 summarizes the device characteristics. Overall, these results reveal a great potential to prepare fully water-processed solar cells. The increase of the film thickness up to 250 nm leads to an enhancement of J_{SC} to 0.369 mA cm^{-2} owing to the right balance between high absorption intensity and low bulk electrical resistivity of the photoanodes (see above). In stark contrast, devices with a thickness of up to 700 nm show a significant reduction of J_{SC} with values of 0.228 mA cm^{-2}. This drop in *J* relates quite likely to the high bulk electrical resistivity and, in turn, hampers the charge collection due to efficient electron recombination processes across the film/electrolyte interface. V_{OC}, seem to continuously decrease from 46 to 16 mV upon increasing the film thickness. As consecuence, the device with a 250 nm photoanode shows the best performance. Importantly, the incident IPCE spectrum resembles the absorption features of **16**, showing maxima of 0.6% and 0.25% at the Soret- and Q-band wavelengths, respectively (Figure 77d). This result is in perfect agreement with the solution based photophysical data – an efficient charge separation sets in only when ZnPcs are excited. The fact that energy conversion is restricted to photons absorbed by ZnPc limits their efficiency, but leaves much room for improvement through the use of additional and complementary photoactive layers in tandem solar cells.

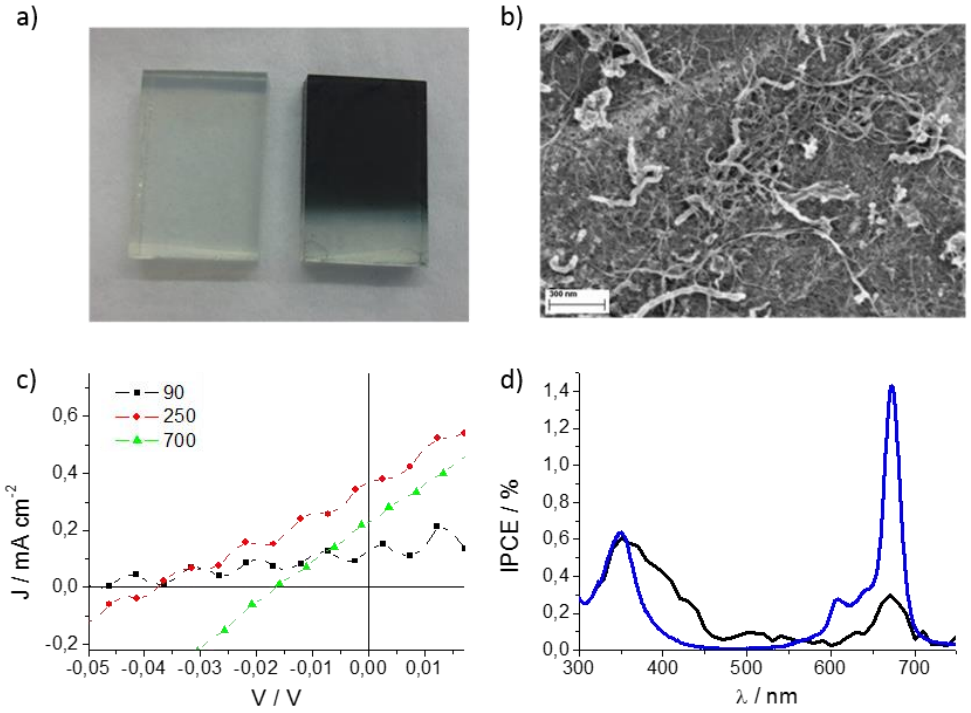

Figure 77. a) Pictures of a FTO substrate (left) and CoMoCAT SWCNT/**16** thin-film (right) deposited onto FTO substrate by spray pyrolysis. b) SEM image of a CoMoCAT SWCNT/**16** thin-film deposited onto FTO substrate by spray pyrolysis. c) J-V curves of devices with CoMoCAT SWCNT/**16** photoelectrodes featuring 90, 250 and 700 nm thickness. d) Photoaction spectrum (black) of a device with a 250 nm thick CoMoCAT SWCNT/**16** photoelectrode, measured under AM 1.5/ 1 sun conditions. For comparison purposes, the absorption spectrum of **16** is shown in blue.

Table 10. Device characteristics under 1 sun illumination at AM 1.5 conditions of devices with CoMoCAT SWCNT/**16**-based photoelectrodes featuring different thicknesses.

Photoelectrode Thicknesses	**V_{OC}/ mV**	**J_{SC}/mA cm^{-2}**	**FF**	**η / %**
90 nm	46	0.125	0.26	0.0015
250 nm	37	0.369	0.29	0.0040
700 nm	16	0.228	0.31	0.0011

Altogether, this proof-of-concept demonstration of the SWCNT/ZnPc hybrids' capacity for energy conversion shows low values in comparison with other optimized systems. Nonetheless, this work represents a first milestone towards fully aqueous-processed photovoltaic devices.

3.4. Aqueous zinc phthalocyanine/fullerene supramolecular complexes as a more realistic artificial photosynthetic reaction centre.

Mimicking natural processes has been employed as strategy to circumvent a broad variety of nowadays problems. In the particular case of energy conversion, plants, algae and bacteria solved the synthesis of highly energetic molecules through photoinduced CO_2 fixation. Natural photosynthesis[277] is a highly sophisticated process that generates organic molecules that are the building blocks of all living organisms. Its success is based on the fact that sunlight, water, and carbon dioxide are available in abundant quantities. Still, the evolution of plants was governed by survival and successful reproduction rather than by the maximum efficiency of biomass production. Despite the aforementioned, natural photosynthesis, especially the early events, that is, light harvesting (LH), energy transfer (EnT), and electron transfer, proceed with unit quantum efficiencies. Solar energy is absorbed, for example, by chlorophylls, carotenoids, and other pigments and is consequently funnelled to the photosynthetic reaction centre, where the initial charge separation takes place. One photoexcited either by direct light absorption or by transduction of singlet excited state energy from the antenna systems, it donates an electron to a neighbouring pheophytin (Figure 78). Remarkably, electron transfer processes tend to be rather slow over large distances and, thus, are non-competitive with respect to energy dissipating reactions. In order to avoid this inherent problem, photosynthetic organisms have developed sequences of short-range electron transfer events (i.e. electron transport chain), which finally generate long lived transmembrane charge-separated states. Adenosine triphosphate (ATP) is generated at the end of the electron transport chain from adenosine diphosphate (ADP). The former is required, along with dihydronicotinamide adenine dinucleotide phosphate (NADPH), to the ultimate objective of convert CO_2 into energy rich carbon hydrates.

---

277 a) M. Rudolf, S.V. Kirner and D.M. Guldi, *Chem. Soc. Rev.*, **2016**, *45*, 612-630. b) J. Barber and P.D. Tran*, J. R. Soc., Interface*, **2013**, *10*, 20120984–20120999. c) R.E. Blankenship, D.M. Tiede, J. Barber, G.W. Brudvig, G.Fleming, M. Ghirardi, M.R. Gunner, W. Junge, D.M. Kramer, A. Melis, T.A. Moore, C.C. Moser, D.G. Nocera, A.J. Nozik, D.R. Ort, W.W. Parson, R.C. Prince and R.T. Sayre, *Science*, **2011**, *332*, 805–809. d) J. Barber, *Chem. Soc. Rev.*, **2009**, *38*, 185–196. e) S. Fukuzumi, K. Ohkubo and T. Suenobu, *Acc. Chem. Res.*, **2014**, *47*, 1455–1464.) J. Messinger, W. Lubitz and J.R. Shen, *Phys. Chem. Chem. Phys.*, **2014**, *16*, 11810–11811. g) D. Gust, T.A. Moore and A.L. Moore, *Acc. Chem. Res.*, **2009**, *42*, 1890–1898. h) D. Gust and T.A. Moore, *Science*, **1989**, *244*, 35–41. i) C.C. Moser, C.C. Page and P.L. Dutton, in *Electron Transfer in Chemistry*, ed. V. Balzani, Wiley-VCH, Weinheim, **2001**, vol. III, pp. 24–38. j) S. Berardi, S. Drouet, L. Francas, C. Gimbert-Surinach, M. Guttentag, C. Richmond, T. Stoll and A. Llobet, *Chem. Soc. Rev.*, **2014**, *43*, 7501–7519. k) P.D. Frischmann, K. Mahata and F. Wurthner, *Chem. Soc. Rev.*, **2013**, *42*, 1847–1870.

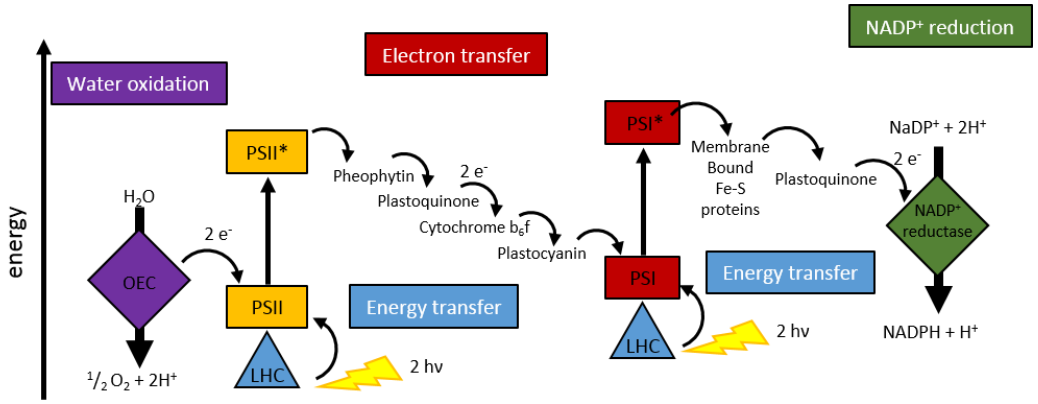

Figure 78. Schematic representation of the early events in natural photosynthesis with light absorbing units (LHC) of photosystem I (PSI) and photosystem II (PSII), the electron transport chain with its principal components, on the one hand, the oxygen evolving complex (OEC), and, on the other hand, the $NADP^+$ reductase as catalytic centers.[277j]

Artificial photosynthesis is, therefore, based in the key concepts mentioned above: light harvesting, energy transfer, and electron transfer. The former is important and requires to be optimized – the more light is harnessed the more charges are likely be separated and consequently be utilized. A rather elegant but yet simple approach involves electron donors or acceptors with high extinction coefficients in the visible part of the solar spectrum. The complexity is kept at a comparably simple level. To increase the absorption characteristics in the long wavelength region an extensively employed strategy is the extension of the delocalized π, resulting at the same time into changes in the electronic properties – most notable are the HOMO and LUMO levels and redox potentials. Development of relatively simple, donor-acceptor model systems to mimic the events of the photosynthetic reaction center targeted two main applications: (i) conversion of solar energy into chemical energy, e.g. in form of H_2 by photocatalytic water splitting and (ii) utilizing these compounds in the development of optoelectronic devices.

On this behalf, nature has developed a variety of chromophores with electron-donating and accepting properties such as chlorophyll a and b, as well as carotenoids. For artificial photosynthesis this family of visible-range absorbing chromophores has been further enlarged by the employment of synthetic carotenoids,[278] subphthalocyaines,[279]

[278] a) H. Hashimoto, Y. Sugai, C. Uragami, A.T. Gardiner and R.J. Cogdell, *J. Photochem. Photobiol. C*, **2015**, *25*, 46-70. b) M. Kloz, S. Pillai, G. Kodis, D. Gust, T.A. Moore, A.L. Moore, R. van Grondelle and J.T.M. Kennis, *Chem. Sci.*, **2012**, *3*,

BODIPY,[280] PDI,[45] tetrathiafulvalenes (TTF),[268c,281] π-extended tetrathiafulvalene (exTTF),[46] and tetrapyrrolic macrocycles such as chlorines, Pors[ref] or Pcs.[ref] Moreover, other non-absorbing, electronically active molecules has been widely employed (e.g. ferrocene,[282] anilines and nanocarbon materials[283] like fullerene derivatives[277a,284] among others) in conjugation with the aforementioned chromophores, creating an extensive library of donor-acceptor building blocks for artificial photosynthesis.

2052-2061. c) D.M. Niedzwiedzki, *Chem. Phys. Lett.*, **2014**, *601*, 74-80. d) S. Pillai, J. Ravensbergen, A. Antoniuk-Pablant, B.D. Sherman, R. van Grondelle, R.N. Frese, T.A. Moore, D. Gust, A.L. Moore and J.T.M. Kennis, *Phys. Chem. Chem. Phys.*, **2013**, *15*, 4775-4784.

45 a) S.T.J. Ryan, R.M. Young, J.J. Henkelis, N. Hafezi, N.A. Vermeulen, A. Henning, E.J. Dale, Y. Wu, M.D. Krzyaniak, A. Fox, W.M. Nau, M.R. Wasielewski, J.F. Stoddart and O.A. Scherman, *J. Am. Chem. Soc.*, **2015**, *137*, 15299-15307. b) A.J. Jimenez, R.M.K. Calderon, M.S. Rodriguez-Morgade, D.M. Guldi and T.Torres, *Chem. Sci.*, **2013**, *4*, 1064-1074. c) S. Stappert, C. Li, K. Muellen and T. Basche, *Chem. Mater.*, **2016**, *28*, 906-914. d) S. Suzuki, M. Kozaki, K. Nozaki and K. Okada, *J. Photochem. Photobiol. C*, **2011**, *12*, 269-292.

46 a) F.G. Brunetti, J.L. Lopez, C. Atienza and N. Martin, *J. Mater. Chem.*, **2012**, *22*, 4188-4205. b) A. Molina-Ontoria, M. Gallego, L. Echegoyen, E.M. Perez and N. Martin, *RSC Advances*, **2015**, *5*, 31541-31546. c) Y. Takano, C. Schubert, N. mizorogi, L. Feng, A. Iwano, M. Katayama, M.A. herranz, D.M. Guldi, N. Martin, S. Nagase and T. Akasaka, *Chem. Sci.*, **2013**, *4*, 3166-3171.

279 a) C.G. Claessens, D. Gonzalez-Rodriguez, M.S. Rodriguez-Morgade, A. Medina and T. Torres, *Chem. Rev.*, **2014**, *114*, 2192-2277. b) D. Gonzalez-Rodriguez, T. Torres, D.M. Guldi, J. Rivera, M.A. Herranz and L. Echegoyen, *J. Am. Chem. Soc.*, **2004**, *126*, 6301-6313. c) D. Gonzalez-Rodriguez, T. Torres, M.M. Olmstead, J. Rivera, M.A. Herranz, L. Echegoyen, C.A. Castellanos and D.M. Guldi, *J. Am. Chem. Soc.*, **2006**, *128*, 10680-10681. d) M.E. El-Khouly, J.-H. Jong, J.-H. Kim, K.-Y. Kim, K.-Y. Kay and S. Fukuzumi, *J. Phys. Chem. C*, **2012**, *116*, 19709-19717. e) M. Rudolf, O. Trukhina, J. Perles, L. Feng, T. Akasaka, T. Torres and D.M. Guldi, *Chem. Sci.*, **2015**, *6*, 4141-4147.

280 a) A. Bessette and G.S. hanan, *Chem. Soc. Rev.*, **2014**, *43*, 3342-3405. b) M.E. El-Khouly, S. Fukuzumi and F. D'Souza, *ChemPhysChem*, **2014**, *15*, 30-47. c) V. Bandi, F.P. D'Souza, H.B. Gobeze and F. D'Souza, *Chem. Eur. J.*, **2015**, *21*, 2669-2679. d) J. Liao, H. Zhao, Y. Xu, Z. Cai, Z. Peng, W. Zhang, W. Zhou, B. Li, Q. Zong and X. Yang, *Dyes Pigments*, **2016**, *128*, 131-140.

281 a) J.J. Bergkamp, S. Decurtins and S.-X. Liu, *Chem. Soc. Rev.*, **2015**, *44*, 863-874. b) S. Castellanos, A.A. Viera, B.M. Illescas, V. Sacchetti, C. Schubert, J. Moreno, D.M. Guldi, S. Hecht and N. Martin, *Angew. Chem. Int. Ed.*, **2013**, *52*, 13985-13990. c) N. Martin, *Chem. Commun.*, **2013**, *49*, 7025-7027.

282 a) M. Souto, D.C. Dayana, J. Guasch, I. Ratera, C. Rovira, A. Painelly and J. Veciana, *J. Phys. Org. Chem.*, **2014**, *27*, 465-469. b) D. Gonzalez-Rodriguez, E. Carbonell, G.M. Rojas, C. Atienza, D.M. Guldi and T. Torres, *J. Am. Chem. Soc.*, **2010**, *132*, 16488-16500.

283 a) J. Mateos-Gil, L. Rodriguez-Perez, M.M. Oliva, G. Katsukis, C. Romero-Nieto, M.A. Herranz, D.M. Guldi and N. Martin, *Nanoscale*, **2015**, *7*, 1193-1200. b) T. Umeyama, H. Imahori, *J. Phys. Chem. C*, **2013**, *117*, 3195-3209.

284 a) S. Kirner, M. Sekita and D.M. Guldi, *Adv. Mater.*, **2014**, *26*, 1482-1493. b) T. Higashino, T. Yamada, M. Yamamoto, A. Furube, N.V. Tkachenko, T. Miura, Y. Kobori, J. yasuhiro, R. Jono, K. Yamashita and H. Imahori, *Angew. Chem. Int. Ed.*, **2016**, *55*, 629-633.

3.4.1. **Short introduction to Pc-[C_{60}]-fullerenes as artificial photosynthetic centres**

The preparation and study of donor-acceptor (D-A) hybrids involving Pcs and fullerenes present multiple advantages. Pcs are thermally and chemically stable compounds, which present a rich redox chemistry that can be tuned by inclusion of different metal centres or by peripheral/axial substitution. Moreover, their intense optical absorption in the red/NIR part of the solar spectrum renders the perfect light-harvesting systems for photovoltaic devices. The unique physicochemical properties of Pcs have prompted their incorporation into a large number of D-A systems where their role is (i) to harvest light efficiently, and (ii) once photoexcited, to act as an electron donor *versus* for an acceptor moiety.[285] Among electron-acceptors, carbon nanostructures such as fullerenes, carbon nanotubes and, more recently, graphene, hold a privileged position. These nanostructures exhibit a number of characteristic electronic and photophysical properties that make them paramount photo- and electroactive material. In particular, the [C_{60}]-fullerene is especially appealing because of its small reorganization energy in light-induced electron transfer reactions,[286] as a consequence of its unique 3D rigid structure and symmetry.[284a] This structural aspects can give rise, when implemented in D-A systems, to the formation of very stable radical ion pair species. In addition, C_{60} presents a low first reduction potential, and can reversibly accept up to six electrons.

Up to date, a large variety of both covalent and supramolecular Pc-C_{60} systems have been described, and the photophysical properties of some of these D-A materials studied.[269a,c] When comparing the covalent *versus* supramolecular approaches, the later present some advantages. Specifically, supramolecular strategies allow obtaining, in a straightforward manner, thermodynamically reversible supramolecular assemblies of these functional entities, whose stability can be influenced by the careful choice of the non-covalent interaction(s) as well as by other external factors such as the temperature or the solvent.[ref] Additionally, an ulterior challenge has recently arisen consisting in the synthesis and characterization of D-A hybrids in aqueous media. Aqueous solubility of artificial photosynthetic centers is a desirable property not only regarding environmentally related issues, for many applications where water solubility is indispensable but to mimic in a more realistic way its natural counterpart. Among potential uses of this approach, we highlight

---

[285] a) M.R. Wasielewski, *Chem. Rev.*, **1992**, *92*, 435-461. b) M.R. Wasielewski, *J. Org. Chem.*, **2006**, *71*, 5051-5066.

[286] D.M. Guldi and K.-D. Asmus, *J. Am. Chem. Soc.*, **1997**, *119*, 5744-5745.

the implementation of hydrogen-producing cells, the photoinactivation of artificial photonucleases, and the development of OSCs fully processed from aqueous solution. This challenging goal has been previously undertaken with Por-based D-A systems,[287] remaining uncharted for Pc-based hybrids until the present work.

Taking into account the aforementioned ideas, the preparation of two supramolecular ZnPc-C_{60} hybrids that present solubility in aqueous media will be described within this section (Figure 79). The supramolecular complexation process is driven by electrostatic and π-π interaction in between a tetracationic ZnPc (**31**) and two different tetra- and octaanionic water-soluble, regioisomerically pure fullerene derivatives (**39** and **40**, respectively). Charge balance between the cationic Pc and the anionic fullerene determines the stoichiometry of thes complexes to be 1:1 and 2:1, respectively. Importantly, spectroscopic characterization of **31**-**39** and **31**-**40** has been carried out during a short internship in the group of Prof. Dirk M. Guldi in Erlangen (Germany), revealing photoinduced electron transfer events, from the Pc to the C_{60} moiety, in both cases.

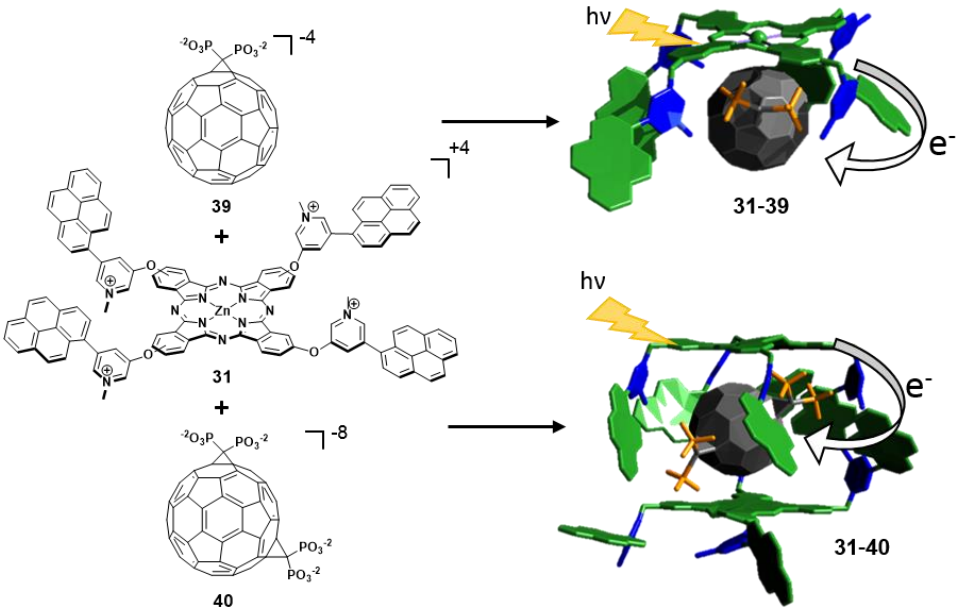

Figure 79. Chemical structures of the studied electron donor ZnPc **31**, and two water-soluble fullerene derivatives (**39** and **40**), which form the 1:1 and 2:1 complexes **31**-**39** and **31**-**40**, as schematically depicted on the right side of the figure. Counterions of the molecules are not shown for clarity porpoises.

[287] E. Krokos, F. Spänig, M. Ruppert, A. Hirsch and D.M. Guldi, *Chem. Eur. J.*, **2012**, *18*, 1328-1341.

3.4.2. **Synthesis of water-soluble fullerene derivatives as electron-acceptors**

In the design of suitable water-soluble electron-acceptor counterparts for the tetracationic ZnPc **31**, a tetraanionic solubilizing group is desirable in order to provide a proper charge balance between both components of the complex. Employing methylene diphosphonic acid groups provides, in its basic form, a tetraanionic moiety suitable to be incorporated into C_{60} through a classical Bingel-Hirsch reaction.[288] Our target fullerene components to build aqueous supramolecular donor-acceptor complexes with ZnPc **31** were the tetraanionic monoadduct **39** and the octaanionic bisadduct **40** (Figure 79). Thus, such compounds were synthesized by adapting a previously described methodology.[289] Briefly, fullerenes **42** and **43** were synthesized via Bingel-Hirsch reaction between previously described tetraethyl bromomethylenediphosphonate (**41**),[290] and pristine C_{60}, dissolved in toluene in the presence of NaH as base (Figure 80). The fullerene monoadduct **42** was separated from the reaction mixture via column chromatography, using chloroform as eluent. The second fraction, containing **43** as a mixture of bisadduct regioisomers, was subsequently purified via column chromatography, employing an eluent gradient from $CHCl_3$ to $CHCl_3$/THF in a 1:1 ratio, leading to a complete separation of 4 of the 5 regioisomers.

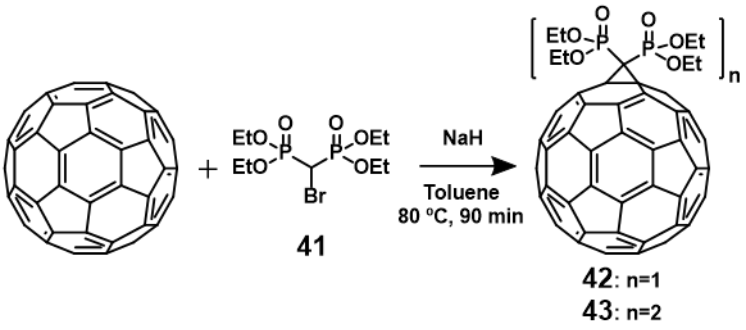

Figure 80. Synthesis of fullerene mono- and bisadduct derivatives **39** and **40**, respectively.

All fullerene derivatives were thoroughly characterized by different techniques. First, HPLC chromatograms of the reaction mixture, **42** and the different regioisomers of **43** were

[288] a) M. Prato, *J. Mater. Chem.*, **1997**, *7*, 1097-1109. b) N. Martin, L. Sanchez, B. Illescas and I. Perez, *Chem. Rev.*, **1998**, *98*, 2527-2547.

[289] A.L. Mirakyan and L.J. Wilson, *J. Chem. Soc. Perkin Trans. 2*, **2002**, 1173-1176.

[290] B. Iorga and P. Savignac, *J. Organomet. Chem.*, **2001**, *624*, 203-207.

recorded employing a Cosmosil Buckyprep column and using a linear gradient of eluents from t_0 = toluene to t_{40} = toluene/THF (85:15). These chromatogram reveals a good degree of separation for aforementioned regioisomers (Figure 81a). The assignment of each fraction was done by comparison with the calculated dipolar moment of each species (Figure 81b). These calculations were performed at semiempirical level (PM3) with *Spartan '14* software, fixing the phosphonic acid conformation. The complete purification of regioisomers **43**-*e* was not possible by column chromatography, showing traces of regioisomer **43**-*trans4*, due to their similar dipolar moments (11.98 and 10.04 D, respectively). Probably owing to steric hindrance between adjacent the ethyl phosphonic esters, no signal of the *cis* regioisomers formation was detected. Additionally, ^{31}P-NMR was carried out for compounds **41**, **42** and each of the regioisomers of **43** (Figure 82). The signals chemical shift and multiplicity for to the different regioisomers match those previously described,[289] supporting our assignment of product in the HPLC chromatograms.

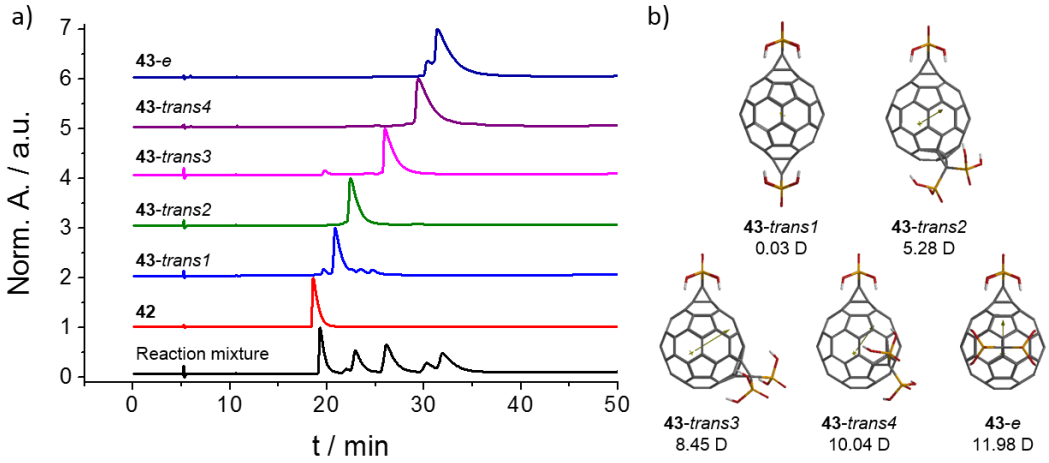

Figure 81. a) HPLC chromatograms of **42**, regioisomers of **43** and the reaction mixture. Conditions: Buckyprep column, using a linear gradient of eluents: t_0 = toluene (t_0); t_{40} = toluene/THF (85:15). b) Calculated dipolar moments of the fullerene **43** regioisomers.

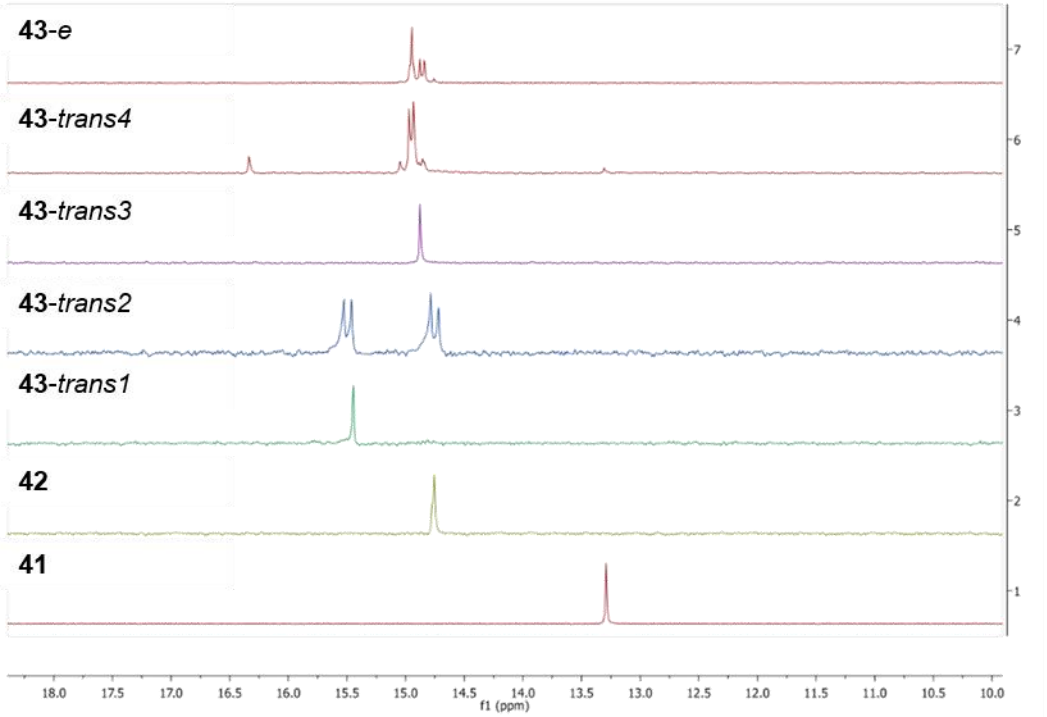

Figure 82. ^{31}P-NMR spectra of **41**, **42** and the **43** regioisomers in $CDCl_3$. All spectra are calibrated with an internal reference (H_3PO_4 in a sealed glass capillary; δ (ppm) = 0.0).

The electron-acceptor behaviour of these fullerene-derivatives was then evaluated, using cyclic voltametry (CV) (Figure 83). Due to the experimental difficulties to separate the **43**-*trans4* and **43**-*e* regioisomers in relatively large amounts, their electrochemical properties will be studied jointly. In all the samples, four different reduction peaks are discernible (ca. 1.20, 1.50, 1.85 and 2.35 V – Table 11), resembling the features of pristine C_{60}. However, there are two main differences when comparing to the voltamograms of this reference compound: (i) an irreversible reduction peak appears at ca. -1.6 V, probably due to the cyclopropanation reaction on the fullerene, and (ii) a noticeably decrease in the first reduction potential occurs, rendering slightly worse electron acceptors than the actual C_{60} fullerene. On the other hand, the substitution pattern does not seems to affect in a logic manner the electron-acceptor properties of each bisadduct regioisomer, especially the first reduction potential. Taking this into account, the selection of one of them as electron-acceptor toward the preparation of artificial-water-soluble D-A photosynthetic reaction

centres attended exclusively to their synthetic availability. **43**-*trans3* was obtained in the highest yield (9%), thus being our choice for futher complexation studies with the ZnPc **31**.

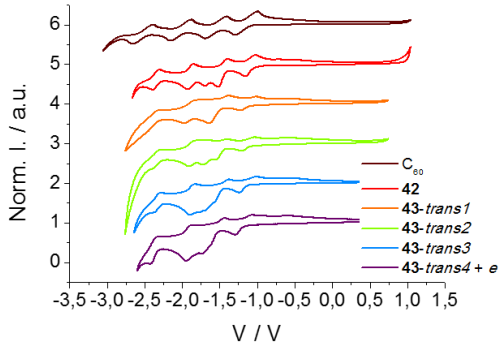

Figure 83. Electrochemical characterization of **42** and the **43** regioisomers by CV in an anhydrous *o*-DCB/dioxane (4:1) mixture, employing $TBAPF_6$ 0.1 M as background electrolyte. Spectra corrected to Fc/Fc^+ as reference.

Table 11. Electrochemical data for all the fullerene derivatives, **42** and **43**, determined by CV.

Molecule	**1st E ½**	**2nd E ½**	**Irrev. Red.**	**3rd E ½**	**4th E ½**
C_{60}	-1.11	-1.52	-	-1.99	-2.49
42	-1.19	-1.53	-1.68	-1.95	-2.42
43-*trans1*	-1.19	-1.50	-1.70	-1.89	-2.36
43-*trans2*	-1.15	-1.49	-1.69	-1.88	-2.35
43-*trans3*	-1.18	-1.46	-1.68	-1.85	-2.34
43-*trans4 + e*	-1.24	-1.51	-1.67	-1.90	-2.37

The last step in the synthesis of the anionic fullerene derivatives consists in the hydrolysis of the ethyl ester derivatives **42** and **43**-*trans3* in mild conditions (i.e. trimethylsilyl iodide and CCl_4 as solvent at 40 °C), followed by addition of water (Figure 84). Subsequently, the aqueous phase was subjected to ion exchange (Amberlite IR-120 Plus) in order to obtain the products in their acid form. In their acid form, these fullerene

compounds present low solubility in both organic and aqueous media. Addition of triethylamine (TEA) in concentrations of 1% in mater increase drastically their solubility by forming "*in situ*" the corresponding trimethylammonium salt derivatives.

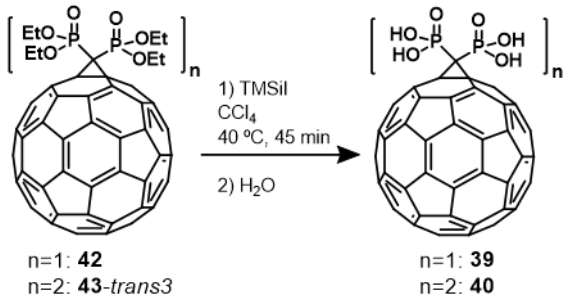

Figure 84. Synthesis of fullerenes **39** and **40** by mild hydrolysis of the corresponding fullerenes **42** and **43**-*trans3*, respectively.

3.4.3. **Aqueous ZnPc-fullerene supramolecular complexes**

In order to reproduce as strictly as possible the conditions studied in Chapter 1.3.3., all aqueous samples studied in the present section have been prepared in water/DMSO (95:5) solutions, containing an overall 1% of TEA to ensure the fullerene component solubility.

First, absorption and fluorescence titrations were conducted (Figure 85), proving the interaction between the photoactive components. Absoption titration shown (Figure 85a) was obtained by substracting the corresponding fullerene absorption to the titration spectra, monitoring the variations on ZnPc **31** upon complex **31-39** formation in water/DMSO/TEA (95:5:1). A noticeable decrease in the ZnPc **31** Q-band absorption coefficient was observed along, with a bathochromic shift upon the addition of **39** up to 1 equivalent. Furthermore addition caused only minor changes. Fluorescence titration (Figure 85b), on the other hand, shows a strong intensity decrease upon addition of 1 equivalents, becoming a complete quenching when furthermore equivalents were added.

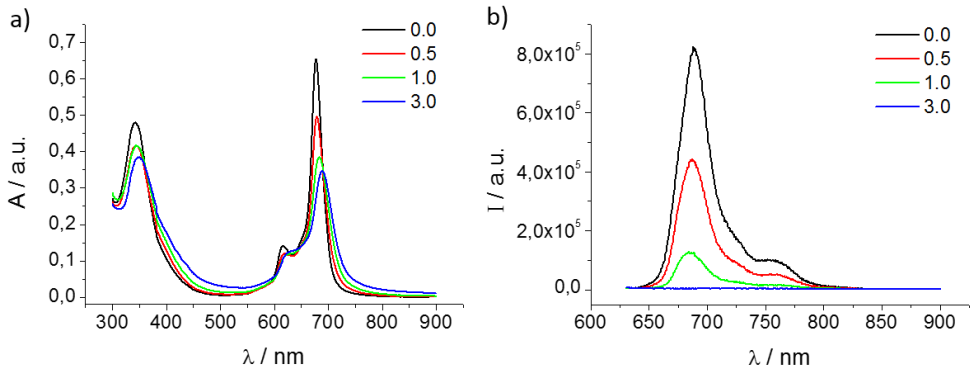

Figure 85. a) Absorption and b) fluorescence spectra of ZnPc **31** with growing ammounts of fullerene derivative **39** in water/DMSO/TEA (95:1:1), at 5.0 x 10^{-6} M. Emission spectra recorded by excitation at 615 nm, 5 nm slit.

The stoichiometry of the supramolecular assemblies between ZnPc **31** and the fullerenes **39** and **40** was determined through the method of *continues variation* or Job's plot, carried out by absorption spectroscopy (Figure 86). These experiments confirmed the importance of electrostatic interactions as main driving force of the self-assembly process, since **31**-**39** and **31**-**40** bind in a 1:1 and 2:1 ratios, respectively, following charge compensation between both the cationic and anionic moieties.

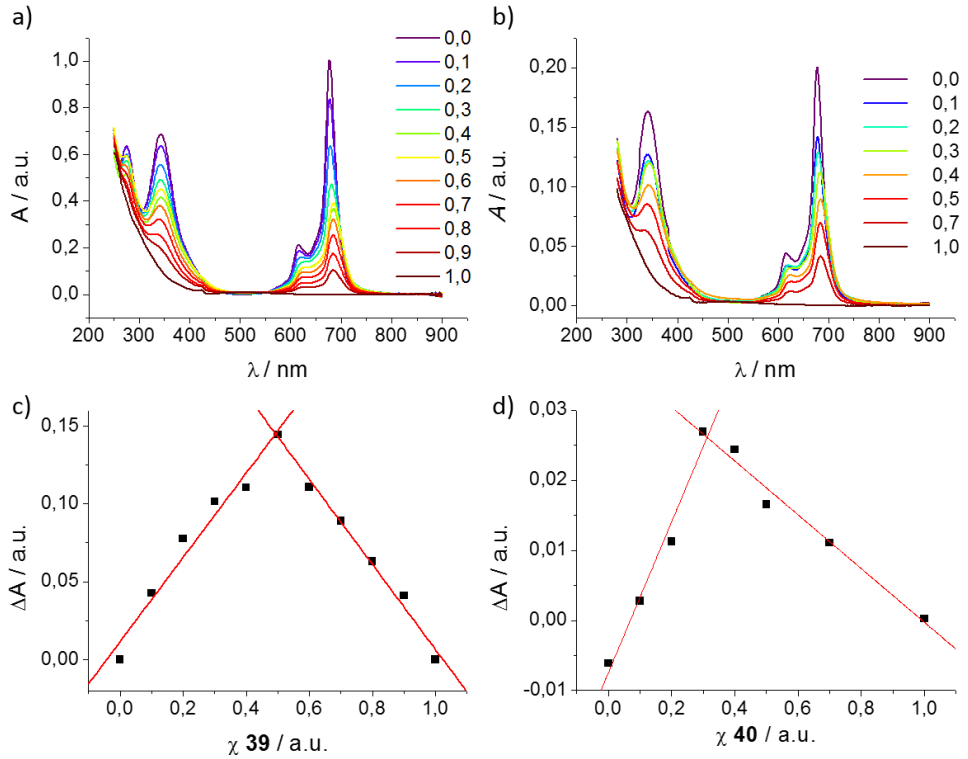

Figure 86. (Top) Absorption spectra of all **31**-**39** (a) and **31**-**40** (b) samples measured for the Job's plot experiment. The overall concentration stays constant at 5.0 x 10^{-6} M and 1.0 x 10^{-6} M, respectively, during the experiments. (Bottom) Job's plot diagrams of the complexes **31**-**39** (c) and **31**-**40** (d), centered in 0.5 (1:1 stoichiometry) and 0.33 (2:1 stoichiometry), respectively. The experiments were monitored at 707 and 702 nm, respectively.

Formally, the formation of the **31**-**39** complex consists in a one-step process, as showed in eq. (1), while the formation of **31**-**40** would involve two steps, i.e. eq.(1) and (2). In addition, a third process involving self-aggregation of the ZnPc **31** could be taken into account but, in the presen case, will be dismissed due to its low association constant (i.e. 8.4 x 10^3 M^{-1} – Chapter 1.3.3.3.) in comparison to the electrostatically driven high binding association constants of the heterocomplexes (see below).

$$H + G \leftrightarrow HG \qquad K_1 = [HG]/[H][G] \qquad \text{Eq.(1)}$$

$$HG + H \leftrightarrow H_2G \qquad K_2 = [H_2G]/[HG][H] \qquad \text{Eq.(2)}$$

where *H* is the host (ZnPc **31**), *G* is the guest (i.e. the fullerene derivative), *HG* is the 1:1 complex and H_2G the 2:1 complex. *K* denotes binding constants for each of the described processes. Values in brackets denote concentrations of the species in the corresponding equilibrium.

With this scheme in hand, the absorption and fluorescence titrations previously conducted allowed determining the association constants values (K_{abs} and K_{em}, respectively) displayed in Table 12. Such values were fitted using Reactlab® Equilibria fitting software, with the aforementioned equations. For clarity reasons, all titrations and the corresponding fitted curves are depicted at the end of this chapter's experimental section. Additionally to the previously discussed hybrids, ZnPc **32** has been employed as reference in the formation of an additional complex (**32**-**39**), where no pyrene moieties are displayed.

Table 12. Binding constants for different combinations of ZnPc **31** and **32**, and fullerenes **39** and **40**.

Solvent	Host (H)	Guest (G)	K_{abs}/ M^{-1}	K_{em}/ M^{-1}
Water/DMSO/TEA (95:5:1)	ZnPc **31**	**39**	$(1.12 \pm 0.03) \times 10^6$	$(6.53 \pm 0.03) \times 10^6$
		40	$K_1 = (1.18 \pm 0.06) \times 10^6$ $K_2 = (1.10 \pm 0.06) \times 10^6$	-[a]
DMSO	ZnPc **31**	**39**	$(3.57 \pm 0.02) \times 10^6$	$(6.48 \pm 0.03) \times 10^6$
		40	$K_1 = (3.62 \pm 0.05) \times 10^6$ $K_2 = (3.48 \pm 0.05) \times 10^6$	$K_1 = (6.97 \pm 0.06) \times 10^6$ $K_2 = (1.98 \pm 0.06) \times 10^6$
	ZnPc **32**	**39**	$(1.32 \pm 0.03) \times 10^5$	$(2.1 \pm 0.03) \times 10^5$

ZnPc concentration: 5.0×10^{-6} M for absorption titrations and 1.0×10^{-6} M for fluorescence titrations. [a] Data not suitable for fitting.

From the Table 12, it is noteworthy to mention the difference between K_a of **31**-**39** and **32**-**39** ($(1.12 \pm 0.03) \times 10^6$ *versus* $(1.32 \pm 0.03) \times 10^5$ M^{-1}, respectively). The primary electrostatic interaction, present in both complexes, is furthermore stabilized in **31**-**39** due to a secondary π-π interaction between the aromatic surfaces of the fullerene and the pyrene moieties present in ZnPc **31** (see Figure 79, top right). The present data thus allow

estimating the contribution of π-π interactions to the K_a of **31**-**39** in about one order of magnitude. Besides, the titrations performed in aqueous media yielded remarkably high association constants values ((1.12 ± 0.03) x 10^6 M^{-1}) for **31**-**39**. K_a obtained in DMSO, where the ZnPc behave as a monomer, are slightly highers, yet in the same order of magnitude as those obtained in aqueous media (i.e. (1.12 ± 0.03) x 10^6 *versus* (3.57 ± 0.02) x 10^6 M^{-1}, in water/DMSO/TEA (95:5:1) and DMSO, respectively). Such similarity validates our starting approach of neglecting the ZnPc self-aggregation process due to the difference in two orders of magnitude between K_{HG} and K_{HH} (i.e. 1.1 x 10^6 *versus* 8.4 x 10^3 M^{-1}, respectively – Chapter 1.3.3). In addition, the K_a of the two processes involved in **31**-**40** formation are very similar to each other and in comparison to that of the **31**-**39** hybrid. We ascribe these obervations to the facts that (i) the electrostatic interaction is the main recognition driving force, and (ii) the formation of the **31-40** 1:1 complex does not inhibits, by kinetic means, the addition of a second ZnPc to reach the most thermodynamically favoured 2:1 hybrid. In turn, this might be consequence of (i) the spatial separation of the phosphonate groups on the fullerene scaffold and (ii) the degree of freedom in the rotation of the pyrene moieties, allowing the incorporation of a second ZnPc.

3.4.4. **Photophysical characterization of aqueous ZnPc-fullerene complexes**

In order to evaluate the donor-acceptor properties of the aforementioned hybrids, spectroscopic studies of both complexes **31**-**39** and **31**-**40** were conducted. First, NIR fluorescence spectra of **31**-**39** were recorded in water/DMSO (95:5) upon excitation in the area from 640 to 720 nm (Figure 87b). In the spectra, the fluorescence emission is strongly quenched when compared to that of ZnPc **31** at the same concentration (Figure 87a). Moreover, upon excitation at the absorption maximum of the complex (λ_{exc} = 687 nm), a bathocrhomical shift was observed evolving an emission maximum strongly shifted (λ_{em} = 930 nm). Both the quenching and the shift in the absorption-emission maxima suggest an energy or electron transfer upon illumination, wich deactivates the singlet excited state of ZnPc **31.** Unfortunately, time-correlated single photon counting (TCSPC) measurements were not possible to be carried out due to the low emission of the **31**-**39** hybrid.

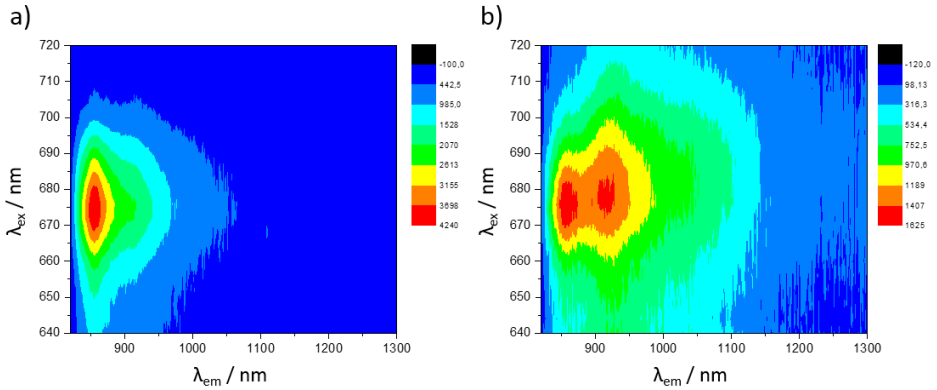

Figure 87. NIR fluorescence spectra of a) the ZnPc **31**, and b) the **31**-**39** complex. The spectra were measured in water/DMSO (95:5), with a 800 nm filter for the emission wavelength in order to ensure better resolution.

The nature of the excited-state interactions between the ZnPc **31** and the fullerene were probed by means of transient absorption measurements. A first set of measurements in DMSO were carried out for **31**, **31**-**39**, and **31**-**40**, in order to determine the typical charge-transfer features of the donor and acceptor moieties without any interference of ZnPc self-aggregation related process. The second experiment, conducted in D_2O/DMSO/TEA (95:5:1), was designed to better understand the complex behaviour of the above systems in aqueous media.

The excitation of ZnPc **31** in DMSO at 694 nm results in typical singlet decay features, e.g. the maximum evolution at 633 nm (Figure 88a), with a fitted lifetime of 2.6 ns. Upon addition of the corresponding acceptor moiety, the **31**-**39** and **31**-**40** hybrids show an immediate quenching of the singlet feature at 633 nm and the evolution of two maxima in the NIR region, at 837 and 1010 nm, which are assigned to the ZnPc radical cation ($ZnPc^{\cdot+}$) and the C_{60} radical anion ($C_{60}^{\cdot-}$), respectively (Figure 88b and c).[291] The charge-separation lifetimes have been preliminarily fitted to 119 and 510 ps, with intersystem crossing lifetimes of 2.2 and 13 ps for **31-39** and **31**-**40**, respectively.

On the other hand, preliminary results are currently under discussion about transient absorption spectrum of ZnPc **31** in D_2O/DMSO (95:5). Upon excitation at 676 nm (Figure 89a), the ZnPc **31** presents maxima evoluving at 525, 580, 750, 834, and 982 nm,

[291] A. de la Escosura, O. Trukhina and T. Torres, *Struct. Bond.*, **2014**, *159*, 145-192.

together with the typical minima at 615 and 680 nm, thus resembling the absorption spectrum. Based on previous works, most relevant features at the NIR region of the spectrum can be assigned to both $ZnPc^{\cdot+}$ (837 nm)[291] and, tentatively, $ZnPc^{\cdot-}$ (982 nm).[292] In particular, the latter signature has been observed by spectroelectrochemical reduction of the closely related ZnPcs **16** and **17**, reported in the present chapter (Chapter 3.3.1 – Figure 76c and d). This would represent quite a surprising result. Indeed, we are still working on proving the formation of the $ZnPc^{\cdot-}$, and searching for an adequate explanation of this phenomenon if it is finally confirmed. In this respect, spectroelectrochemistry of **31** and **32** did not provide a satisfactory resolution, due to the strong self-aggregation of these systems. Moreover, kinetics of the selected features confirms a relatively long-living kinetic event, fitted to 230 ± 60 ps for **31** (Figure 89b) in both features. Same kinetics of both features supports our hypothesis of a tentative assignment to charge dissociation. DFT calculations in the proposed geometry of ZnPc **31** in the aggregation regime B (see Chapter 1.3.3.3) will then be conducted in order to understand the charge dissociation observed for ZnPc **31** in this experiment.

[292] a) A. Roth, M.-E. Ragoussi, L. Wibmer, G. Katsukis, G. de la Torre, T. Torres and D.M. Guldi, *Chem. Sci.*, **2014**, *5*, 3432-3438. b) O. Trukhina, M. Rudolf, G. Bottari, T. Akasaka, L. Echegoyen, T. Torres and D.M. Guldi, *J. Am. Chem. Soc.*, **2015**, *137*, 12914-12922.

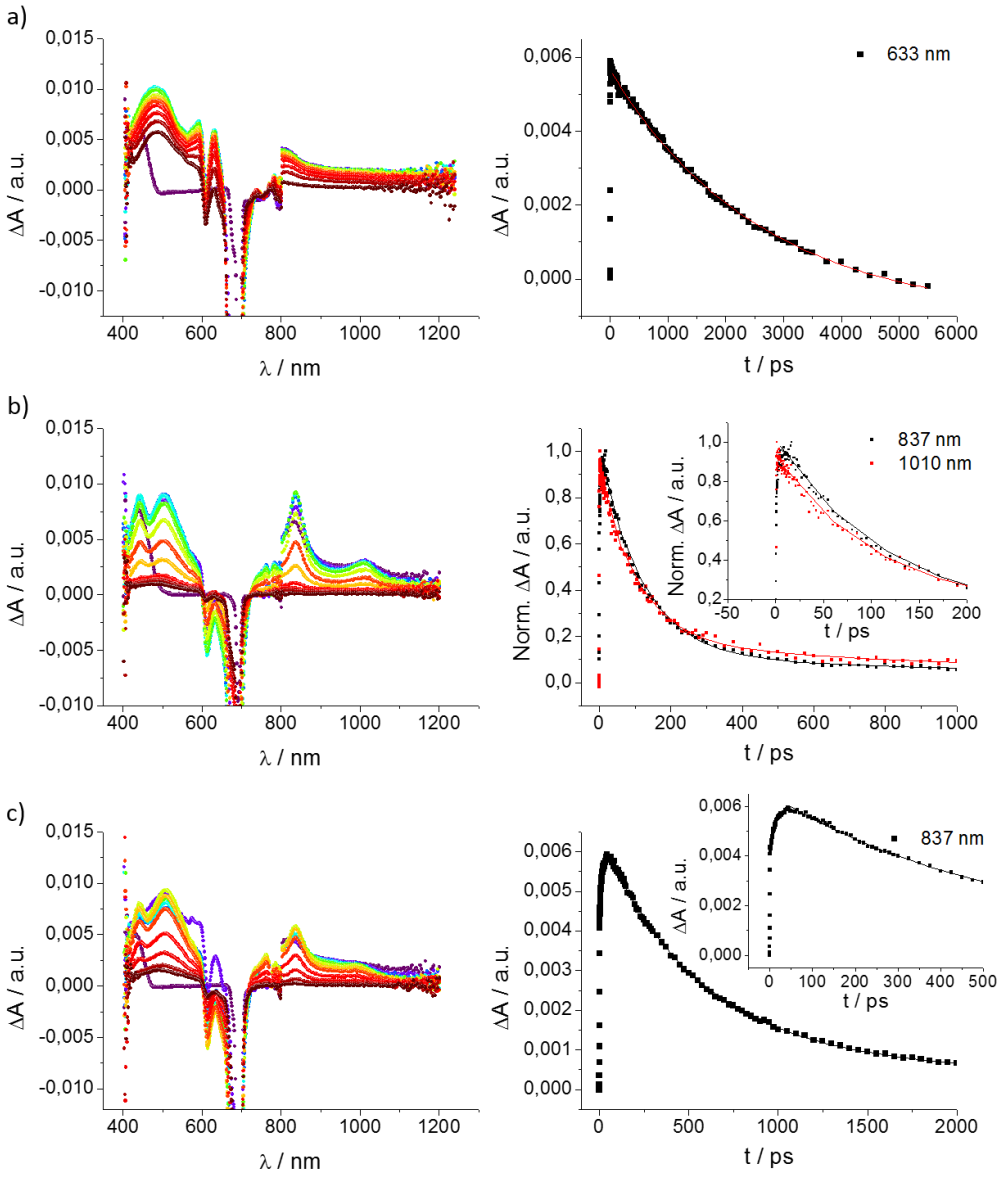

Figure 88. Differential visible and NIR absorption spectra obtained upon femtosecond pump probe experiments exciting at 694 nm (left) with several time delays between 1 (purple) and 5000 ps (dark red), and detailed kinetics of the most relevant features (right) for a) ZnPc **31**, and the b) **31**-**39** and c) **31**-**40** hybrids. All the experiments were conducted in anhydrous DMSO at room temperature.

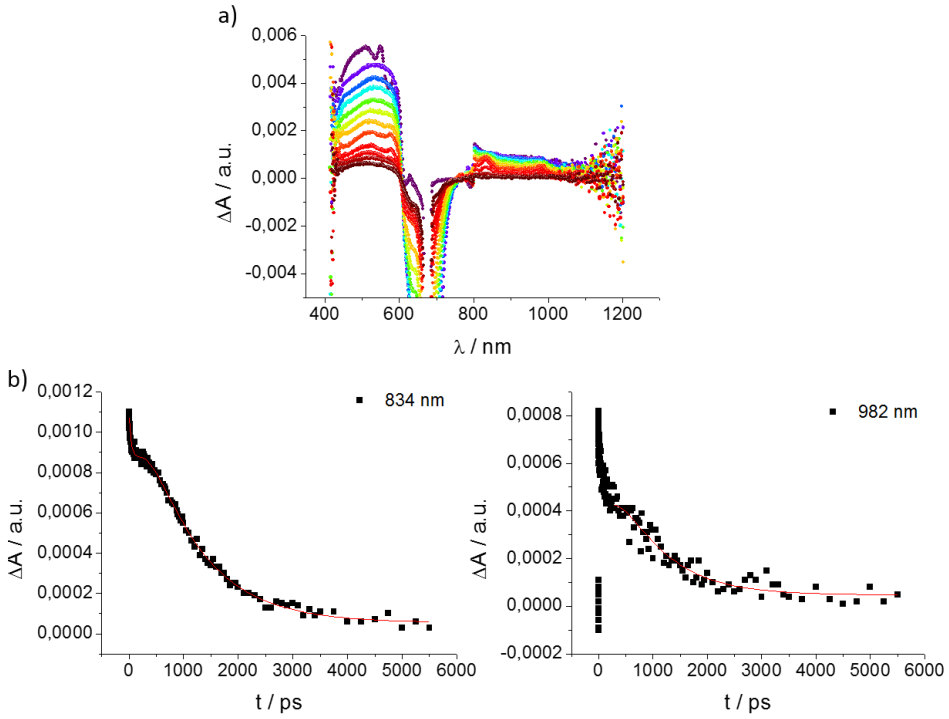

Figure 89. Differential visible and NIR absorption spectra obtained upon femtosecond pump probe experiments for the ZnPc **31** (a) with several time delays between 1 (purple) and 5000 ps (dark red), and detailed kinetics of the most relevant features upon excitation at 676 nm (b and c). All the experiments were conducted in D_2O/DMSO/TEA (95:5:1) at room temperature.

Finally, transient absorption experiments for the ZnPc **31**, and the **31**-**39** and **31**-**40** hybrids were carried out in D_2O/DMSO/TEA (95:5:1), exciting at 694 nm (Figure 90). The spectrum of ZnPc **31** in these conditions presents well the assigned $ZnPc^{\cdot+}$ and $ZnPc^{\cdot-}$ features, as we described in the previous paragraph. Kinetic events at ca. 10 and 200 ps, found under excitation at 676 nm (Figure 89a) are. Upon addition of fullerene derivatives, **31**-**40** and, more clearly, **31**-**39** complexes shows the $ZnPc^{\cdot+}$ signature at 837 nm and a broad maximum over 990 nm that can be assigned to the $C_{60}^{\cdot-}$ in aqueous media. Interestingly, kinetics of these peaks, especially of the well-known $ZnPc^{\cdot+}$, does not present the kinetic event at ca. 200 ps in presence of strong electron acceptors such as **39** or **40**, observed in both Figure 89 and Figure 90a. These kinetic feature quenching, assigned to charge dissociation event, supports our hypothesis of the formation of most thermodynamically stable $ZnPc^{\cdot+}$-$C_{60}^{\cdot-}$ charge separated state, instead of the $ZnPc^{\cdot+}$- $ZnPc^{\cdot-}$ formed in the absence of strong electron acceptors.

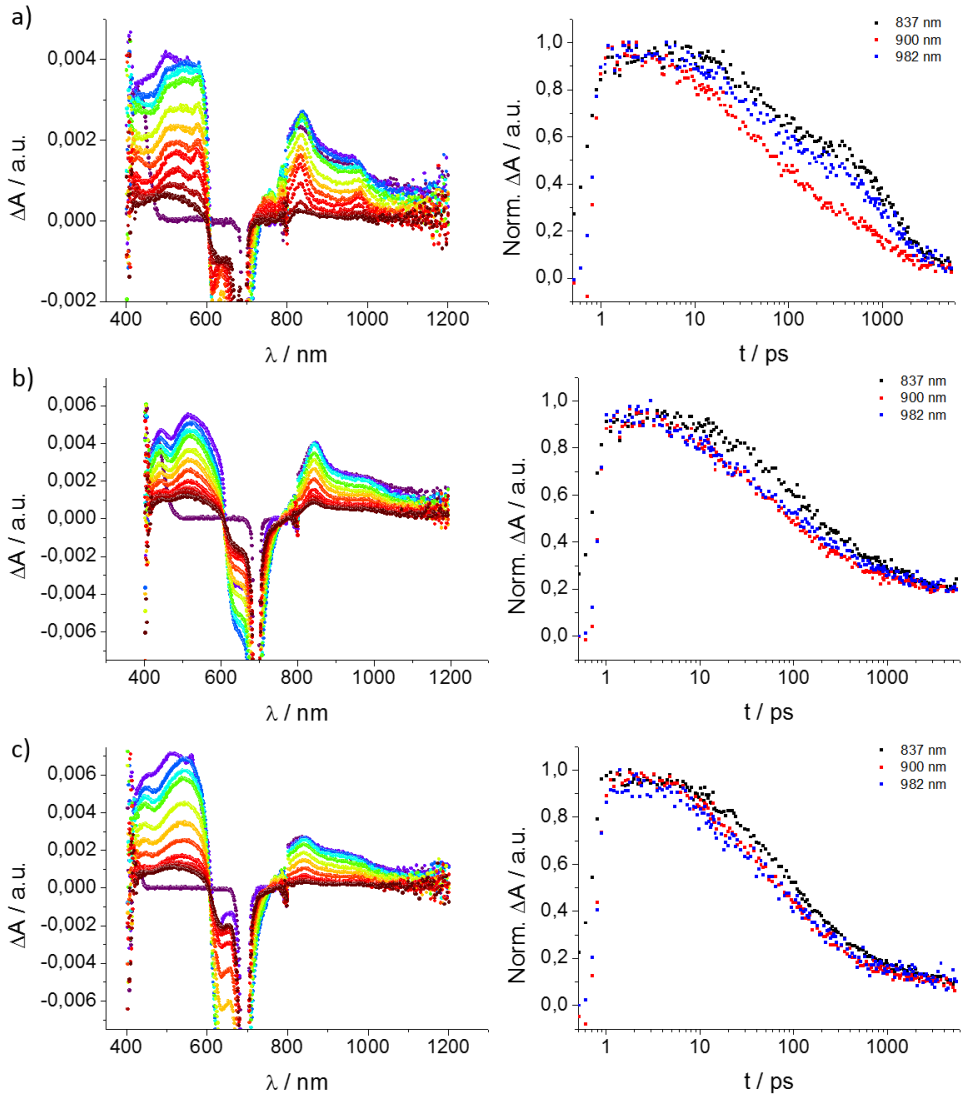

Figure 90. Differential absorption spectra (visible and NIR) obtained upon femtosecond pump probe experiments exciting at 694 nm (left) with several time delays between 1 (purple) and 5000 ps (dark red), and detailed kinetics of the most relevant features (right) of a) ZnPc **31**, b) **31**-**39** and c) **31**-**40** hybrids. All the experiments were conducted in anhydrous D_2O/DMSO/TEA (95:5:1) at room temperature.

In sum, despite the fact that complementary experiments must be conducted to unequivocally characterization of the charge-separation states, the preliminary photophysical studies shown in this section represent a very promising starting point

toward the fully understanding of the complex processes involved in **31**-**39** and **31**-**40** hybrids, and therefore, toward their application in artificial photovoltaics.

3.5. Conclusions

In the present chapter, three different approaches to photovoltaic systems have been prepared by combining water-soluble ZnPcs and well known carbon nanostructures such as SWCNTs and fullerene derivatives.

In the first example we have shown that the role of the substituents in ZnPc molecules is paramount for tuning the performance of OSC based on water-soluble Pcs. This finding has led to significant improvement in device performance by tuning the energy levels of the donor ZnPc to achieve a more energetically favourable photooxidation of the C_{60} acceptor layer, resulting in a maximum efficiencies of 0.46 % under standard conditions. Also, the number of substituents controls the morphology of the thin films, which in turn affects device performance. Having successfully demonstrated our first goal, the next step will be to develop a water-soluble acceptor molecule, in order to provide both an environmentally friendly and an inexpensive route towards functional water-processed OSCs.

Secondly, a novel approach is presented toward the production of water-soluble electron donor-acceptor hybrids featuring SWCNTs and ZnPc as electron donors and electron acceptors, respectively. Such a combination of properties is unprecedented for ensembles made of these two photoactive components. Key to our strategy was the immobilization of quaternized pyridyloxy ZnPcs onto CoMoCAT SWCNTs. To this end, a series of ZnPcs bearing a variable number of quaternized pyridyloxy groups was prepared and purified for the first time (Chapter 1.3.2.), as a result of placing *tert*-butyphenyl substituents at the 5-position of the pyridine moieties. Electrochemical assays confirmed the strong electron accepting ability of the ZnPcs, which is comparable to those of the best electron acceptors. Compared to conventional ZnPcs, which act as electron donors when interfaced with SWCNTs, our novel ZnPcs enable a reversed charge transfer in the resulting water-soluble electro donor-acceptor hybrids, namely, from the electron donating SWCNTs to the electron accepting ZnPcs. In proof-of-concept experiments, the obtained SWCNT/ZnPc hybrids have been used for energy conversion in photovoltaic devices, opening the way toward solar cells entirely processable from aqueous solutions.

Finally, two unprecedented D-A systems have been developed by combination of a ZnPc bearing pyrenyl moieties attached at the 5-position of its peripheral pyridinium groups (ZnPc **31**) as electron-donor and a tetra- or octaanionic fullerene derivative as electron-acceptors. The resulting 1:1 and 2:1 supramolecular ZnPc-fullerene ensembles

originate from two different driving forces: (i) electrostatic interaction between the cationic ZnPc and the anionic fullerene, responsible of the stoichiometry of the obtained complexes and (ii) π-π interaction between the pyrene moieties and the C_{60} aromatic surface. The charge separation state $ZnPc^{\cdot+}$-$C_{60}^{\cdot-}$ has been clearly characterized in both complexes by means of transient absorption spectroscopy in DMSO and aqueous media, despite the complexity of the processes involved in the second case. These systems under active investigation represent the first approach to more reliable photoactive centers towards application in artificial photosynthesis in aqueous media. These complexes, still under investigation, are the first case of photoinduced electron transfer within Pc-C_{60} ensembles in aqueous medium, representing a very promising approach toward artificial photosynthetic systems and environmentally friendlier photovoltaic energy conversion.

3.6. Experimental section

3.6.1. **Materials and methods**

Reagents were purchased from Sigma-Aldrich and Alfa-Aesar, and used without further purification. Silica Gel (Merck 60, 230-400 mesh, 60 Å) and TLC plates (Silica gel 60 F254) were purchased from Merck. Solvents were purchased from Carlo Erba Reagents. The ionic exchange resin Amberlite IR-120 (plus) was purchased from SUPELCO.

^{1}H-NMR and ^{31}P-NMR spectra were recorded with a Bruker AV-300. Mass spectra were recorded with a Bruker Ultraflex III spectrometer. HPLC chromatograms were recorded with an Agilent 1290 Infinity LC system, equipped with a Cosmosil Buckyprep 4.6ID x 10mm precolumn and a Cosmosil Buckyprep 4.6ID x 250mm column.

3.6.1.1. Chapter 3.2 specific characterization

UV-Vis measurements of the FTO deposited thin-films were carried out using a Shimadzu UV-2401PC spectrophotometer equipped with a photomultiplier detector, double beam optics, and D_2 and W light sources. Photoluminescence measurements were obtained using on an Aminco-Bowman Series 2 Luminescence spectrofluorimeter equipped with a high voltage PMT detector and continuum Xe Light source.

Differential pulse voltammetry (DPV) experiments were carried out using a CH Instruments 660c Electrochemical Workstation, with a standard three-electrode setup employed that utilized a Pt disc working electrode, Pt wire working electrode and SCE reference electrode. A 0.1 M solution of tetrabutylammonium phosphate in DMSO was used as the background electrolyte. To determine the HOMO of the respective molecules, the following formula:[293]

$$E_{HOMO} = -(1.4 \pm 0.1) \times (qV_{CV}) - (4.6 \pm 0.08)\ eV$$

where V_{CV} corresponds to E_{OX} of the substrate vs. ferrocene/ferrocenyl couple (Fc/Fc^{+}) peak potential (Ep).

Devices were prepared on ITO substrates (5 $\Omega\ \square^{-1}$, Psiotech Ltd. U.K.). The substrates were cleaned by sonicating in acetone and 2-propanol, followed by 20 min exposure to

[293] B.W. D'Andrade, S. Datta, S.R. Forrest, P. Djurovich, E. Polikarpov and E. Thompson, *Org. Electron.*, **2005**, *6*, 11-20.

UV/O_3. Thin films of the sulfonated ZnPc donors were prepared by spin-coating a 10 mg ml^{-1} solution (Mill-Q ultrapure water) of the respective donor, which had been left overnight stirring at 50 °C, and filtered using a 0.2 mm cellulose acetate membrane. The spin-coating conditions employed were 2000 rpm for 1 minute. Subsequently, the films were allowed to dry for 30 min in ambient conditions before transferring to a nitrogen rich glove box, where they were annealed at a temperature of 100 °C for 15 min in an attempt to remove any residual water. Finally the substrates were placed in the evaporator where the C_{60} (40 nm, MER Corp., 99.9+%), BCP (8 nm, Sigma Aldrich), and Al (100 nm, Sigma Aldrich) were deposited at a base pressure of 1 x 10^{-6} mbar. Device J-V curves were recorded using a 150 W solar simulator (Abet Technologies) at 1 sun conditions (AM 1.5, 100 mW cm^{-2}). Incident to photon current efficiency (IPCE) studies were carried out using a home-built system utilising a 150 W Oriel Xenon lamp as the light source.

3.6.1.2. Chapter 3.3 specific characterization

Steady-state UV-Vis/NIR absorption spectroscopy was measured on a Cary 5000 (Varian) two-beam spectrometer. Steady-state fluorescence spectra were taken with a FluoroMax3 spectrometer (HORIBA Jobin Yvon) in the visible detection range and with a FluoroLog3 spectrometer (HORIBA Jobin Yvon) with an IGA Symphony (5121 1 μm) detector in the NIR detection range. The experiments were performed at room temperature.

Time correlated single photon counting (TCSPC) spectra were taken with a FluoroLog system (HORIBA Jobin Yvon). The sample was excited by a NanoLED-650 (peak wavelength 647 nm) and the signal was detected by a Hamamatsu MCP photomultiplier (type R3809U-50). The time profiles were recorded at 680 nm.

Raman spectra were recorded using a Bruker FT Raman RFS 100 system with a liquid N_2 cooled Ge detector upon excitation by a 1064 nm Nd-YAG laser.

Femtosecond transient absorption spectroscopy was performed with 387, 676 and 964 nm laser pulses (1 kHz, 150 fs pulse width) from an amplified Ti:sapphire laser system (Model CPA2101 from Clark-MXR Inc.), the laser energy being 200 nJ. Electrochemical experiments were carried out with a Metrohm FRA 2 μAutolab Type III potentiostat, in deaerated DMSO containing 0.1 M tetrabutylammonium hexafluorophosphate ($TBAPF_6$) as the supporting electrolyte. A single-compartment, three-electrode cell configuration was

used in this work. Glassy carbon (3 mm diameter) or platinum (2 mm diameter) was used as the working electrode, a platinum wire as the counter, and an Ag wire as the reference electrode. All potentials were corrected against Fc/Fc^+ internal reference.

Spectroelectrochemical experiments were performed with a home-made setup containing a potentiostat (Metrohm Autolab PGSTAT 101) and Analytik Jena Specord absorption spectrophotometer. The working electrode has been platinum gauze (99.9%, 1024 mesh/cm^2, 0.06 mm wire diameter) from ChemPur, a platinum wire was used as counter electrode, and an Ag wire as reference electrode.

Photovoltaic devices were prepared as follows: FTO plates were extensively cleaned, using ultrasonication in subsequent baths of detergent, acetone, and isopropanol for 15 min each, and in an air cleaner/ozone generator for 18 min. The spray pyrolysis method was used to prepare the SWCNT/ZnPc hybrid films on pre-cleaned FTO slides. In detail, a thin film was prepared by spraying a solution of CoMoCAT SWCNT/ZnPc hybrids (D_2O) using N_2 air flow at 2 atm onto a FTO substrate placed on top of a heater at 200 °C. Next, key film properties such as morphology, thickness, and conductivity, were investigated by using scanning electron microscopy (SEM, Zeiss Gemini Ultra 55), profilometry (KLA Tencor Alpha Step D-100 Stylus), and the 4-point-probe technique (Jandel H-L, Keithley 2400), respectively. The solar cells were constructed using the latter films featuring different thicknesses together with equimolar 3M Na_2S/S/NaOH electrolyte and Cu_2S-based counter-electrode. Photocurrent measurements were carried out under 1 sun and AM 1.5 conditions using a custom made solar simulator including a 350-1000 Watt adjustable Xe lamp source (LOT) combined with appropriate filters. Current-voltage measurements were measured by using a potentiostat/galvanostat (PGSTAT30N, Autolab equipped with a frequency response analyzer module – FRA) in the range of -0.8 to 0.2 V. Incident photon-to-current conversion efficiencies (IPCE) were performed under 1 sun and AM 1.5 conditions with a Newport system.

3.6.1.3. Chapter 3.4 specific characterization

UV–Vis and fluorescence spectra were recorded using a JASCO V-660 spectrophotometer and fluorometer, respectively, using a Hellma QS quartz cuvette with 1 cm light path. Photophysical and photochemical characterization was performed as in the previous section.

3.6.2. **Synthesis of anionic fullerene derivatives**

Tetraethyl bromomethylenediphosphonate (**41**)

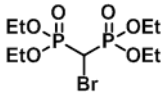

Into a 100 mL round-bottomed flask, *n*-buthyllithium 1.6 M in hexane (6.9 mL, 11.04 mmol) was dissolved into 20 mL of freshly distilled THF at -78 ^{o}C. Subsequently, a solution of di(isopropyl)amine (1.6 mL, 11.4 mmol) in 10 mL of freshly distilled THF and was stirred for 10 min. Thereafter, a solution of tetraethyl methylenediphosphonate (1.2 mL, 4.8 mmol) in 10 mL of freshly distilled THF was added dropwise. When the addition is completed the reaction was left to warm up to rt, followed by the addition of a solution of dibromotetrachloroethane (1.8 g, 5.5 mmol) in 10 mL of freshly distilled THF. After 30 min. the reaction was poured over an H_2SO_4 2M/DCM (1:1) mixture (60 mL) and the phases were separated. The aqueous phase was washed with DCM (2 x 25 mL) and the combined organic phases were dried over anhydrous Mg_2SO_4 and, therefore, dried in vacuo. Dark yellow oil was purified by chromatography column, employing ethylacetate as eluent, resulting into a yellowish oil. Yield: 1.34 g, 75%.

^{1}H-NMR (300 MHz, $CDCl_3$): δ (ppm) = 4.36-4.20 (m, 8H, -OCH_2-), 3.87 (t, *J* = 16.9 Hz, 1H, -CHBr), 1.38 (t, *J* = 7.1 Hz, 12H, -CH_3).

^{31}P-NMR (122 MHz, $CDCl_3$, ref. H_3PO_4 = 0.00 ppm): δ (ppm) = 13.29 (s)

Bingel-Hirsch reaction: general procedure[289]

Into a 1 L round bottomed flask, dry toluene (400 mL) were deaereated, followed by the addition of C_{60} (510 mg, 0.74 mmol) and NaH 60% in mineral oil (200 mg, 5 mmol), previously washed with toluene. The resulting solution was warmed up to 80 ^{o}C, followed by the dropwise addition of **41** (659 mg, 1.79 mmol) in anhydrous toluene (5 mL), resulting in gas evolution (H_2). The reaction mixture was left stirring for 90 minutes. The reaction mixture was then filtered off and the resulting solution was dried under reduced pressure.

Monoadduct (**42**)

Aforementioned reaction mixture was purified by chromatography column, employing $CHCl_3$ as eluent, eluting as first fraction. Yield: 86.7 mg, 12 %.

Mp: 252-254 ^{o}C

^{1}H-NMR (300 MHz, $CDCl_3$): δ (ppm) = 4.48 (q, *J* = 7.2 Hz, 8H, -OCH_2), 1.52 (t, *J* = 7.0 Hz, 12H, -CH_3).

^{31}P-NMR (122 MHz, $CDCl_3$, ref. H_3PO_4 = 0.00 ppm): δ (ppm) = 14.82 (s)

MS (MALDI-TOF, DCTB): *m/z* (%) = 1006.1 [M^+].

Bisadduct (**43**)

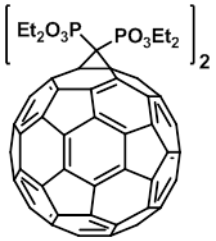

Aforementioned reaction mixture was purified by chromatography column, employing a solvent gradient, from $CHCl_3$ to $CHCl_3$/THF (1:1) as eluent, eluting as second (**43**-*trans1*), third (**43**-*trans2*), fourth (**43**-*trans3*) and fifth (**43**-*trans4* + **43**-*e*) fractions. The latter was furthermore purified, yielding small amounts suitable for characterization purposes.

Mp: 227-229 ^{o}C

MS (MALDI-TOF, DCTB): *m/z* (%) = 1292.1 [M^+]

HRMS (MALDI-TOF, DCTB) m/z: exp. Mass = 1292.1433 calc. Mass = 1292.1465.

43-trans1: Yield: 5.2 mg, 0.6 %.

^{1}H-NMR (300 MHz, $CDCl_3$): δ (ppm) = 4.58 (q, *J* = 7.4 Hz, 16H, $-OCH_2$), 1.59 (t, *J* = 7.1 Hz, 24H, $-CH_3$).
^{31}P-NMR (122 MHz, $CDCl_3$, ref. H_3PO_4 = 0.00 ppm): δ (ppm) = 16.07 (s).
43-trans2: Yield: 38.7 mg, 4 %.

^{1}H-NMR (300 MHz, $CDCl_3$): δ (ppm) = 4.87-4.23 (m, 16H, $-OCH_2$), 1.59 (m, 24H, $-CH_3$).
^{31}P-NMR (122 MHz, $CDCl_3$, ref. H_3PO_4 = 0.00 ppm): δ (ppm) = 16.12 (d, *J* = 8.1 Hz), 15.38 (d, *J* = 8.0 Hz).

43-*trans3*: Yield: 85.3 mg, 9 %.

^{1}H-NMR (300 MHz, $CDCl_3$): δ (ppm) = 4.62-4.24 (m, 16H, $-OCH_2$), 1.58 (t, *J* = 7.6 Hz, 6H, $-CH_3$), 1.49 (t, *J* = 7.8 Hz, 6H, $-CH_3$), 1.48 (t, *J* = 7.8 Hz, 6H, $-CH_3$).
^{31}P-NMR (122 MHz, $CDCl_3$, ref. H_3PO_4 = 0.00 ppm): δ (ppm) = 15.59 (s).

43-*trans4* + **43**-*e*: Yield: 67.2 mg, 7 %.

43-trans4:

^{1}H-NMR (300 MHz, $CDCl_3$): δ (ppm) = 4.53-4.07 (m, 16H, $-OCH_2$), 1.54-1.14 (m, 24H, $-CH_3$).
^{31}P-NMR (122 MHz, $CDCl_3$, ref. H_3PO_4 = 0.00 ppm): δ (ppm) = 15.55 (dd, J_1 = 14.6 Hz, J_2 = 10.2 Hz).
43-*e*:

^{1}H-NMR (300 MHz, $CDCl_3$): δ (ppm) = 4.46-4.23 (m, 16H, $-OCH_2$), 1.49-1.26 (m, 24H, $-CH_3$).
^{31}P-NMR (122 MHz, $CDCl_3$, ref. H_3PO_4 = 0.00 ppm): δ (ppm) = 15.58 (s), 15.55* (dd, J_1 = 14.6 Hz, J_2 = 10.2 Hz).
*signal corresponding to **43**-*trans4* impurity.

Phosphonic acid fullerene derivative, monoadduct (**39**)

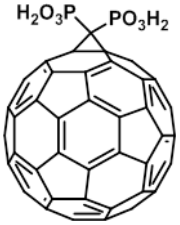

Fullerene **42** (21.8 mg, 0.022 mmol) were dissolved into CCl_4 (5 mL) and was warmed up to 40 ºC. Trimethylsilyl iodide was added dropwise (10 μL, 0.7 mmol) and was reacted for 45 min. Water (10 mL) was added at rt and was left for additional 30 min. The two phases were separated and the organic layer was washed with water (2 x 5 mL). Combined organic phases were then subjected to ion exchange with Amberlite IR-120 (plus) resine, and subsequently evaporation of the solvent under reduced pressure. The resulting solid was crushed with acetone. Yield: 18.7 mg, 96 %.

Mp: >250 ºC

IR:

Ms:

Phosphonic acid fullerene derivative, monoadduct (**40**)

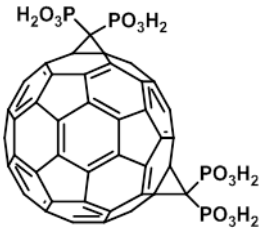

Fullerene **43**-*trans3* (175.3 mg, 0.135 mmol) were dissolved into CCl_4 (10 mL) and was warmed up to 40 ºC. Trimethylsilyl iodide was added dropwise (0.4 mL, 0.25 mmol) and was reacted for 45 min. Water (10 mL) was added at rt and was left for additional 30 min. The two phases were separated and the organic layer was washed with water (2 x 5 mL). Combined organic phases were then subjected to ion exchange with Amberlite IR-120 (plus) resine, and subsequently evaporation of the solvent under reduced pressure. The resulting solid was crushed with acetone. Yield: 125.5 mg, 87 %.

Mp: >250 ºC

IR:

Ms

3.6.3. **ZnPc-fullerene derivatives titrations**

3.6.3.1. Absorption and fluorescence titrations of **31**-**39**

A solution of known concentration of ZnPc was titrated by adding increasing amounts of a mixture of fullerene and ZnPc, the latter in the same concentration, in order to maintain the final ZnPc concentration constant. An additional absorption spectra of the fullerene was also recorded and subsequently substracted from the corresponding ZnPc-fullerene spectra, in order to show exclusively the ZnPc to ZnPc-fullerene transition. Fluorescence titration was recorded in a similar way, without substracting the fullerene spectra, because shows no emission in the optical window employed.

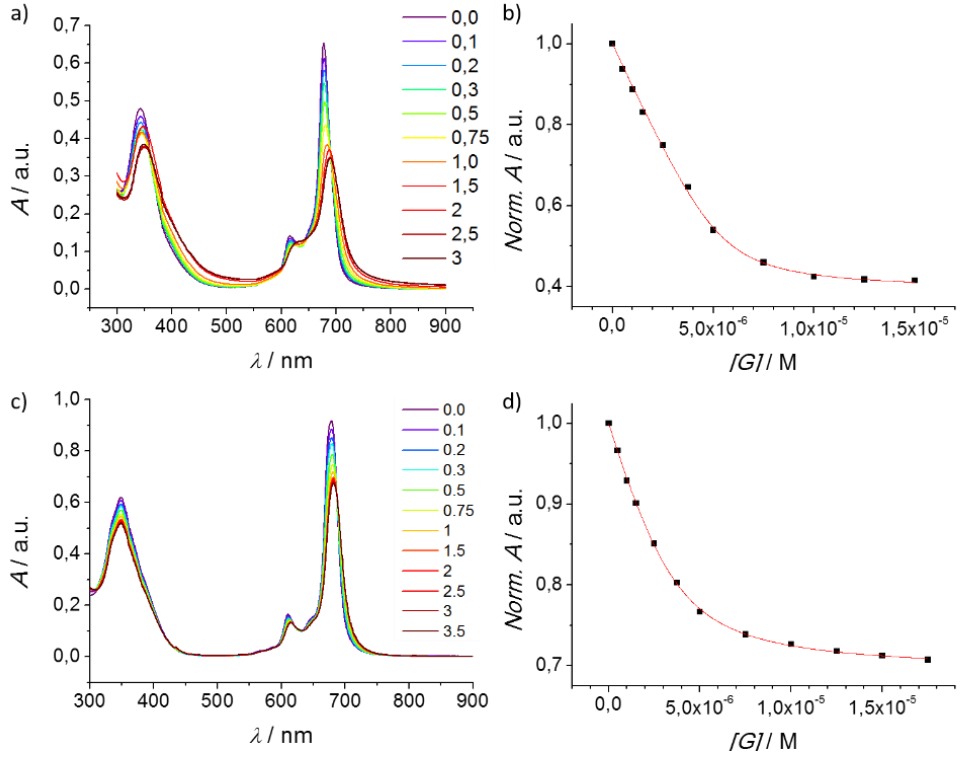

Figure 91: Absorption spectra of **31-39** in water/DMSO/TEA (95:5:1) (a) and normalized absorption at 677.5 nm (b). ZnPc **31** concentration: 5.0 x 10^{-6} M. Absorption spectra of **31-39** in DMSO (c) and normalized absorption at 677.5 nm (d). ZnPc **31** concentration: 5.0 x 10^{-6} M.

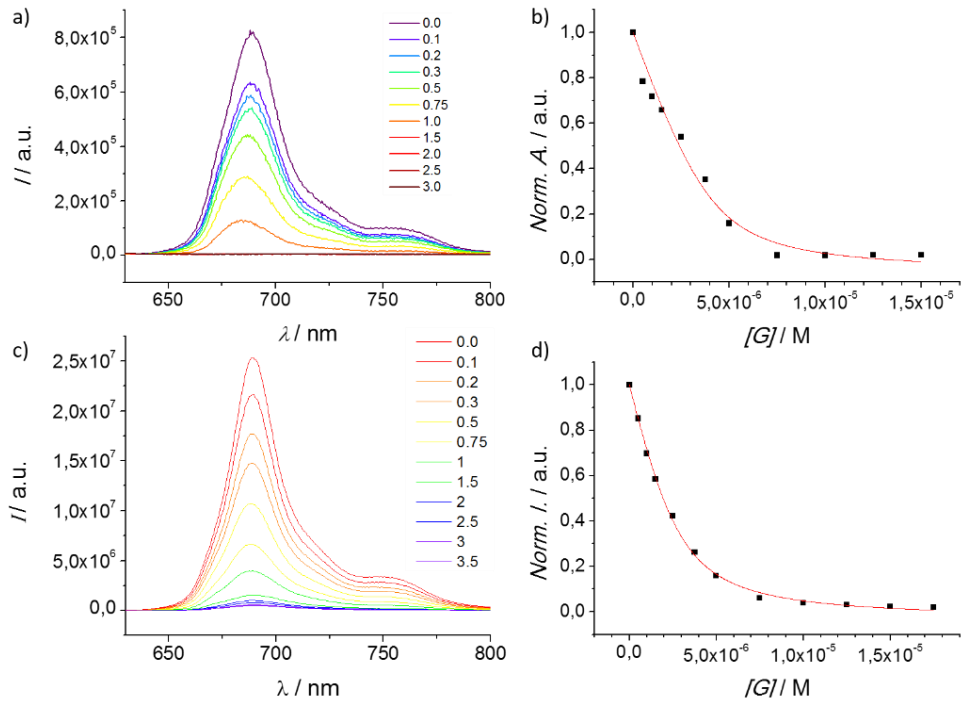

Figure 92: Emission spectra of **31-39** in water/DMSO/TEA (95:5:1) (a) and normalized emission intensity at 689.0 nm (b), exciting at 615 nm. ZnPc **31** concentration: 5.0 x 10^{-6} M. Emission spectra of **31-39** in DMSO (c) and normalized emission intensity at 690 nm (d), exciting at 615 nm. ZnPc **31** concentration: 5.0 x 10^{-6} M.

3.6.3.2. Absorption titrations of **32**-**39**

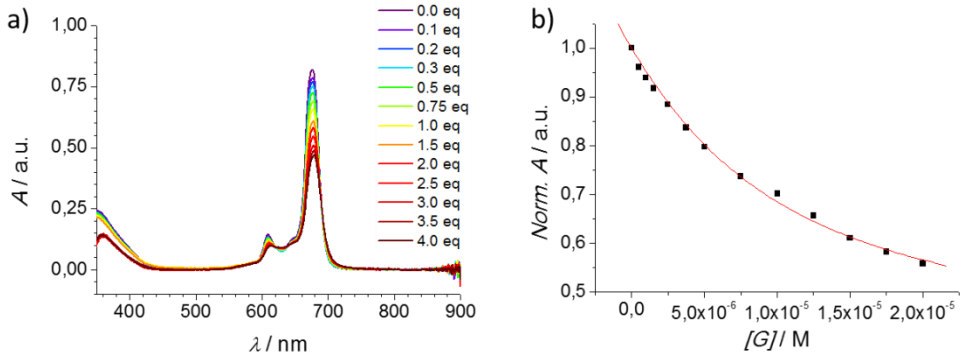

Figure 93. Absorption spectra of **32-39** in DMSO (a) and normalized absorption at 675.5 nm (b). ZnPc **32** concentration : 5.0 x 10^{-6} M.

3.6.3.3. Absorption and fluorescence titrations of **31**-**40**

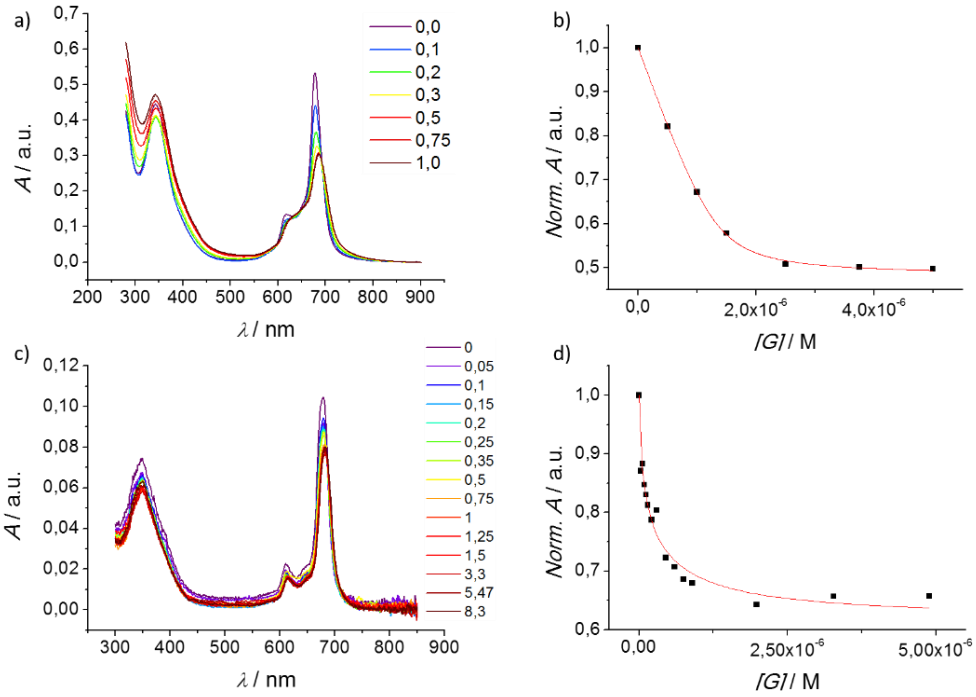

Figure 94. Absorption spectra of **32-39** in water/DMSO/TEA (95:5:1) (a) and normalized absorption at 677.5 nm (b). ZnPc **32** concentration: 5.0 x 10^{-6} M. Absorption spectra of **32-39** in DMSO (c) and normalized absorption at 677.5 nm (d). ZnPc **32** concentration: 5.0 x 10^{-7} M.

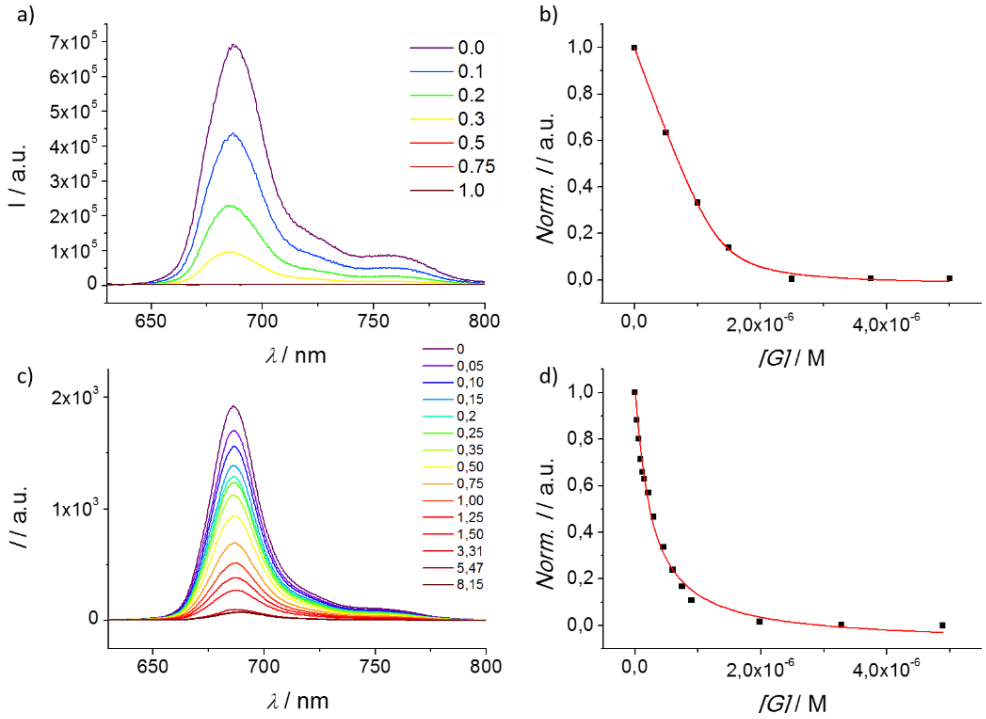

Figure 95. Emission spectra of **32-39** in water/DMSO/TEA (95:5:1) (a) and normalized emission intensity at 689.0 nm (b), exciting at 615 nm. ZnPc **32** concentration: 5.0 x 10^{-6} M. Emission spectra of **31-39** in DMSO (c) and normalized emission intensity at 690 nm (d), exciting at 615 nm. ZnPc **32** concentration: 5.0 x 10^{-7} M.

Resumen y Conclusiones

Resumen y conclusiones

Durante las tres últimas décadas, la nanociencia se ha convertido en uno de los temas más candentes en ciencia, generando un gran impacto en una amplia variedad de áreas, tales como la medicina, las tecnologías de conversión de energía, ciencias ambientales, informática, comunicaciones o industria pesada.

En el campo de la nanomedicina, los materiales nanoestructurados presentan numerosas ventajas y, en particular, en el campo de la nanooncología. Una de las principales dificultades en el tratamiento de esta enfermedad es la amplia distribución genética de la misma, incluso dentro del mismo paciente. La nanomedicina, y la nanooncologia en particular, presenta una amplia variedad de estrategias respecto a la oncología tradicional, facilitando terapias personalizadas que se pueden adaptar a cada individuo. El diseño de un fármaco multifuncional es consecuencia de la adecuada selección de los componentes activos, bien para el diseño de un agente de contraste multimodal, en el que se incluyan dos o más agentes de contraste para diversas técnicas, o bien la combinación de agentes de contraste con agentes terapéuticos, dando como resultado un fármaco teranóstico (aquel que permite tanto terapia como diagnosis en la misma formulación). Actualmente, de entre todas las variedades terapéuticas disponibles, la terapia fotodinámica (PDT, *photodynamic therapy*) destaca entre las más prometedoras. Esta tecnología médica consiste en la interacción entre tres agentes esenciales: una molécula fotoactiva o un fotosensibilizador (PS, *photosensitizer*), luz de una adecuada longitud de onda y oxígeno molecular. La iluminación del PS con luz a la adecuada longitud de onda provoca su excitación al estado triplete excitado, desde donde interactúa con el oxígeno presente en el medio biológico, generando formas reactivas de oxígeno (ROS, *reactive oxygen species*) entre las cuales destaca el oxígeno singlete ($^1O_2$). Un aspecto clave de esta terapia consiste en la selectiva vehiculización del PS, activa o pasiva, típica de los materiales nanoestructurados. Adicionalmente, el $^1O_2$ es una especie clave en otras aplicaciones, tales como el tratamiento de aguas residuales, dispositivos de diagnóstico y como oxidante en síntesis orgánica.

Por otro lado, el desarrollo y optimización de nuevas formas de energía se ha visto fuertemente impulsada, debido a una creciente preocupación sobre el impacto negativo en el medioambiente de los subproductos derivados de los combustibles fósiles. En este sentido, la conversión directa de energía solar en eléctrica a través de dispositivos fotovoltaicos ha sido extensamente estudiada durante las últimas décadas.

Complementariamente a las células inorgánicas, que se encuentran actualmente en uso comercial, se han desarrollado nuevas configuraciones basadas en materiales orgánicos o en la combinación de ambos, presentando varias ventajas como ser fáciles de preparar mediante técnicas de fabricación en disolución, lo que reduce su coste de producción, la ausencia de materiales activos tóxicos y su flexibilidad y reducido peso, abriendo nuevas aplicaciones de las mismas. Adicionalmente, dentro de este último tipo de células ha surgido una nueva preocupación respecto a los disolventes empleados en la fabricación de estos dispositivos, siendo contaminantes al ser usados en grandes cantidades. Por ello, el desarrollo de sistemas fotoactivos solubles en agua representa una aproximación al desarrollo de dispositivos fotovoltaicos más respetuoso con el medio ambiente.

Las ftalocianinas (Pcs, *phthalocyanines*) macrociclos aromáticos formados por cuatro unidades de isoindol unidas mediante átomos de nitrógeno. Su estructura posee una nube de 18 electrones π distribuidos sobre los 16 átomos del anillo interno. Entre otras de sus utilidades, las Pcs son excelentes candidatas como PS gracias a su versatilidad química y sus excelentes propiedades fotofísicas tales como gran estabilidad, alto coeficiente de absorción molar en el la región del rojo e infrarrojo cercano del espectro visible, y altos rendimientos cuánticos de estado triplete excitado y fluorescencia, con largos tiempos de vida media de estos estados. Estas propiedades, así como la posibilidad de modificar de manera su estructura y por lo tanto sus propiedades electroquímicas mediante sustitución periférica convierte a estas moléculas en excelentes moléculas para (i) aplicaciones biomédicas (como PS para PDT), así como para (ii), dentro de los sistemas de conversión de energía, actuar como excelentes antenas absorbiendo luz y posteriormente transferir esa energía absorbida o electrones a un aceptor, en un proceso análogo a la fotosíntesis natural. A pesar de todo, estos macrociclos presentan dos principales desafíos: el primero es que, debido a la lipofilia del anillo central, la solubilidad en agua de estos macrociclos es limitada y, en segundo, una vez solubilizadas en medio acuoso, presentan una alta tendencia a la agregación. Todo esto restringe la eficiencia de los procesos relacionados con el estado excitado tales como la fluorescencia o la producción eficiente de $^1O_2$ a través del estado triplete. Ambos problemas pueden ser paliados mediante la sustitución en la periferia de las Pcs con grupos voluminosos y solubles en agua, que prevengan la agregación y doten de solubilidad en medios biológicos. Por otro lado, nuevas estrategias consisten en el desarrollo de nuevas formulaciones consistentes en la incorporación de Pcs en diferentes sistemas nanoestructurados biohíbridos, posibilitando la solubilidad en medio acuoso, así como la ruptura de la agregación y una elevada biocompatibilidad.

Por todo ello, el principal objetivo de la presente Tesis Doctoral consiste en la síntesis de nuevos derivados de ftalocianina de zinc (ZnPc) solubles en medio acuoso, tanto para su aplicación en nanomedicina como en sistemas de conversión de energía. Así, este trabajo se encuentra dividido en los siguientes tres capítulos:

En el **Capitulo 1** se describe la síntesis de nuevos derivados de ZnPc solubles en agua, enfatizando nuestro interés en aquellos con sustituyentes amonio y piridinio. Estos últimos han sido los más empleados, debido a su versatilidad sintética que presentan previa cuaternización.

En la primera sección dentro de este capítulo se describe la síntesis de una serie de ZnPcs sustituidas simétrica y asimétricamente con derivados sulfónicos, mediante la combinación de diversas metodologías anteriormente descritas. Estas moléculas, así como su composición regioisomérica, han sido caracterizadas en detalle, junto con sus propiedades electroquímicas para posteriormente ser empleadas como materiales fotoactivos en células solares orgánicas procesadas en medio acuoso, tal y como se describe en el Capítulo 3.2.

La segunda sección está dedicada a la síntesis y caracterización de ZnPcs con sustituyentes trimetilamonioetilsulfanil, tanto simétrica como asímetricamente sustituidas. En particular, esto ha permitido el estudio de la inserción de la ZnPc **6** en micelas anionicas acuosas ha sido evaluada, así como el efecto desagregante que esto produce en el PS. Esta ZnPc ha sido estudiada para su incorporación sistemas multimodales con un alto potencial teranóstico, tal y como se describe en el Capitulo 2.2. Adicionalmente, se ha estudiado el efecto que produce el intercambio del contraanión de esta molécula en su agregación, obteniéndose nanopartículas orgánicas mediante el método de reprecipitación, si bien estas presentan una limitada estabilidad. Dentro de este capítulo se abordó la síntesis de derivados funcionales asimétricos de tipo A_3B, con escaso éxito debido a las dificultades en la purificación de estos compuestos, lo que nos llevó a un cambio de diseño en los sustituyentes catiónicos.

La tercera sección se encarga de la síntesis y caracterización de derivados de piridina, bien en su versión simétrica (ZnPc **16** y **17**), así como las versiones asímetricas de esta última, las cuales han sido purificadas gracias a la inclusión del grupo alifático voluminoso *terc*-butilfenilo. La caracterización electroquímica de esta serie ha revelado el

efecto electrón-atractor de estos grupos, haciendo así de estas ZnPcs moléculas aceptoras de electrones en conjunción con nanotubos de carbono, tal y como se recoge en el Capítulo 3.3. Adicionalmente a este trabajo, se ha sintetizado análogos de ZnPc **17**, usando grupos trietilenglicol en vez de metilos en la cuaternización, estudiando así el efecto de una esfera de solvatación neutra.

En cuarto y último lugar, se han sintetizado análogos de estas últimas ZnPcs que presentan derivados de pireno en los grupos piridinio (ZnPc **31**). Estos derivados presentan un tipo de agregación sin precedentes en medio acuoso (agua/DMSO 95:5), que ha sido caracterizado mediante absorción y fluorescencia con gradientes de temperatura y microscopía de transmisión electrónica (TEM, *transmission electron microscopy*), resultando en un mecanismo de polimerización isodésmico. Las propiedades espectroelectroquímicas de estos agregados han sido estudiados en detalle durante una estancia predoctoral en el laboratorio del Prof. Dirk M. Guldi en Erlangen (Alemania), tal y como se describe en el Capítulo 3.4.

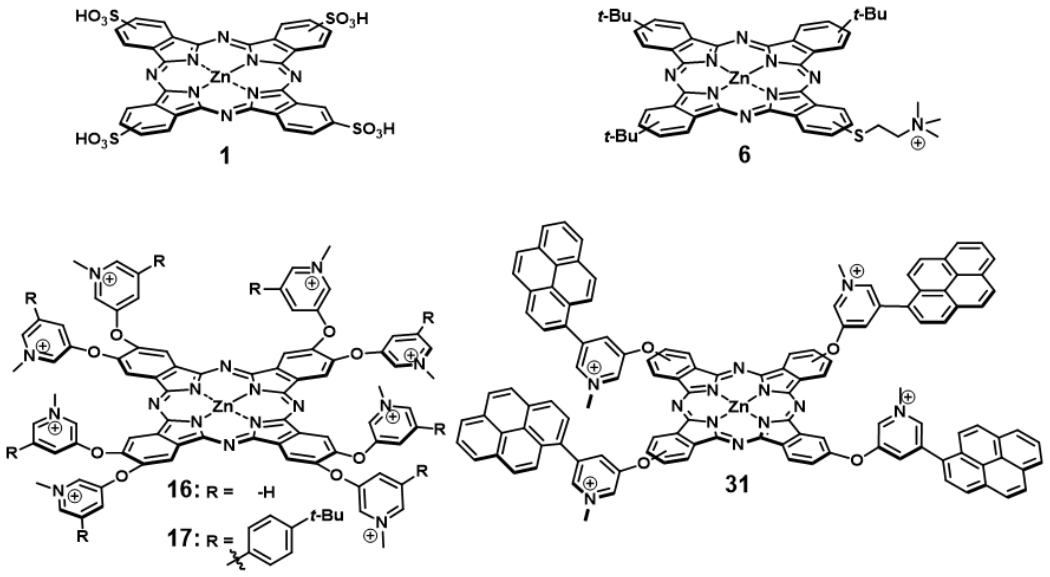

Figura 1: ZnPcs más representativas sintetizadas durante la presente tesis. Los contraaniones no se muestran por motivos de claridad.

El **Capítulo 2** está dedicado a la preparación de tres materiales biohíbridos diferentes, mediante la combinación de ZnPcs catiónicas solubles en agua con biomoléculas o disponibles comercialmente o, en su defecto, de fácil preparación. Estas nanoestructuras han sido seleccionadas cuidadosamente, con el objetivo de mantener o incluso mejorar las extraordinarias características de las ZnPcs, mediante desagregación de las mismas en medios acuosos, además de resultar materiales biocompatibles y monodispersos, dando lugar a sistemas fotoactivos nanoestructurados. Estas biomoléculas son cápsides virales de *cowpea chlorotic mottle virus* (CCMV), apoferritina (aFt) y nanocristales de celulosa (CNCs, *cellulose nanocrystals*). Para la síntesis de estos materiales se ha empleado una aproximación supramolecular que, si bien resulta una estrategia desafiante, permite preparar los materiales de un modo más directo, sencillo y, por lo tanto, económico para futuras aplicaciones comerciales.

En la primera sección de este capítulo se discute un novedoso método de preparación de partículas virales (VLPs, *virus-like particles*), consistentes en una cápside viral de CCMV conteniendo en su interior micelas paramagnéticas cargadas con ZnPcs anfífilas. Este trabajo, realizado en colaboración con el laboratorio del Prof. Jeroen J.L.M. Cornelissen en Twente (Holanda). La formación de estos materiales multimodales discurre mediante un proceso jerárquico de autoensamblaje en el que la anteriormente sintetizada ZnPc **6** se incorpora en micelas paramagnéticas de Gd-DOTAC10 que, a su vez, hacen de plantilla para el autoensamblaje de partículas proteicas virales de CCMV. Las ventajas de esta aproximación consisten en (i) la estabilización de las micelas por debajo de su concentración crítica, (ii) la ruptura en la agregación del cromóforo, lo que recupera sus propiedades fotofísicas como la generación efectiva de $^1O_2$ y (iii) permite una elevada carga micelar dentro de la cápside, aumentando el factor de relajación r_1 de las mismas, lo que se traduce en un contraste mediante resonancia magnética mejorado. En este respecto, si bien las propiedades como agente de contraste y terapéuticas de estas VLPs han de ser estudiados en mayor profundidad, este trabajo representa el primer paso hacia el uso de cápsides proteicas autoensambladas como agentes de contraste multimodales y teranósticos.

La segunda sección de este capítulo describe el desarrollo de un protocolo de ensamblaje jerárquico entre colorantes orgánicos y cajas proteicas en estructuras cristalinas ternarias. Esta estrategia se basa en la formación de un complejo supramolecular, formado por el reconocimiento entre la anteriormente sintetizada ZnPc **16** y un derivado tetraanionico comercial, dirigido por interacciones electrostáticas y de tipo

π-π. Este complejo tetraanionico se une a las regiones negativamente cargadas de la caja proteica de aFt, actuando como pegamento molecular y desencadenando la cocristalización de ambas funcionalidades. Los cristales resultantes son biohíbridos fotoactivos y robustos, que retienen la emisión de los cromóforos y son capaces de generar $^1O_2$ sin autodegradarse. Adicionalmente, estos cristales de estructura cúbica centrada en las caras, con diámetros superiores a 100 µm, pueden ser desensamblados mediante el aumento de concentración de electrolito en el medio. Este tipo de materiales puede ser empleados, por ejemplo, en el desarrollo de agentes reciclables y medioambientalmente benignos para tratamiento de aguas residuales, dispositivos de diagnóstico of cristales fotocatalíticos para procesos de oxidación en síntesis orgánica. Adicionalmente, esta aproximación modular puede ser fácilmente extensible a otros pigmentos orgánicos catiónicos que presenten diferentes propiedades optoelectrónicas, o aFt cargadas con diversas funcionalidades.

En tercer y último lugar, se ha descrito la preparación y caracterización de complejos supramoleculares de ZnPcs catiónicas y CNCs, como una nueva clase de PS nanoestructurados para la fotogeneración de $^1O_2$. Este trabajo, llevado a cabo durante una estancia predoctoral en el laboratorio del Prof. Mauri A. Kostiainen en Espoo (Finlandia) sigue una estrategia basada en la inmovilización mediante interacciones electrostáticas entre derivados catiónicos de ZnPc y la superficie no modificada de los CNCs, que presentan grupos sulfónicos como consecuencia de su síntesis. Los híbridos resultantes han sido caracterizados mediante diversas técnicas, demostrando que no solo la agregación de la ZnPc, si no la tendencia a la agregación de los CNCs juegan un papel clave en la producción de $^1O_2$. Como resultado de esta optimización, los híbridos **16**-**CNC** se presentan como sistemas nanocristalinos fotosensibilizados altamente eficientes.

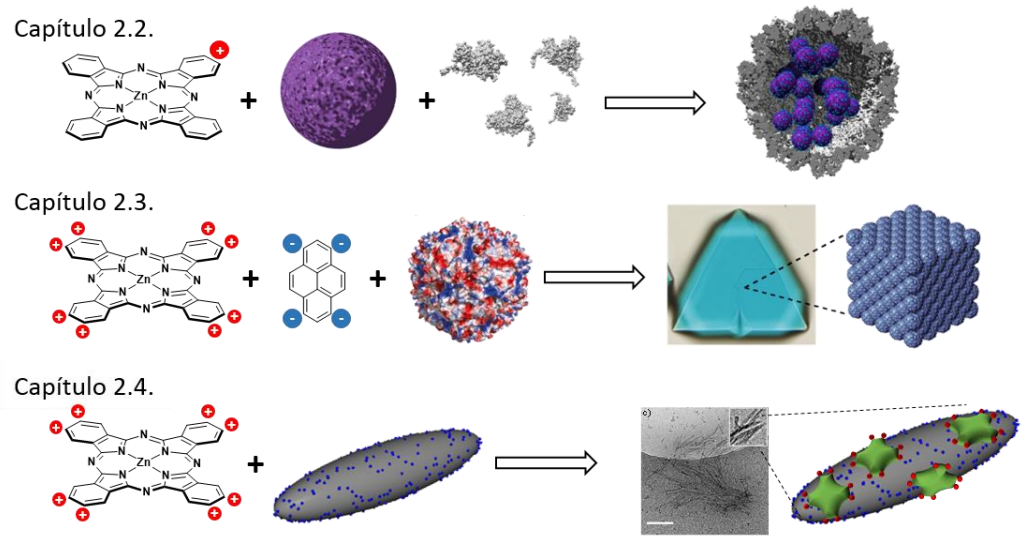

Figura 2: Representación esquemática de la preparación de los materiales biohíbridos descritos en el Capítulo 2.

El **Capítulo 3** está enfocado al desarrollo de tres diferentes aproximaciones a sistemas fotovoltaicos procesados a partir de ZnPcs solubles en agua, en combinación o no con nanoestructuras de carbono como los nanotubos de carbono y los derivados de fullereno.

En el primer ejemplo, se ha demostrado la importancia del patrón de sustitución en ZnPcs sulfónicas para el rendimiento de los dispositivos fotovoltaicos fabricados. Este descubrimiento ha conllevado una mejora significativa respecto al precedente anteriormente descrito, mediante el ajuste de los niveles energéticos del dador ftalocianínico, logrando una fotooxidación más favorable del aceptor de electrones. El número de sustituyentes de la ZnPc afecta también a la morfología de las capas activas, que a su vez afecta al rendimiento de los dispositivos. Una vez alcanzado este primer punto, se estudiará en un futuro la síntesis de un aceptor de electrones soluble en agua para la completa preparación de dispositivos mediante procesado en medio acuoso.

En el segundo ejemplo de este capítulo se presenta una nueva aproximación a la producción de pares dador-aceptor de electrones solubles en agua, consistentes en nanotubos de carbono como dadores y ZnPcs como aceptores. Esta combinación de propiedades no tiene precedentes para esta combinación de componentes fotoactivos. La

clave en nuestra estrategia fue la inmovilización de las ZnPcs **16** y **17** a la superficie aromática de los nanotubos de carbono, mediante interacción supramoleculares, evitando así modificar la naturaleza electrónica de estos últimos. Adicionalmente, estos híbridos han sido probados en una primera aproximación en dispositivos fotovoltaicos, abriendo la puerta a células solares procesadas en medio acuoso en su totalidad.

Para concluir el capítulo, se han preparado dos sistemas dador-aceptor sin precedentes, basados en la combinación de la ZnPc **31** tetracatiónica como dador de electrones y dos derivados tetra- y octacaniónico de fullereno como aceptores de electrones, formando complejos de estequiometría 1:1 y 2:1, respectivamente. Los híbridos supramoleculares resultantes han sido formados mediante la combinación de dos interacciones moleculares como son la atracción electrostática y las interacciones π-π, resultando en complejos fuertemente ligados. Adicionalmente, se han llevado a cabo estudios fotofísicos durante una estancia predoctoral en el laboratorio del Prof. Dirk M. Guldi en Erlangen (Alemania). Estos han permitidio caracterizar estado de separación de cargas $ZnPc^{\bullet+}$-$C_{60}^{\bullet-}$ mediante espectroscopia de absorción transitoria tanto en DMSO como en medio acuosa. Los procesos implicados en estos complejos están aún bajo discusión activa, si bien presentan resultados prometedores en el campo de la fotosíntesis artificial desarrollada en medio acuoso.

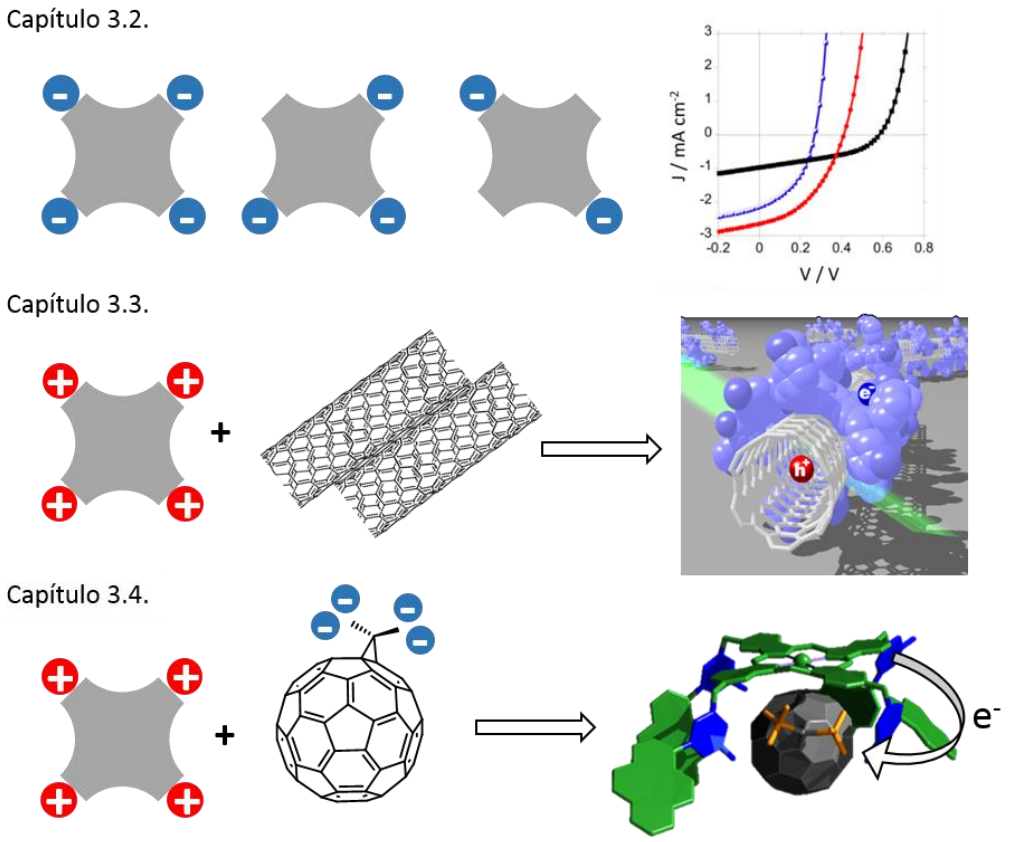

Figura 3: Representación esquemática de la preparación de los híbridos descritos en el Capítulo 3 para su aplicación en sistemas de conversión de energía.